



HAL
open science

Stratégie de réduction de modèle appliquée à un problème de fissuration dans un milieu anisotrope : application à la modélisation de la plasticité cristalline.

Walid Tezeghdanti

► To cite this version:

Walid Tezeghdanti. Stratégie de réduction de modèle appliquée à un problème de fissuration dans un milieu anisotrope : application à la modélisation de la plasticité cristalline.. Mécanique des solides [physics.class-ph]. Université Paris Saclay (COMUE), 2019. Français. NNT : 2019SACLN006 . tel-02130767

HAL Id: tel-02130767

<https://theses.hal.science/tel-02130767>

Submitted on 16 May 2019

HAL is a multi-disciplinary open access archive for the deposit and dissemination of scientific research documents, whether they are published or not. The documents may come from teaching and research institutions in France or abroad, or from public or private research centers.

L'archive ouverte pluridisciplinaire **HAL**, est destinée au dépôt et à la diffusion de documents scientifiques de niveau recherche, publiés ou non, émanant des établissements d'enseignement et de recherche français ou étrangers, des laboratoires publics ou privés.

A model reduction strategy to predict plasticity induced memory effects in fatigue crack growth in an anisotropic medium: application to crystal plasticity.

Thèse de doctorat de l'Université Paris–Saclay
préparée à l'École Normale Supérieure Paris–Saclay

École doctorale n°579 : Sciences Mécaniques et Energétiques,
Matériaux et Géosciences (SMEMAG)
Spécialité de doctorat : Solides, Structures et Matériaux

Thèse présentée à Cachan, le 26 février 2019, par

M. Walid Tezeghdanti

Composition du Jury :

Mme. Marion Risbet		
Professeure, Université de Technologie de Compiègne		Présidente du jury
M. Nicolas Moës		
Professeur, École Centrale Nantes		Rapporteur
M. Henry Proudhon		
Chargé de recherche CNRS, Centre des Matériaux Mines Paristech		Rapporteur
M. David Nowell		
Professeur, Imperial College London		Examineur
M. Julien Réthoré		
Directeur de recherche CNRS, École Centrale Nantes		Examineur
Mme. Veronique Doquet		
Directrice de recherche CNRS, École Polytechnique		Examinatrice
Mme. Sylvie Pommier		
Professeure, École Normale Supérieure Paris–Saclay		Directrice de thèse
M. Yoann Guilhem		
Maître de conférences, École Normale Supérieure Paris–Saclay		Co-encadrant de thèse

Titre : Stratégie de réduction de modèle pour prédire les effets mémoire de la plasticité en fissuration par fatigue dans un milieu anisotrope: application à la plasticité cristalline.

Mots clés : Fissuration par fatigue, Plasticité condensée, Réduction de modèle, Anisotropie, Plasticité cristalline

Résumé : Les aubes des turbines à haute pression des réacteurs d'avion subissent des chargements complexes dans un environnement réactif. Prédire leur durée de vie peut nécessiter une approche en tolérance aux dommages basée sur la prédiction de la propagation d'une fissure supposée. Mais cette approche est confrontée au comportement non linéaire sous des chargements à amplitudes variables et au coût énorme des calculs elasto-plastiques des structures 3D complexes sur des millions des cycles. Dans ce cadre, un modèle incrémental de fissuration a été proposé. Ce modèle est basé sur la plasticité comme mécanisme principal de propagation de fissure par fatigue pure. Cette modélisation passe par une réduction de modèle de type POD. La plasticité en pointe de la fissure est alors modélisée par un nombre réduit de variables non locales $(\underline{\dot{K}}^\infty, \underline{\dot{\rho}})$ et des variables internes. Un ensemble d'hypothèses doit être respecté pour garantir la validité de cette modélisation. Pour décliner ce modèle dans le cas d'un matériau anisotrope représentatif du comportement des monocristaux, une première étude a été faite sur le cas d'une élasticité cubique avec de la plasticité de Von-Mises. Une stratégie a été proposée pour identifier un modèle matériau basé sur les facteurs d'intensité non locaux $(\underline{\dot{K}}^\infty, \underline{\dot{\rho}})$. Cette stratégie comporte une détermination de la fonction critère basée sur les solutions élastiques en anisotrope. L'étude des directions d'écoulement plastique avec les variables non locales montre une forte dépendance à l'anisotropie élastique du modèle même avec une plasticité associée de Von-Mises. La stratégie comporte également une identification des variables internes. Dans la deuxième partie, le problème d'une fissure avec un modèle de plasticité cristalline a été traité. L'activation de différents systèmes de glissement a été alors prise en compte dans la modélisation. Finalement, différentes méthodologies ont été explorées en vue de transposer le modèle local de plasticité cristalline à l'échelle non locale de la région en pointe de la fissure.



Title: A model reduction strategy to predict plasticity induced memory effects in fatigue crack growth in an anisotropic medium: application to crystal plasticity.

Keywords: Fatigue crack growth, Condensed plasticity, Model reduction, Anisotropy, Crystal plasticity

Abstract: The fatigue life prediction of high pressure turbine blades may require a damage tolerance approach based on the study of possible crack propagation. The nonlinear behavior of the material under complex nonproportional loadings and the high cost of running long and expensive elastic-plastic FE computations on complex 3D structures over millions of cycles are some major issues that may encounter this type of approach. Within this context, an incremental model was proposed based on plasticity as a main mechanism for fatigue crack growth. A model reduction strategy using the Proper Orthogonal Decomposition (POD) was used to reduce the cost of FEA. Based on a set of hypotheses, the number of the degrees of freedom of the problem is reduced drastically. The plasticity at the crack tip is finally described by a set of empirical equations of few nonlocal variables ($\underline{\dot{K}}^\infty, \dot{\rho}$) and some internal variables. In order to apply this modeling strategy to the case of anisotropic materials that represent the behavior of single crystals, a first study was done with cubic elasticity and a Von-Mises plasticity. Elastic and plastic reference fields, required to reduce the model, were determined. Then, a material model of the near crack tip region was proposed based on nonlocal intensity factors ($\underline{\dot{K}}^\infty, \dot{\rho}$). A yield criterion function was proposed based on Hoenig's asymptotic solutions for anisotropic materials. The study of plastic flow directions with the nonlocal variables of the model shows a strong dependency on the cubic elasticity. A strategy to identify internal variables is proposed as well. In the second part, a crystal plasticity model was implemented. The activation of different slip systems was taken into account in the model reduction strategy. A kinematic basis was constructed for each slip system. Finally, a strategy was proposed to transpose the local crystal plasticity model to the nonlocal scale of the crack.



Contents

Nomenclature	10
Introduction	13
1 State of the art	17
1.1 Defect tolerant design and LEFM	18
1.1.1 Defect tolerant approach	18
1.1.2 Fracture mechanics: a brief history	19
1.1.3 Elements for fracture mechanics	20
Stress intensity factors	20
Griffith's energy	21
J-integral: a path independent integral	22
1.1.4 Crack tip region	23
1.2 Fatigue crack growth	24
1.2.1 Mechanisms of propagation	25
1.2.2 Fatigue crack growth under constant amplitudes	26
1.2.3 Crack closure effect	27
1.2.4 Crack growth under variable amplitudes fatigue	28
1.2.5 Cycle counting methods	29
1.3 Incremental plasticity model – Pommier	29
1.3.1 Hypotheses	30
1.3.2 Methodology	31
1.3.3 Evolution of the model	33
1.4 Anisotropy	34
1.4.1 Composites	35
1.4.2 Single crystals	35
2 Model reduction protocol and 2D application case	39
2.1 State of the art	40
2.1.1 Model reduction	40
Karhunen Loève decomposition	40

2.1.2	Asymptotic elastic solutions	41
	Isotropic: Westergaard's asymptotic solution	42
	Orthotropic: Sih, Paris and Irwin's solution	42
2.2	Incremental model	43
2.2.1	Hypotheses	43
2.2.2	Kinematic field decomposition	44
2.3	Protocol for the kinematic basis	46
2.3.1	Finite element model and mesh	46
2.3.2	Material	47
2.3.3	Kinematic fields extraction and correction	49
2.3.4	Elastic reference fields	50
2.3.5	Complementary reference fields based on the POD approach	52
2.3.6	Validity of the approach	54
	Minimum loading range	54
	Maximum loading range	55
	Example	55
2.3.7	Reconstruction error	55
2.4	Condensed material model for the near crack tip region	56
2.4.1	Yield criterion	57
	Local Von-Mises criterion	57
	Extended Von-Mises criterion under LEFM	58
2.4.2	Yield surface	60
2.4.3	Plastic flow directions	63
2.5	Conclusion	64
3	Mixed $I+II+III$ modes with cubic elasticity and Von-Mises plasticity	67
3.1	State of the art	68
3.1.1	Influence of the crystallographic orientation	68
3.1.2	Asymptotic elastic solutions and resolution formalisms	69
3.2	Material model and finite element implementation	70
3.2.1	Cubic elasticity and studied material orientations	70
	Constitutive model	70
	Material orientation	71
	Stiffness and compliance tensors rotation	72
	Hoening's analytical solution	73
3.2.2	FE Model: mesh and boundary conditions	75
	Stress intensity factors extraction	77
	Stress intensity factors monitoring	80
3.3	Multiscale approach	80
3.4	Kinematic basis	81
3.4.1	Elastic fields and analytical solution	81
3.4.2	Complementary plastic reference fields	90
	Decomposition	90
	Extraction method	91
	Rescaling and results	94
	Orthogonality and reconstruction	98
3.4.3	Reconstruction errors	98
	Results	99

3.4.4	Other yield criteria	103
3.5	Incremental material model	104
3.5.1	Yield locus	104
3.5.2	FE simulation: ellipsoid exploration	108
	Ellipsoid loading path	108
	Reconstruction errors	109
	Plastic flow directions	109
3.5.3	FE simulation: Ramified exploration	118
	Loading path	118
3.5.4	Plastic flow directions	119
3.6	Conclusion	122
4	Reduced basis of a crystal plasticity model	123
4.1	State of the art	124
4.1.1	Material and microstructure	124
4.1.2	The Schmid law	125
4.1.3	Models	126
4.2	Material model and finite element computational tools	127
4.2.1	Crystallographic phenomenological model	127
	Hypotheses	128
	Formulation of the model	128
4.2.2	Numerical model	130
4.2.3	Cubic elasticity and crystal plasticity	132
4.2.4	Z-mat (Integration method, material orientation and stress intensity factors (SIF) determination)	133
	Stress intensity factors	133
4.3	Kinematic basis	135
4.3.1	Elastic reference fields	136
4.3.2	Complementary reference fields: Geometric decomposition by fracture modes	138
	Validity of the approach	138
	Radial and angular functions	140
	Reconstruction errors	144
4.3.3	Complementary reference fields: Decomposition into fracture modes and into slip systems	146
	Results	146
	Reconstruction errors	152
4.4	Yield surface	154
4.4.1	In-plane exploration	155
	Exploration path	155
	Simulations and results	157
4.4.2	3D exploration	159
	Exploration path and speedup analysis	159
	Simulations and results	160
	Exploration of other yield planes	164
4.4.3	Yield domain	166
4.5	Updated reference fields	168
4.5.1	Decomposition principle	168

4.5.2	Reference fields	168
4.5.3	Schmid factor based on Hoenig analytical solutions and slip systems	
	“nonlocal” dominance criterion	173
	Dominant slip system	173
	Dominance criterion	173
	Hoenig’s stress solution and corresponding Schmid factor	174
	Comparison between theoretical, numerical and experimental analyses	175
	Non linear basis	179
4.6	Conclusion	186
	Conclusion and perspectives	187
	Appendices	191
	A Asymptotic linear elastic solutions	193
	B Interaction integral method for a general anisotropic case	201
	Bibliography	205

Acknowledgment

This PhD work was developed at the laboratory of Mechanics and Technology LMT at the ENS Paris-Saclay. I would like to thank the director Mr Frederique Ragueneau for receiving me at the LMT. I am grateful also to the responsible of the material sector Mr Olivier Hubert not only for receiving me but also for his help and precious advices since the beginning of this journey.

I would like to thank the members of my PhD defense committee for accepting to judge my work. I was honored to have Mr Nicolas Moes and Mr Henry Proudhon as reviewers of my thesis. Their feedbacks were very precious. They allowed me to have a different vision of my work. I would like to thank Mme Marion Risbet for accepting to be the president of the jury and Mme Veronique Doquet, Mr David Nowell and Mr Julien Réthoré for examining my work and for the discussion we had.

I'm grateful to Mme Sylvie Pommier, this work wouldn't have seen the light without her. Thank you Sylvie for always believing in your students, giving them the flexibility to express and apply their ideas and defending their works. Thank you also for transmitting a part of your immense knowledge through all the long discussions we had. You always managed to make difficult approaches look easy thanks to your teaching abilities. It was a real pleasure and an honor to work with you.

This PhD started as a Master 2 internship. The first contact I had was with Mr Yoann Guilhem who later became my PhD second supervisor. Thank you Yoann for everything; for your advices, for your time and for your help. I learned a lot from your multiple skills in mechanics, materials science and numerics. I'm honored to be your first PhD student and I wish you the best in your academic career.

Living away from home and family is not usually an easy task. In my case, I had the chance to have two different families:

A family at the LMT with friends from all over the world: Boubou, Besnik, Arturo, Bhimal, Oristis, Zvone, Ante, Sam ... Thank you guys for your support and for the funny moments we spent together to forget about the rush of life.

A family outside the LMT with my childhood friends: Wadie, Nejib, Rostom, Hamza, Skander, Haythem, Tawfik, Sabrine... Thank you guys for your help, encouragement and for the long discussions we had.

Last but not the least, I owe this achievement to my parents for their enormous help, sacrifices and care, to my brothers and sister for supporting me and to my life partner, Ameni, for her care, love and encouragement.

*As time teaches me, it shows me my lack of knowledge.
And as I learn more, I learn more about my ignorance.*

كلما أدبني الدهر ... أراني نقص عقلي
وإذا ما أزددت علما ... زادني علما بجهلي

Nomenclature

Abbreviations

CTOD Crack Tip Opening Displacement.

CTSD Crack Tip Sliding Displacement.

FCC Face-Centered Cubic.

FE/FEA Finite Element/Finite Element Analysis.

KL Karhunen-Loeve decomposition.

LEFM Linear Elastic Fracture Mechanic.

POD Proper Orthogonal Decomposition.

SIF Stress Intensity Factor.

Crystallography

(hkl) Crystallographic plane.

$(hkl)[uvw]$ A slip system with (hkl) is the slip plane and $[uvw]$ the slip direction.

$[uvw]$ Crystallographic direction.

$\langle uvw \rangle$ Family of crystallographic directions.

$\gamma_{[uvw]}^{(hkl)}$ Orientation of the crystal with respect to the crack: (hkl) normal to the crack plane and (uvw) normal to the crack front.

$\{hkl\}$ Family of crystallographic planes.

Fields and functions

$f^{el}(r)$ Elastic radial dependency.

$f^{pl}(r)$ Plastic radial dependency.

$g_i^{el}(\theta)$ Elastic angular dependency of fracture mode i .

$g_i^{pl}(\theta)$ Plastic angular dependency of fracture mode i .

$\phi_i^{el}(\underline{x})$ Elastic reference field of fracture mode i .

$\phi_i^{pl,s}(\underline{x})$ Plastic reference field of fracture mode i and slip system s .

$\underline{\phi}^{pl,s}(\underline{x})$ Plastic reference field of slip system s .

$\underline{\phi}_i^{pl}(\underline{x})$ Plastic reference field of fracture mode i .

$\underline{v}^{FE}(\underline{x}, t)$ Finite element kinematic field.

$\underline{v}_i^{FE}(\underline{x}, t)$ Finite element kinematic field of a pure fracture mode i .

$\underline{v}_s^{FE}(\underline{x}, t)$ Finite element kinematic field with a one implemented slip system s .

Intensity factors

$\dot{K}_i(t)$ Rate of pseudo-elastic intensity factor of fracture mode i .

$\dot{\rho}_i(t)$ Rate of blunting intensity factor of fracture mode i .

$\dot{\rho}_i^s(t)$ Rate of blunting intensity factor of fracture mode i and slip system s .

$\dot{\rho}^s(t)$ Rate of blunting intensity factor of slip system s .

G_i Energy release rate of mode i .

K_i^∞ Nominal stress intensity factor of fracture mode i .

K_i^X Component i of the position of the yield domain in the nominal stress intensity factors space.

K_i^Y Size of the yield domain in the direction i in the nominal stress intensity factors space.

Operators

\dot{x} Rate of x .

$\Im(x)$ Imaginary part of x .

$\Re(x)$ Real part of x .

Notations and variables

$\underline{\underline{\mathbb{S}}}$ Compliance fourth order tensor.

$\underline{\underline{M}}, M_{ij}$ Matrix, second order tensor.

τ^s Resolved shear stress of slip system s .

$\underline{\underline{\mathbb{C}}}$ Stiffness fourth order tensor.

$\underline{\underline{\sigma}}$ Cauchy stress tensor.

$\underline{\underline{\sigma}}, \underline{\underline{\varepsilon}}, \underline{\underline{C}}$ Voigt notation.

\underline{x} Vector, field.

$\underline{\underline{\varepsilon}}$ Strain tensor.

Introduction

Life prediction of industrial components is a key point to prevent their service failures. Nowadays, manufacturers tend to have more precise life predictions in order to lower the safety margin which grants a good compromise between safety, economical and technological solutions. Fatigue is one of the major phenomena that concerns life predictions. It affects components subjected to cyclic loadings. High pressure turbine blades of jet engines are such components that work under very aggressive environments.

Within this context, the design of components subjected to fatigue requires a damage tolerance approach. This approach considers the existence of potential flaws in the structure under the most critical conditions (position, service loadings, environment, etc). Then it aims to study the growth of these cracks and the possibility of failure. Nevertheless, this approach encounters two main issues.

The first one is linked to the nonlinear behavior of the material under random nonproportional mixed modes loadings where the definition of fatigue cycle is no longer obvious. Thus, the direct use of conventional cycle-based models may not precisely estimate failure. Besides, anisothermal loadings and the coupling with other damage mechanisms such as oxidation present a challenge for this study.

Existing numerical simulation tools to model three-dimensional complex cracks under mixed fracture modes are mainly based on a linear elastic analysis. However, it is a matter of common knowledge that the plasticity developed at the near crack tip region affects significantly the fatigue crack propagation rate and direction. These statements lead to the second issue which is the lack of resources to run simulations on complex 3D structures over millions of fatigue cycles while taking into account the elastic-plastic behavior of the material.

In order to address these issues, Pommier and co-workers [[Pommier and Risbet, 2005](#)] [[Pommier and Hamam, 2007](#)] proposed an incremental model based on a set time-derivative equations. This model requires a set of hypotheses related to the geometry and kinematics of the crack tip region. One major hypothesis is assuming that pure fatigue crack growth is mainly plasticity-induced which introduces the crack tip blunting as a leading mechanism of crack propagation. This concept was already presented in many previous works that relate the crack growth to the Crack Tip Opening Displacement (CTOD).

In order to model crack tip plasticity while reducing computational costs, a multiscale approach based on a model reduction strategy was proposed. The kinematic field at the crack tip is hence described with a reduced number of degrees of freedom. This allows the modeling of the cyclic elastic-plastic behavior of the crack tip region based on a set of empirical equations written with a reduced number of nonlocal quantities. These quantities

will serve as input variables for the incremental study of crack propagation.

Many studies were previously done at the LMT (ENS Paris-Saclay, CNRS, Université Paris-Saclay), with various industrial partners, toward the establishment of this approach. These works tried to solve different multiphysical fatigue crack growth problems. For ductile materials, some works were developed for three-dimensional cracks under mixed fracture modes [Pommier and Hamam, 2007], [Pommier et al., 2009], [Fremy et al., 2012], oxidation under nonisothermal loadings [Ruiz-Sabariego and Pommier, 2009], generalized plasticity case [Zhang, 2016] and short cracks with T-stresses [Brugier, 2017]. An extension of the model to the case of quasi-brittle materials (mortar) [Morice, 2014] was made as well.

However, these studies were all developed for the case of isotropic materials. The work presented in this PhD thesis follows in the footsteps of these aforementioned studies and aims to further extend the approach to the case of an anisotropic material. In fact, a wide range of industrial components that require a damage tolerance design present an anisotropic behavior. For instance, many high pressure turbine blades are made out as a single crystal of Nickel base superalloy. This structure, in regards to its direction dependent behavior, creates a challenge in studying crack propagation in anisotropic materials. This behavior emerges in the linear elastic constitutive law as well as in the nonlinear response aided by the presence of easy slip planes and directions in the crystal.

Therefore, this work is presenting a strategy to describe crack tip plasticity of a three-dimensional stationary crack under mixed fracture modes $I + II + III$ in an anisotropic medium. The local plasticity model at the vicinity of the crack tip is transposed to the scale of the crack via a set of nonlocal intensity factors of elastic and plastic kinematic fields.

The focus on mixed fracture modes $I + II + III$ stems, on the one hand, from the variety of boundary conditions to which the structure can be subjected and the complexity of the geometry. On the other hand, the presence of the anisotropy may create a mixed fracture modes condition at the crack scale even under simple loadings such as uniaxial loading. Thus, it is more judicious to make a global study of crack under mixed fracture modes without decoupling them.

The strategy presented in this work can lead to a condensed modeling of crack tip plasticity. The final purpose of this nonlocal model is its implementation in an incremental model to study the crack growth in anisotropic materials. This approach can be directly applied to single crystals and composites, but also to polycrystalline materials.

The first chapter contains the scientific framework of this study. The history of linear elastic fracture mechanics and some fatigue crack growth models are briefly introduced. Then, the chapter presents the incremental model and it ends with a general discussion about the anisotropic behavior.

The second chapter presents the main ingredients of the model and the numerical protocol used in the model reduction. It gives an application case of mixed fracture modes $I + II$ for a cubic elasticity and Von-Mises isotropic plasticity. A 2D model with plane strain assumption is used. The study is restrained to some special cases of crystallographic orientations in order to ensure the mixture of only fracture modes $I + II$.

The third chapter generalizes the study presented in the second chapter. It extends the analysis to the 3D case with mixed fracture modes $I + II + III$ and a random material orientation but always characterized by a cubic elasticity and Von-Mises plasticity. The fourth chapter deals with the three-dimensional problem of mixed fracture modes $I + II + III$ in the case of a crystal plasticity model. Different methodologies are presented to take into account slip systems activity in the incremental model.

Chapter 1

State of the art

1.1 Defect tolerant design and LFM

1.1.1 Defect tolerant approach

Based on the understanding of Fracture Mechanics, the damage tolerant approach is mainly adopted by the aircraft, aerospace, land transportation and nuclear industries. This disciplinary field aims to predict the life of critical components and prevent their failure during service. Especially that in these sensitive industries, the destructive influence of cracks is a matter of common knowledge and service failures are susceptible to provoke disastrous consequences. Various cases of structural failures can be cited. Among these examples, the Liberty Ships failures may be the first that attracted the attention of mechanics and materials communities. Over 4000 of these cargo ships were mass produced during the World War II in different shipyards in the United States and Canada. Some of these ships, similar to the one presented in figure 1.1, experienced brittle fracture of the hull before even leaving the shipyard. In order to increase largely the production of these ships in short periods of time, engineers changed the construction method from the traditional time consuming riveting to electric-arc welding. These welding operations caused the modification of the micro-structure of the steel and increased its ductile-to-brittle transition temperature. They also created internal stresses in the material. These unexpected consequences of welding, combined with the poor design, led to the brittle failure of these ships under cyclic loadings, occasional peak loads, highly corrosive conditions and low temperature.

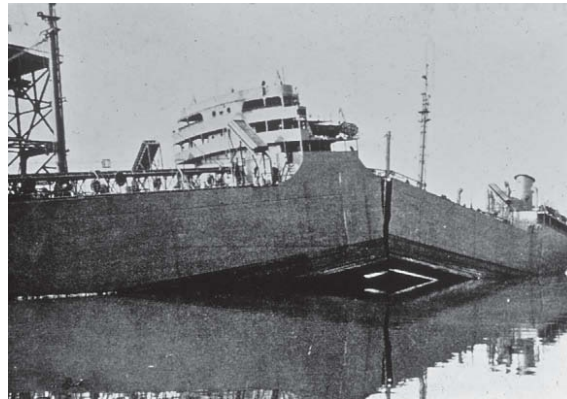


Figure 1.1: The Liberty ship S.S. Schenectady that failed in 1943 before leaving the shipyard [[Metallurgyandmaterials.wordpress.com](https://metallurgyandmaterials.wordpress.com), 2015].

Few years later, in the fifties, other structural failures occurred; those of the Comet I jet-propelled airplanes produced by British company Havilland. Many of these passengers aircraft crashed during service. After recurrent incidents, the certificate of airworthiness was withdrawn and the Comets were grounded. Tests were performed on one of these aircraft by applying cyclic loading under water in order to simulate pressurized flights. Some overloads were performed also each 1000 cycle interval and soon after a couple of thousands of cycles, the cabin failed. The crack initiated from the corner of the rectangular passengers' window and then propagated under fatigue loading. The rectangular shape of the windows was later replaced by oval shape in order to prevent the stress concentration in the corners. Soon after this, Paris [[Paris, 1961](#)] developed his fatigue crack growth law.

Some of these fatal failures were caused by inherent flaws and service-induced damages and others were caused by poor design. This was later improved by better choice of

materials and enhanced production methods. These failures posed many questions about the understanding of material behavior under actual service loads, temperatures and environment. These questions had led scientists and engineers to the development of the damage tolerant design.

The main idea of the defect tolerant design is to assume the worst possible scenarios by, for instance, considering the presence of flaws and potential cracks in the structure, then to study the possibility of service failure caused by these defects once the structure is subjected to extreme conditions. This study is mainly based on fracture mechanics theories. The last step is to predict the consequences, if the failure occurs, by studying the size, velocity and trajectory of the fragments [Pommier, 2017].

1.1.2 Fracture mechanics: a brief history

The industrial revolution in the nineteenth century resulted in an enormous increase in the use of iron and steel for structural applications instead of wood and masonry. Nevertheless, several catastrophic accidents of boilers, railways-bridges and railways equipments took place resulting in loss of lives and properties. Various theories of rupture were proposed in order to understand the failure of structures. By that time, the common knowledge about rupture was still that of Coulomb's from the previous century, considering that fracture will occur when the greatest shear strain surpasses a critical limit of the material strength [Timoshenko, 1983]. Lamé [Lamé, 1833] assumed that the greatest tension in the body should remain below a certain limit. Later, Poncelet [Todhunter and Pearson, 1886] and Saint Venant [Barré de Saint Venant and Navier, 1864] stated that the extension is the measurement that should remain under a certain limit to consider the safety of the structure. Tresca [Tresca, 1869] assumed that his famous equivalent stress computing the maximum difference between highest and least principal stresses is the one to consider as an indicator of "tendency to rupture". However, all these theories to measure the "tendency to rupture" didn't take into account the eventual existence of flaws and cracks in the structure. At the dawn of the twentieth century, Love [Love, 1906] raised the question about the proper limit of safety and its dependency on the applied loading and on other accidental circumstances and that "a satisfactory answer to it might suggest in many cases causes of weakness previously unsuspected". With this question, Love pointed to the importance of incorporating fracture mechanics to understand structural failures.

Few years later, Inglis [Inglis, 1913] started the first steps toward the modern fracture mechanics. He made a geometrical assumption that the crack can be modeled by an elliptical hole in a plate. Under biaxial loading σ^∞ for a semi major axis a and a very small radius of curvature at the tip ρ , the maximum stress concentration he found was equal to $\sigma_{max} = 2\sigma^\infty \sqrt{a/\rho}$. Thus, degenerating the ellipse to a sharp crack by taking ρ equal to 0 was problematic. This theory evolved today to the stress approach of fracture. From his side, Griffith [Griffith, 1920] [Griffith, 1924] developed an energy approach of fracture. He measured experimentally the surface tension γ (specific surface energy) of an amorphous cracked glass envelope (a sphere and a cylinder) under internal pressure in order to determine the resistance to crack growth and therefore the energy δW_s necessary to create a cracked area δS .

From the critical energy balance for crack growth and based on Inglis's solutions [Inglis, 1913] for an elliptical hole in a uniformly loaded plate, he obtained the stress

corresponding to fracture as follows:

$$\sigma\sqrt{a} = \sqrt{\frac{2\gamma E^*}{\pi}} \quad (1.1)$$

With a is the half length of the crack and E^* is equal to E for plane stress and to $E/(1-\nu^2)$ for planes strain.

In the forties, scientists worked on two systematic events that attracted the attention of solid mechanics communities during World War II concerning the T2 tankers and the “Liberty” cargo ships (see figure 1.1). These large scale structures exhibited recurrent failures. Irwin [Irwin, 1948] and Orowan [Orowan, 1948] reconsidered the energy balance approach proposed by Griffith to understand these failures. This approach was considered until that time available only for perfectly brittle materials like glass. They noticed that even for brittle fracture, the crack faces exhibited “extensive plastic deformation”. They concluded that a plastic energy rate term γ_p is contributing as a dissipative energy and should be added to the surface tension γ in the expression of stress given by Griffith (equation 1.1). Despite Orowan estimated that γ_p is one thousand time higher than γ for typical metals, large steel plates experienced failures while having globally an elastic behavior. This observation explained the use of Griffith’s elastic energy balance with an additional plastic energy rate. This assessment was later reinforced by Irwin [Irwin and Kies, 1954] assuming that under small scale yielding, it means when the plastic zone is too small compared to the size of the crack, the energy responsible for the creation of a new cracked area will flow from the elastic bulk since the plastic zone is embedded in this region. Pure elastic solution can then be used for the assessment of the energy release rate.

1.1.3 Elements for fracture mechanics

Stress intensity factors

Irwin [Irwin, 1957] used Westergaard’s method [Westergaard, 1939] for solving elastic plane solutions for cracks to determine asymptotically the elastic stress state around a penny shaped crack. The stress field series expansion gave the following expression:

$$\sigma_{ij} = \frac{\sqrt{EG}}{\sqrt{2\pi r}} f_{ij}(\theta) + \text{terms of } r^{1/2} \text{ and higher} \quad (1.2)$$

With G is the Griffith’s elastic energy rate per unit of new area of crack extension. $f_{ij}(\theta)$ is the predefined universal tensor giving the spatial distribution of the stress field no matter the crack geometry and loading conditions. The term \sqrt{EG} is what is known today as the “stress intensity factor”. It was later denoted by Irwin as “ K ” to honor his friend and co-worker Joseph A. Kies. Then, Irwin further generalized these results for general loading conditions and he defined the three intensity factors K_I , K_{II} and K_{III} associated respectively to the symmetric, asymmetric and anti-plane opening modes of the crack as shown in figure 1.2. Besides, he associated to each one of these modes a corresponding energy release rate (G_I , G_{II} and G_{III}) that give, once summed, the Griffith’s energy release rate G . Soon after this, Irwin defined the fracture toughness G_{IC} as a material constant that designates the resistance energy to fracture.

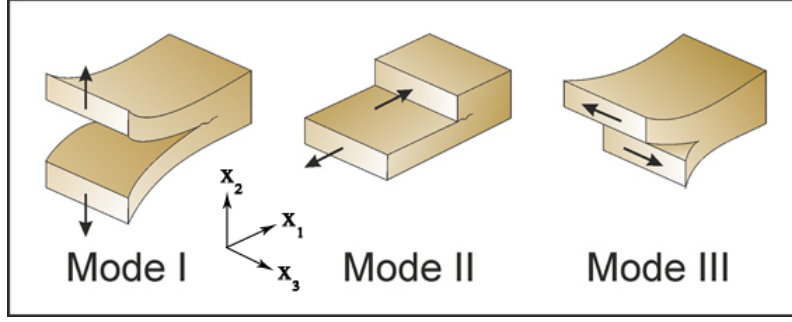


Figure 1.2: The three elementary modes of a three-dimensional crack; *mode I* for opening, *mode II* for in-plane sliding and *mode III* for anti-plane sliding (figure from [Philipp et al., 2013]).

All these fundamental concepts formed together the key and basic elements for the expansion of the fracture mechanics to the studying of static failure of pre-cracked samples and then fatigue crack growth. Further remarkable elements of this field are introduced more in details in next sections.

Note: A more detailed history of the theories of rupture and fracture mechanics can be found in [Love, 1906], [Irwin, 1958], [Erdogan, 2000] and [Paris, 2014].

Griffith's energy

As mentioned before, the Griffith's energy approach [Griffith, 1920] aims to determine δW_s the energy per unit area necessary to create a new area δS based on the specific surface energy γ .

The relation between this quantities is then written:

$$\delta W_s = 2\gamma\delta S \quad (1.3)$$

The energy balance gives:

$$\delta W_{tot} = \delta W_{elast} + \delta W_{kin} + \delta W_{ext} + \delta W_s = 0 \quad (1.4)$$

where δW_{elast} the elastic strain energy, δW_{kin} the kinematic energy and δW_{ext} the work of external forces.

At the equilibrium for a stationary crack where $\delta W_{kin} = 0$, equations 1.3 and 1.4 give:

$$\delta W_{elast} + \delta W_{ext} + 2\gamma\delta S = 0 \quad (1.5)$$

The energy release rate can be written as follows:

$$2\gamma = -\frac{\delta(W_{elast} + W_{ext})}{\delta S} \quad (1.6)$$

The Griffith criterion for unsteady crack propagation is written as follows:

$$\begin{aligned} \text{-propagation if:} & \quad G - 2\gamma \geq 0 \\ \text{-no propagation if:} & \quad 0 \geq G - 2\gamma \end{aligned} \quad (1.7)$$

When the energy release rate reaches a critical value G_c , the cohesion energy released by the structure reaches the energy required to create a new cracked surfaces and an unsteady crack growth occurs.

J-integral: a path independent integral

In 1968, Rice [Rice, 1968] proposed a path independent integral surrounding the tip of a notch when the crack faces are free surfaces. This integral permits the evaluation of the state of mechanical fields near the notch.

$$J = \int_{\Gamma} \left(W dy - T_i \cdot \frac{\partial u_i}{\partial x} \right) ds \quad (1.8)$$

The strain-energy density W is defined by:

$$W = \frac{1}{2} \sigma_{ij} \varepsilon_{ij} \quad (1.9)$$

$T_i = \sigma_{ij} n_j$ is the traction vector, u_i is the displacement vector, n_i is the outward normal to the contour Γ describing the integration path and ds is the element of the arc length along this contour as shown in figure 1.3.

For cracked material with linear elastic isotropic behavior under small scale yielding, the J integral is evaluated, by applying equation 1.8 to the Westergaard stress displacement fields, as function of stress intensity factors. It can be written under plane strain assumption as follows:

$$J = \frac{(1 - \nu^2)}{E} K_I^2 + \frac{(1 - \nu^2)}{E} K_{II}^2 + \frac{(1 + \nu)}{E} K_{III}^2 \quad (1.10)$$

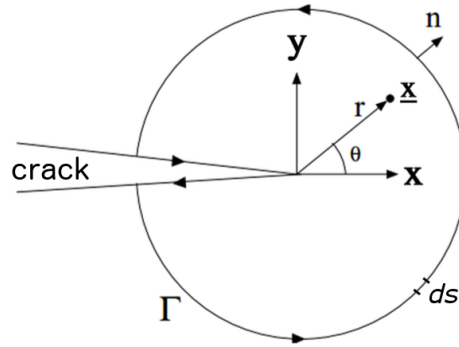


Figure 1.3: Crack tip coordinates and path of the J-integral

For the general case of an anisotropic material, Hoenig [Hoenig, 1982] proposed a three-dimensional general solution of stress and displacement of a through crack. This solution is given and discussed in chapter 3. Concerning the J integral, Hoenig used an alternative definition for J based on the crack closure integral and based on his analytical solution of stresses and displacement. The J integral is finally obtained through this relation:

$$J = \frac{1}{2} \left[K_I \Im(m_{2i} N_{ij}^{-1} K_j) + K_{II} \Im(m_{1i} N_{ij}^{-1} K_j) + K_{III} \Im(m_{3i} N_{ij}^{-1} K_j) \right] \quad (1.11)$$

$\Im(*)$ is the imaginary part of the quantity $*$, K_i is the vector of stress intensity factors $K_i = [K_I, K_{II}, K_{III}]$, N_{ij} and m_{ij} are two matrices depending on the elasticity constants

of the material. These quantities and Hoenig's analytical solutions are presented in details in [chapter 3](#) and in [Appendix A](#).

Compared to the expression of the J integral given in [equation 1.10](#) for an isotropic material, the expression given by Hoenig introduces a coupling between different fracture modes I , II and III .

This coupling between stress intensity factors vanishes in a transient manner with respect to the degree of the anisotropy seen by the crack. For instance, for a material presenting a monoclinic behavior at the crack coordinates in which $z = 0$ is a plane of symmetry, the coupling between the third fracture mode and other modes disappear [[Hoenig, 1982](#)], [[Banks-Sills et al., 2005](#)]. A total decoupling between LEFM modes is reached for orthotropic material where the material axes coincide with the crack coordinates system and for the isotropic case which lead to the expression in [equation 1.10](#).

The J-integral was used by Hutchinson [[Hutchinson, 1968](#)], Rice and Rosengren [[Rice and Rosengren, 1968](#)] as the intensity factor of crack tip plastic stress field of the so called HRR field for materials presenting a power law hardening. The HRR stress field is written as follows:

$$\sigma_{ij} = \sigma_0 \left(\frac{J}{\sigma_0 \varepsilon_0 r} \right)^{\frac{n}{n+1}} \tilde{\sigma}_{ij}(r, \theta) \quad (1.12)$$

Where n is the power hardening coefficient of the Holomon stress-strain law:

$$\frac{\varepsilon}{\varepsilon_0} = \left(\frac{\sigma}{\sigma_0} \right)^n \quad (1.13)$$

When the material is linear elastic, $n = 1$ and the HRR field reduces to Irwin's field previously defined in [equation 1.2](#) where $J = G = \frac{(1-\nu^2)}{E} K^2$.

1.1.4 Crack tip region

The asymptotic solutions of the elastic mechanical fields at the crack tip region are available in a given elastic bulk known also as the K-dominance zone where the stress intensity factors are stabilized. Regarding their radial factor $r^{-1/2}$, linear elastic stress solutions, presented in [equation 1.2](#), exhibit a singularity near the crack tip region. A first process zone appears at the vicinity of the crack tip. Because of the huge stress concentration at crack tip, damage mechanisms arise within the process zone which is usually a few micrometers in size.

A second plastic zone, appears but remains constrained by the elastic bulk. This zone has shown its importance in the development and growth of cracks under fatigue loadings. This zone is confined in the K-dominance elastic area where stress fields are described by the first order of the asymptotic solutions of LEFM. An illustration of the repartition of these regions at the crack tip is shown in [figure 1.4](#).

Irwin [[Irwin, 1960a](#)] evaluated approximatively the size of the plastic zone. A distinction was made between the plane stress and the plane strain case. For an elastic perfectly plastic material under fracture *mode I* loading, the radius of the extension of this zone along the crack front is given as follows:

$$\begin{aligned} Z_p &= \frac{1}{\pi} \left(\frac{K_I}{R_e} \right)^2 && \text{under plane stress condition} \\ Z_p &= \frac{1}{3\pi} \left(\frac{K_I}{R_e} \right)^2 && \text{under plane strain condition} \end{aligned} \quad (1.14)$$

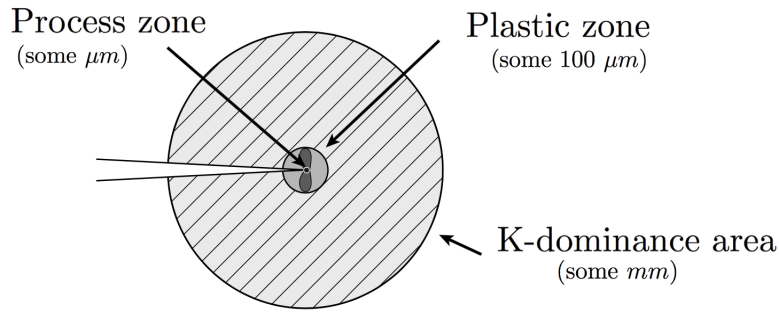


Figure 1.4: Illustration of the crack tip region.

with K_I is the stress intensity factor and R_e the yield stress of the material. The distinction between plane stress and plane strain cases explains the dog-bone shaped plastic zone along the crack front as shown in figure 1.5a. In fact, with the free surface condition, the plastic zone is less constrained and therefore has a bigger extension compared to its extension inside the material. This puts in consideration the thickness effects observed and discussed by Paris [Paris, 1957] and Irwin [Irwin, 1960b].

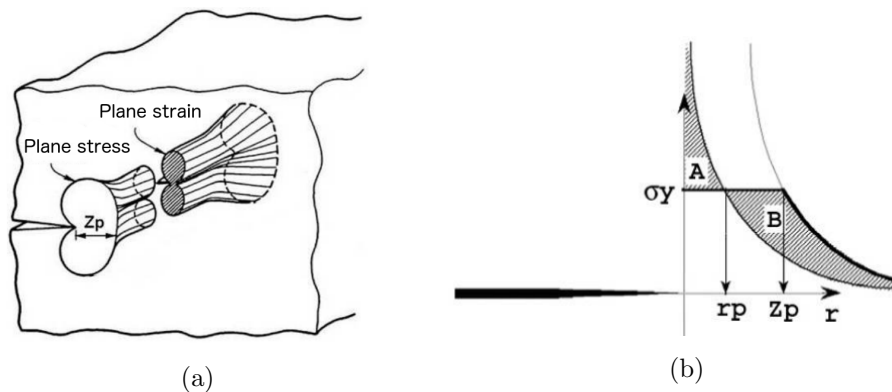


Figure 1.5: (a) The plastic zone in 3D along the crack front and (b) the evaluation of the Irwin plastic zone.

As shown in figure 1.5b, the initial plastic zone radius r_p is computed based on the Von-Mises yield criterion. The dimension Z_p of the zone in which stress fields are perturbed is then determined based on a mechanical balance. The size and shape of this zone depend on the applied stress intensity factor and the yield stress. They also depend on the T stress and on the hardening of the material [Pommier, 2002].

1.2 Fatigue crack growth

Many service components are subjected to cyclic loadings. The existence of flaws in the structure may cause the initiation and the propagation of a cracks under these fatigue loadings. This fatigue crack growth is assessed by means of the stress intensity factors of the three fracture modes K_I , K_{II} and K_{III} .

1.2.1 Mechanisms of propagation

In order to give the fatigue crack growth a simplified description, many models were proposed. However, none of these models exhibited a universal explanation of the cracking mechanism of the wide range of ductile materials under multiaxial and variable loading conditions. Nevertheless, some of these models presented a good description of the mechanism under specific conditions. Two models are highlighted below; the Neumann's model based on the coarse slip process and the plastic blunting model based on the development of a new surface due to plasticity of the crack tip. Both models present a geometric description of the crack extension per cycle of fatigue. This type of description tends to explain the appearance of the striations on the faces of a fatigue fracture (see figure 1.6).

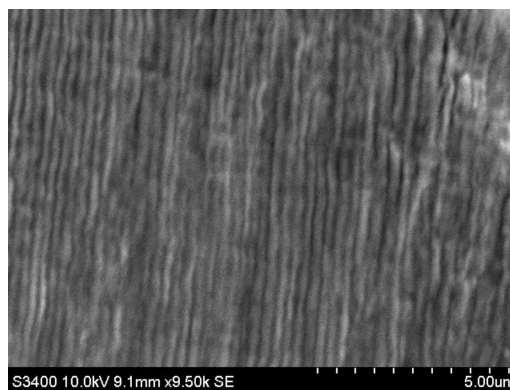


Figure 1.6: Striation of the fractography of the 316L stainless steel under fatigue crack growth [Frémy, 2012].

Neumann's coarse slip model [Neumann, 1969]: As illustrated in figure 1.7, this model describes the crack growth under fatigue loading as an alternating activation of slip systems at the crack tip. A single slip system is initially activated, the crack propagates by sliding along this system. This slip is limited by the work hardening of the activated slip system. When the stress amplitude is high enough, a second glide system, not yet work hardened, is activated. The compression causes back-sliding with a new surface created along slip systems. The second loading phase causes the repetition of the same process on the new slip systems at the new crack tip position and so on.

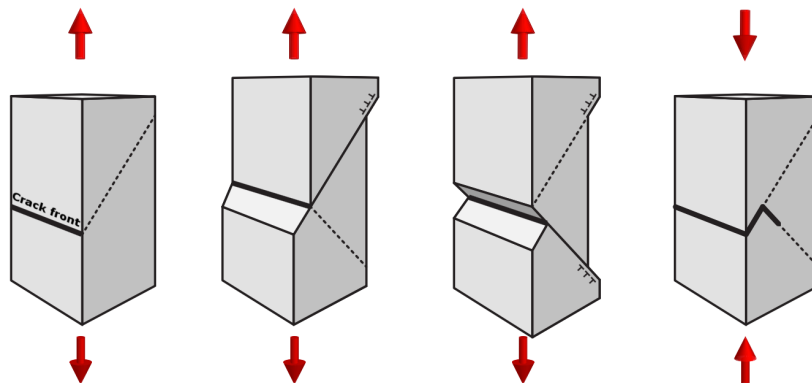


Figure 1.7: Illustration of Newman's coarse slip model for fatigue crack growth [Neumann, 1969].

Plastic blunting model [Laird, 1967] and [Pelloux, 1969]: This model describes the crack growth as a process of repetitive crack tip blunting and resharpening. The process of this model is illustrated in figure 1.8. Once submitted to a tensile loading, the crack opens. With the increasing loading, the crack tip starts to blunt and a new surface is created. While unloading, the crack closes, the newly created surface is then folded in the crack propagation direction. Therefore, the crack advances. The process is repeated with subsequent cycles. Regarding this mechanism, each striation mark is associated to a loading cycle which means that the spacing between striations reflects the crack growth rate.

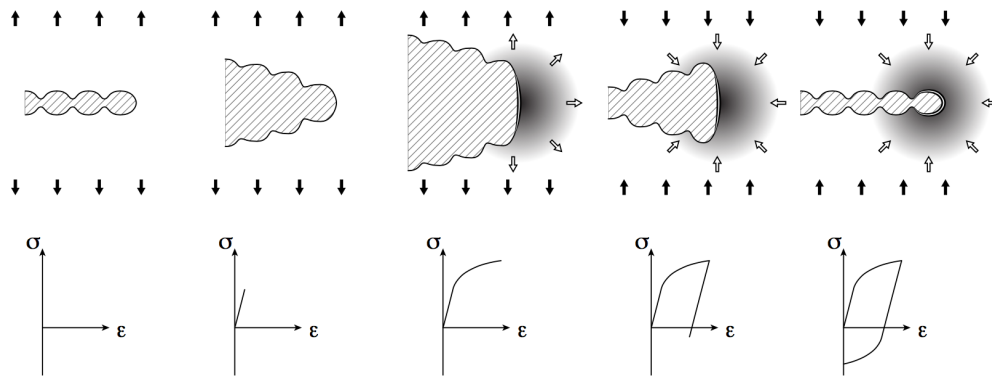


Figure 1.8: Illustration of the crack growth mechanism based on the plastic blunting of the crack tip region (figure from [Brugier, 2017]).

1.2.2 Fatigue crack growth under constant amplitudes

Under the hypothesis of small scale yielding, the plastic zone remains confined in a K - dominance zone governed by asymptotic elastic stress fields. The stress intensity factor, as defined by Irwin, is considered as a scale factor of the effects of the geometry and applied loadings on the state of the elastic field near the crack tip. As the loads vary during a cycle of loading and as the crack changes its length, “the instantaneous values of K reflect these changes” [Paris, 1961]. In light of this, Paris assumed that the phenomena occurring in the region near the crack are governed by a parameter related to the SIF. Thus, he stated that the amount of crack extension per cycle is related to the amplitude of the stress intensity factor in the following functional form:

$$\frac{da}{dN} = C \Delta K^m \quad (1.15)$$

with ΔK is the amplitude of the applied nominal stress intensity factor during a loading cycle, C and m are constants related to material properties.

Further experimental analyses have shown that the crack growth rate as function of the amplitude of stress intensity factor in a bi-logarithmic scale exhibits three stages as illustrated in figure 1.9:

- Stage I: The crack growth rate is lower than the one predicted by Paris’ law. As the loading decreases, the crack extension velocity drops and become intermittent until being barely detectable when the amplitude of the stress intensity factor goes below

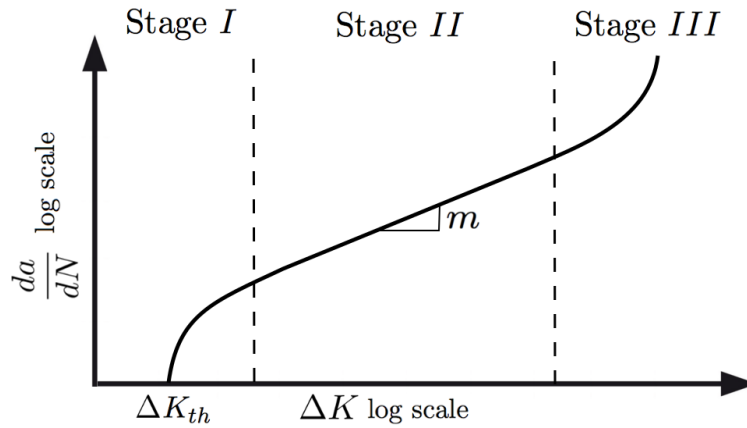


Figure 1.9: Illustration of the Paris law and the three stages of crack growth

the non-propagation threshold ΔK_{th} . The crack propagation during this phase is very dependent on the micro-structural barriers and the environment effects.

- Stage II: Also known as the Paris regime in which the relation proposed by Paris is applicable. The crack growth rate $\frac{da}{dN}$ is stable and is a power law of the amplitude of the stress intensity factor ΔK as shown in equation 1.15. During this stage, the crack propagates in a continuous manner and the crack faces present striations caused by the cyclic blunting at the crack tip.
- Stage III: As the loading approaches a critical value K_c , the crack propagation enters an unstable regime and the crack growth rate are greater than the ones presented in Paris law. The crack faces caused by this regime present striations, cleavage and inter-granular facets.

1.2.3 Crack closure effect

It was observed that the crack can remain closed during a significant proportion of the fatigue cycle. When a crack is closed, it does not act as a stress concentrator. Thus, the loading is only effective during a limited part of the fatigue cycle denominated as the “effective stress intensity factor amplitude ΔK_{eff} ”.

Different phenomena can stand behind the crack closure such as plasticity, roughness of the crack faces, a phase transformation caused by the stress at the crack tip region and oxidation. The crack closure caused by plasticity is mainly explained by two phenomena. The first is the plastic wake created by the plastic zone along the crack path. The second is the occurrence of compressive residual stresses opposed to the crack opening stresses [Elber, 1971]. The plastic deformation developed at the crack tip during one cycle of fatigue creates compressive residual stresses which reduces the effect of subsequent cycles. Regarding this sensitivity to history effects, it is important to introduce an opening stress intensity factor K_{op} that represents the stress intensity factor required to open the crack. This parameter helps modeling the interaction between fatigue cycles and hence load history effects. As crack growth rate takes into account the crack closure effects, the Paris

law's expression becomes:

$$\frac{da}{dN} = C\Delta K_{eff}^m = C(K_{max} - K_{op})^m \quad (1.16)$$

where $K_{op} = f(R, T, K_{max}, S_{ymin})$, R is the loading ratio, the T-stress represents the biaxiality of stresses around the crack and S_{ymin} the minimal applied stress perpendicular to the crack.

The challenge in this approach is to identify evolution laws for the level of crack closure (K_{op}). Once this law is identified, it can be integrated in the Paris law based on the stress intensity factor amplitude. Under constant amplitude, the identification of the evolution law of K_{op} is not possible experimentally because of the large number of tests required to identify each parameter (R, T, K_{max}, S_{ymin}). The procedure remains possible numerically using Finite Element Analyses. However, under variable amplitudes, both experimental and numerical methods of identification cannot be used regarding the high cost and the time consuming procedure in order to identify all possible configurations over millions of cycles.

Even though the plasticity has an effect on the crack closure, all the history effects related to plasticity are not only caused by the crack closure. Crack closure is one consequence among other of crack tip plasticity, other memory effects induced by plasticity may be observed even though the crack remains opened.

1.2.4 Crack growth under variable amplitudes fatigue

As mentioned before, history effects are crucial in the assessment of the fatigue crack growth rate. They were the subject of various crack growth models that aimed to take into consideration the retardation phenomenon. Wheeler [Wheeler, 1972] introduced a retardation factor ϕ to penalize the crack growth rate computed using the Paris law. This factor is an indicator of the ratio between the size of the plastic zone of the current amplitude and the one associated to the overload. This model provides a good description of a single overload. However, it does not exhibit a good agreement with experiments when multiple overloads are performed. Willenborg [Willenborg et al., 1971] developed another model by operating directly on the crack growth driving force ΔK . He introduced an effective amplitude of the stress intensity factor that takes into account the applied stress intensity factors, the “reduction” stress intensity factor caused by internal stresses and the “required” stress intensity factor to create a plastic zone equal to the one created by the overload. This model managed to represent well the history effect of one or multiple overloads. However, it overestimates the retardation effect caused by high amplitude overloads which tend to close the crack.

Another typical example of history effects is the application of one or several overloads on the structure. Experimental observations have shown that this phenomenon provokes a retardation effect on the fatigue crack growth [Suresh, 1983], [Suresh, 1985], [Sander and Richard, 2006]. After unloading, the bulk material tends to come back to a zero strain which creates a plasticity-induced residual stresses in the plastic zone, when it is well confined inside the elastic bulk. These stresses depend on the cyclic response of the material and they exhibit a long range effect. Even after the crack crosses the large plastic zone created by the overload, residual stresses participate in the crack closure and reduce the impact of the applied loading. This effect vanishes with continuous crack propagation and the crack growth retakes transiently its rate before the overload.

1.2.5 Cycle counting methods

All these cycle-based models need informations about ranges, mean values and number of loading cycles. For this reason, the number of cycles within a random loading series needs to be determined. Various counting algorithms were proposed such as level-crossing counting, range-pair counting, reservoir counting and rainflow counting. The Rainflow [Matsuishi and Endo, 1968] algorithm is the most widely used and recommended method for cycle counting under random signals. The identification of cycles is analogous to the path drawn by rain falling down a Japanese pagoda roof. A Rainflow method known as the three-point criteria is illustrated in the example in figure 1.10. The time-stress loading spectrum is plotted vertically and the stress-strain curve corresponding to the reconstructed cycles is plotted directly below.

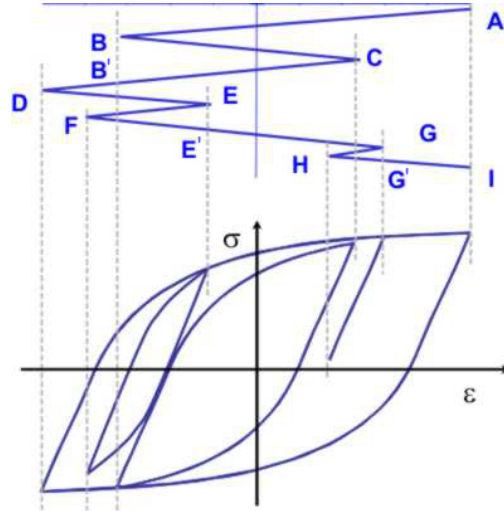


Figure 1.10: Illustration of the Rainflow counting method and the corresponding stress-strain hysteresis loops [efatigue, 2008].

In this example, four loading cycles are reconstructed. Each cycle corresponds to a loop in the stress-strain plot: the first overall cycle A-D-I, one intermediate cycle B-C-B', a smaller one E-F-E' and a pure elastic one G-H-G'. An other Rainflow reconstruction method is based on four-point criteria [McInnes and Meehan, 2008]. The residue of this method is concatenated, reconstructed as cycles and then joined to the already reconstructed cycles.

1.3 Incremental plasticity model – Pommier

Classical models for fatigue crack growth based on the direct or the modified Paris law are governed by cycle-derivative equations (da/dN). Nevertheless, service loadings are often far from being cyclic and the definition of a cycle is not obvious. Furthermore, cycle counting methods aim to reconstruct cycles from random loading spectrum, to rearrange reconstructed cycles and finally to study crack propagation using cycle-based crack growth models. However, regarding the history effects phenomena and the nonlinear behavior of the structure, the order of cycles is crucial and cannot be modified which makes these methods highly dependent on the cycle extraction process and on the sequences chosen to describe the loading spectrum. On the other hand, simulating the whole loading spectrum by performing elastic-plastic simulations on complex structures over millions of cycles is extremely time consuming and costly, it remains unattainable. To overcome these issues, Pommier and co-workers [Pommier and Risbet, 2005], [Hamam et al., 2007], [Pommier et al., 2009], [Decreuse, 2010], [Frémy, 2012] developed an incremental model for random and noncyclic loadings. This model describes the instantaneous crack growth

rate using a set of time-derivative equations (da/dt) instead of the usual cycle-based equation (da/dN). Furthermore, the plasticity at the crack region is considered as the main mechanism of the fatigue crack growth [Neumann, 1969][Li, 1989]. This crack tip plasticity is modeled by an incremental and nonlocal approach formulated for fracture mechanics in the sense that it is based on intensity factors (LEFM stress intensity factors and additional intensity factors relative to the development of the plastic zone). This plasticity model is assessed through an off-line multiscale approach that condenses the material behavior, history effects and interactions between modes under multiaxial loadings. This final condensed model is based on a set of scalar empirical equations. It will provide a global description of confined plasticity near the crack tip to the incremental model. Proceeding with these informations, the final model is adapted to simulate the crack growth rate over millions of cycles for different crack geometries with reasonable computation time.

1.3.1 Hypotheses

This approach is based on a set of hypotheses mainly related to the kinematic behavior near the crack tip:

- The model is developed in the framework of infinitesimal strain.
- The order of magnitude of the crack extension during a loading step is lower than one micrometer, while the plastic zone size is around hundreds of micrometers. This difference of scales allows the modeling of plasticity at the crack region while neglecting the motion of the crack tip during one loading step. Besides, the problem's coordinate system is attached to the crack front and to the crack plane and it moves with the crack as it grows. The crack is assumed to remain planar with a straight front in this local curvilinear coordinate system.
- The plastic zone remains confined into the K-dominance area, which is a common hypothesis for the cycle based crack growth models. This confinement constrains this zone which reduces drastically the number of degrees of freedom of the problem.
- The geometry of the crack is assumed to be locally scale invariant and to remain scale invariant with the hypothesis of infinitesimal strain and the confinement of the plastic zone. Moreover, the local geometry of the crack is assumed to dominate the spatial distribution of the fields at that region. Therefore, the applied boundary conditions and their history only affect the intensity of these fields and not their shape. This implies that the local solution of the problem is scale invariant and it can be represented by a superposition of terms, each one is decomposed into an intensity factor, that serves as an input variable for the incremental model, and a spatial distribution given once for all for a given material.
- At a given loading point while yielding, it is possible to continue the plastic flow. It is as well possible to obtain always a linear elastic behavior during an infinitesimal load reversal no matter the elastic-plastic strain previously produced. Therefore, the elastic and plastic components of the of the incremental displacement field can be considered as kinematically independent. Each one of them respects the aforementioned hypotheses and its intensity factor represents a degree of freedom for the problem.

Once these kinematic considerations are assumed for a given crack problem. The relative velocity is considered in a reference attached to the crack front and plane. Let R_T be this reference, R_0 the global reference and T the crack tip. For a given point P near the crack tip region, the velocity field is decomposed as follows:

$$\underline{v}(P, t)|_{R_0} = \underbrace{\underline{v}(P, t)|_{R_T}}_{\text{velocity at the crack tip}} + \underbrace{\underline{v}(T, t)|_{R_0} + \underline{w}(R_T/R_0) \wedge \underline{TP}}_{\text{crack growth}} \quad (1.17)$$

The kinematics field attached to the crack tip $\underline{v}(P, t)|_{R_T}$ can be decomposed into a linear elastic part and a nonlinear plastic part. Each one of them is independent from the other and respects the decomposition into different fracture modes. Finally, each component is described by an intensity factor ($\dot{K}_i(t)$ and $\dot{\rho}_i(t)$) and a spatial distribution ($\phi_i^{el}(\underline{x})$ and $\phi_i^{pl}(\underline{x})$) that represents the shape of the solution near the crack tip region.

$$\underline{v}^{FE}(\underline{x}, t) = \sum_{i=1}^3 \dot{K}_i(t) \phi_i^{el}(\underline{x}) + \sum_{i=1}^3 \dot{\rho}_i(t) \phi_i^{pl}(\underline{x}) \quad (1.18)$$

1.3.2 Methodology

The model is based on two main laws:

1. **A crack propagation law** based on a time derivative equation. This incremental law helps getting rid of the definition of cycles and relates directly the instantaneous crack growth rate to the blunting of the crack tip.

$$\frac{da}{dt} = \alpha \left| \frac{d\rho}{dt} \right| \quad (1.19)$$

This law is analogous to the fatigue crack growth rate models that interpret fatigue striations using the approach of the CTOD (Crack Tip Opening Displacement).

2. **A blunting law** Since plasticity is considered to be the origin of crack growth, a blunting law is developed by condensing the cyclic plasticity behavior of the region near the crack tip. This law relates the blunting of the crack tip to the applied loading. The strong point of this law that it uses nonlocal quantities obtained from the aforementioned decompositions. These quantities are the nominal stress intensity factors considered as scale factors of the elastic fields and blunting intensity factors that represent scale factors of the plastic fields. For both elasticity and plasticity, a scale factor is defined for each fracture mode. The blunting law is written as follows:

$$\dot{\rho} = g(\underline{\dot{K}}^\infty, V_{int}) \quad (1.20)$$

This vectorial description of cyclic plasticity is analogous to the common tensorial description of the behavior law but with a nonlocal approach. Internal variables V_{int} are important in the modeling of cyclic plasticity. They describe the existence of material hardening, internal stresses and other effects of the nonlinear behavior of the material that can be interpreted as history effects.

A general illustration of the steps of the incremental model is represented in figure 1.11. The main challenge is to obtain the blunting law that condenses cyclic plasticity effects. The procedure consists in identifying the cyclic elastic-plastic behavior of the considered material based on experimental results or on literature. The behavior is implemented in a finite element software and a campaign of simulations under specific conditions is performed on a representative structure with a stationary crack. Kinematic fields of these computations are extracted from a region of interest near the crack tip and then post-processed finely based on model reduction methods in order to construct a basis of reference fields. A reference field is associated to each mechanism (elasticity/plasticity) and to each fracture mode, it represents the spatial distribution of the corresponding degree of freedom. This process is largely detailed in the next chapters.

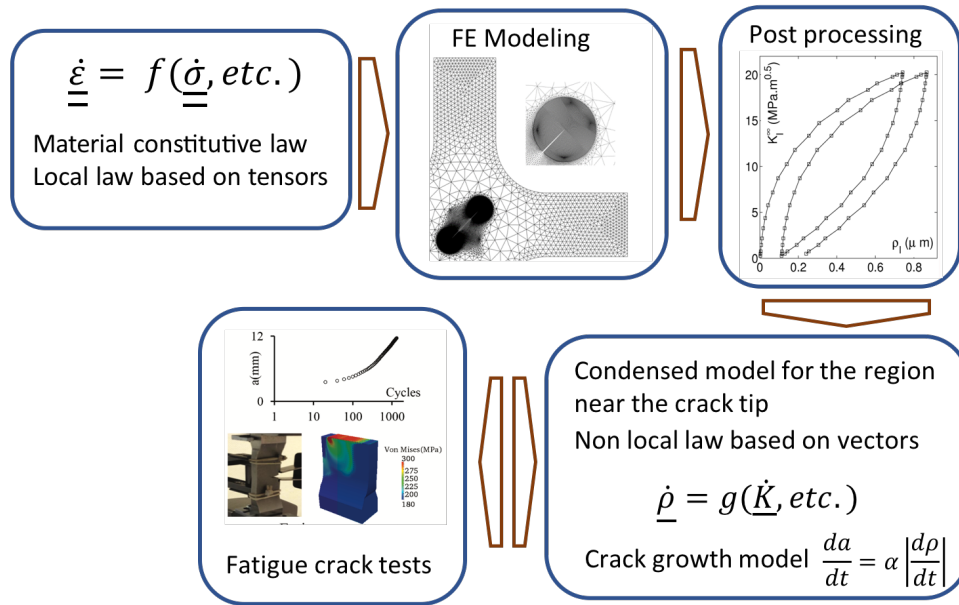


Figure 1.11: Multi-scale approach for a condensed plasticity model.

Finite element simulations are performed on the same model under complex loadings. Kinematic fields of the crack tip region are extracted from these computations then projected on the previously obtained reference fields in order to identify the evolution of different intensity factors of the plastic part (blunting intensity factors) as function of the intensity factors of the elastic part (nominal stress intensity factors). These evolutions describe the elastic-plastic behavior of the whole crack tip region with nonlocal quantities. As shown in equation 3.33, a global model of this behavior can then be assessed based on these evolutions. As a result, the behavior of the crack tip region is reduced to a set of scalar differential equations. Once the model is set up, the blunting of the crack tip is determined by the simple knowledge of the nominal stress intensity factors seen by the crack. Regarding this, these constitutive equations can serve as a complement for linear elastic simulations of cracked structures in order to assess the cyclic plasticity at the crack region.

As shown in equation 1.19, the instantaneous crack growth rate is deduced from the evolution of the blunting intensity factors. Some simple experiments of *mode I* crack propagation are performed in order to identify the proportionality coefficient α between the two evolutions.

1.3.3 Evolution of the model

The incremental approach was developed at the LMT. A set of time derivative equations for fatigue crack growth under *mode I* was initially proposed by Pommier and Risbet [Pommier and Risbet, 2005]. Further development was then carried by Hamam [Hamam et al., 2007] by studying fatigue crack growth under variable amplitudes of *mode I* loading at room temperature for low carbon steel used in train wheels. The model had shown good agreement with experiments and managed to take into account history effects caused by overloads at different amplitudes. Figure 1.12 is one among various validation cases of the model done by Hamam [Hamam et al., 2007].

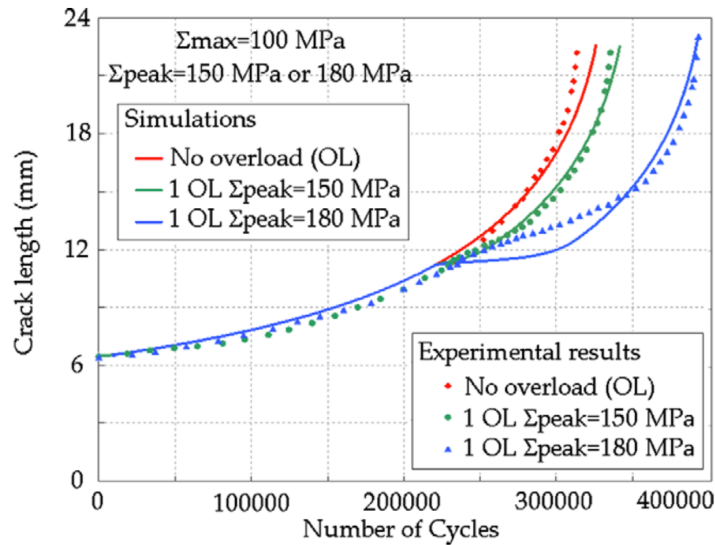


Figure 1.12: Retardation effect after a single overloading at different amplitudes, comparison between incremental model and experiments [Hamam et al., 2007].

The model introduced two elastic domains that represent the cyclic plastic zone (*cpz*) and the monotonic plastic zone (*mpz*). Each domain is characterized by its size (K_R^{cpz} and K_R^{mpz}) and the position of its center (K_X^{cpz} and K_X^{mpz}). As summarized in figure 1.13, these parameters were interpreted as internal variables to enrich the confined plasticity model.

Later, the model was extended in order to take into account complex non-isothermal conditions and corrosion effects on fatigue crack growth in the work of Ruiz-Sabariego [Ruiz-Sabariego and Pommier, 2009]. The model was confronted to experimental results carried on the N18 Nickel base superalloy at different elevated temperatures between 450 °C and 650 °C to imitate the service conditions of a turbine disc in aircraft engines. Comparisons gave satisfactory results.

The development of the model continued with Decreuse [Decreuse et al., 2009] by introducing nonproportional mixed mode *I + II* and then with Fremy [Freymy et al., 2012] for nonproportional mixed mode *I + II + III*. A framework was provided in these works to reduce the confined plasticity behavior near the crack tip for mixed fracture modes. Based on this framework, the model succeeded to predict the load path effect of mixed mode loadings. Zhang [Zhang, 2016] studied the extension of the model under large scale yielding conditions. New degree of freedom was added to the decomposition of the kinematic field in order to account for the generalized plasticity effects. Recently, Brugier

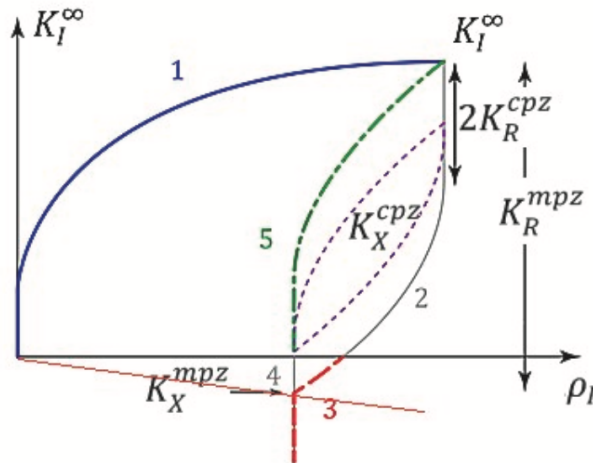


Figure 1.13: Evolution of nominal stress intensity factor K_I^∞ as function of blunting intensity factor ρ_I under *mode I* cyclic loading and illustration of the role of internal variables of the model [Pommier, 2017]

[Brugier, 2017] examined the fatigue crack growth of short cracks by taking into account the T-stresses. Further developments of this aspect, including the effect of residual stresses and their integration in the model, are still ongoing.

These aforementioned works were developed for different ductile materials presenting elastic-plastic behavior with different hardening laws (linear and nonlinear) but always with an isotropic constitutive model. This behavior was adequate to describe the used material and sufficient for the considered industrial demand. Nevertheless, among components that require a tolerant design for industrial use, several are exhibiting an anisotropic behavior. Thus, it seems important to extend the incremental model to the case of anisotropic materials. The present work is developed towards this aim. As explained previously, the first step of the incremental model is to condense the cyclic plasticity behavior of the region near the crack tip into an extended nonlocal model. For this reason, the following work is exploring possible strategies to develop a framework for anisotropic elasticity and plasticity that can serve to condense plasticity effects of the crack tip region.

1.4 Anisotropy

From a mechanics of solid point of view, the anisotropic behavior is the dependency of the material response on the direction of the applied loading. It means that the material behavior is not invariant under arbitrary orthogonal transformations. This direction-dependent response concerns different behaviors of the material, e.g. elastic, plastic and damage. In the presented work, the elastic and the plastic anisotropies of the material are considered.

The elastic anisotropy is introduced in the Hooke's law through the stiffness and compliance tensors. Components of these tensors are expressed by different material constants. As the degree of symmetry in the material behavior decreases the number of independent material parameters required to model that behavior increases. Components of stiffness/compliance tensors can be expressed using two independent material parameters for the isotropic case, three independent parameters for cubic anisotropy and so on

until reaching 21 independent parameters for fully anisotropic material.

Concerning the plastic anisotropy, for metals, irreversible deformations can be explained by the motion of dislocations on different slip systems. Thus, the presence of some densely packed planes and closely packed directions favors the plastic deformations on these some systems more than others. Accordingly, the plastic behavior is related to the orientation of the crystal, to the number of these easy slip systems and to their critical resolved shear stress (CRSS). The modeling of this behavior is based on different approaches. Some approaches use explicitly the dislocations density or other mechanically based variables for the model. These approaches are known as crystallographic micromechanical approaches. Others are phenomenological approaches that incorporate implicitly the physics behind plastic deformations into the model. Different approaches are discussed in more details in [chapter 4](#).

The anisotropic behavior concerns a wide range of materials used for industrial applications. Some of these applications are critical to ensure the proper functioning of the structure. An example of these materials is the insulation foam used by NASA to insulate the external tank of space shuttle. This foam exhibits a transversely anisotropic behavior. The fracture of some parts of this foam is believed to be the major cause of the failure of the space shuttle Columbia in 2003 during re-entry. This accident motivated some studies about the determination of stress intensity factors, fracture toughness and the crack path in anisotropic materials [[Arakere et al., 2008](#)].

Composites and superalloys cast as a single crystal are other examples of materials exhibiting anisotropic behavior and used in critical industrial applications.

1.4.1 Composites

Composite materials are fast becoming a key point in various applications due to their very attractive specific mechanical properties. Structured composites are mainly composed of a matrix and fibers as reinforcement. These fibers are oriented with respect to directions that withstand main stresses. This helps homogenizing the stress distribution in all the structure and improving its stiffness. The presence of these reinforcements results in a direction dependent response, i.e. anisotropic behavior. Thus, unlike “naturally anisotropic” materials, composite materials acquire their anisotropic behavior from their design.

The field of use of composites is expanding progressively and their use in aeronautic industry is increasing. An example is the development of 3D woven carbon fiber composites in the industrial scale. This material was used in the manufacturing of turbo fan blades and fan case of the new generation of aircraft engines (LEAP) by Safran Aircraft Engines and General Electrics. The implication of composites in this industry requires a damage tolerant design for anisotropic materials once they become used in more critical applications.

1.4.2 Single crystals

Materials used as single crystals are an example of naturally anisotropic materials. They inherit their anisotropy from their lattice structure. This microscopic structure results in an elastic anisotropic response at the macroscopic scale. Moreover, plastic deformation takes place in a crystal when the dislocations slips along easy slip systems. These slip systems are defined by the most closely packed directions lying in the most densely packed

planes. According to Schmid criterion, the slip occurs on a slip system depending on the orientation of the crystal with respect to the applied loading.

Application case: Nickel base superalloys for high pressure turbine blades

An important progress was made on materials used in the manufacturing of high pressure turbine blades. Polycrystalline nickel base alloys with coarse grains were used at the beginning. The presence of grain boundaries presented a weakness point in these components from which cracks can initiate and grow. An other process was presented by using directionally solidified alloys where all grains have a principal axis [001] along the direction of the blade axis. Secondary directions were oriented arbitrary. The process continued to progress by using a single crystal oriented along the principal axis of the blade. Thus, the whole blade has the same crystallographic orientation in particular [001] along its principal axis. This implies an anisotropic behavior.

As shown in figure 1.14a, at the microscale, the AM1 Nickel base superalloy is well structured. It represents two phases, a γ matrix and a γ' cubic precipitates. Both phases have an FCC structure. The presence of two phases gives the superalloy a strengthening effect that results in a structural hardening. One of the sources of this property is the difference between the lattice parameters of the two phases. This misfit creates local coherency stresses. These stresses contribute in the increase of threshold stress of a dislocation motion, which helps reducing the slip of dislocations. An other source of hardening is the ordering effect of γ' . Besides, alloys usually display a high content of alloying elements in the matrix, such as Chromium or Cobalt. These mixture, among other effects, modify the stacking fault energy and allows the dislocation to dissociate into pairs of partial dislocations. This dissociation modifies the interactions between the slip system and the history effects in the material behavior. It was cited as a reason for the over-hardening effect for multiaxial strain path in some alloys [Doquet, 1993], [Doquet and Clavel, 1996].

Being made as a single crystal gave high pressure turbine blades higher resistance along the principal direction that withstand centrifugal forces. Nevertheless, the failure of these components during service is still occurring. In May 2011, an engine of Qantas B744 shut down during a flight near Singapore. The investigation report released by the Australian Transportation Safety Board (ATSB) reported that *“a single intermediate-pressure turbine blade failed as a result of high-cycle fatigue cracking, producing high levels of vibration and the subsequent commanded shut-down of the No.4 engine”*.

This accident, among many others, is just an example of what could occurs because of single cracked turbine blade. In fact, these components are exposed to a very aggressive environment due to high temperature (600 °C to 1100 °C) and to different kinds of loadings (gas pressure, centrifugal forces, vibrations, etc). Their main cause of failure remains the fatigue loading that enhances the propagation of flaws. The development of these cracks is almost entirely plasticity induced, and for the case of single crystals, it is the result of vast amounts of localized inelastic straining (see figure 1.14b).

Proceeding with these observations, a conclusion can be drawn that it is indispensable to incorporate a direction dependency in the study of crack growth. In concordance with the incremental model presented in this work, the condensed plasticity model has to account for this anisotropic behavior. The following work grants a particular interest

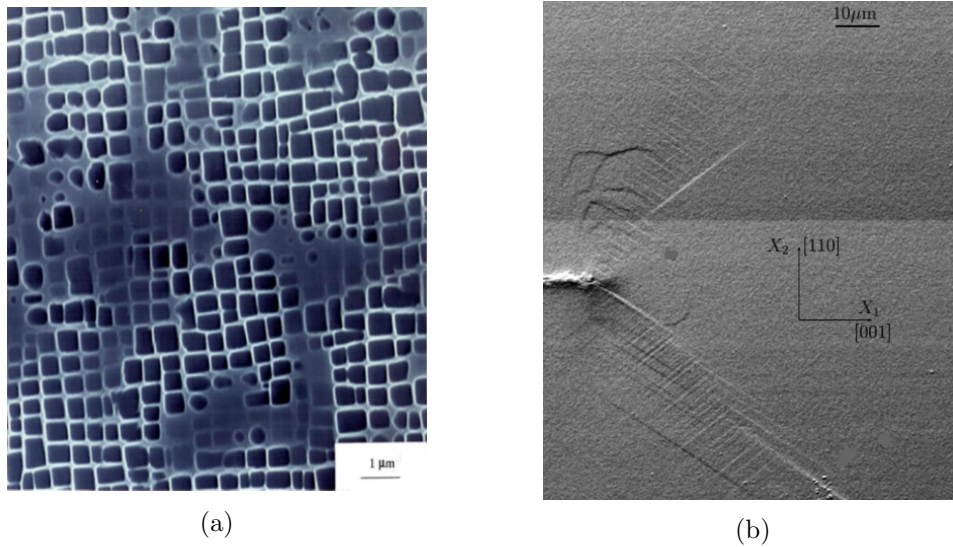


Figure 1.14: AM1 nickel base superalloy single crystal, (a) micro-structure of the γ' cubic precipitates in a dendrite [Kaminski, 2007] and (b) SEM micrograph of slip traces around the crack tip [Flouriot, 2004].

to the AM1 nickel base superalloy single crystal. However, the study remains applicable to other cases of anisotropic materials and it can be extended to the case of composites. Furthermore, it can present a starting point to a future refined study of a cracked grain in polycrystalline materials.

Model reduction protocol and 2D application case

This chapter presents some key elements required for the understanding of the rest of the presented work. It introduces, a simple 2D application case of a crack under mixed fracture modes $I+II$ in a continuum isotropic medium and a cubic medium with $z = 0$ is a plane of symmetry for the material. The chapter starts with a brief introduction to model reduction concepts and the Karhunen-Loeve algorithm used in this work. Based on these tools and on a set of hypotheses, the velocity field in the reference frame attached to the local crack front and plane is decomposed into intensity factors and spatial distributions. These nonlocal intensity factors constitute the degrees of freedom of the problem. They are used as the main ingredients to define an extended material model that condenses plasticity effects at the near crack tip region.

2.1 State of the art

This section contains an introduction to some basic elements required to understand the rest of the study presented in following sections. The Karhunen-Loeve decomposition is presented as a model reduction tool. It will be used in this work to reduce the number of degrees of freedom of the crack problem. The other part of this section presents asymptotic elastic solutions of displacement field at the region near the crack tip for an isotropic case and for a monoclinic case where material axes coincide with the crack coordinates system.

2.1.1 Model reduction

The main aim of model reduction strategies is to reduce drastically the size of a given numerical problem while maintaining a reliable outcome. This simplification helps reducing simulations time and storage capacities, i.e. simulations cost. Having a reduced model with an acceptable computational speed makes it possible to perform on-line predictions of the behavior. The process consists in capturing the fundamental features of a structure during an early stage of the process. To do so, an off-line analysis is performed while stimulating, then capturing the essential properties of the model and getting rid of redundancy of information.



Figure 2.1: Graphical illustration of model reduction [Turk and Levoy, 1994].

Figure 2.1 is a graphical illustration of the model reduction concept. The “Stanford Bunny” [Turk and Levoy, 1994] is still recognized even with only few facets of the mesh. Following the same line, the outcome of a model reduction process describes a model with few degrees of freedom and sufficient precision.

Karhunen Loève decomposition

The Karhunen Loève algorithm [Karhunen, 1947] also known as the Proper Orthogonal Decomposition (POD) is used, among other similar algorithms, as a model reduction procedure. The method was basically developed to be used in Computational Fluid Dynamics CFD. Its use was extended to different fields such as computational mechanics of materials and structures. This method can be used on functions defined explicitly as solution of a given problem. It can also be applied on functions defined implicitly as solutions of nonlinear Partial Derivative Equations.

In this study, the function used in the model reduction is the kinematic field defined explicitly as the time response of a crack tip region. Let $\underline{v}(P, t)$ be this field known for N given points during T time increments $(P_{i=1,N}, t_{k=1,T})$ as function of time t and space $P(\underline{x})$. These variables can be separated. The kinematic field $\underline{v}(P, t)$ can be approximated

to a field $\tilde{v}(P, t)$ expressed as a truncated sum of the products of functions of each variable, e.g. space fields $\underline{\phi}_m(P)$ and their intensity factors $\dot{\lambda}_m(t)$:

$$\underline{v}(P, t) \approx \tilde{v}(P, t) = \sum_{m=1}^{m_0} \dot{\lambda}_m(t) \underline{\phi}_m(P) \quad (2.1)$$

In order to obtain this approximation, the kinematic field is regrouped in a matrix \underline{V} also known as “snapshots” matrix. A snapshot consists of a column vector that describes the state at a certain time increment:

$$V_{ij} = \underline{v}(P_i, t_j) \quad (2.2)$$

The spatial auto-correlation matrix \underline{C} of size $N \times N$ is defined as follows:

$$C_{ij} = \sum_{k=1}^T \underline{v}(P_i, t_k) \underline{v}(P_j, t_k) \quad (2.3)$$

The matrix C_{ij} is self-adjoint. Thus, its eigenvalues are positive and can be ordered in decreasing order. Their first, say m_0 , corresponding eigenvectors $\underline{\phi}_m(P)$ form an optimal basis of spatial fields for the POD. These vectors are orthogonal and normalized by construction. They form a basis that represents kinematic fields as the sum of spatially independent fields. On the other hand, temporal coefficients $\dot{\lambda}_m(t)$ constitute kinematic variables of the problem. They are computed as follows:

$$\dot{\lambda}_m(t_k) = \sum_{i=1}^N V_{ik} \underline{\phi}_m(P_i) \quad (2.4)$$

The error of the approximation in equation 2.1 of the order m_0 can be calculated as follows:

$$C(m_0) = \sqrt{\frac{\sum_{i,k} (\underline{v}(P_i, t_k) - \tilde{v}(P_i, t_k))^2}{\sum_{i,k} (\underline{v}(P_i, t_k))^2}} \quad (2.5)$$

2.1.2 Asymptotic elastic solutions

Coming back to the problem of a crack, distributions of linear elastic mechanical fields are discontinuous across the crack faces. This discontinuity disappears at the crack front which creates a singularity in the near crack tip region ($r \rightarrow 0$). Westergaard [Westergaard, 1939] gave an exact solution of displacement and stress fields for an isotropic material. This solution presented later the first term of an asymptotic expansion function of r given by [Irwin, 1957] (section 1.1.3) as a solution to the problem. Williams [Williams, 1957] established later a similar asymptotic expansion function of r based on an eigenfunction approach as a solution to a similar problem with some differences in boundary conditions. The stress field series expansion is written as follows:

$$\sigma(r, \theta) = \sum_{i=I}^{III} K_i f_i(\theta) r^{-\frac{1}{2}} + \text{regular terms of } r^{\frac{1}{2}} \text{ and higher} \quad (2.6)$$

Isotropic: Westergaard's asymptotic solution

Westergaard [Westergaard, 1939] gave an exact solution of isotropic linear elastic fields at the near crack tip region for every fracture mode.

$$\begin{aligned}
 \text{mode I} & \begin{cases} u_x = \frac{K_I}{2\mu} \sqrt{\frac{r}{2\pi}} \cos\left(\frac{\theta}{2}\right) [\kappa - \cos\theta] \\ u_y = \frac{K_I}{2\mu} \sqrt{\frac{r}{2\pi}} \sin\left(\frac{\theta}{2}\right) [\kappa - \cos\theta] \end{cases} \\
 \text{mode II} & \begin{cases} u_x = \frac{K_{II}}{2\mu} \sqrt{\frac{r}{2\pi}} \sin\left(\frac{\theta}{2}\right) [\kappa + 2 + \cos\theta] \\ u_y = -\frac{K_{II}}{2\mu} \sqrt{\frac{r}{2\pi}} \cos\left(\frac{\theta}{2}\right) [\kappa - 2 + \cos\theta] \end{cases} \\
 \text{mode III} & \begin{cases} u_z = 2\frac{K_{III}}{\mu} \sqrt{\frac{r}{2\pi}} \sin\left(\frac{\theta}{2}\right) \end{cases}
 \end{aligned} \tag{2.7}$$

with $\mu = \frac{E}{2(1+\nu)}$ the Lamé coefficient, $\kappa = \frac{3-\nu}{1+\nu}$ under plane stress and $\kappa = 3 - 4\nu$ under plane strain.

Orthotropic: Sih, Paris and Irwin's solution

Based on a complex variables approach, Sih and co-workers [Sih et al., 1965] gave the first term of the asymptotic expansion of the stress and displacement for a crack in a monoclinic material where the crack is aligned with the material axes, i.e. $z = 0$ is a plane of symmetry for the material. The elastic stress singularity of the order $r^{-\frac{1}{2}}$, presented in Westergaard solutions for isotropic materials, is always present. For the displacement, it can be written as follows:

$$\begin{aligned}
 \text{mode I} & \begin{cases} u_x = K_I \sqrt{\frac{2r}{\pi}} \Re\left[\frac{1}{\mu_1 - \mu_2} (\mu_1 p_2 \sqrt{\cos\theta + \mu_2 \sin\theta} - \mu_2 p_1 \sqrt{\cos\theta + \mu_1 \sin\theta})\right] \\ u_y = K_I \sqrt{\frac{2r}{\pi}} \Re\left[\frac{1}{\mu_1 - \mu_2} (\mu_1 q_2 \sqrt{\cos\theta + \mu_2 \sin\theta} - \mu_2 q_1 \sqrt{\cos\theta + \mu_1 \sin\theta})\right] \end{cases} \\
 \text{mode II} & \begin{cases} u_x = K_{II} \sqrt{\frac{2r}{\pi}} \Re\left[\frac{1}{\mu_1 - \mu_2} (p_2 \sqrt{\cos\theta + \mu_2 \sin\theta} - p_1 \sqrt{\cos\theta + \mu_1 \sin\theta})\right] \\ u_y = K_{II} \sqrt{\frac{2r}{\pi}} \Re\left[\frac{1}{\mu_1 - \mu_2} (q_2 \sqrt{\cos\theta + \mu_2 \sin\theta} - q_1 \sqrt{\cos\theta + \mu_1 \sin\theta})\right] \end{cases} \\
 \text{mode III} & \begin{cases} u_z = K_{III} \sqrt{\frac{2r}{\pi}} \Re\left[\frac{\sqrt{\cos\theta + \mu_3 \sin\theta}}{S''_{45} + \mu_3 S''_{44}}\right] \end{cases}
 \end{aligned} \tag{2.8}$$

where μ_i , p_i and q_i have complex values issued from the resolution of the characteristic equations of compatibility (more details are provided in Appendix A). They depend on materials parameters. S''_{ij} are reals directly related to materials parameters and to the plane strain or plane stress assumptions.

Note: A noteworthy property of these aforementioned solutions is that they can be written as a scale factor that describes the loading (K_i) and a spatial distribution function of polar coordinates (r, θ). The shape of this spatial distribution is independent from the applied loading and the crack length. Besides, this spatial distribution can be decomposed into a radial scale function in \sqrt{r} and an angular shape that depends on θ .

2.2 Incremental model

The incremental model is used to predict the crack growth rate with a reasonable precision and a reduced cost when nonlinear material behavior and complex loading conditions are met. It presents a set of time derivative equations that allow the direct use of loading spectra instead of cycle reconstruction procedure. The model assumes that fatigue crack growth is mainly plasticity-induced. Thus, the **propagation law** relates the crack growth rate to the blunting of the crack tip region as shown in the equation below [Pommier and Risbet, 2005], [Pommier and Hamam, 2007]:

$$\frac{da}{dt} = \alpha \left| \frac{d\rho}{dt} \right| \quad (2.9)$$

This equations derives directly from the CTOD equation from [Laird, 1967] and [Pelloux, 1969]:

$$\frac{da}{dN} = \alpha \frac{\Delta CTOD}{dN} \quad (2.10)$$

The parameter α serves as a coefficient to adjust the model. It can be obtained by minimizing the error between the crack growth rate simulated with incremental model and the one resulting from a simple fatigue test performed in *mode I* with constant amplitude. This tuning parameter does not change the proportion between ΔK and the crack growth rate in the logarithmic scale of Paris diagram, it only adjusts the vertical position of the curve [Pommier and Hamam, 2007], [Hamam et al., 2007].

The blunting ρ of the region near the crack tip is described through a reduced model of the plasticity at that region. This model is obtained through a model reduction process. It condenses the material behavior and memory effects in a set of vectorial equations. This final **blunting law** is based on the minimum possible number of degrees of freedom. It relates plasticity effects described by the blunting intensity factors ρ_i to the applied loading described by the nominal stress intensity factors K_i^∞ (i.e. due to external loads). The model incorporates also internal variables to account for internal stresses, material hardening and more generally of any other effects related to the nonlinear behavior of the material and to the confinement of the crack tip plastic zone. These effects are crucial in the modeling of history effects in fatigue crack growth.

$$d\rho_I, d\rho_{II}, d\rho_{III} = f(dK_I^\infty, dK_{II}^\infty, dK_{III}^\infty, V_{int}) \quad (2.11)$$

The generic aspect of the model allows its extension to describe various material behaviors under multiphysics conditions. In this chapter, a material presenting cubic elasticity and Von-Mises plasticity is studied.

In order to fulfill this aforementioned model reduction strategy, a set of hypotheses have to be assumed after discussion.

2.2.1 Hypotheses

The main hypothesis in the model is a simplified description of the kinematics. For this purpose, the velocity field of the cracked component $\underline{v}(P, t)|_{R_0}$ is partitioned into a term that stems from crack growth and a second term that provides the velocity field relative

to the reference frame attached to the crack front and plane. Figure 2.2 illustrates this local coordinate system. The velocity of a given point P is obtained as follows:

$$\underline{v}(P, t)|_{R_0} = \underbrace{\underline{v}(P, t)|_{R_T}}_{\text{velocity at the crack tip}} + \underbrace{\underline{v}(T, t)|_{R_0} + \underline{w}(R_T/R_0) \wedge \underline{TP}}_{\text{crack growth}} \quad (2.12)$$

where $\underline{v}(P, t)|_{R_T}$ is the velocity field expressed in a reference R_T attached to the local crack front and plane.

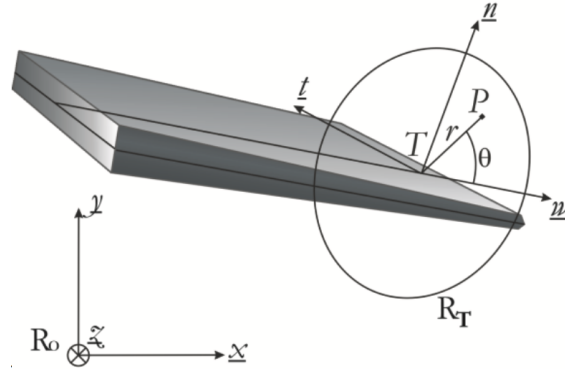


Figure 2.2: Local coordinate system attached to the local crack front and plane.

The crack is assumed to be locally planar, with a locally straight crack front, which ensures that the velocity fields could be partitioned into modes *I*, *II* and *III*. A plane strain condition is assumed along the crack front.

At the vicinity of the crack tip, the geometry is assumed to be locally self-similar. It means that zooming in and out of this region will keep the geometry invariant. This helps decomposing fields at the crack tip as a product of an intensity factor and a spatial function that is itself searched as a product of separate variables for the scale (r) and the angular position within a cross section normal to the crack front (θ).

The plastic zone at the crack tip remains confined and constrained by the elastic bulk. Because of this constraint, the number of degrees of freedom required to describe the behavior of the confined plastic zone is expected to be limited. Besides, the small scale yielding condition, ensures that the crack geometry remains coarsely unchanged by the plastic deformation and hence the elastic response of the crack tip region remains also unchanged.

Finally, at each point during a loading cycle, it is always possible to apply a load reversal, and hence to get a transiently elastic behavior or to continue along the same loading direction and hence to get an elastic-plastic behavior and a plastic flow within the plastic zone. This means that we are dealing with two kinematically independent mechanisms, a linear elastic one and a nonlinear plastic one, each one presents a degree of freedom for the problem.

2.2.2 Kinematic field decomposition

As a consequence of all the aforementioned assumptions, the velocity field at the crack tip is described as a superposition of three fracture modes. Each mode is decomposed into two degrees of freedom, a first term that is responsible for representing the elastic part of

the velocity field and a second one to represent the plastic flow. This second field should be a no-volume change transformation, in order to be consistent with the description of a plastic flow. Each part is a product of an intensity factor rate and a spatial distribution field [Pommier et al., 2009], [Pommier, 2016], [Decreuse, 2010], [Frémy, 2012].

$$\underline{v}^{FE}(\underline{x}, t) = \sum_{i=1}^3 \dot{\check{K}}_i(t) \underline{\phi}_i^{el}(\underline{x}) + \sum_{i=1}^3 \dot{\rho}_i(t) \underline{\phi}_i^{pl}(\underline{x}) \quad (2.13)$$

where $\underline{\phi}_i^{el}(\underline{x})$ and $\underline{\phi}_i^{pl}(\underline{x})$ are the elastic and plastic reference fields respectively. $\dot{\rho}_i(t)$ is the rate of the blunting intensity factor that presents crack tip plasticity created by a crack in mode i . $\dot{\check{K}}_i(t)$ is the stress intensity factor of a fracture mode i . In the case of a linear elastic behavior, this factor is equal to the nominal stress intensity factor \dot{K}_i^∞ . In the presence of a nonlinear behavior, this quantity contains the effects of elasticity through the applied loading \dot{K}_i^∞ and the effects of internal stresses induced by the confinement of the plastic zone also known as the shielding effect [Rice and Thomson, 1974].

Note: In their work, Decreuse [Decreuse, 2010] and Frémy [Frémy, 2012] had shown that $(\dot{\check{K}}_i(t) - \dot{K}_i^\infty)$ is proportional to $\dot{\rho}_i$. As a matter of fact, the difference between the two stress intensity factors is directly related to the “shielding effect” due to the internal stresses that stem from the confinement of the plastic zone inside the K -dominance area.

It can be concluded that the velocity field of a mixed mode loaded crack in an elastic-plastic material can be represented using kinematically independent variables that are non-local by construction since they are a set of intensity factors ($K_I^\infty, K_{II}^\infty, K_{III}^\infty, \rho_I, \rho_{II}, \rho_{III}$) of the crack tip kinematic fields basis ($\underline{\phi}_I^{el}(\underline{x}), \underline{\phi}_{II}^{el}(\underline{x}), \underline{\phi}_{III}^{el}(\underline{x}), \underline{\phi}_I^{pl}(\underline{x}), \underline{\phi}_{II}^{pl}(\underline{x}), \underline{\phi}_{III}^{pl}(\underline{x})$). In order to have a full description of the crack kinetics, history effects, internal stresses and other phenomena, other additional internal variables have to be incorporated into the model. This work provides some preliminary ideas about the evolution of some of these internal variables.

In addition, the elastic-plastic kinematic field can be partitioned using the Karhunen-Loeve (KL) decomposition (see 2.1.1) into a sum of temporal factors and space fields products. It was shown that the two first modes of this decomposition are sufficient to reconstruct the total kinematic field with a reasonable error [Pommier and Hamam, 2007]. It was shown as well that the first spatial mode of this decomposition is similar to the displacement obtained from a pure linear elastic FE simulation (see figure 2.3). Therefore, the complementary part (second KL mode) can be considered as a description of the nonlinear behavior, i.e. the plasticity. Based on this description, elastic and plastic spatial fields can form an orthogonal basis which is coherent with the hypothesis that elasticity and plasticity are kinematically independent. Moreover, temporal coefficients of the two first modes correspond respectively to $\dot{\check{K}}$ and $\dot{\rho}$ considered as degrees of freedom of the problem.

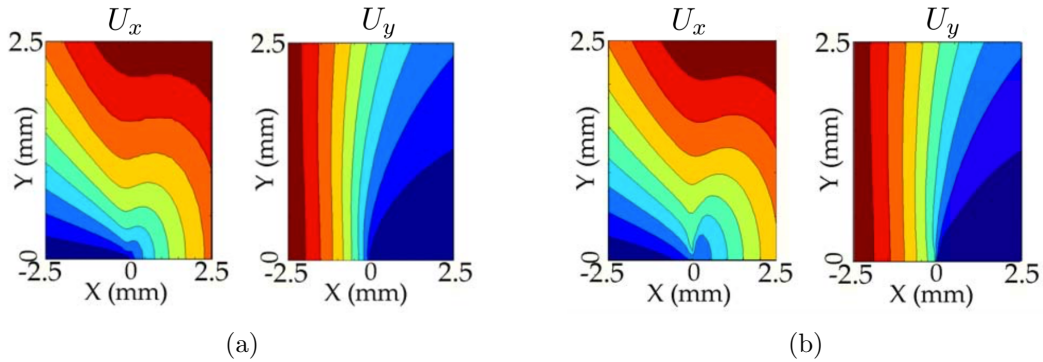


Figure 2.3: Comparison between (a) the elastic reference field obtained by elastic FE simulations and (b) the first Karhunen-Loeve mode [Hamam, 2006]

The starting point for the condensed modeling of plasticity near the crack tip is the determination of the elastic and plastic kinematic bases $\phi_i^{el}(\underline{x})$ and $\phi_i^{pl}(\underline{x})$. These bases depend on the material constitutive model. Thus, for the case of an anisotropic material, kinematic bases depend on the orientation of the material with respect to the crack. The identification is based on a set of finite element simulations. The numerical protocol and the methodology, followed to obtain elastic and plastic reference fields in a first step and then to identify an extended material model based on this kinematic bases, are presented in next sections within an application case.

2.3 Protocol for the kinematic basis

2.3.1 Finite element model and mesh

The next part of this chapter is dedicated to the 2D application of the model reduction strategy. To do so, a 2D finite element model was used. The model is a $2\text{ m} \times 2\text{ m}$ plate. A 2D through thickness crack of length $2a = 20\text{ mm}$ is modeled under plane strain assumption. The crack tip is clamped while forces are applied on the summits of the plate through rigid body ties (see figure 2.4).

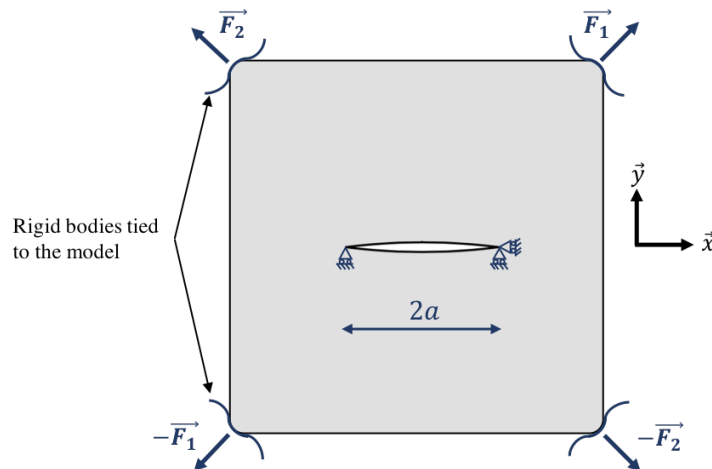


Figure 2.4: Illustration of the crack and boundary conditions of the 2D FE model.

Flourirot [Flourirot, 2004] investigated the influence of the mesh type and element size on the evolution of plasticity at the crack tip region of an elastic ideally plastic FCC single crystal. A comparison was made between a regular grid and a fan-like mesh as the one used in [Cuitino and Ortiz, 1996]. No major effects were observed between the two mesh types. Another comparison was made between the radii of the plastic zones for different mesh sizes. It confirmed that the plastic zone size does not depend on the mesh size. A conclusion was drawn that the evolution of plasticity at the crack tip can be considered as independent from the mesh type and element size provided that the number of elements is high enough.

Following these aforementioned observations, a fan-like mesh was used near the crack tip region. As shown in figure 2.5, all fields are extracted from this region. This circular domain is big enough to exclude singularity zone ($r_{min} = 30 \mu\text{m}$) and small enough to remain into the Irwin plastic zone ($r_{max} = 250 \mu\text{m}$). The size of this zone is adjusted as function of the loading type and range and of the material orientation.

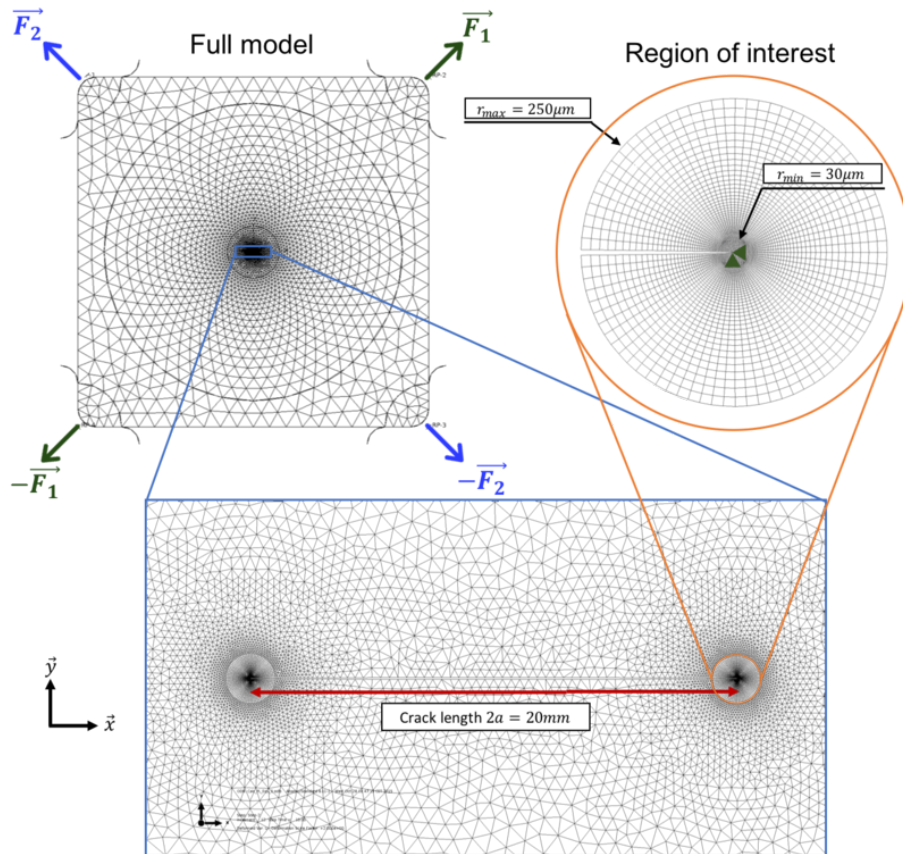


Figure 2.5: Illustration of the 2D Finite element model, boundary conditions and fan-like mesh of the near crack tip region.

2.3.2 Material

The anisotropic elasticity of the FCC single crystal of the AM1 Nickel base superalloy can be modeled with cubic elasticity.

For elasticity, the constitutive law is written as follows

$$\underline{\underline{\sigma}} = \underline{\underline{\mathbb{C}}} : \underline{\underline{\epsilon}}^e \quad (2.14)$$

The 2D Voigt notation is used:

$$\boldsymbol{\sigma} = \begin{pmatrix} \sigma_{11} \\ \sigma_{22} \\ \sigma_{12} \end{pmatrix} \quad \boldsymbol{\varepsilon} = \begin{pmatrix} \varepsilon_{11} \\ \varepsilon_{22} \\ 2\varepsilon_{12} \end{pmatrix} \quad \underline{\underline{\mathbb{C}}} = \begin{pmatrix} C_{11} & C_{12} & 0 \\ C_{12} & C_{11} & 0 \\ 0 & 0 & C_{44} \end{pmatrix} \quad (2.15)$$

With $\underline{\underline{\mathbb{C}}}$ is the stiffness tensor. For cubic elasticity, it depends on three material constants: $C_{11} = 197$ GPa, $C_{12} = 144$ GPa and $C_{44} = 90$ GPa. An isotropic case was studied as a reference in order to compare and identify the effect of the cubic anisotropic. Material parameters used for this reference case are $E = 210$ GPa and $\nu = 0.3$.

The presence of the cubic anisotropy creates a mixed mode condition near the crack tip region. For the sake of simplicity, the application case presented in this chapter is a 2D case of a stationary crack. Thus, the study is restrained to fracture modes *I* and *II*. For this reason, the material is assumed to have the plane $z = 0$ as a symmetry plane as illustrated on figure 2.6. The following range of material orientations with respect to the crack is studied: $\beta = 0^\circ, 15^\circ, 30^\circ$ and 45° .

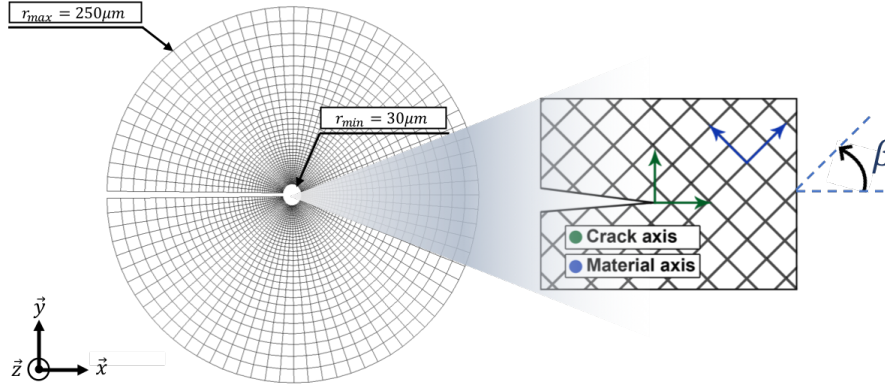


Figure 2.6: Illustration of the region of interest and the material orientation.

Using the aforementioned material parameters, tensile and shear moduli are shown on figure 2.7 as function of the material orientation with respect to the crack plane and front.

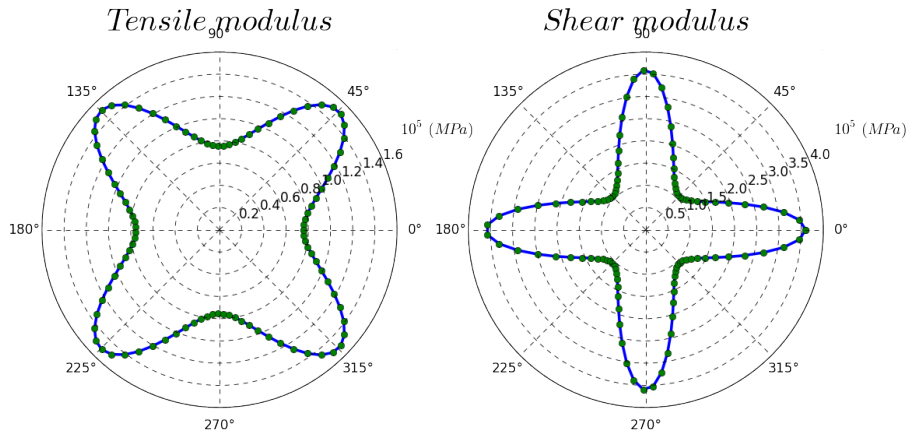


Figure 2.7: Tensile and shear moduli as function of the material orientation with respect to the crack.

An isotropic Von-Mises criterion with a nonlinear combined hardening are implemented to describe the nonlinear behavior of the material. Hardening parameters are presented in table 2.1.

- Von-Mises yield criterion:

$$f = \sqrt{\frac{3}{2}(\underline{\underline{\sigma}}^D - \underline{\underline{X}}) : (\underline{\underline{\sigma}}^D - \underline{\underline{X}})} - R \quad (2.16)$$

based on the deviatoric stress:

$$\underline{\underline{\sigma}}^D = \underline{\underline{\sigma}} - \frac{1}{3}Tr(\underline{\underline{\sigma}})\underline{\underline{I}} \quad (2.17)$$

- Consistency conditions for plasticity:

$$\begin{cases} f = \dot{f} = 0 & \Rightarrow \underline{\underline{\dot{\epsilon}}}_p \neq \underline{\underline{0}} \\ f < 0 \text{ or } (f = 0 \ \& \ \dot{f} < 0) & \Rightarrow \underline{\underline{\dot{\epsilon}}}_p = \underline{\underline{0}} \end{cases} \quad (2.18)$$

- The normality flow rule:

$$\underline{\underline{\dot{\epsilon}}}_p = \lambda \frac{\partial f}{\partial \underline{\underline{\sigma}}} \quad (2.19)$$

- The nonlinear isotropic hardening:

$$R = R_0 + Q_{inf}(1 - e^{-bp}) \quad (2.20)$$

- The nonlinear kinematic hardening following Armstrong-Frederick law [Armstrong and Frederick, 1966]:

$$\underline{\underline{X}} = \frac{2}{3}C\underline{\underline{\dot{\epsilon}}}_p - \gamma\underline{\underline{X}}\dot{p} \quad (2.21)$$

With \dot{p} the equivalent plastic strain rate:

$$\dot{p} = \sqrt{\frac{2}{3}\underline{\underline{\dot{\epsilon}}}_p : \underline{\underline{\dot{\epsilon}}}_p} \quad (2.22)$$

Table 2.1: Parameters of the isotropic and kinematic hardening of the model

Isotropic hardening		Kinematic hardening		
R_0 (MPa)	Q_{inf} (MPa)	b	C (MPa)	γ
250	5	25	75000	250

2.3.3 Kinematic fields extraction and correction

The aforementioned finite element model is created and simulations were performed using the commercial finite element solver *ABAQUS*.

In a first step, different elastic and elastic-plastic monotonic loadings were performed. Kinematic fields are extracted from the region of interest presented on figures 2.5 and 2.6. Extracted fields are corrected in order to get rid of rigid body transformation and the rotation of the crack plane that can be enhanced by the presence of the anisotropy. The following section describes the procedure followed to extract elastic and plastic reference fields.

2.3.4 Elastic reference fields

To obtain elastic reference fields of different fracture modes (*mode I* and *mode II*) and for different material orientations, linear elastic simulations were performed as follows:

- For $\phi_I^{el}(\underline{x})$, a pure *mode I* loading was performed with $K_I^\infty = 1 \text{ MPa}\sqrt{\text{m}}$ and $K_{II}^\infty = 0 \text{ MPa}\sqrt{\text{m}}$.
- For $\phi_{II}^{el}(\underline{x})$, a pure *mode II* loading was performed with $K_{II}^\infty = 1 \text{ MPa}\sqrt{\text{m}}$ and $K_I^\infty = 0 \text{ MPa}\sqrt{\text{m}}$.

The kinematic field $\underline{v}_i^{FE}(\underline{x}, t)$ extracted from the elastic simulation of the fracture mode i can be directly read as the corresponding elastic reference field:

$$\underline{v}_i^{FE}(\underline{x}, t) = 1 \text{ MPa}\sqrt{\text{ms}}^{-1} \cdot \phi_i^{el}(\underline{x}) = \underline{\phi}_i^{el}(\underline{x}) \quad (2.23)$$

These reference fields can be determined analytically based on Westergaard solutions (see section 2.1.2) for the isotropic case and on Sih, Paris and Irwin's solutions (see section 2.1.2) for the cubic material with $z = 0$ a plane of symmetry for the material.

As shown in these analytical solutions, reference fields can be decomposed into a radial scale function $f_i^{el}(r)$ and an angular distribution $\underline{g}_i^{el}(\theta)$.

$$\underline{\phi}_i^{el}(\underline{x}) = f_i^{el}(r) \cdot \underline{g}_i^{el}(\theta) \quad (2.24)$$

Besides, all fracture modes share the same radial function. Thus, elastic reference fields obtained from simulations of different fracture modes can be gathered in the same snapshot matrix and a Karhunen-Loeve decomposition is performed in order to separate radial and angular dependencies. This decomposition gives one radial scale function $f^{el}(r)$ and an angular distribution for each fracture mode $\underline{g}_i^{el}(\theta)$.

Figures 2.8, 2.9 and 2.10 show elastic reference fields for an isotropic case and for two anisotropic cases ($\beta = 0^\circ$ and $\beta = 15^\circ$). The plot in the middle shows the evolution of the radial scale function $f^{el}(r)$. As predicted by the analytical solution, it fits a \sqrt{r} function. This evolution shows that elasticity starts increasing away from the crack tip, i.e. the plastic zone, while approaching the K-dominance elastic zone. Angular distributions $\underline{g}_i^{el}(\theta)$ are shown on plots on left and right for *mode I* and *mode II* respectively. These plots show the deformed shape of a trigonometric circle once the corresponding distribution is applied on it. These distributions are rescaled in order to obtain a crack tip opening displacement (CTOD) equal to 1 for *mode I* and a crack tip sliding displacement (CTSD) equal to 1 for *mode II*. Comparisons between numerical solutions obtained from a Proper Orthogonal Decomposition (POD) and analytical solutions for the isotropic and for anisotropic cases show a good agreement between both solutions.

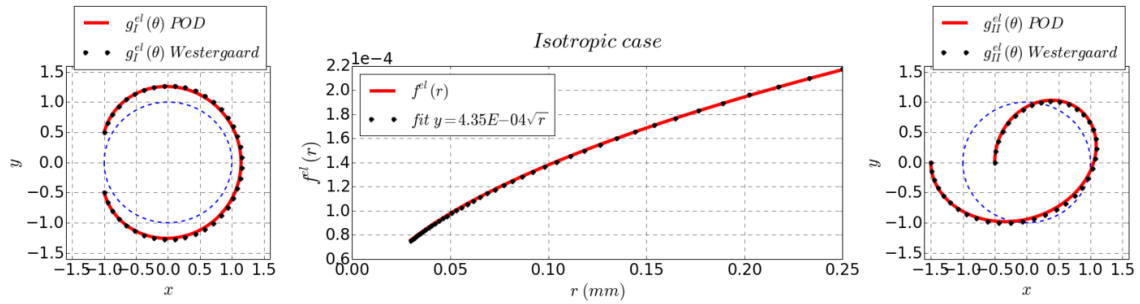


Figure 2.8: Elastic reference fields for an isotropic case, comparison with Westergaard analytical solution [Westergaard, 1939].

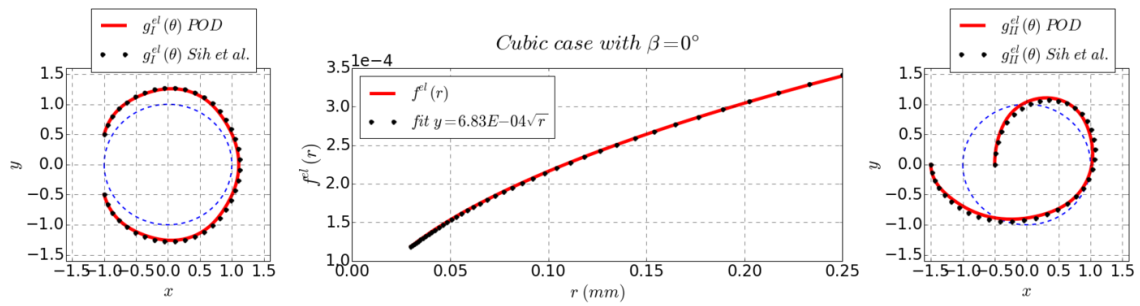


Figure 2.9: Elastic reference fields for a cubic material with $\beta = 0^\circ$, comparison with Sih's analytical solution [Sih et al., 1965].

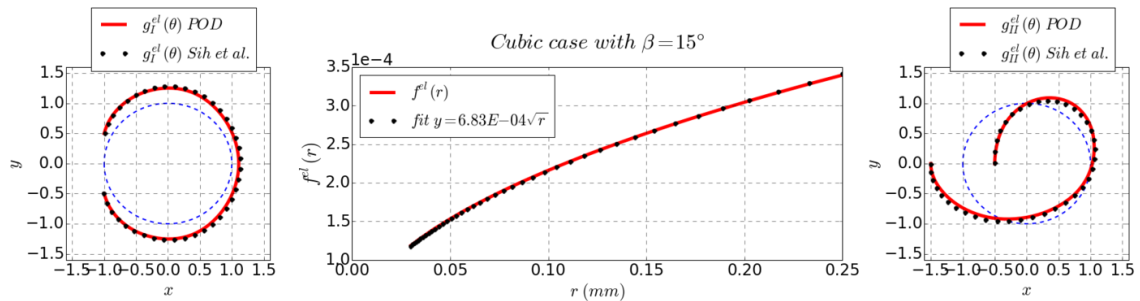


Figure 2.10: Elastic reference fields for a cubic material with $\beta = 15^\circ$, comparison with Sih's analytical solution [Sih et al., 1965].

2.3.5 Complementary reference fields based on the POD approach

A first attempt was made in [Pommier and Hamam, 2007] to analytically evaluate the complementary reference field of fracture *mode I* based on a dislocation distribution approach. This field arises from the existence of dislocations at the crack tip that are geometrically necessary in order to restore the traction-free boundary condition along the crack faces.

Later, a different approach was proposed based on finite element computations and the Proper Orthogonal Decomposition [Decreuse et al., 2009] and [Fremy et al., 2012]. In this approach, the plastic reference field of a fracture mode i is obtained by performing an elastic-plastic computation in pure mode i loading conditions, with $K_i^\infty = K_{max}$ and $K_{j \neq i}^\infty = 0$. The kinematic fields of each computation $\underline{v}_i^{FE}(\underline{x}, t)$ are extracted from the region of interest. Then, the elastic part is subtracted from the total elastic-plastic kinematic field (see equation 2.25). Since plasticity is the only source of dissipation in the model (no friction between crack faces, no damage, etc), this complementary non linear part is considered as the result of the plastic dissipation.

$$\tilde{\underline{v}}_i^{pl}(\underline{x}, t) = \underline{v}_i^{FE}(\underline{x}, t) - \sum_{i=1}^2 \dot{K}_i(t) \underline{\phi}_i^{el}(\underline{x}) \quad (2.25)$$

with

$$\dot{K}_i = \frac{\sum_{P \in D} \underline{v}_i^{FE}(P, t) \cdot \underline{\phi}_i^{el}(P)}{\sum_{P \in D} \underline{\phi}_i^{el}(P) \cdot \underline{\phi}_i^{el}(P)} \quad (2.26)$$

The plastic reference field $\underline{\phi}_i^{pl}(\underline{x})$ is the obtained by performing a Proper Orthogonal Decomposition on this plastic kinematic field in order to separate time and space dependencies. The first mode of this decomposition was found to be sufficient to describe the field with a reasonable error.

$$\tilde{\underline{v}}_i^{pl}(\underline{x}, t) \approx \dot{\rho}_i(t) \underline{\phi}_i^{pl}(\underline{x}) \quad (2.27)$$

The model is attached to the local coordinates system attached to the crack and the geometry is scale-invariant. This implies that the spatial distribution $\underline{\phi}_i^{pl}(\underline{x})$ of the solution is scale invariant too. Hence, it can be decomposed into a radial scale function and an angular distribution:

$$\underline{\phi}_i^{pl}(\underline{x}) = f_i^{pl}(r) \cdot \underline{g}_i^{pl}(\theta) \quad (2.28)$$

The plastic zone is assumed to remain confined into an elastic bulk. Thus, plasticity vanishes away from the crack which implies that the scale function $f^{pl}(r)$ verifies $f^{pl}(r) \xrightarrow{r \rightarrow \infty} 0$. Besides, the crack tip displacement is maximum and finite at the vicinity of the crack, which means that $f^{pl}(r) \xrightarrow{r \rightarrow 0} max$. The function is locally self-similar in a local coordinates system attached to the crack front and within the K-dominance area. Thus, it can be written as follows:

$$f^{pl}(\alpha r) - f^{pl}(0) = \beta(f^{pl}(r) - f^{pl}(0)) \quad (2.29)$$

All these properties can be verified by an exponential decay function at the first order of Taylor's development.

$$f^{pl}(r) \approx Ae^{-\frac{r}{p}} \quad (2.30)$$

A convention was made to rescale the radial function so that $f^{pl}(r) \xrightarrow[r \rightarrow 0]{} 1$. In addition, as it was done for the elastic part, angular functions $\underline{g}_i^{pl}(\theta)$ were rescaled so that the discontinuity between crack faces is equal to 1:

$$\left\| \underline{\Delta g}_i^j \right\| = \left\| \underline{g}_i^j(\theta = \pi) - \underline{g}_i^j(\theta = -\pi) \right\| = 1 \quad (2.31)$$

Finite element analyses were performed on different cases of material orientations. Figure 2.11 represents these complementary reference fields. The plot in the middle presents radial scale functions $f^{pl}(r)$. As discussed before, these functions can be fitted to an exponential decay function. Plots on the left and on the right present plastic angular distributions for fracture modes *I* and *II* respectively. Despite the anisotropy is only expressed by the cubic elasticity, a clear difference between different material orientations can be observed on these plastic distributions. The difference can be understood based on the distribution of tensile and shear moduli shown on figure 2.7.

For instance, under a pure fracture *mode II*, the shear modulus is the main parameter in action. As shown on figure 2.7, this modulus is maximum for $\beta = 0^\circ$. It decreases until reaching a minimum for $\beta = 45^\circ$. Thus, in order to obtain the same CTSD at $\theta = 0^\circ$ for all material orientations on the right plot on figure 2.11, higher applied stress is required for $\beta = 0^\circ$ compared to $\beta = 45^\circ$. This stress creates a more deformed shape of $\underline{g}_{II}^{pl}(\theta)$ for other angular positions θ different from zero where the tensile modulus enters in action in the material response.

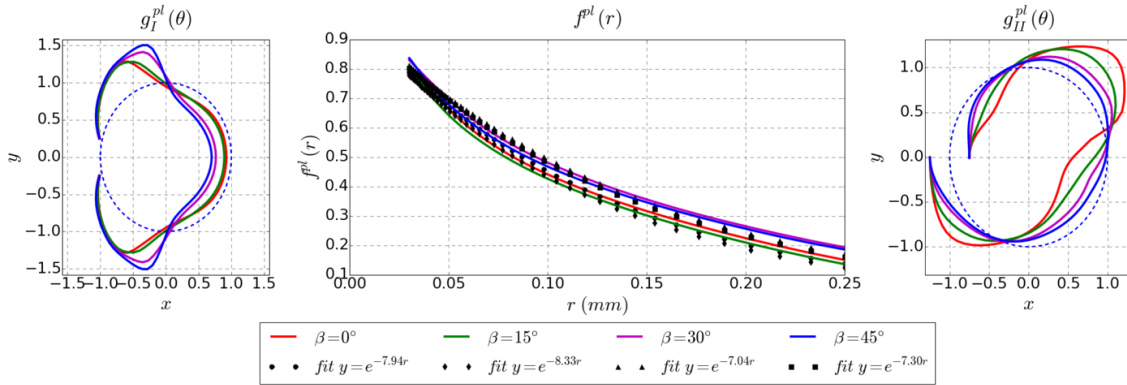
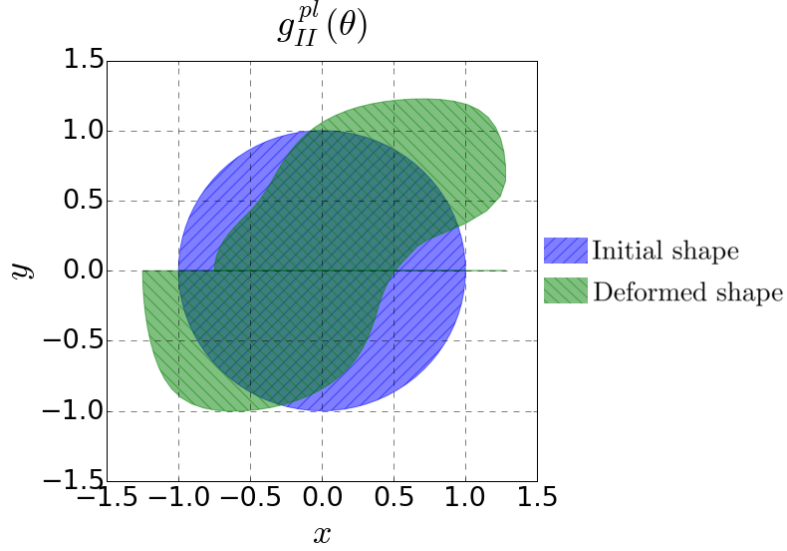


Figure 2.11: Plastic reference fields for different material orientations with respect to the crack.

Table 2.2 presents the ratio of the surface change between the initial trigonometric circle and the deformed shape under $\underline{g}_{II}^{pl}(\theta)$ transformation for the isotropic case and anisotropic case with different material orientations. One can note that the deformed shape of the plastic angular distribution has the same area as the initial trigonometric circle. This observation is in coherence with the fact that plasticity occurs without any volume change [Lemaitre and Chaboche, 1994]. Figure 2.12 illustrates this isochoric transformation.

Table 2.2: Surface change between the initial and deformed shape under $\underline{g}_{II}^{pl}(\theta)$ transformation

	Isotropic	$\beta = 0^\circ$	$\beta = 15^\circ$	$\beta = 30^\circ$	$\beta = 45^\circ$
Surf. change (%)	0.48	0.51	0.72	0.29	0.15

Figure 2.12: Illustration of the isochoric transformation by $\underline{g}_{II}^{pl}(\theta)$ for $\beta = 0^\circ$.

2.3.6 Validity of the approach

With the presence of plasticity in the model, the applied loading range should respect the hypothesis proposed at the beginning while extracting plastic reference fields. Concerned hypotheses here are the local self-similarity of both the structure and the displacement field around the crack tip, the small strain condition and the confinement of the plastic zone into an elastic bulk. For these reasons, the Karhunen-Loeve decomposition should be performed on a range where plasticity remains confined within the region of interest. In this same loading range, plasticity should be pronounced enough so that both elastic and plastic kinematics have close weights in the total motion of the structure.

In this chapter, the following procedure was used in order to define the convenient loading range that from which plastic reference fields can be extracted. Next chapters discuss further procedures.

Minimum loading range

The minimum of loading range is computed so that the plastic zone is large enough into the region of interest. In fact when the behavior is linear elastic, \tilde{K}_i is the same as the nominal stress intensity factor K_i^∞ . When there is plasticity in the model, \tilde{K}_i accounts for the applied loading through K_i^∞ and for the “shielding effect” K_i^{shield} [Rice and Thomson, 1974] caused by internal stresses and the confinement of the plastic zone.

Based on this statement, the plasticity at the region of interest can be evaluated by the indicator E_i^{Shield} , which is defined as the difference between the nominal stress intensity factor K_i^∞ and the stress intensity factor obtained from the projection of the velocity field

on the elastic basis \tilde{K}_i . For a given fracture mode i :

$$E_i^{Shield}(t) = |\tilde{K}_i(t) - K_i^\infty(t)| \quad (2.32)$$

Maximum loading range

Defining a maximum of the loading range is mandatory to ensure the confinement of the plastic zone and the local self-similarity of the crack tip geometry. To obtain this maximum, two types of computations are performed. The first takes into account the non linearity of the geometry caused by large deformation by re-adapting the shape of elements at each time increment. This option is available in the commercial FE solver *ABAQUS* and known as the *NLGEOM* simulation. The second type is known as *LGEOM* computation. It assumes that FE simulations are performed under small strain conditions. The idea here is to catch the difference between these two analyses. This difference is supposed to be an indicator of the self-similarity and small strain hypotheses. The maximum nominal stress intensity factor is obtained once the difference reaches a threshold value.

$$E_i^{L-NL}(t) = |\tilde{K}_i^{LGEOM}(t) - \tilde{K}_i^{NLGEOM}(t)| \quad (2.33)$$

Example

These computations were applied for both fracture modes simulations and for every studied case of material orientation. Figure 2.13 shows an example of this study under fracture mode *I* for material orientation $\beta = 15^\circ$. Figure 2.13a shows the evolution of different stress intensity factors: K_I^∞ , \tilde{K}_I^{LGEOM} and \tilde{K}_I^{NLGEOM} . Figure 2.13b shows the evolution of differences E_I^{Shield} and E_I^{L-NL} as function of the applied loading. A threshold value was assigned to each difference in order to illustrate the choice of minimum and maximum loadings.

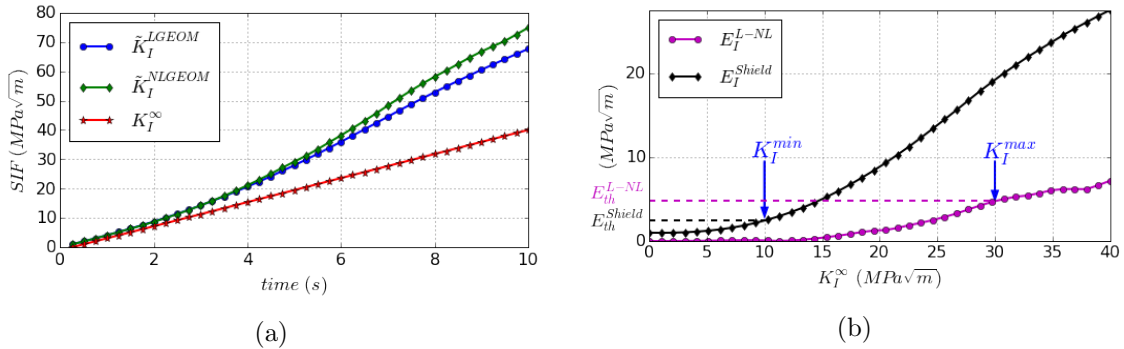


Figure 2.13: (a) Different stress intensity factors: the nominal one, the one obtained from an *LGEOM* simulation and from *NLGEOM* simulation and (b) differences E_I^{Shield} and E_I^{L-NL} used to define the loading range for the case of material orientation $\beta = 15^\circ$.

2.3.7 Reconstruction error

Once the kinematic basis is determined for each fracture mode, the stress intensity factor $\tilde{K}_i(t)$ and the blunting intensity factor $\dot{\rho}_i(t)$ corresponding to a fracture mode i of a

given elastic-plastic kinematic field $\underline{v}^{FE}(\underline{x}, t)$ are obtained by the projection of this field on the corresponding reference field:

$$\dot{\tilde{K}}_i(t) = \frac{\sum_{P \in D} \underline{v}^{FE}(P, t) \cdot \underline{\phi}_i^{el}(P)}{\sum_{P \in D} \underline{\phi}_i^{el}(P) \cdot \underline{\phi}_i^{el}(P)} \quad (2.34)$$

$$\dot{\rho}_i(t) = \frac{\sum_{P \in D} \underline{v}^{FE}(P, t) \cdot \underline{\phi}_i^{pl}(P)}{\sum_{P \in D} \underline{\phi}_i^{pl}(P) \cdot \underline{\phi}_i^{pl}(P)} \quad (2.35)$$

In order to evaluate the quality of this approximation at each time increment, two fields $\tilde{\underline{v}}^{el}(\underline{x}, t)$ and $\tilde{\underline{v}}(\underline{x}, t)$ are reconstructed as follows:

$\tilde{\underline{v}}^{el}(\underline{x}, t)$ is the kinematic field approximated only with the elastic basis:

$$\tilde{\underline{v}}^{el}(\underline{x}, t) = \sum_{i=1}^2 \dot{\tilde{K}}_i(t) \cdot \underline{\phi}_i^{el}(\underline{x}) \quad (2.36)$$

$\tilde{\underline{v}}(\underline{x}, t)$ is the kinematic field approximated with both elastic and plastic bases:

$$\tilde{\underline{v}}(\underline{x}, t) = \sum_{i=1}^2 \dot{\tilde{K}}_i(t) \cdot \underline{\phi}_i^{el}(\underline{x}) + \dot{\rho}_i(t) \cdot \underline{\phi}_i^{pl}(\underline{x}) \quad (2.37)$$

A reconstruction error is associated to each reconstructed field as follows:

$$C_e = \sqrt{\frac{\sum_{P \in D} (\underline{v}^{FE}(P, t) - \tilde{\underline{v}}^{el}(P, t))^2}{\sum_{P \in D} (\underline{v}^{FE}(P, t))^2}} \quad (2.38)$$

$$C_{ep} = \sqrt{\frac{\sum_{P \in D} (\underline{v}^{FE}(P, t) - \tilde{\underline{v}}(P, t))^2}{\sum_{P \in D} (\underline{v}^{FE}(P, t))^2}} \quad (2.39)$$

C_e is the error of a reconstruction of the kinematic field using only a pure elastic field. C_{ep} is the error of the reconstruction based on both elastic and plastic reference fields. If C_{ep} is lower than C_e , the plastic field is improving the solution. This means also that there is plasticity around the crack tip. It can be concluded that the difference $C_e - C_{ep}$ between both errors can be used as an indicator of the yielding at the region near the crack tip.

2.4 Condensed material model for the near crack tip region

The incremental model describes pure fatigue crack growth as a plasticity induced phenomenon. Therefore, the determination of the crack growth needs a precise study of the plasticity and its evolution near the crack tip. On the other hand, the number of degrees of freedom of the problem needs to be reduced in a way that allows the incremental study of crack growth. For these reasons, the plasticity at the crack tip is described by a condensed model based on nonlocal quantities. These quantities are the stress intensity factors and the blunting intensity factors obtained from projection on the elastic and plastic frameworks previously defined. In order to take into account internal stresses and the history effect, the evolution of internal variables has to be studied as well.

This section discusses some strategies followed to determine main ingredients of an extended material model of the region near the crack tip based on nonlocal quantities. These ingredients are a yield criterion for this region and a plastic flow rule. The study is restrained in this chapter to the case of a mixed fracture mode $I + II$. [chapter 3](#) discusses in more details these strategies for the more general case of a mixed fracture mode $I + II + III$.

2.4.1 Yield criterion

Pommier and co-workers [[Pommier et al., 2009](#)] proposed a nonlocal yield surface criterion similar to the Von Mises criterion at the region near the crack tip but applied to LEFM fields for the case of mixed *mode I* and *mode II* crack. Later, this criterion was extended to the 3D case but always for isotropic materials using Westergaard asymptotic solutions [[Fremy et al., 2012](#)].

The presented work deals with a cubic elasticity. Thus, the stress state at the crack tip depends on the material parameters and the crystal orientation with respect to the crack plane. The aforementioned yield criterion is determined in the following work based on anisotropic analytical solutions.

Local Von-Mises criterion

For a given volume element undergoing small strains, the strain energy density can be written as:

$$U = \frac{1}{2} \underline{\underline{\sigma}} : \underline{\underline{\varepsilon}} \quad (2.40)$$

Knowing that the deviatoric parts of stress and strain are given by:

$$\begin{aligned} \underline{\underline{\sigma}}^D &= \underline{\underline{\sigma}} - \frac{1}{3} \text{Tr}(\underline{\underline{\sigma}}) \underline{\underline{I}} \\ \underline{\underline{\varepsilon}}^D &= \underline{\underline{\varepsilon}} - \frac{1}{3} \text{Tr}(\underline{\underline{\varepsilon}}) \underline{\underline{I}} = \underline{\underline{\mathbb{S}}} : \underline{\underline{\sigma}}^D \end{aligned} \quad (2.41)$$

The elastic strain energy density becomes:

$$2U = \underbrace{\underline{\underline{\sigma}}^D : \underline{\underline{\mathbb{S}}} : \underline{\underline{\sigma}}^D}_{\text{distortional elastic energy}} + \underbrace{\frac{1}{9} \text{Tr}(\underline{\underline{\sigma}}) \text{Tr}(\underline{\underline{\varepsilon}})}_{\text{volume change energy}} \quad (2.42)$$

The strain energy density can be partitioned into a volume change energy and a distortional elastic energy. Regarding that plasticity occurs without volume change, the Von-Mises yield criterion is computed only from the distortional elastic energy:

$$U^D = \frac{1}{2} \underline{\underline{\sigma}}^D : \underline{\underline{\mathbb{S}}} : \underline{\underline{\sigma}}^D \quad (2.43)$$

The main idea is that plastic yield occurs when elastic shear energy reaches a critical distortional value. This helps computing an equivalent stress value for a multiaxial loading

case and to compare it with the yield stress σ^Y obtained from a simple uniaxial loading case. The criterion is written as follows:

$$U^D(\underline{\underline{\sigma}}) = U^D(\underline{\underline{\sigma}}^Y) \quad (2.44)$$

Which implies, for the case a multi-axial loading, the following criterion based on the equivalent Von Mises stress:

$$\sqrt{\frac{3}{2} \underline{\underline{\sigma}}^D : \underline{\underline{\sigma}}^D} = \sigma^Y \quad (2.45)$$

Extended Von-Mises criterion under LFM

The Von-Mises criterion was extended to the case a cracked structure based on LFM fields [Pommier et al., 2009]. The elastic shear energy is computed on a circular region around the crack tip.

$$E^D = \int_{\theta=-\pi}^{\pi} \int_{r=0}^{\delta} \frac{1}{2} \underline{\underline{\sigma}}^D : \underline{\underline{\mathbb{S}}} : \underline{\underline{\sigma}}^D r dr d\theta \quad (2.46)$$

When the loading state is inside the yield domain, the material response is elastic. With fracture mechanics quantities, the applied loading is expressed with the stress intensity factors $\underline{K}^\infty = (K_I^\infty, K_{II}^\infty)$. Lets also assume that $\underline{K}^X = (K_I^X, K_{II}^X)$ is the position of the yield surface under mixed fracture modes *I* and *II*. An assumption is made that LFM fields are valid as long as the position of the center of the yield domain is extracted from the loading state. Therefore, the stress intensity factor used in the expression of LFM fields is then $\underline{K}^* = (K_I^\infty - K_I^X, K_{II}^\infty - K_{II}^X)$.

Once the elastic distortional energy is expressed with linear elastic fracture mechanics quantities, a criterion similar to the Von-Mises criterion is considered. It assumes that yielding starts when this energy reaches a pure *mode I* yield threshold K_I^Y . The criterion is written as follows:

$$E^D(K_I^\infty - K_I^X, K_{II}^\infty - K_{II}^X) = E^D(K_I^Y, 0) \quad (2.47)$$

Isotropic case:

Based on Westergaard solutions of stress at the region near the crack tip [Westergaard, 1939] (see Appendix A), the case of an isotropic material under fracture modes *I* and *II* was presented in the work of [Decreuse et al., 2009]. The criterion presented in 2.4.1 gives the following yield function criterion:

$$f = \frac{(K_I^\infty - K_I^X)^2}{(K_I^Y)^2} + \frac{(K_{II}^\infty - K_{II}^X)^2}{(K_{II}^Y)^2} - 1 \quad (2.48)$$

with:

$$\frac{K_{II}^Y}{K_I^Y} = \sqrt{\frac{7 - 16\nu(1 - \nu)}{19 - 16\nu(1 - \nu)}} = 0.48 \quad \text{for } \nu = 0.3 \quad (2.49)$$

The corresponding yield surface is an ellipse in the $K_I^\infty - K_{II}^\infty$ plane (see figure 2.14a).

Cubic case with $z = 0$ a plane of symmetry:

For the studied case in this chapter, Sih Paris and Irwin's solutions [Sih et al., 1965] were implemented in the expression of the elastic shear energy presented in equation 2.46. As it was for for the isotropic case, the position \underline{K}^X of the yield domain is subtracted from the nominal stress intensity factor \underline{K}^∞ . Solutions are finally given as follows:

$$\begin{aligned}
 \text{mode I} & \left\{ \begin{aligned} \sigma_{xx} &= (K_I^\infty - K_I^X) \frac{1}{\sqrt{2\pi r}} \Re \left[\frac{\mu_1 \mu_2}{\mu_1 - \mu_2} \left(\frac{\mu_2}{\sqrt{\cos \theta + \mu_2 \sin \theta}} - \frac{\mu_1}{\sqrt{\cos \theta + \mu_1 \sin \theta}} \right) \right] \\ \sigma_{yy} &= (K_I^\infty - K_I^X) \frac{1}{\sqrt{2\pi r}} \Re \left[\frac{1}{\mu_1 - \mu_2} \left(\frac{\mu_1}{\sqrt{\cos \theta + \mu_2 \sin \theta}} - \frac{\mu_2}{\sqrt{\cos \theta + \mu_1 \sin \theta}} \right) \right] \\ \sigma_{xy} &= (K_I^\infty - K_I^X) \frac{1}{\sqrt{2\pi r}} \Re \left[\frac{\mu_1 \mu_2}{\mu_1 - \mu_2} \left(\frac{1}{\sqrt{\cos \theta + \mu_1 \sin \theta}} - \frac{1}{\sqrt{\cos \theta + \mu_2 \sin \theta}} \right) \right] \end{aligned} \right. \\
 \text{mode II} & \left\{ \begin{aligned} \sigma_{xx} &= (K_{II}^\infty - K_{II}^X) \frac{1}{\sqrt{2\pi r}} \Re \left[\frac{1}{\mu_1 - \mu_2} \left(\frac{\mu_2^2}{\sqrt{\cos \theta + \mu_2 \sin \theta}} - \frac{\mu_1^2}{\sqrt{\cos \theta + \mu_1 \sin \theta}} \right) \right] \\ \sigma_{yy} &= (K_{II}^\infty - K_{II}^X) \frac{1}{\sqrt{2\pi r}} \Re \left[\frac{1}{\mu_1 - \mu_2} \left(\frac{1}{\sqrt{\cos \theta + \mu_2 \sin \theta}} - \frac{1}{\sqrt{\cos \theta + \mu_1 \sin \theta}} \right) \right] \\ \sigma_{xy} &= (K_{II}^\infty - K_{II}^X) \frac{1}{\sqrt{2\pi r}} \Re \left[\frac{1}{\mu_1 - \mu_2} \left(\frac{\mu_1}{\sqrt{\cos \theta + \mu_1 \sin \theta}} - \frac{\mu_2}{\sqrt{\cos \theta + \mu_2 \sin \theta}} \right) \right] \end{aligned} \right. \quad (2.50) \\
 \text{mode III} & \left\{ \begin{aligned} \sigma_{xz} &= -(K_{III}^\infty - K_{III}^X) \frac{1}{\sqrt{2\pi r}} \Re \left[\frac{\mu_3}{\sqrt{\cos \theta + \mu_3 \sin \theta}} \right] \\ \sigma_{yz} &= (K_{III}^\infty - K_{III}^X) \frac{1}{\sqrt{2\pi r}} \Re \left[\frac{1}{\sqrt{\cos \theta + \mu_3 \sin \theta}} \right] \end{aligned} \right.
 \end{aligned}$$

Details about these solutions are presented in the Appendix A.

These fields are implemented in the criterion 2.47. The final criterion is given as follows:

$$f = \frac{(K_I^\infty - K_I^X)^2}{(K_I^Y)^2} + \frac{(K_{II}^\infty - K_{II}^X)^2}{(K_{II}^Y)^2} + \frac{(K_I^\infty - K_I^X)(K_{II}^\infty - K_{II}^X)}{(K_{I+II}^t)^2} - 1 \quad (2.51)$$

This criterion draws a tilted ellipse in the $K_I^\infty - K_{II}^\infty$ plane as shown on figure 2.14b. The size of the ellipse is calibrated based on the parameter K_I^Y . The angle of tilting with respect to the K_I^∞ axis and the ratio between the ellipse minor and major axes K_{II}^Y/K_I^Y depend on material parameters and the crystallographic orientation. These quantities are shown on figure 2.15 as function of the crystallographic orientation β .

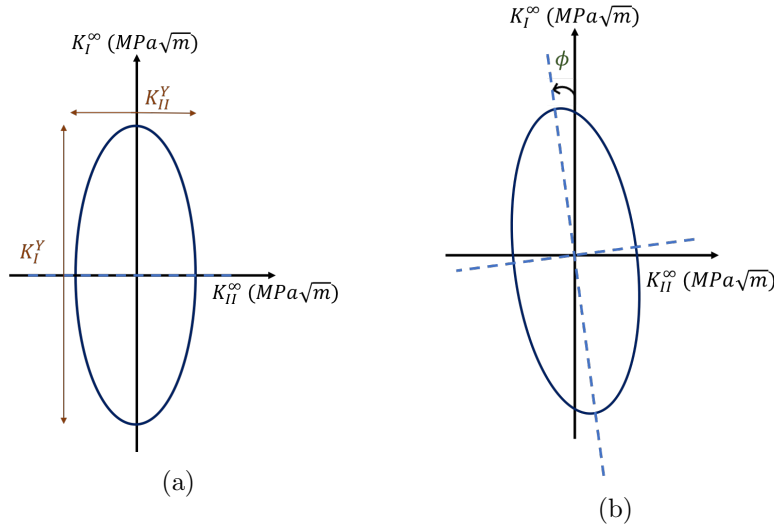


Figure 2.14: Illustration of the yield locus of the region near the crack tip in the $K_I^\infty - K_{II}^\infty$ plane (a) for an isotropic case and (b) for a cubic material.

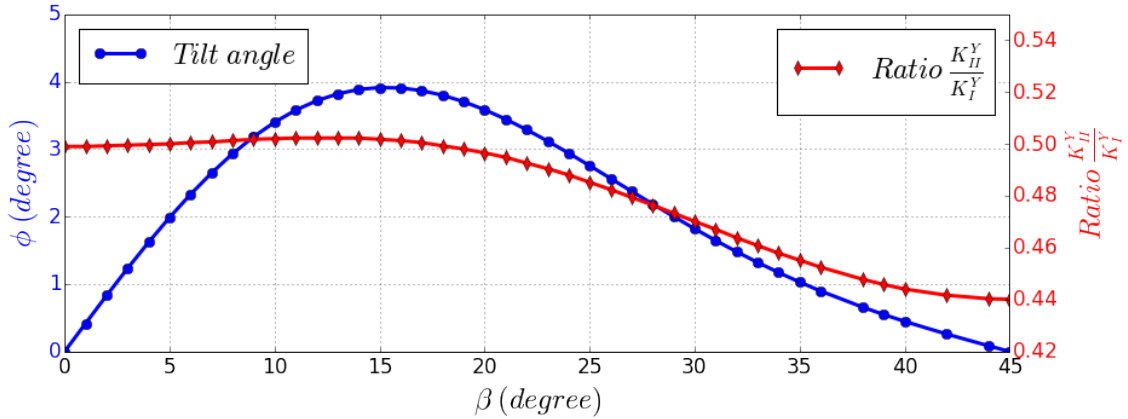


Figure 2.15: The tilt angle of the major yield surface axis with respect to the K_I^∞ axis and the ratio between the minor and the major axes for different crystallographic orientations.

2.4.2 Yield surface

In his work, Decreuse [Decreuse et al., 2009] explored the shape and position of the yield domain of the near crack tip region based on a set of finite element simulations for the case of an isotropic material. This section presents the same idea of investigating the yield surface in the space of nominal stress intensity factors $K_I^\infty - K_{II}^\infty$ based on the framework of elastic and plastic reference fields previously identified.

The idea is to perform an initial elastic-plastic loading with a given mixture ratio between fracture modes I and II . This loading is assumed to cause the yielding of the region near the crack tip and to move the center of the yield domain. A small elastic back-loading is performed to move back the loading state inside the yield surface. Then, different computations are performed in different directions taking each time the results of the initial computation as a restart point. This loading path is illustrated on figure 4.24.

On each loading branch of the star, kinematic reference fields are extracted from the region of interest. These fields are corrected then projected on the kinematic basis in order to obtain intensity factors $\dot{K}_i(t)$ and $\dot{\rho}_i(t)$ (see equations 2.34 and 2.35). At each time increment on this loading branch, reconstruction errors C_e and C_{ep} are computed (see equations 2.38 and 4.35). The difference $C_e - C_{ep}$ between the two errors is used as an indicator of plasticity at the region of interest. Thus, when this difference reaches a critical value, the region near the crack tip is assumed to start yielding and a point is plotted on the loading branch. A yield surface that describes the elasticity domain of the region near the crack tip can finally be constructed in the $K_I^\infty - K_{II}^\infty$ plane.

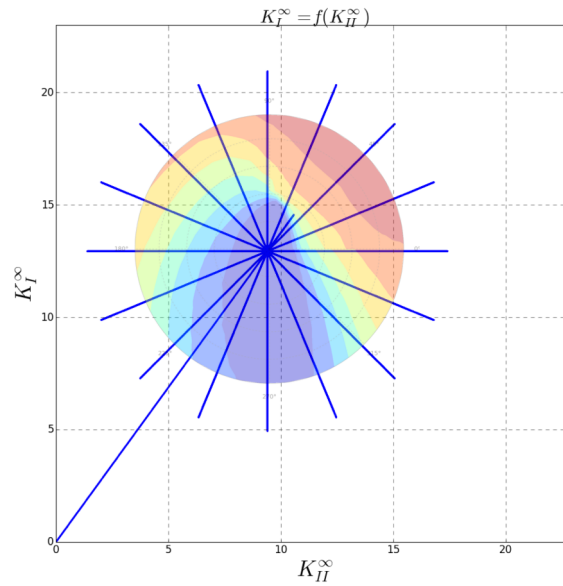


Figure 2.16: Exploration path in the $K_I^\infty - K_{II}^\infty$ plane and the map of the difference between reconstruction errors $C_e - C_{ep}$.

Flow directions can be represented by the vector of the blunting intensity factors $\dot{\rho} = (\dot{\rho}_{II}, \dot{\rho}_I)$ computed at the moment the loading reaches the limit of the yield locus. This procedure was followed in order to identify the yield domain. Figure 2.17 shows the obtained yield surface for the isotropic case for two different initial loadings.

Both yield surfaces have an elliptical lookalike shape. These shapes are in coherence with the yield criterion previously presented (see equation 2.48). However, a sharp distortion of these yield surfaces can be noted especially at the area where the initial loading was applied. Plastic flow directions are different from the loading directions and oriented outward the yield surface but they are perturbed by the distorted shape of the yield locus.

Aubin [Aubin, 2001] investigated experimentally the yield surface of a duplex stainless steel without and with initial monotonic loadings. As shown on figure 2.18, the shape of yield surface is distorted because of the initial loading. After the yielding of the material during the initial loading, the yield surface experiences a distortion in this loading direction and loses its elliptical shape. A surface in the shape of a “Half-moon” is identified instead. The conventional criteria based only on the kinematic and the isotropic hardening are no more representative of this distorted yield locus. This shape was observed in literature by many authors ([Bui, 1969], [Philipps and Lee, 1979], [Khan and Wang, 1993],

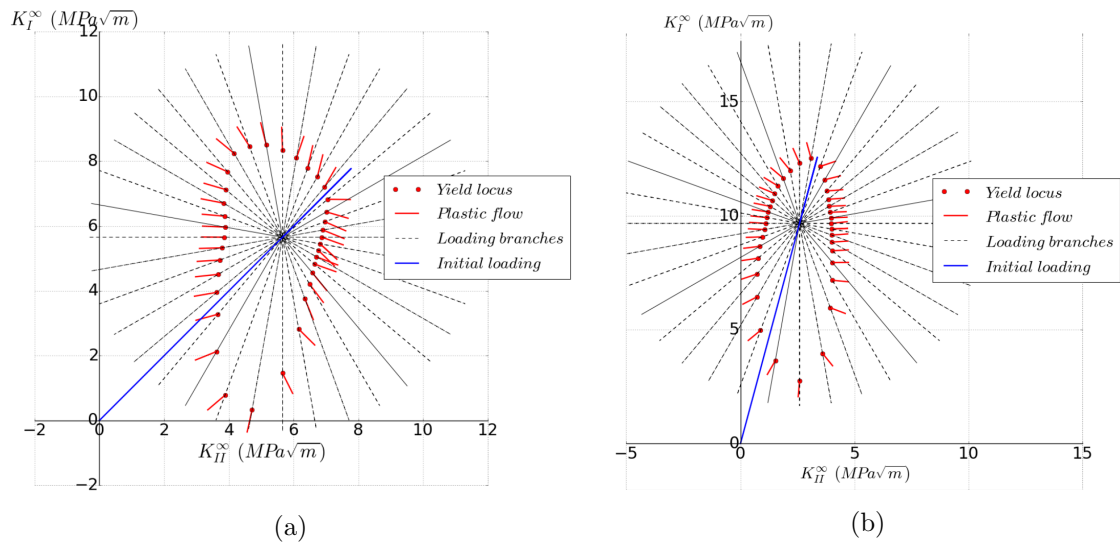


Figure 2.17: Yield surfaces and flow directions obtained for an isotropic case for (a) an initial loading $K_{II}^{\infty} = 8 \cos(\frac{\pi}{4})\text{MPa}\sqrt{\text{m}}$, $K_I^{\infty} = 8 \sin(\frac{\pi}{4})\text{MPa}\sqrt{\text{m}}$ and (b) an initial loading $K_{II}^{\infty} = 10 \cos(\frac{5\pi}{12})\text{MPa}\sqrt{\text{m}}$, $K_I^{\infty} = 10 \sin(\frac{5\pi}{12})\text{MPa}\sqrt{\text{m}}$.

[Wu and Yeh, 1991], [Aubin, 2008]).

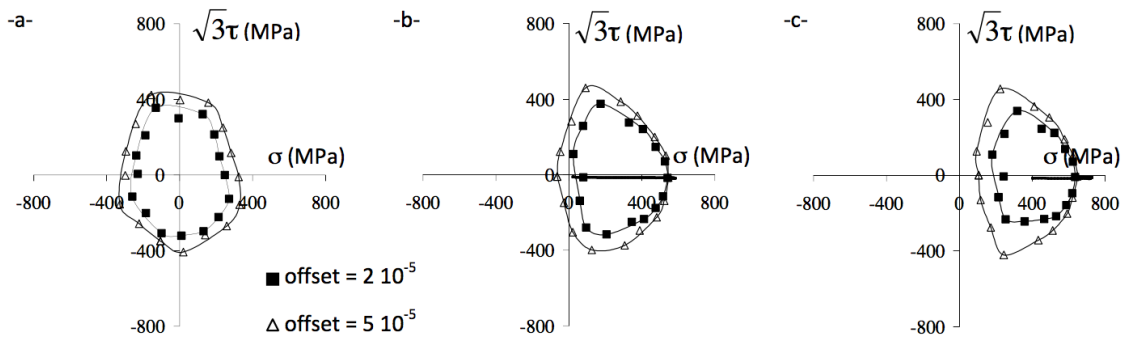


Figure 2.18: Yield surfaces obtained from experiences on the duplex stainless steel (a) without initial loading and after an initial monotonic loading at (b) $\varepsilon = 0.5\%$ and (c) $\varepsilon = 4\%$ [Aubin, 2008].

2.4.3 Plastic flow directions

As it was shown in the previous section, the loading history affects drastically the shape of the yield locus.

Moreover, the distortion of the elasticity domain influences plastic flow directions. The aim of this section is to explore plastic flow directions without being affected by the loading history presented by the initial loading. On the other hand, the Von-Mises criterion transposed to the scale of the crack shows that the yield surface has an elliptical shape in the $K_I^\infty - K_{II}^\infty$ plane. The ratio between minor and major axes can be obtained analytically. Therefore, the idea is to load the crack in an elliptical loading path in the $K_I^\infty - K_{II}^\infty$ plane that has the same major and minor axes ratio as the one obtained theoretically. The size of the elliptical loading path is increased incrementally as shown on figure 2.19. Four cycles are performed on each elliptical loading path before increasing the shape. The aim of this loading path is to approach the limits of the yield surface and to yield the region near the crack tip without causing its distortion. With the yielding of the crack tip region, plastic flow directions can be studied.

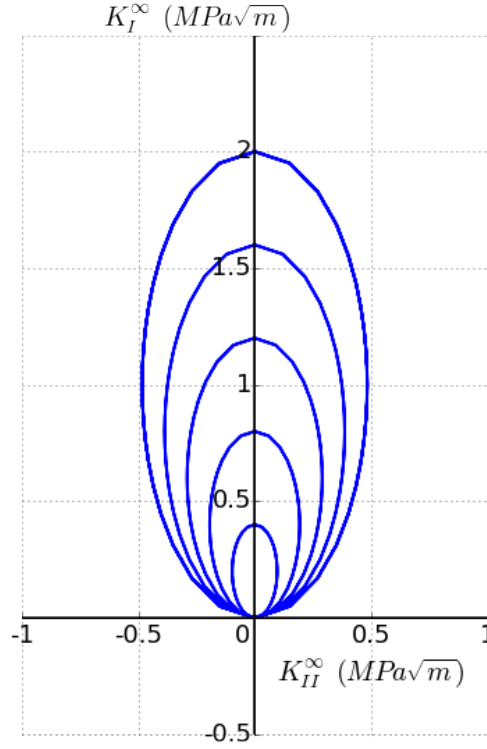


Figure 2.19: Loading path following five elliptical shapes with an increasing size while cycling four times per ellipse.

At each time increment during loading, kinematic fields $\underline{v}^{FE}(\underline{x}, t)$ are extracted from the region of interest. Blunting intensity factors $\dot{\rho}_i(t)$ are obtained from projection on the elastic reference fields $\underline{\phi}_i^{pl}(\underline{x})$ (see equation 2.52).

$$\dot{\rho}_i(t) = \frac{\sum_{P \in D} \underline{v}^{FE}(P, t) \cdot \underline{\phi}_i^{pl}(P)}{\sum_{P \in D} \underline{\phi}_i^{pl}(P) \cdot \underline{\phi}_i^{pl}(P)} \quad (2.52)$$

These rates of blunting intensity factors are integrated in order to obtain the evolution of the blunting at the crack tip region as function of time:

$$\rho_i(t) = \int_0^t \dot{\rho}_i(x) dx \quad (2.53)$$

Figures 2.20 and 2.21 show the evolution of blunting intensity factors in the $\rho_I - \rho_{II}$ plane for an isotropic case and for a cubic case with the crystallographic orientation $\beta = 30^\circ$. Figures 2.20a and 2.21a present the evolution of these quantities during the full

loading path. Figures 2.20b and 2.21b show this same evolution during the four cycles of the last elliptical loading path.

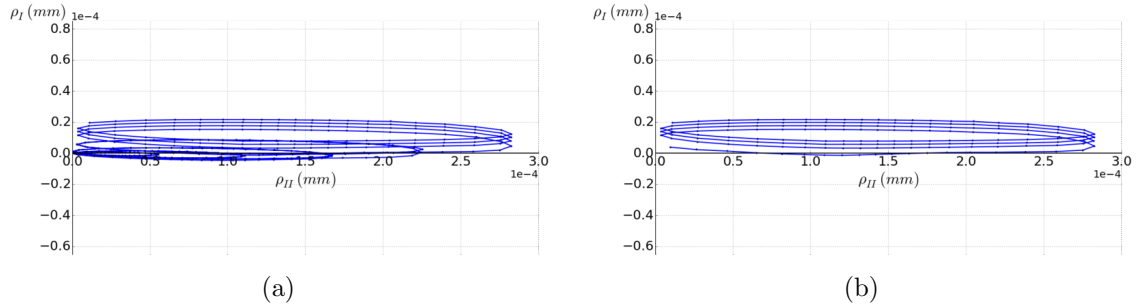


Figure 2.20: Evolution of blunting intensity factors $\rho_I = f(\rho_{II})$ for an isotropic case (a) during the whole exploration path and (b) during the cyclic loading along the last elliptical loading path.

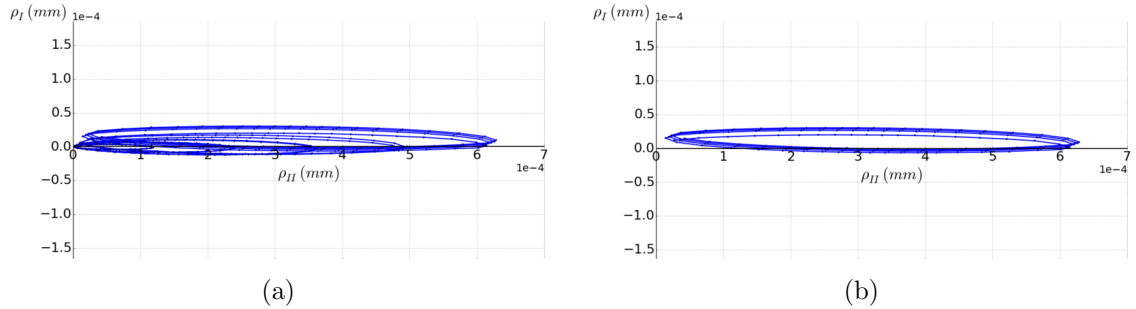


Figure 2.21: Evolution of blunting intensity factors $\rho_I = f(\rho_{II})$ for a cubic case with $\beta = 30^\circ$ (a) during the whole exploration path and (b) during the cyclic loading along the last elliptical loading path.

As a first observation from figures 2.20 and 2.21, the evolutions of the blunting intensity factors ρ_i for both isotropic and anisotropic cases present elliptical shapes rotated at an angle of 90° when compared to the elliptical loading path. It can be noted also that these shapes are quite symmetric and smooth and do not exhibit perturbations caused by the loading history effect. Considering that plastic flow directions can be represented by the intensity factor of the plastic kinematic fields, these directions are totally different from the applied loading path. This observation is in coherence with the positive dissipation principle where the plastic flow directions are outward normals to the yield locus shape. Despite both analyses have the same Von-Mises yield criterion with the same hardening parameters, different elasticity parameters create different plastic flow directions.

2.5 Conclusion

This chapter presents some basic steps followed in this work in order to transpose the local plasticity model at the region near the crack tip to a nonlocal scale. It deals with the problem of a crack under mixed fracture modes $I + II$ in a material presenting a cubic elasticity and a Von-Mises associated plasticity. To keep this study under fracture modes $I + II$, the elastic anisotropy was restrained to the case where $z = 0$ is a plane of

symmetry for the material, i.e. monoclinic case where material axes are along the crack coordinates system.

In order to describe crack tip plasticity with the minimum possible number of degrees of freedom, a model reduction is proposed based on the decomposition of kinematic fields into a sum of products of intensity factors and spatial distributions. These spatial distributions present the kinematic basis of the problem. It can be determined for a given material once for all then used for more complicated analyses to extract the degrees of freedom of the problem.

Elastic reference fields obtained from the Karhunen-Loeve decomposition coincide with the Sih, Paris and Irwin's asymptotic elastic solutions of displacement near the crack tip of a monoclinic case in which $z = 0$ is a plane of symmetry for the material.

A yield criterion at the scale of the crack for mixed fracture modes $I + II$ was proposed. This criterion is based on the elastic shear energy and LEFM fields. Plastic flow directions are studied based on the elastic and the plastic frameworks previously defined for a given material. These directions are shown to be different from loading direction and the are influenced by the loading history.

Many elements presented in this chapter are discussed in more details in the rest of this work for a more generalized case of cubic anisotropy under the three fracture modes $I + II + III$.

Mixed $I+II+III$ modes with cubic elasticity and Von-Mises plasticity

This chapter studies crack tip plasticity under mixed fracture modes $I + II + III$ of a nickel base superalloy single crystal. The material behavior is modeled using cubic elasticity and an isotropic criterion for plasticity (Von-Mises criterion). The main aim is to explore a strategy of modeling the crack tip plasticity based on a set of nonlocal variables. The study starts by finding a convenient framework for the state of kinematic fields. This framework is meant to be the best possible description of both elasticity and near crack tip plasticity. Once this framework is obtained, it will be used in a second step to identify principle ingredients of an incremental and nonlocal plasticity model for the region near the crack tip. These ingredients are a plastic flow rule, a yield criterion and a set of internal variables, such as the size and the center of the yield surface. This study will help writing the model in a thermodynamic context as it is usually done for an elastic-plastic constitutive law. The work is developed for a range of crystallographic orientations with respect to the crack coordinates. An isotropic case is studied as well to be used as a basis for comparison.

3.1 State of the art

The first part of this section highlights the effect of the crystallographic orientation of a nickel base single crystal on the cyclic behavior, on the evolution of plasticity around a notch and on the crack growth rate. The second part gives a brief discussion about the asymptotic elastic solutions near the crack tip region and the formalisms used for these solutions.

3.1.1 Influence of the crystallographic orientation

Hanriot [Hanriot, 1993] had studied the cyclic behavior of the single crystals of the AM1 superalloy for various crystal orientations at low and high temperatures. Figure 3.1a shows the effect of the material orientation on the shape of the stabilized stress-total strain curves while applying the same inelastic strain amplitude. Figure 3.1b compares the stress amplitudes of cyclic hardening at the first cycle, the stabilized cycle of the [001] orientation and the stabilized cycle of the [111] orientation. This latter orientation exhibits higher hardening. These figures highlight the importance of the crystallographic orientation in the material response to cyclic loadings.

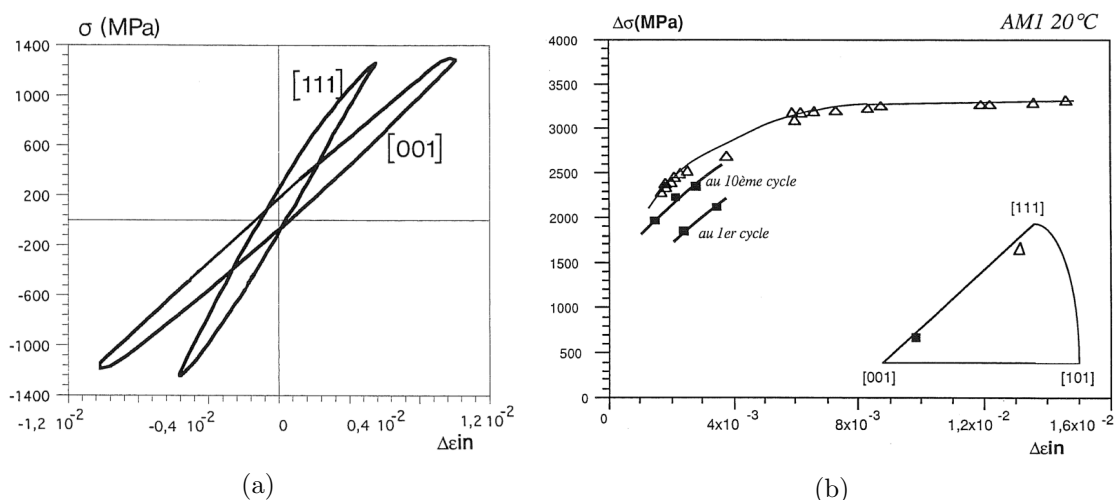


Figure 3.1: Effect of the crystallographic orientation on the cyclic behavior of the AM1 at 20 °C [Hanriot, 1993] (a) Stress-total strain loops under equivalent plastic strain amplitudes and (b) Cyclic hardening curves of the stress amplitudes as function of the inelastic strain: 1st cycle & 10th cycle for a crystal orientation close to [001] (squares), 10th cycle for another close to [111] (empty triangles).

Arakere [Arakere et al., 2009] compared 3D elastic finite element analyses of both an isotropic and a cubic anisotropic cases. He had shown that incorporating elastic anisotropy exhibits a noticeable effect on the predicted evolution of plasticity at the region near a notch. Figure 3.2 shows, for both cases, the distribution of slip sectors i.e. sectors of constant stresses, near the notch of nickel base superalloy single crystal.

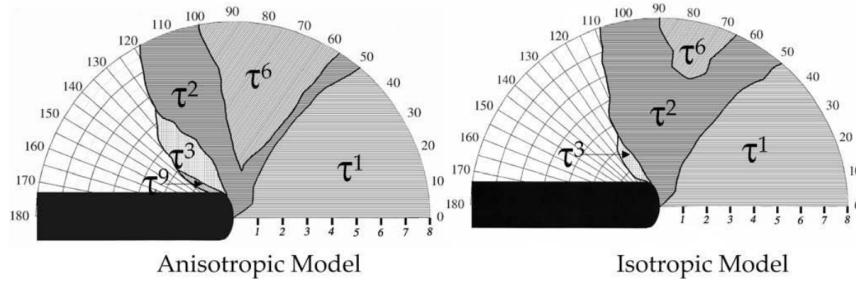


Figure 3.2: Comparison between the effect of cubic elasticity and isotropic elasticity on the predicted distribution of slip fields around a notch based on 3D elastic FEA [Arakere et al., 2009].

In addition to its effect on the cyclic behavior and on the evolution of plasticity near a stress concentration region, the crystallographic orientation impacts the crack growth rate and direction as well. Fleury [Fleury, 1991] had observed an obvious effect of the material orientation in the crack propagation in the AM1 at 650 °C. This effect mainly appears at low crack growth rates ($da/dN < 10^{-7}$) with a ratio $R = 0.1$. The crack growth rate is multiplied by a coefficient of 4 when switching the material orientation with respect to the crack front and plane from $(001)[110]$ to $(001)[100]$.

Marchal [Marchal, 2006] studied the crack propagation under fatigue and creep loadings in these single crystals at high temperatures. He observed that at low frequency and at $\Delta K < 25 \text{ MPa}\sqrt{\text{m}}$, the crack growth rate is higher when the material is oriented at $\gamma_{[100]}^{(001)}$ compared to the orientation $\gamma_{[110]}^{(001)}$.

3.1.2 Asymptotic elastic solutions and resolution formalisms

Since 1939, Westergaard [Westergaard, 1939] developed an asymptotic solution of elastic fields surrounding the crack tip of an isotropic material based on the Airy's stress functions. Sih, Paris and Irwin [Sih et al., 1965] extended in 1965 these solutions to the case of a monoclinic anisotropy by presenting elastic fields near the crack tip region in a rectilinearly anisotropic bodies. This work was developed for materials presenting certain symmetries with the crack plane ($z = 0$ plane of symmetry). Hoenig [Hoenig, 1982] proposed in 1982 a three-dimensional general solution of stress and displacement of a through crack for a fully anisotropic material based on the Lekhnitskii formalism [Lekhnitskii, 1963].

The Lekhnitskii formalism [Lekhnitskii, 1963] serves to solve a two-dimensional linear anisotropic elasticity problem. It is known that basic equations of anisotropic elasticity are the equilibrium equations under static loading conditions, compatibility equations under small strain assumption and the constitutive law equations relating stress to strain.

$$\sigma_{ij,j} + f_i = 0, \quad \varepsilon_{ij} = \frac{1}{2}(u_{i,j} + u_{j,i}), \quad \sigma_{ij} = C_{ijkl}\varepsilon_{kl}, \quad i, j, k, l = 1, 2, 3 \quad (3.1)$$

When two-dimensional deformations are considered, i.e. field quantities depend solely upon two coordinates (x, y) , a complex variables formulation can be used. The Lekhnitskii formalism [Lekhnitskii, 1963] introduces two Airy's stress functions. It starts with solving

the equilibrated stress equation in a way that satisfies the stress-strain relation and the strain-displacement relation.

The Stroh formalism [Stroh, 1958], [Stroh, 1962] and [Ting, 1996] aims to solve the same problem of linear anisotropic elasticity by using the same complex variables formulation. It starts with the compatible displacements and assumes that they depend only on two coordinates x and y . Then it verifies the equilibrium equation.

3.2 Material model and finite element implementation

This section gives some details about the constitutive law used to simulate the single crystal superalloy behavior. It explains also the linear elastic solution near the crack tip for a general anisotropic material. The finite element model used in simulations is presented as well with some technical details about the mesh, boundary conditions, the extraction of stress intensity factors and their employment to monitor the applied loading.

3.2.1 Cubic elasticity and studied material orientations

Constitutive model

As mentioned previously, the anisotropic behavior of the single crystal of the AM1 Nickel base superalloy presents a convenient application case for this case. The elastic behavior of the FCC lattice structure of this material can be described by the cubic anisotropy. The stiffness tensor C_{ijkl} is then characterized by three elastic parameters at a given temperature. The linear elastic behavior of the single crystal is written as follows:

$$\underline{\underline{\sigma}} = \underline{\underline{\mathbb{C}}} : \underline{\underline{\varepsilon}}^e \quad (3.2)$$

The Voigt notation is used:

$$\underline{\underline{\sigma}} = \begin{pmatrix} \sigma_{11} \\ \sigma_{22} \\ \sigma_{33} \\ \sigma_{23} \\ \sigma_{13} \\ \sigma_{12} \end{pmatrix} \quad \underline{\underline{\varepsilon}} = \begin{pmatrix} \varepsilon_{11} \\ \varepsilon_{22} \\ \varepsilon_{33} \\ 2\varepsilon_{23} \\ 2\varepsilon_{13} \\ 2\varepsilon_{12} \end{pmatrix} \quad \underline{\underline{\mathbb{C}}} = \begin{pmatrix} C_{11} & C_{12} & C_{12} & 0 & 0 & 0 \\ C_{12} & C_{11} & C_{12} & 0 & 0 & 0 \\ C_{12} & C_{12} & C_{11} & 0 & 0 & 0 \\ 0 & 0 & 0 & C_{44} & 0 & 0 \\ 0 & 0 & 0 & 0 & C_{44} & 0 \\ 0 & 0 & 0 & 0 & 0 & C_{44} \end{pmatrix} \quad (3.3)$$

with the following values of these parameters: $C_{11} = 197$ GPa, $C_{12} = 144$ GPa and $C_{44} = 90$ GPa. An isotropic case was studied as a reference in order to compare and identify the effect of the cubic anisotropy. Material parameters used for this reference case are $E = 200$ GPa and $\nu = 0.3$.

For plasticity, simulations are restrained in this chapter on the isotropic Von Mises criterion with a combined nonlinear hardening. The model and material parameters are the same used in [chapter 2](#) (see [2.3.2](#)). [Table 3.1](#) recalls the used hardening parameters.

Table 3.1: Parameters of the isotropic and kinematic hardening of the model

Isotropic hardening		Kinematic hardening		
R_0 (MPa)	Q_{inf} (MPa)	b	C (MPa)	γ
250	5	25	75000	250

Material orientation

The material orientation is given using the Miller-Bravais notation $(hkl) [uvw]$ (see figure 3.3). The vector (hkl) can be read as the normal to the crack plane expressed in the crystal coordinates and $[uvw]$ as the crack propagation direction expressed in the crystal coordinates. The orientation is written as $\succ_{[uvw]}^{(hkl)}$ in order to refer to the existence of both a crack and a crystal coordinates systems.

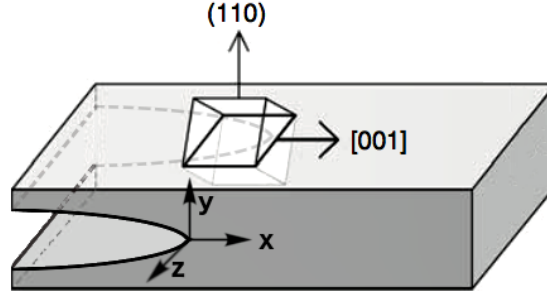


Figure 3.3: Example of the orientation $\succ_{[001]}^{(110)}$ of the crystal with respect to the crack coordinates.

The rotation matrix Ω_{ij} relating the crack coordinates system and Miller-Bravais indices can be written as follows ([Randle and Engler, 2014]):

$$\Omega_{ij} = \begin{pmatrix} u/N_1 & h/N_2 & -q/N_3 \\ v/N_1 & k/N_2 & -r/N_3 \\ w/N_1 & l/N_2 & -s/N_3 \end{pmatrix} \quad (3.4)$$

The first and second columns of the matrix correspond to the \vec{x} and \vec{y} axes of the model representing the crack direction (normal to the crack front) and the normal to the crack plane respectively, both expressed in the crystal coordinates system. The third column is \vec{z} axis with $[qrs] = (hkl) \wedge (uvw)$. N_i are the norms of the three columns of the matrix that serve to normalize these vectors to unity.

A range of crystallographic orientations was studied in this chapter in order to identify the effect of the orientation on the spatial distributions and evolutions of reference fields. Figure 3.4 summarizes the various studied cases.

Five different material orientations were explored. Four of them exhibit a symmetry with respect to the crack plane, while the fifth one $\succ_{[3\bar{1}\bar{1}]}^{(121)}$ doesn't display any symmetry with respect to the crack plane. The isotropic case was used as a base for comparison to compare the effect of the elastic anisotropy on the state of mechanical fields near at the crack tip region.

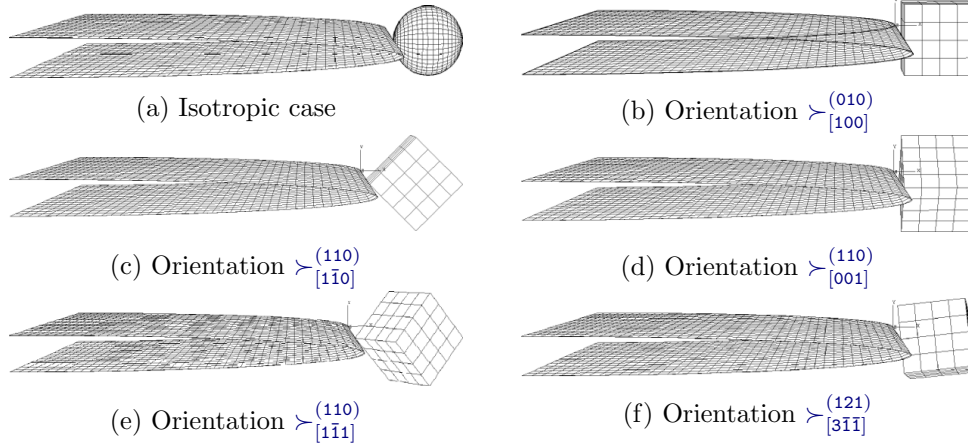


Figure 3.4: Illustrations of the crystallographic orientations with respect to the crack orientation.

Stiffness and compliance tensors rotation

In the material definition of the numerical part, the crystal orientation is assigned through the rotation matrix and the stiffness tensor is given in this crystal coordinates system. The material behavior seen by the crack is then systematically computed by the finite element software. However, the analytical analysis requires the computation of the rotated stiffness tensor in order to express it in the crack coordinates system since all analytical solutions are given in this reference. To do so, the following method and notations were used:

Let Ω_{ij} be the already defined transformation matrix between the material and the crack coordinates systems (equation 3.4). The fourth order stiffness and compliance tensors are expressed in the crack reference as follows:

$$\begin{aligned} C_{ijkl}^{(crack)} &= \Omega_{ip}\Omega_{jq}C_{pqrs}^{(crystal)}\Omega_{kr}\Omega_{ls} \\ S_{ijkl}^{(crack)} &= \Omega_{ip}\Omega_{jq}S_{pqrs}^{(crystal)}\Omega_{kr}\Omega_{ls} \end{aligned} \quad (3.5)$$

which, once written in matrix Voigt notation, give the following expressions:

$$\begin{aligned} \underline{\underline{C}}^{(crack)} &= \underline{\underline{K}}\underline{\underline{C}}^{(crystal)}\underline{\underline{K}}^T \\ \underline{\underline{S}}^{(crack)} &= \underline{\underline{K}}^{-T}\underline{\underline{S}}^{(crystal)}\underline{\underline{K}}^{-1} \end{aligned} \quad (3.6)$$

Matrices $\underline{\underline{K}}$ and $\underline{\underline{K}}^{-T}$ are 9 by 9 matrices constructed as a patchwork of different 3 by 3 matrices $\underline{\underline{k}}^{(1)}, \underline{\underline{k}}^{(2)}, \underline{\underline{k}}^{(3)}$ and $\underline{\underline{k}}^{(4)}$:

$$\underline{\underline{K}} = \begin{bmatrix} \underline{\underline{k}}^{(1)} & 2\underline{\underline{k}}^{(2)} \\ \underline{\underline{k}}^{(3)} & \underline{\underline{k}}^{(4)} \end{bmatrix} \quad \text{and} \quad \underline{\underline{K}}^{-T} = \begin{bmatrix} \underline{\underline{k}}^{(1)} & \underline{\underline{k}}^{(2)} \\ 2\underline{\underline{k}}^{(3)} & \underline{\underline{k}}^{(4)} \end{bmatrix} \quad (3.7)$$

where:

$$\begin{cases} k_{ij}^{(1)} = \Omega_{ij}^2 \\ k_{ij}^{(2)} = \Omega_{il}\Omega_{in} \\ k_{ij}^{(3)} = \Omega_{kj}\Omega_{mj} \\ k_{ij}^{(4)} = \Omega_{kl}\Omega_{mn} + \Omega_{kn}\Omega_{ml} \end{cases} \quad \text{with} \quad \begin{cases} i, j \in \{1, 2, 3\} \\ k = (i + 1) \pmod 3 \\ l = (j + 1) \pmod 3 \\ m = (i + 2) \pmod 3 \\ n = (j + 2) \pmod 3 \end{cases} \quad (3.8)$$

with

$$i \pmod 3 = \begin{cases} i & i \leq 3 \\ i - 3 & i > 3 \end{cases} \quad (3.9)$$

This method merely derives from a pure algebra analysis. T.C. Ting detailed in his book [Ting, 1996] the origin of these expressions.

Hoening's analytical solution

Hoening [Hoening, 1982] used the Lekhnitskii formalism to solve the problem of a through crack for a fully anisotropic material. In a local polar coordinates system (see figure 3.5), the general solution of displacement field near the crack tip can be written as follows:

$$u_i = \sqrt{\frac{2r}{\pi}} \Re \left[\sum_{j=1}^3 m_{ij} N_{jl}^{-1} K_l^\infty Q_j \right] \quad (3.10)$$

with $i \in \{1, 2, 3\}$ which is equivalent to $i \in \{x, y, z\}$, $\Re[*]$ is the real part of $*$ and m_{ij} is a matrix defined as follows:

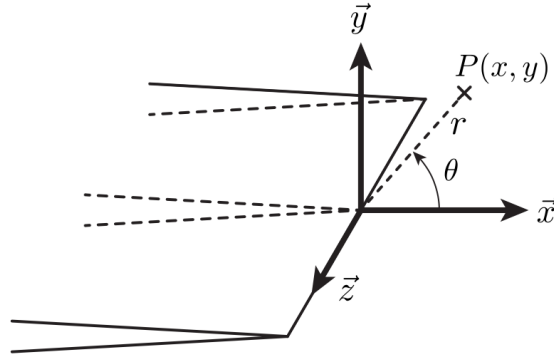


Figure 3.5: Cartesian and polar coordinates systems at the crack tip region.

$$\begin{aligned} m_{1i} &= S'_{11}p_i^2 - S'_{16}p_i + S'_{12} + \lambda_i(S'_{15}p_i - S'_{14}) \\ m_{2i} &= S'_{21}p_i - S'_{26} + \frac{S'_{22}}{p_i} + \lambda_i(S'_{25} - \frac{S'_{24}}{p_i}) \\ m_{3i} &= S'_{41}p_i - S'_{46} + \frac{S'_{42}}{p_i} + \lambda_i(S'_{45} - \frac{S'_{44}}{p_i}) \end{aligned} \quad (3.11)$$

$$Q_i = \sqrt{\cos \theta + p_i \sin \theta} \quad (3.12)$$

with θ the angular position with respect to the crack ligament (see figure 3.5).

N_{ij}^{-1} and K_i^∞ are respectively the inverse of the matrix N_{ij} defined below and the vector of stress intensity factors:

$$N_{ij} = \begin{pmatrix} 1 & 1 & 1 \\ -p_1 & -p_2 & -p_3 \\ -\lambda_1 & -\lambda_2 & -\lambda_3 \end{pmatrix} \quad K_i^\infty = \begin{pmatrix} K_I^\infty \\ K_{II}^\infty \\ K_{III}^\infty \end{pmatrix} \quad (3.13)$$

$$\lambda_i = -\frac{l_3(p_i)}{l_2(p_i)} \quad (3.14)$$

where p_i are the roots of the characteristic sixth order polynomial equation 3.15 obtained by coupling two compatibility equations that derive from the combination of the strain-displacement equations and of the anisotropic Hooke's law (see Appendix A). These roots are always complex and are obtained as pairs of complex conjugates. Distinct roots with the same sign of the imaginary part have to be chosen.

$$l_4(p)l_2(p) - l_3^2(p) = 0 \quad (3.15)$$

with

$$\begin{aligned} l_2(p) &= S'_{55}p^2 - 2S'_{45}p + S'_{44} \\ l_3(p) &= S'_{15}p^3 - (S'_{14} + S'_{56})p^2 + (S'_{25} + S'_{46})p - S'_{24} \\ l_4(p) &= S'_{11}p^4 - 2S'_{16}p^3 + (2S'_{12} + S'_{66})p^2 - 2S'_{26}p + S'_{22} \end{aligned} \quad (3.16)$$

S'_{ij} is the reduced compliance matrix derived from the compliance matrix S_{ij} written in Voigt notation:

$$S'_{ij} = S_{ij} - \frac{S_{i3}S_{3j}}{S_{33}} \quad \text{under plane strain condition} \quad (3.17)$$

There are some special cases of anisotropy that lead to a mathematically degenerate development. These cases can be summarized in the cases where the plane $z = 0$ is a symmetry plane for the material. This includes the monoclinic, the orthotropic and the cubic anisotropies where the crystal axes are normal to symmetry planes and of course the isotropic case.

The most general case among these special cases is the monoclinic anisotropy with $z = 0$ a plane of symmetry:

$$S'_{14} = S'_{24} = S'_{15} = S'_{25} = S'_{46} = S'_{56} = 0 \quad (3.18)$$

These symmetries imply that $l_3(p) = 0$ which means that the coupling between the two compatibilities equations that led to equation 3.15, is no more valid. This requires another development. The matrix m_{ij} (equation A.18) is redefined as follows:

$$\left. \begin{aligned} m_{1i} &= S'_{11}p_i^2 - S'_{16}p_i + S'_{12} \\ m_{2i} &= S'_{21}p_i - S'_{26} + \frac{S'_{22}}{p_i} \\ m_{3i} &= 0 \end{aligned} \right\} \text{ for } i \in \{1, 2\} \text{ and } \left\{ \begin{aligned} m_{13} &= 0 \\ m_{23} &= 0 \\ m_{33} &= S'_{45} - \frac{S'_{44}}{p_3} \end{aligned} \right. \quad (3.19)$$

These special cases lead to a solution in displacement that agrees with the solution given by Sih, Paris and Irwin [Sih et al., 1965] developed for materials with $z = 0$ presenting a plane of symmetry. Hoenig [Hoenig, 1982] and then Banks-Sills and co-workers [Banks-Sills et al., 2005][Banks-Sills et al., 2007] presented these solutions as follows:

$$u_i = \sqrt{\frac{2r}{\pi}} \Re \left[\sum_{j=1}^3 m_{ij} B_j Q_j \right] \quad (3.20)$$

where:

$$\begin{pmatrix} B_1 \\ B_2 \\ B_3 \end{pmatrix} = \frac{1}{p_2 - p_1} \begin{pmatrix} p_2 & 1 & 0 \\ -p_1 & -1 & 0 \\ 0 & 0 & p_1 - p_2 \end{pmatrix} \begin{pmatrix} K_I^\infty \\ K_{II}^\infty \\ K_{III}^\infty \end{pmatrix} \quad (3.21)$$

We note also that these solutions lead to Westergaard asymptotic solutions when applied to an isotropic case [Westergaard, 1939].

3.2.2 FE Model: mesh and boundary conditions

In order to simulate the near crack tip elastic-plastic behavior in a small scale yielding, a set of finite element simulations were automated with *Python* scripts and performed on the computation center and the cluster of the *LMT* using *ABAQUS/Standard* finite element solver. Results of these analyses were then post-processed using *Python*, *IPython Notebook* and in some cases *Matlab* scripts.

The presence of an anisotropic behavior imposes the study of the three fracture modes simultaneously. This implies the use a 3D model with volume elements for the mesh. Thus, for finite element implementation, a 3D thin plate ($2 \text{ m} \times 2 \text{ m}$) with a 20 mm through thickness crack is used. Periodicity conditions were applied on the two opposite big faces of the model to ensure the same displacement on both faces. The purpose of this modeling is to imitate the behavior of a solid with infinite thickness and to inhibit the effect of the free surfaces on the evolution of mechanical fields near the crack tip region. A mixture of Neumann and Dirichlet boundary conditions were used as follows:

- The displacement of the crack front line in the plane $z = 0$ is blocked.
- Imposed forces applied on reference points of discrete rigid bodies tied to the corners of the model. These in-plane and out-of-plane forces will ensure all ratios of mixed mode loadings.

As shown in figure 3.6, all fields are extracted from the middle section of a circular domain big enough to exclude singularity zone ($r_{min} = 30 \mu\text{m}$) and small enough to remain into the Irwin plastic zone ($r_{max} = 250 \mu\text{m}$). The size of this zone is adjusted as function of the loading type and range and of the material orientation. The procedure performed to chose the region of interest is described in section 3.4.2.

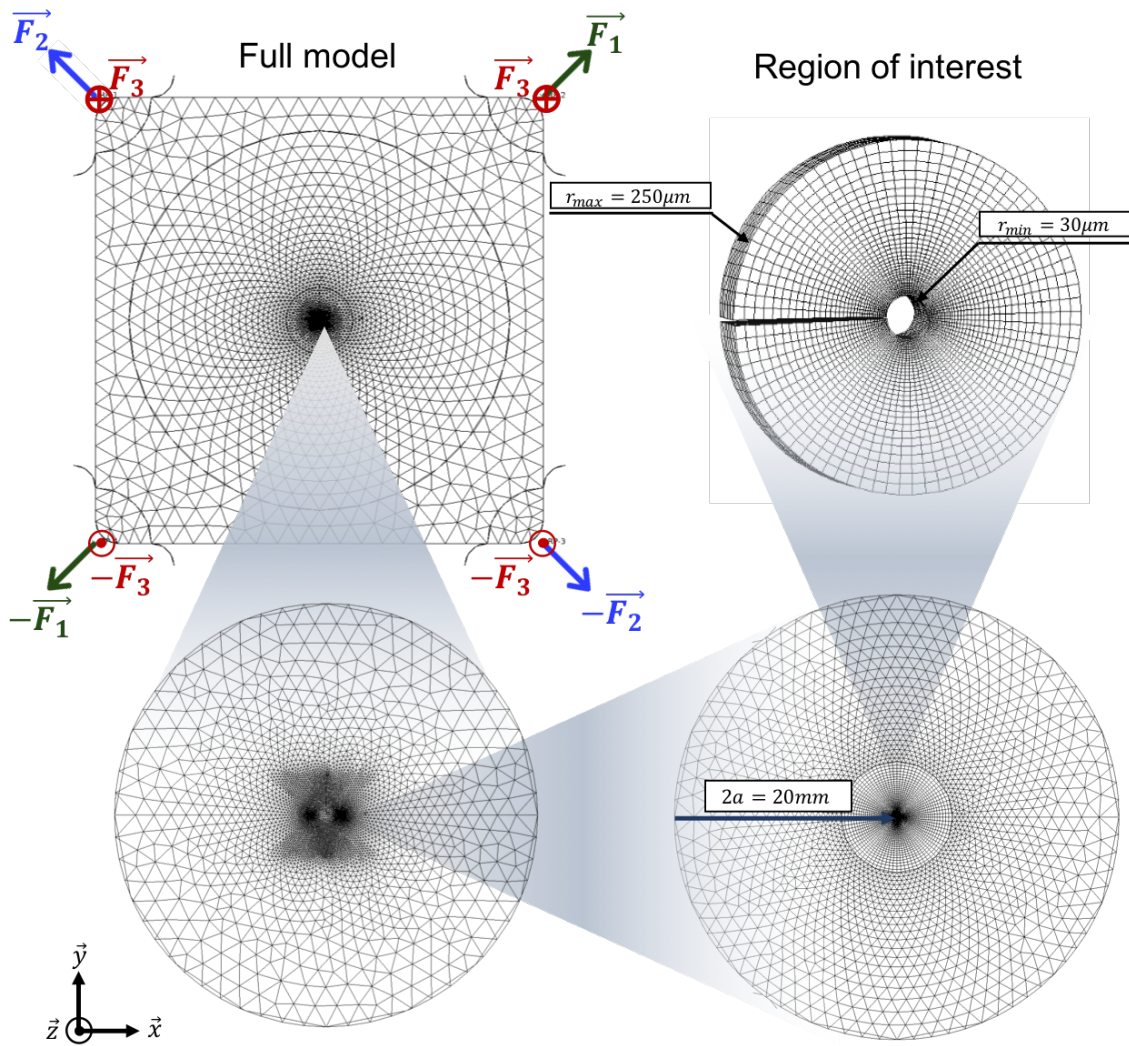


Figure 3.6: Full geometry of the finite element model and a zoom on the region of interest surrounding the crack tip.

Stress intensity factors extraction

In order to get rid of the geometry dependencies, the numerical model was monitored through the stress intensity factors experienced by the crack tip region. For this reason, two different methods were used to extract these quantities.

- **Interaction integral:** This energy based method is summarized in Appendix B. Known also as the M-Integral method, it derives from the computation of the path independent J-Integral. This method is general and can be applied to all cases of anisotropies. Besides, it gives precise results of the stress intensity factors and the accuracy of this method is mesh independent [Banks-Sills et al., 2005]. The M-integral is complicated to implement but fortunately, it is already integrated in the finite element software *ABAQUS*.
- **Displacement extrapolation method:** The displacement field presented in Hoenig's analytical solution [Hoenig, 1982] in equation 3.10 can be re-written as follows:

$$u_i(r, \theta) = \sqrt{\frac{2r}{\pi}} \sum_{j=1}^3 g_i^j(\theta) K_j^\infty \quad (3.22)$$

The displacement discontinuity vector between crack faces is then computed as follows:

$$\begin{aligned} \Delta u_i(r) &= u_i(r, \pi) - u_i(r, -\pi) \\ &= \sqrt{\frac{2r}{\pi}} \sum_{j=1}^3 \Delta g_i^j K_j^\infty \end{aligned} \quad (3.23)$$

which gives the following vectorial equation:

$$\underline{\Delta u}(r) = \sqrt{\frac{2r}{\pi}} \underline{\underline{G}} \cdot \underline{\underline{K}}^\infty \quad (3.24)$$

with

$$\underline{\underline{G}} = \begin{pmatrix} \Delta g_x^I & \Delta g_x^{II} & \Delta g_x^{III} \\ \Delta g_y^I & \Delta g_y^{II} & \Delta g_y^{III} \\ \Delta g_z^I & \Delta g_z^{II} & \Delta g_z^{III} \end{pmatrix} \quad \text{and} \quad \underline{\underline{K}}^\infty = \begin{pmatrix} K_I^\infty \\ K_{II}^\infty \\ K_{III}^\infty \end{pmatrix} \quad (3.25)$$

For a given elastic computation, the components of the numerical displacement discontinuity vector are extracted along the crack faces and plotted as function of $\sqrt{\frac{2r}{\pi}}$. A fit line is associated to each plot and the slopes a_i of these lines compose a vector $\underline{\underline{A}} = (a_x, a_y, a_z)$. Thus, equation 3.24 gives:

$$\underline{\underline{K}}^\infty = \underline{\underline{G}}^{-1} \cdot \underline{\underline{A}} \quad (3.26)$$

Note: Computing the displacement discontinuity vector and not the displacement in a radial path along a fixed θ is a convenient choice. In fact, computing the difference between crack faces erases the rigid body displacement and the rotation of the crack that can be caused by the elastic anisotropy.

Tables on figure 3.7 show a comparison of nominal stress intensity factors prescribed based on the interaction integral method and then extracted based on the displacement extrapolation method. Results are shown for different cases: a pure *mode I* case with $K_I^\infty = 1 \text{ MPa}\sqrt{\text{m}}$ for orientation $\gamma_{[3\bar{1}\bar{1}]^{(121)}}$, a pure *mode II* case with $K_{II}^\infty = 1 \text{ MPa}\sqrt{\text{m}}$ for orientation $\gamma_{[1\bar{1}\bar{1}]^{(110)}}$ and a pure *mode III* case with $K_{III}^\infty = 1 \text{ MPa}\sqrt{\text{m}}$ for orientation $\gamma_{[100]^{(010)}}$. The evolutions of the components of the displacement discontinuity $\underline{\Delta u}$ are shown as function of $\sqrt{\frac{2r}{\pi}}$.

The displacement extrapolation method is known to be simple to implement but gives less accurate results compared to energy-based methods [Banks-Sills et al., 2005], [Banks-Sills et al., 2007]. However, in the studied cases in this work, resulting intensity factors from this method are in a good agreement with the ones found using the interaction integral method.

This comparison served to compare explicitly the two extraction methods. Moreover, it helped verifying the auxiliary solutions (see Appendix B for more details) used in the interaction integral method implemented in the commercial software *ABAQUS*. In fact, the interaction integral method is mainly based on the computation of the J-Integral. This quantity is defined as follows:

$$J = \frac{1}{8\pi} K_i^\infty \cdot B_{ij}^{-1} \cdot K_j^\infty \quad (3.27)$$

where B_{ij} is called the pre-logarithmic energy factor matrix. This matrix is implemented in *ABAQUS* based on the works of [Shih and Asaro, 1988], [Suo, 1990] and [Gao et al., 1992]. In these works, different general problems of interface cracks between two dissimilar anisotropic materials are solved. These works were developed on the footsteps of Barnett and Asaro [Barnett and Asaro, 1972] who solved the problem of a slit like crack in anisotropic materials using the method of continuously distributed dislocations. The final solution is given in a formulation different from the one given by Hoenig [Hoenig, 1982].

The stress intensity factors are computed in two different ways. The first is based on the interaction integral where the auxiliary fields are those presented on the work of Barnett and Asaro [Barnett and Asaro, 1972]. The second is using the displacement extrapolation method and based on Hoenig's analytical solutions. Despite these works use two different approaches to solve the problem of a crack in anisotropic materials, the stress intensity factors exhibited good agreement as shown on the tables of figure 3.7.

Note: The separated J-integrals is an other method for calculating stress intensity factors. For mixed fracture modes I + II, it consists in separating the J-integral into J_I and J_{II} integrals associated to the two fracture modes I and II. This method is limited to the case of orthotropic material in which the material and the crack axes coincide [Banks-Sills et al., 2005]. Thus this method is not discussed in this work. Further details about the separation are discussed in subsection 3.5.2.

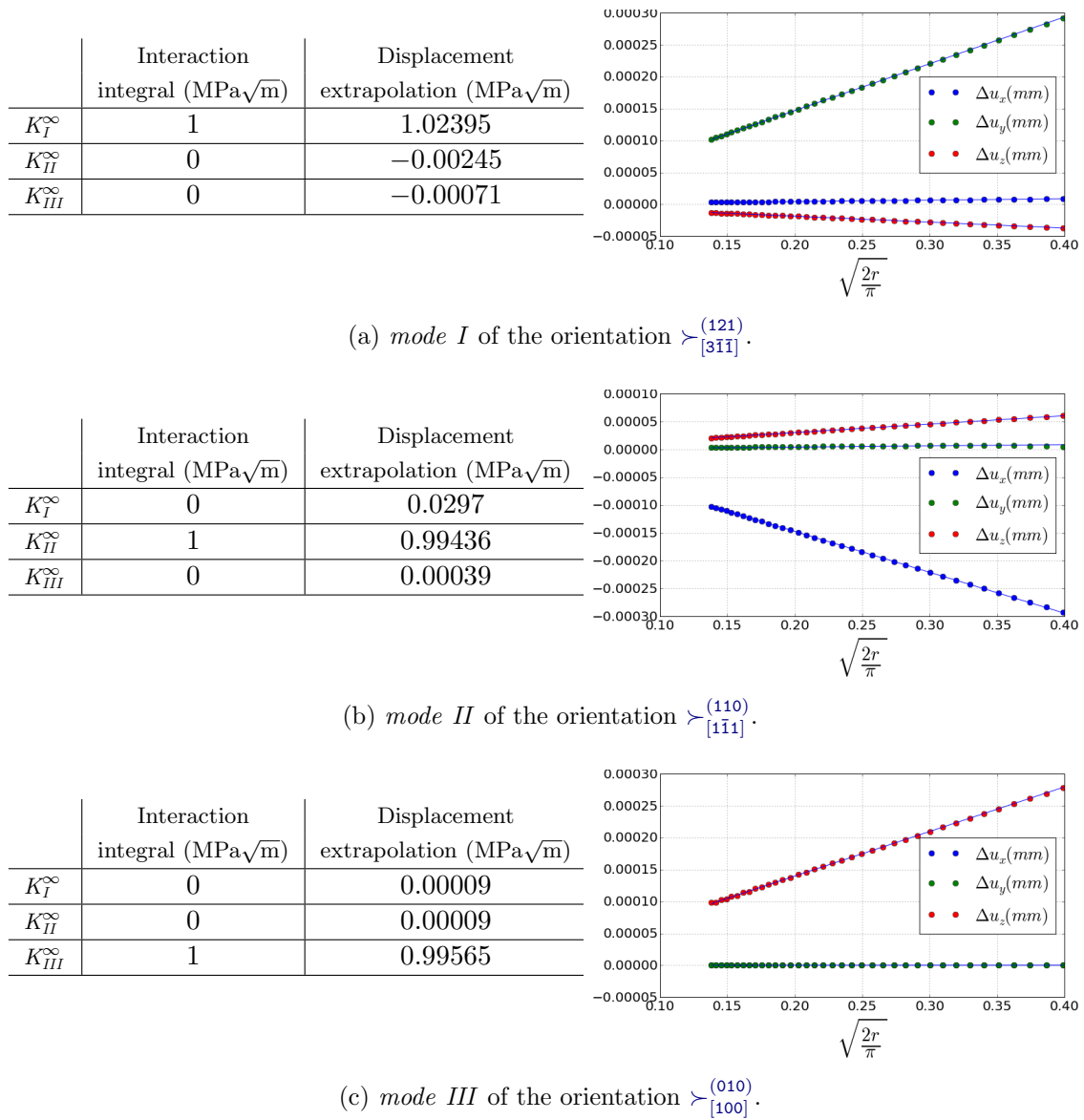


Figure 3.7: The table on the left gives nominal stress intensity factors prescribed based on the interaction integral method and extracted using the displacement extrapolation method, the plot on the right gives the evolution of displacement discontinuity components along the crack faces. Different loading cases and material orientations are presented.

Stress intensity factors monitoring

Applied loadings are monitored using stress intensity factors. Therefore, a transformation matrix was computed for each tested material orientation to obtain the relation between the sought stress intensity factors and loadings to apply. Let T_{ij} be this 3 by 3 transformation matrix. This matrix is obtained by applying 3 random linear elastic computations and extracting from each analysis different stress intensity factors values. Let $F_1^{(i)}$, $F_2^{(i)}$ and $F_3^{(i)}$ be the three forces applied to the model for a random computation (i) with $F_j^{(i)} = \|\vec{F}_j^{(i)}\|$ (see figure 3.6).

The linear behavior of the model indicates that for the computation i :

$$\begin{pmatrix} F_1^{(i)} \\ F_2^{(i)} \\ F_3^{(i)} \end{pmatrix} = \begin{pmatrix} T_{11} & T_{12} & T_{13} \\ T_{21} & T_{22} & T_{23} \\ T_{31} & T_{32} & T_{33} \end{pmatrix} \begin{pmatrix} K_I^{\infty(i)} \\ K_{II}^{\infty(i)} \\ K_{III}^{\infty(i)} \end{pmatrix} \quad (3.28)$$

After applying three different mixed modes tests, a linear system of nine equations is solved to obtain the nine parameters of the transformation matrix T_{ij} :

$$\begin{pmatrix} F_1^{(1)} & F_1^{(2)} & F_1^{(3)} \\ F_2^{(1)} & F_2^{(2)} & F_2^{(3)} \\ F_3^{(1)} & F_3^{(2)} & F_3^{(3)} \end{pmatrix} = \begin{pmatrix} T_{11} & T_{12} & T_{13} \\ T_{21} & T_{22} & T_{23} \\ T_{31} & T_{32} & T_{33} \end{pmatrix} \begin{pmatrix} K_I^{\infty(1)} & K_I^{\infty(2)} & K_I^{\infty(3)} \\ K_{II}^{\infty(1)} & K_{II}^{\infty(2)} & K_{II}^{\infty(3)} \\ K_{III}^{\infty(1)} & K_{III}^{\infty(2)} & K_{III}^{\infty(3)} \end{pmatrix} \quad (3.29)$$

The loading to apply can be obtained by the following relation:

$$F_i = T_{ij} \cdot K_j^{\infty} \quad (3.30)$$

with

$$F_i = \begin{pmatrix} F_1 \\ F_2 \\ F_3 \end{pmatrix} \quad \underline{K}^{\infty} = \begin{pmatrix} K_I^{\infty} \\ K_{II}^{\infty} \\ K_{III}^{\infty} \end{pmatrix} \quad (3.31)$$

The linear transformation matrix T_{ij} depends on the geometry of the used model, the length $2a$ of the crack and the material behavior seen by the crack.

3.3 Multiscale approach

As detailed previously in [chapter 1](#) and [chapter 2](#), first steps of the incremental model were developed at the LMT by Pommier and co-workers [[Pommier and Risbet, 2005](#)], [[Pommier and Hamam, 2007](#)]. The model assumes that pure fatigue crack growth is plasticity induced [[Pelloux, 1969](#)], [[Laird, 1967](#)], [[Neumann, 1969](#)]. Thus, it focuses on modeling crack tip plasticity to study the crack growth. Besides, real service loadings are complex and the definition of fatigue cycle is not trivial. Hence, models based on cycle

derivative equations need an efficient cycle reconstruction procedure. To overcome this issue, the incremental model is proposed based on a set of time derivative equations. The propagation law is written as follows:

$$\frac{da}{dt} = \alpha \left| \frac{d\rho}{dt} \right| \quad (3.32)$$

This law is coupled with a blunting law that relates the evolution of plasticity at the crack tip defined by ρ as function of the applied loading described by the stress intensity factor K . Taking account of each fracture modes, this can be written as a vector equation:

$$\dot{\rho} = g(\underline{\dot{K}}^\infty, \underline{V}_{int}) \quad (3.33)$$

In order to obtain this condensed nonlocal plasticity model of the region near the crack tip, a multiscale approach is proposed based on a model reduction procedure. This procedure is based on a set of hypotheses, previously discussed, that permit the decomposition of kinematic field near the crack tip region. Thus, velocity field is described as a superposition of three fracture modes. Each mode is decomposed into two degrees of freedom, a first linear part presenting elastic kinematic fields and a second nonlinear part that contains all plasticity effects. Each part is a product of an intensity factor rate and a spatial distribution [Pommier et al., 2009], [Pommier, 2016], [Decreuse, 2010], [Frémy, 2012].

$$\underline{v}^{FE}(\underline{x}, t) = \sum_{i=1}^3 \dot{K}_i(t) \underline{\phi}_i^{el}(\underline{x}) + \sum_{i=1}^3 \dot{\rho}_i(t) \underline{\phi}_i^{pl}(\underline{x}) \quad (3.34)$$

where $\underline{\phi}_i^{el}(\underline{x})$ and $\underline{\phi}_i^{pl}(\underline{x})$ are the elastic and plastic reference fields respectively. $\dot{\rho}_i(t)$ is the rate of the blunting intensity factor that presents crack tip plasticity created by a crack in mode i .

3.4 Kinematic basis

An elastic and a plastic kinematic bases are discussed in this section. The idea is to find the best framework that condenses the elastic and the plastic behavior of the region near the crack tip. This framework should account for the anisotropic behavior of the material. To do so, finite element simulations are performed. For the elastic basis, linear elastic computations are performed under specific boundary conditions for different fracture modes. For the non linear basis, elastic-plastic computations are performed then post-treated based on the elastic basis. The study is performed under different orientations of the material with respect to the crack.

3.4.1 Elastic fields and analytical solution

Elastic reference fields of different modes $\underline{\phi}_i^{el}(\underline{x})$ are obtained by applying a pure elastic computation with a normalized value of the stress intensity factor of the sought mode. For instance, for mode I, a loading is applied so that $K_I^\infty = 1 \text{ MPa}\sqrt{\text{m}}$ and the other two stress intensity factors are maintained equal to zero.

Fields are then extracted from the region of interest and saved as an elastic basis. Regarding the local self-similarity aspect around the crack tip, a Proper Orthogonal Decomposition (POD) can be applied on these reference fields in order to separate the scale radial function and the angular distribution giving the shape of the field around the crack tip. It was shown that the first mode of this decomposition is enough to describe reference fields with an acceptable error. Hence, we obtain:

$$\underline{\phi}_i^{el}(\underline{x}) = f_i^{el}(r) \cdot \underline{g}_i^{el}(\theta) \quad (3.35)$$

These functions are represented of figures from 3.9 to 3.13, for an isotropic case and for different material orientations.

The three reference fields of the three fracture modes were grouped together in the same snapshot matrix then the Proper Orthogonal Decomposition was performed on this matrix. Thus, the obtained radial evolution $f^{el}(r)$ is the same for the three fracture modes. As shown on figures from 3.9b to 3.13a and as found in the analytical solution, this radial function fits with the \sqrt{r} function.

$\underline{g}_i^j(\theta)$ are plotted on figures from 3.9a to 3.13a on two types of plots; a 3D plot and a linear 2D plot. As illustrated in figure 3.8, 3D graphs show the deformed shape of a unit circle once the corresponding distribution is applied on it. Thus, the deformed shape that represents $\underline{g}_i^j(\theta)$ has the following coordinates:

$$\begin{aligned} X_i^j(\theta) &= \sin(\theta) + g_{ix}^j(\theta) \\ Y_i^j(\theta) &= \cos(\theta) + g_{iy}^j(\theta) \\ Z_i^j(\theta) &= g_{iz}^j(\theta) \end{aligned} \quad \text{with } i \in \{I, II, III\} \text{ and } j \in \{el, pl\} \quad (3.36)$$

These fields were rescaled to obtain a $CTOD$ equal to 1 for mode I and an in-plane $CTSD_{II}$ equal to 1 for mode II and an out of plane $CTSD_{III}$ equal to 1 for mode III.

$$\left\| \underline{\Delta g}_i^j \right\| = \left\| \underline{g}_i^j(\theta = \pi) - \underline{g}_i^j(\theta - \pi) \right\| = 1 \quad (3.37)$$

Linear plots, shown on the left of figures from 3.9a to 3.13a, present the variation of the three components of $\underline{g}^{el}(\theta)$ of different fracture modes as function of the angle θ . These evolutions are compared to the analytical solution proposed by Hoenig.

As shown in these plots, the angular distribution extracted using the Proper Orthogonal Decomposition fits perfectly with the analytical solution of Hoenig for the isotropic case and for different anisotropic cases. For material orientation $\succ_{[3\bar{1}\bar{1}]}^{(121)}$ that represents no symmetry with respect to the crack plane, a slight difference is observed between the two solutions for the fracture *mode III*.

When the crack plane presents a symmetry plane for the crystal lattice, angular distributions $\underline{g}_i^{el}(\theta)$ correspond to either an even or an odd function. The decomposition of reference fields based on symmetry consideration is then possible. The *mode I* elastic reference field corresponds to the in-plane symmetric part of the elastic field, *mode II* to the in-plane antisymmetric part and *mode III* to the anti-plane part. Nevertheless, in a more general case as shown in figure 3.14, angular functions have no symmetrical distributions. For this reason, elastic reference fields were extracted from pure *mode I*, *mode II* and *mode III* elastic computations without decomposing them based on their symmetry with the crack plane.

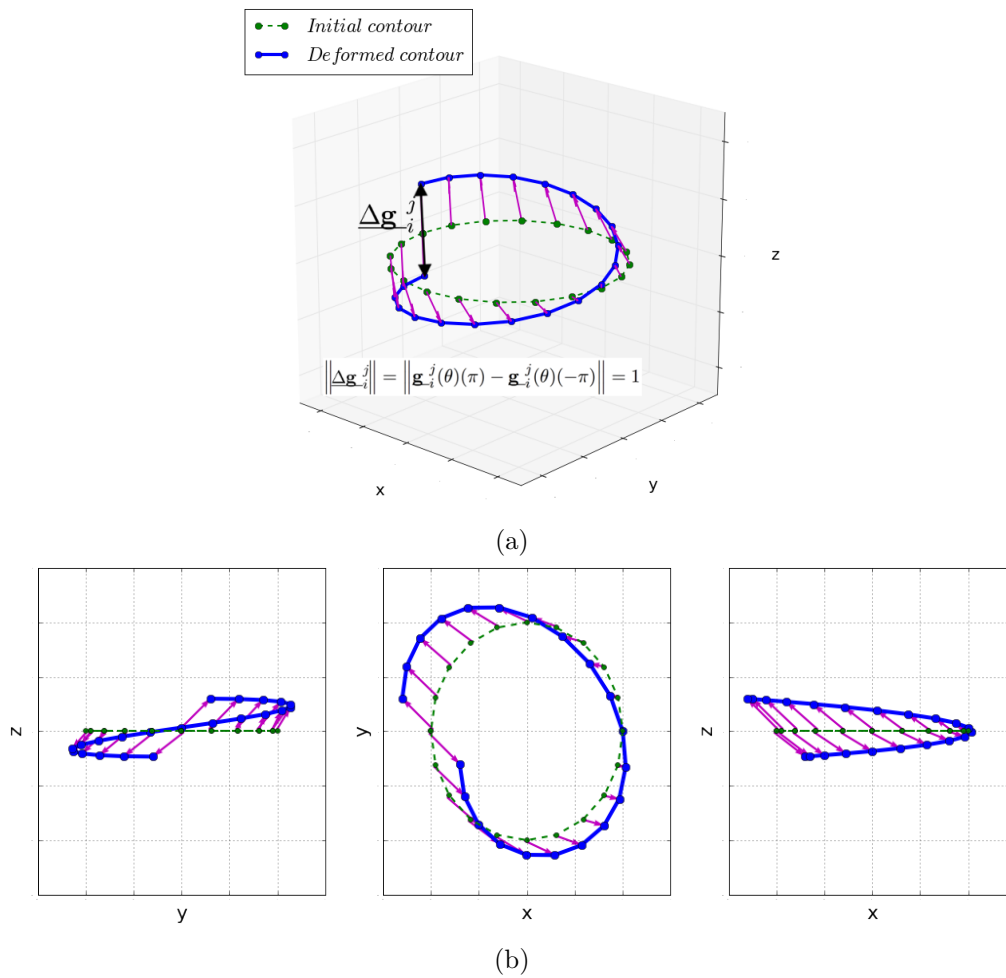
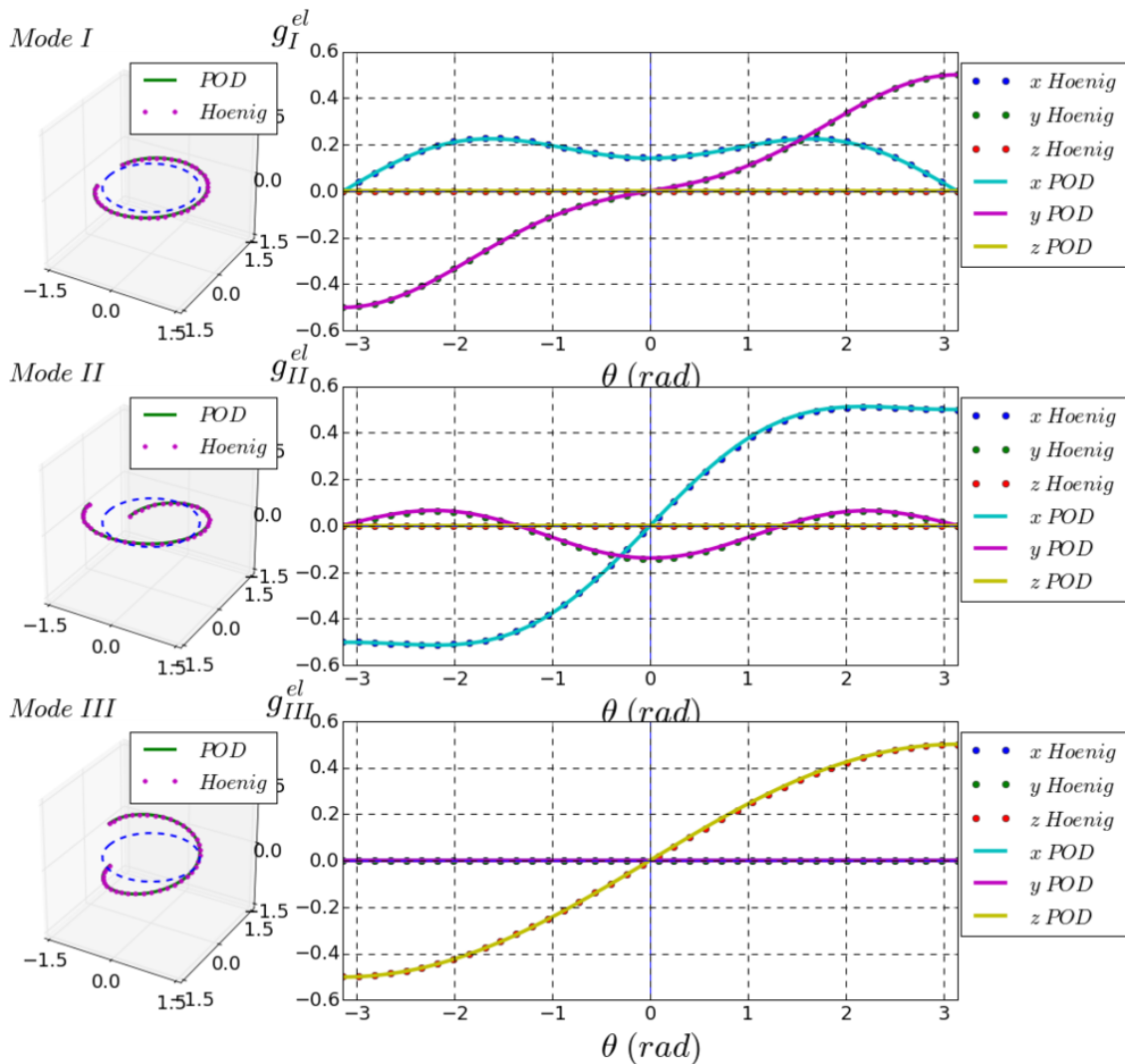
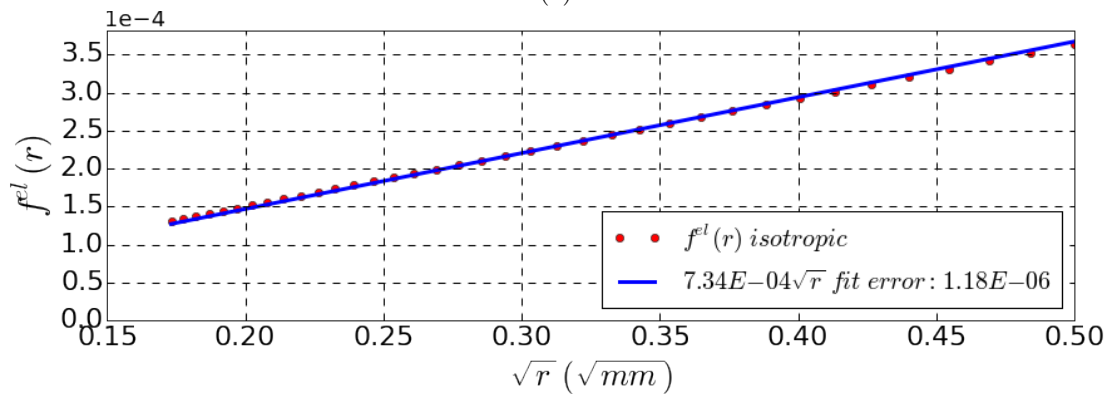


Figure 3.8: The $\underline{g}_i^j(\theta)$ function plot (a) on a 3D plot and (b) its projections on different planes for an isotropic case under mixed fracture modes.

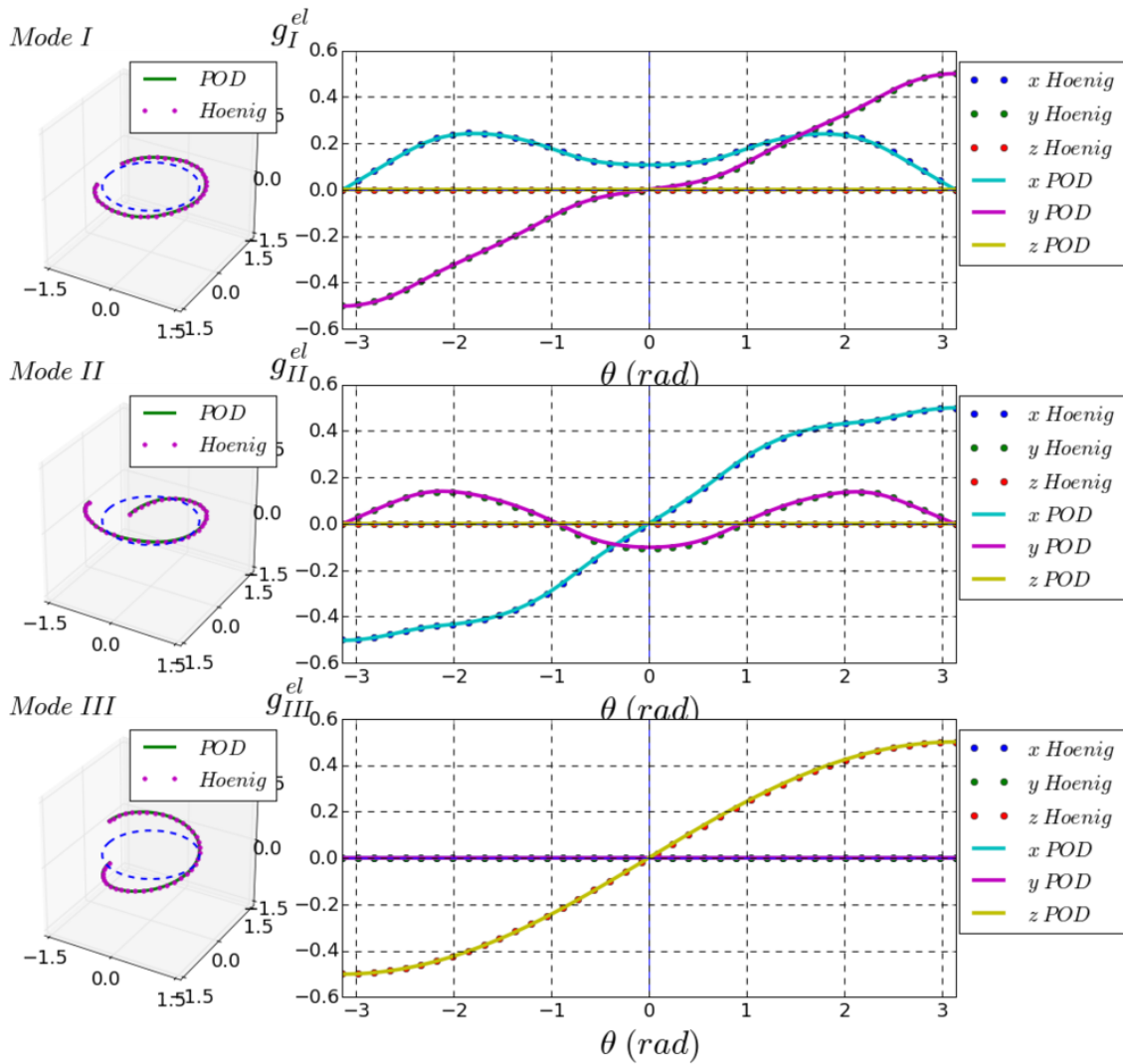


(a)

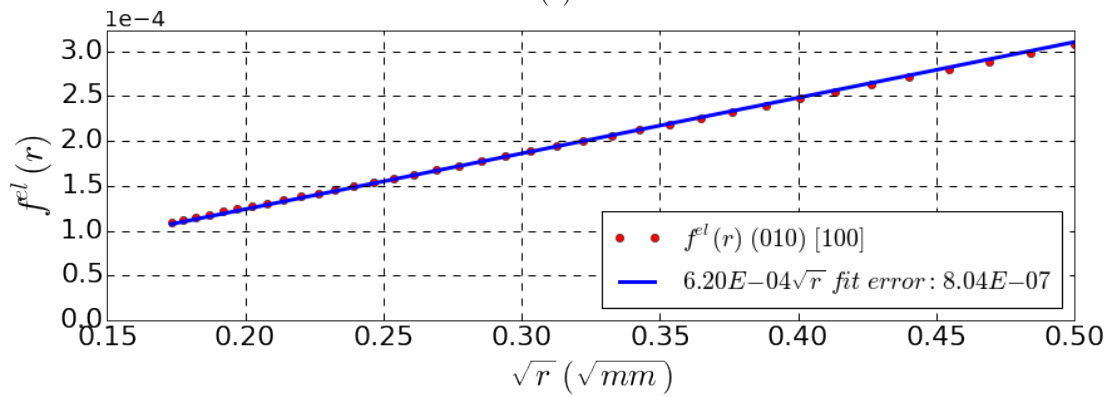


(b)

Figure 3.9: Elastic reference fields of an isotropic case decomposed into (a) $g_i^{el}(\theta)$ functions of the three fracture modes in a deformed angular plot (on left) and in linear plots of different components (on right) and (b) radial function $f^{el}(r)$.

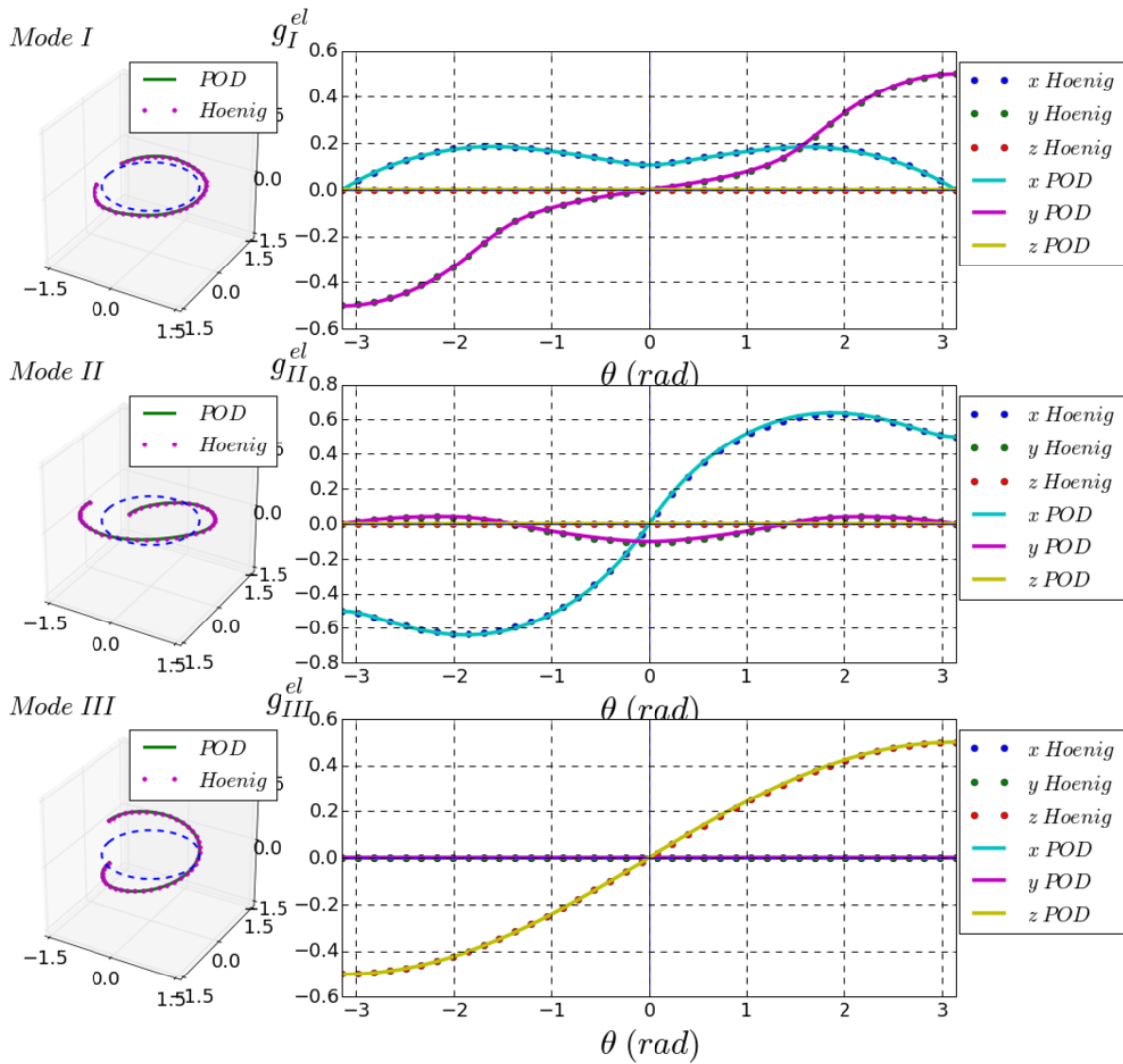


(a)

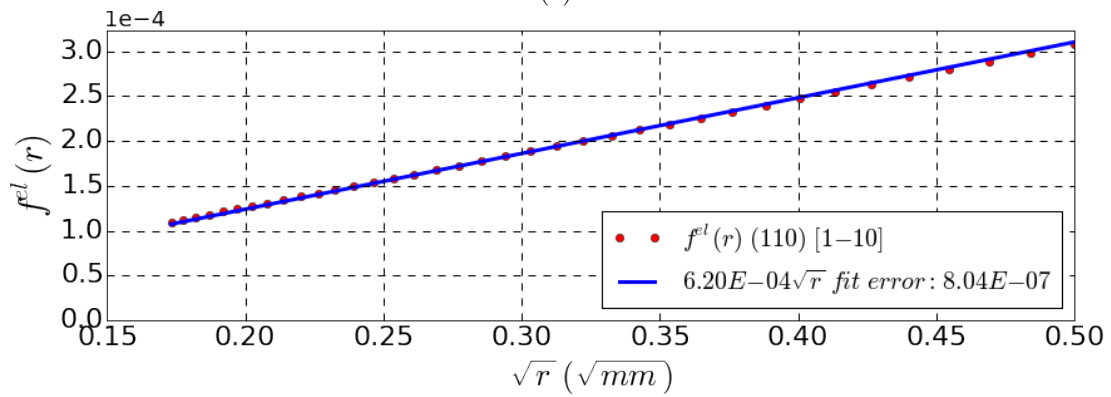


(b)

Figure 3.10: Elastic reference fields of the orientation $\gamma_{[100]}^{(010)}$ decomposed into (a) $g_i^{el}(\theta)$ functions of the three fracture modes in a deformed angular plot (on left) and in linear plots of different components (on right) and (b) radial function $f^{el}(r)$.

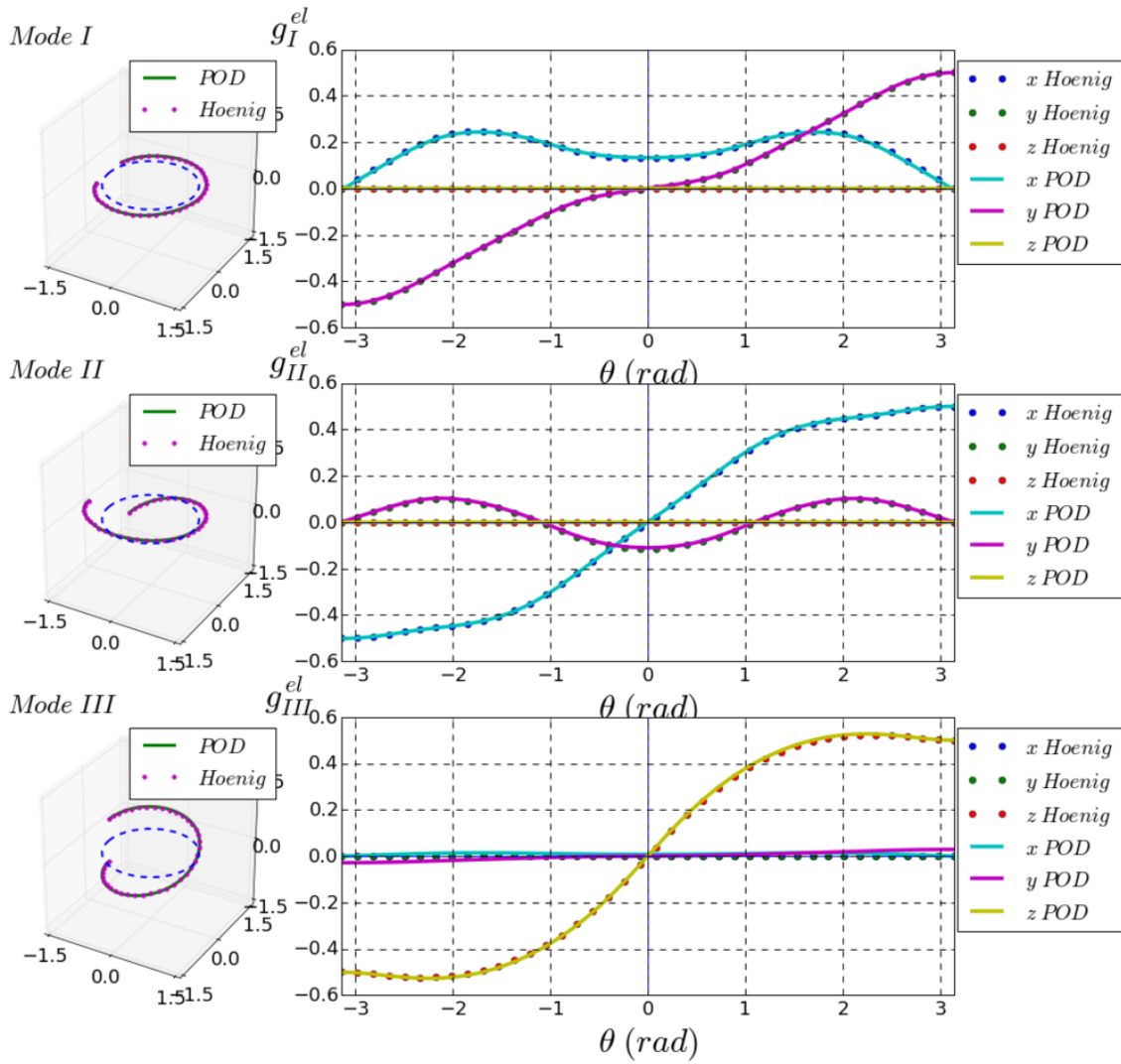


(a)

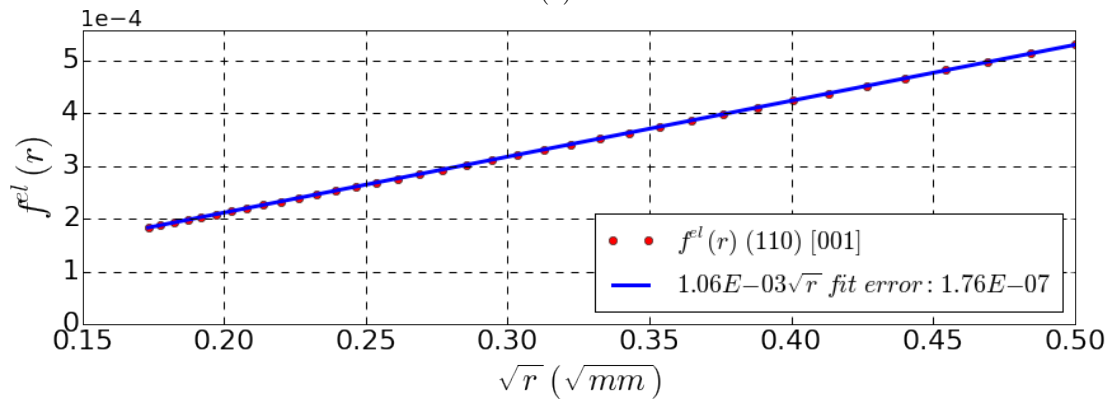


(b)

Figure 3.11: Elastic reference fields of the orientation $\gamma_{[110]}^{(110)}$ decomposed into (a) $g_i^{el}(\theta)$ functions of the three fracture modes in a deformed angular plot (on left) and in linear plots of different components (on right) and (b) radial function $f^{el}(r)$.

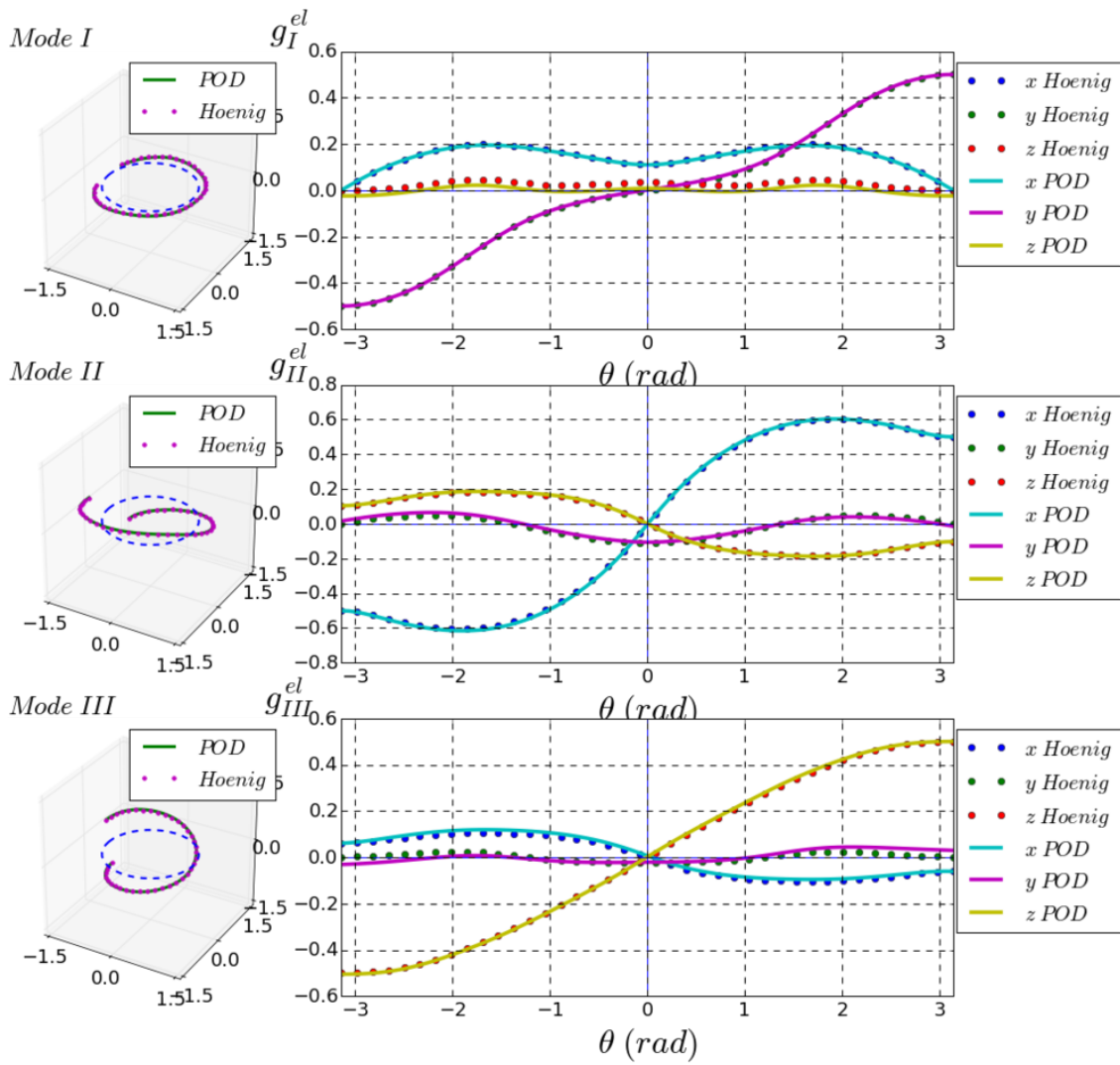


(a)

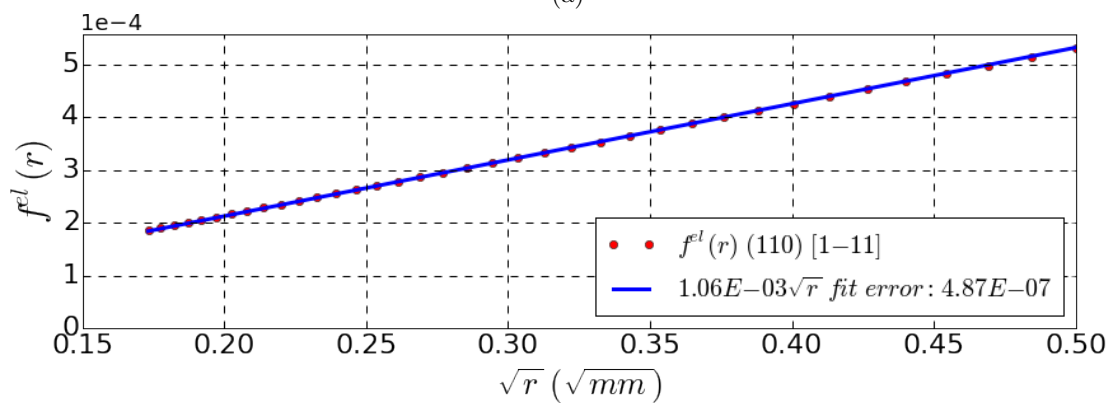


(b)

Figure 3.12: Elastic reference fields of the orientation $\succ_{[001]}^{(110)}$ decomposed into (a) $g_i^{el}(\theta)$ functions of the three fracture modes in a deformed angular plot (on left) and in linear plots of different components (on right) and (b) radial function $f^{el}(r)$.



(a)



(b)

Figure 3.13: Elastic reference fields of the orientation $\gamma_{[111]}^{(110)}$ decomposed into (a) $g_i^{el}(\theta)$ functions of the three fracture modes in a deformed angular plot (on left) and in linear plots of different components (on right) and (b) radial function $f^{el}(r)$.

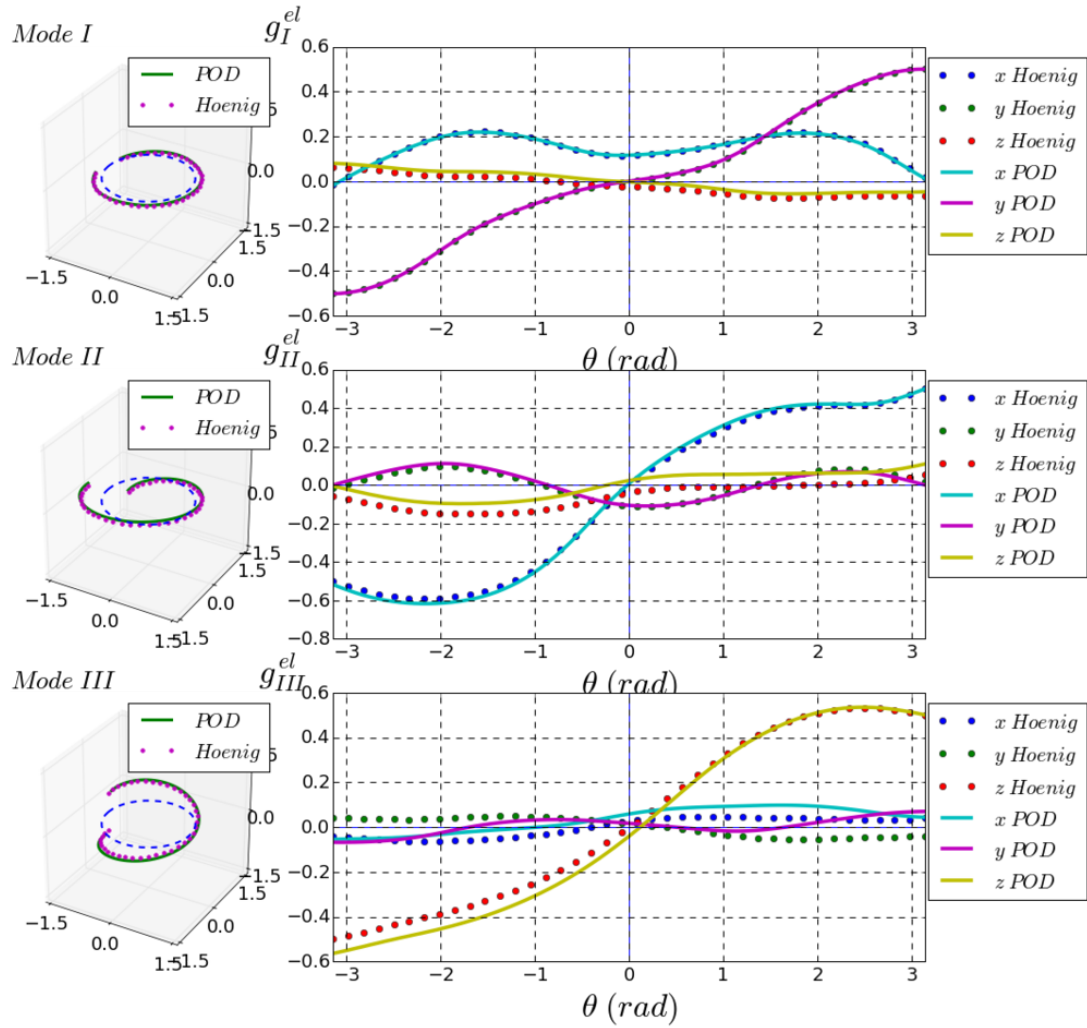


Figure 3.14: $\underline{g}_i^{el}(\theta)$ functions of the three fracture modes in a deformed angular plot (on left) and in linear plots of different components (on right) of the orientation $\succ_{[3\bar{1}\bar{1}]}^{(121)}$.

The elastic part of an elastic-plastic finite element kinematic field $\underline{v}^{FE}(\underline{x}, t)$ is finally approximated as follows:

$$\begin{aligned}\tilde{\underline{v}}^{el}(\underline{x}, t) &\approx \sum_{i=1}^3 \dot{\underline{K}}_i(t) \cdot \underline{\phi}_i^{el}(\underline{x}) \\ &\approx \sum_{i=1}^3 \dot{\underline{K}}_i(t) \cdot f^{el}(r) \cdot \underline{g}_i^{el}(\theta)\end{aligned}\quad (3.38)$$

with

$$\dot{\underline{K}}_i = \frac{\sum_{P \in D} \underline{v}^{FE}(P, t) \cdot \underline{\phi}_i^{el}(P)}{\sum_{P \in D} \underline{\phi}_i^{el}(P) \cdot \underline{\phi}_i^{el}(P)} \quad (3.39)$$

3.4.2 Complementary plastic reference fields

Decomposition

Once the elastic basis is obtained, a kinematic field from an elastic plastic finite element simulation can be projected on this field to obtain the stress intensity factors $\dot{\underline{K}}_i$ (see equation 3.39). The elastic field is then reconstructed (see equation 3.38) and extracted from the total field (see equation 3.40). It can be assumed that the residual presents the nonlinear behavior derived from the plasticity near the crack tip.

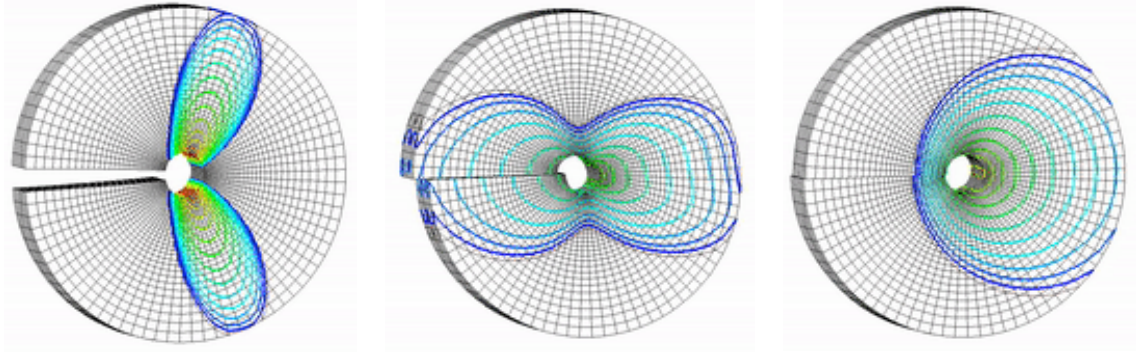
A Karhunen-Loève decomposition is applied on this complementary field in order to separate time dependency $\dot{\rho}_i(t)$ from spatial one $\underline{\phi}_i^{pl}(\underline{x})$. The first mode of this decomposition is enough to reconstruct the field with a reasonable error. This can be firstly explained by the self-similarity of the geometry near the crack tip and secondly by the confinement of the plastic zone into the massive K-dominance bulk, which reduces drastically the number of degrees of freedom of the physics behind plasticity (see equation 3.40).

$$\begin{aligned}\tilde{\underline{v}}^{pl}(\underline{x}, t) &= \underline{v}^{FE}(\underline{x}, t) - \sum_{i=1}^3 \dot{\underline{K}}_i(t) \underline{\phi}_i^{el}(\underline{x}) \\ &\approx \sum_{i=1}^3 \dot{\rho}_i(t) \underline{\phi}_i^{pl}(\underline{x})\end{aligned}\quad (3.40)$$

The residual is finally considered as the superposition of plastic behaviors generated by each fracture mode independently. As mentioned before for elastic fields, because of the cubic anisotropy, this decomposition cannot be made based on the symmetry with respect to the crack as it was done in previous works in the case of an isotropic material [Pommier and Hamam, 2007], [Decreuse, 2010], [Frémy, 2012]. The separation is simply made by assuming that the residual of an elastic-plastic analysis of a pure fracture mode i ($\underline{v}_i^{FE}(\underline{x}, t)$) is the plastic field of the fracture mode i ($\tilde{\underline{v}}_i^{pl}(\underline{x}, t)$) described by the degree of freedom of the mode i ($\dot{\rho}_i(t)$) and the spatial reference field of mode i ($\underline{\phi}_i^{pl}(\underline{x})$):

$$\begin{aligned}\tilde{\underline{v}}_i^{pl}(\underline{x}, t) &= \underline{v}_i^{FE}(\underline{x}, t) - \sum_{i=1}^3 \dot{\underline{K}}_i(t) \underline{\phi}_i^{el}(\underline{x}) \\ &\approx \dot{\rho}_i(t) \underline{\phi}_i^{pl}(\underline{x})\end{aligned}\quad (3.41)$$

Plots on figure 3.15 show the contours of the cumulated plastic strain at the region of interest in a logarithmic scale for an example of material orientation $\succ \begin{pmatrix} 110 \\ 1\bar{1}0 \end{pmatrix}$. These plots display a series of homothetic isocontours, with a regular spacing. This observations



(a) *mode I* $K_I^\infty = 12 \text{ MPa}\sqrt{\text{m}}$ (b) *mode II* $K_{II}^\infty = 12 \text{ MPa}\sqrt{\text{m}}$ (c) *mode III* $K_{III}^\infty = 12 \text{ MPa}\sqrt{\text{m}}$

Figure 3.15: Contours of cumulated plastic strain at the region of interest near the crack tip plotted in logarithmic scale under different fracture modes loadings for the orientation $\gamma_{[1\bar{1}0]}^{(110)}$.

supports the hypothesis of the self-similarity of plastic flow in the crack tip region. It can then be concluded that complementary reference fields can be locally represented by an angular function that gives the shape and a radial dependent function that describes the scale.

$$\underline{\phi}_i^{pl}(\underline{x}) = f_i^{pl}(r) \underline{g}_i^{pl}(\theta) \quad (3.42)$$

Extraction method

An elastic-plastic analysis was performed to extract plastic reference fields. For each mode, a loading then an unloading ramps were applied to enhance the appearance of the sought mode. The principle aim is to treat separately the plastic behavior of the region near the crack tip. Therefore, this loading-unloading process helps getting rid of the reversible elastic mechanism and hence reduces the error when this field is approximated and extracted from the total kinematic field. For instance for *mode I*, at a given orientation, K_I^∞ rises to K_I^{max} then comes back to $0 \text{ MPa}\sqrt{\text{m}}$ while K_{II}^∞ and K_{III}^∞ remains equal to $0 \text{ MPa}\sqrt{\text{m}}$. The maximum value of loading varies with respect to the material orientation and to the loading mode since we have to ensure that, for all cases, plasticity remains confined near the crack tip.

Note: For *mode II* and *mode III*, a slight *mode I* opening is applied to avoid crack faces friction, since we assume that plasticity is the only source of dissipation in the model. Especially that cubic anisotropy may causes the crack closure under pure shear loadings.

The complementary reference field should be the best possible description of the plastic behavior and the best possible spatial field to approximate the velocity field in equation 3.34. It is important then that the extracted representative field obey to the principle hypotheses of the model. As discussed before in 2.3.5, the hypothesis of the confinement of the plastic zone and the local self-similarity hypothesis can be satisfied by an exponential

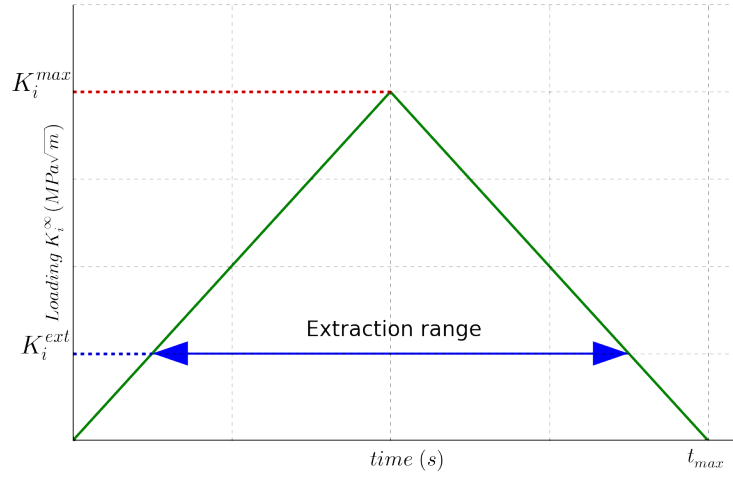


Figure 3.16: The applied loading ramps and the extraction range to obtain complementary reference fields of a fracture mode i .

decay function:

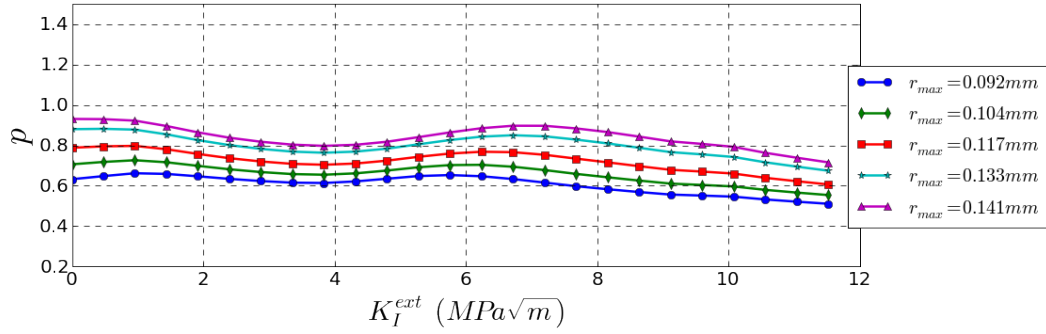
$$f^{pl}(r) \approx Ae^{-\frac{r}{p}} \quad (3.43)$$

In order to ensure this exponential decay behavior that summarizes the aforementioned hypotheses, a campaign of tests were performed for each material orientation. This tests consist in extracting finite element velocity fields from different loading ranges K_i^{ext} (figure 3.16) and from different sizes of the region of interest. Then, a full post-processing was performed on each extracted field to obtain the exponential decay coefficient p . The size of this extraction region and the range of extraction loading are chosen so that exponential decay coefficient p presents a positive and quite constant curve for the three fracture modes. The best representative loading range is then chosen for each fracture mode separately so that functions of different modes $f_i^{pl}(r)$ present almost the same evolution. Figures 3.17 show the evolution of the exponential decay function for material orientation $\succ_{[100]}^{(010)}$ under different fracture modes and with various external radii of the region of interest r_{max} .

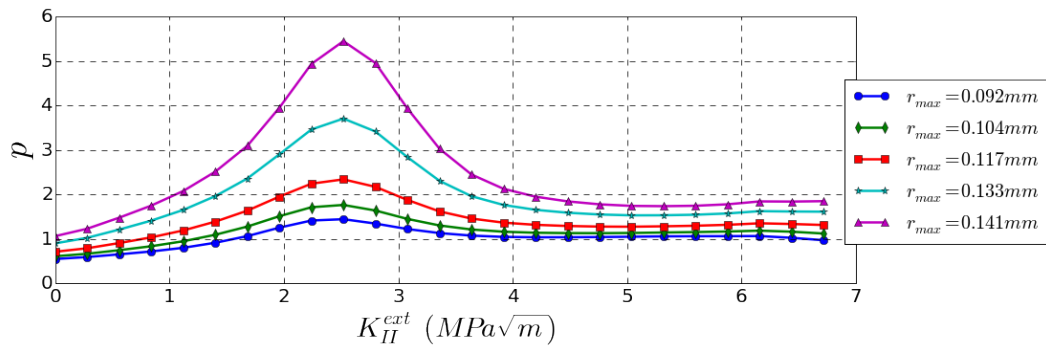
As an example, for the material orientation $\succ_{[100]}^{(010)}$, the external radius of the region of interest was taken equal to $r_{max} = 0.141$ mm and the extraction loading ranges :

- For *mode I* with $K_I^{max} = 12 \text{ MPa}\sqrt{\text{m}}$: $K_I^{ext} = 8 \text{ MPa}\sqrt{\text{m}}$.
- For *mode II* with $K_{II}^{max} = 7 \text{ MPa}\sqrt{\text{m}}$: $K_{II}^{ext} = 5 \text{ MPa}\sqrt{\text{m}}$.
- For *mode III* with $K_{III}^{max} = 7 \text{ MPa}\sqrt{\text{m}}$: $K_{III}^{ext} = 2.5 \text{ MPa}\sqrt{\text{m}}$.

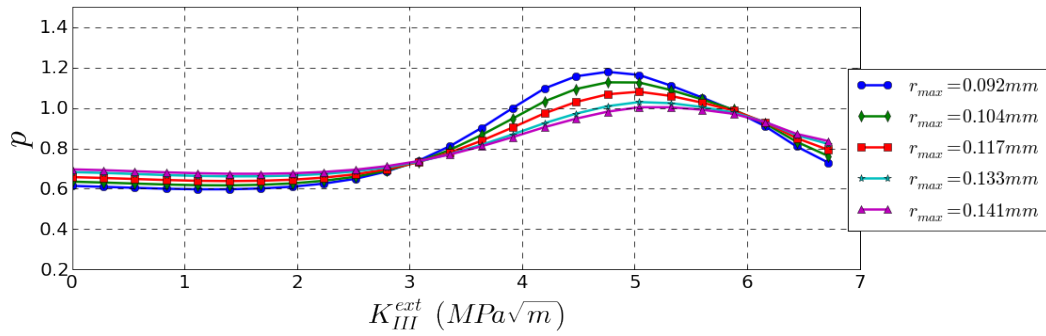
This process was performed for each material orientation separately since, even under a Von-Mises isotropic plasticity, the elastic anisotropy and the crystal orientation affect the evolution of the plasticity near the crack tip region.



(a) mode I



(b) mode II



(c) mode III

Figure 3.17: Exponential decay coefficient as function of the extraction loading range for different external radii of the region of interest for the orientation $\gamma_{[100]}^{(010)}$.

Rescaling and results

Once the latter analyses are performed, the obtained complementary reference fields $\underline{\phi}_i^{pl}(\underline{x})$ for a given material orientation are grouped together in one snapshot matrix and a POD is performed on this matrix in order to obtain different $\underline{g}_i^{pl}(\theta)$ functions for different fracture modes and one common radial scale function $f^{pl}(r)$. The reconstructed complementary field can finally be written as:

$$\tilde{\underline{v}}^{pl}(\underline{x}, t) \approx f^{pl}(r) \sum_{i=1}^3 \hat{\rho}_i(t) \underline{g}_i^{pl}(\theta) \quad (3.44)$$

Discontinuities of angular functions $\underline{g}_i^{pl}(\theta)$ were rescaled to obtain a $CTOD = 1$ for *mode I*, a $CTSD_{II} = 1$ for *mode II* and a $\overline{CTSD}_{III} = 1$ for *mode III*.

$$\left\| \underline{g}_i^{pl}(\pi) - \underline{g}_i^{pl}(-\pi) \right\| = 1 \quad (3.45)$$

The radial function was also rescaled to obtain $f^{pl}(r) = 1$ when $r \rightarrow 0$. These treatments rescale the discontinuity of a complementary reference field $\underline{\phi}_i^{pl}(\underline{x})$ when $r \rightarrow 0$ to a unit vector.

$$\left\| \underline{\phi}_i^{pl}(\underline{x})(r \rightarrow 0, \pi) - \underline{\phi}_i^{pl}(\underline{x})(r \rightarrow 0, -\pi) \right\| = 1 \quad (3.46)$$

After this rescaling, the blunting intensity factor $\hat{\rho}_i(t)$ obtained from the projection of an elastic plastic kinematic field on $\underline{\phi}_i^{pl}(\underline{x})$ can be considered as the non linear $CTOD$ for *mode I*, $CTSD_{II}$ for *mode II* and \overline{CTSD}_{III} for *mode III* [Pommier, 2016].

Figures from 3.18 to 3.23 show the plot of complementary reference fields. Figures (a), (b) and (c) show the deformed shape of a trigonometric circle submitted to $\underline{g}_I^{pl}(\theta)$, $\underline{g}_{II}^{pl}(\theta)$ and $\underline{g}_{III}^{pl}(\theta)$ respectively. Figure (d) show the evolution of the logarithm of the common radial function $f^{pl}(r)$.

Radial scale functions can be fitted with an exponential function, which is reasonable since plasticity is maximum near the crack tip ($r \rightarrow 0$) then it decreases when going away from the crack tip ($r \rightarrow \infty$). For a better overview of the graphical representations, angular distributions were rescaled to an opening equal to 1/2. The deformed shape has the same area as the initial trigonometric circle which is normal since plasticity occurs without volume change [Lemaitre and Chaboche, 1994].

Some crystallographic orientations have shown that even a pure *mode I* opening can cause some out of plane displacements, which was shown for instance in figures 3.22 and 3.23 with the crystallographic orientations $\succ_{[111]}^{(110)}$ and $\succ_{[3\bar{1}1]}^{(121)}$ respectively.

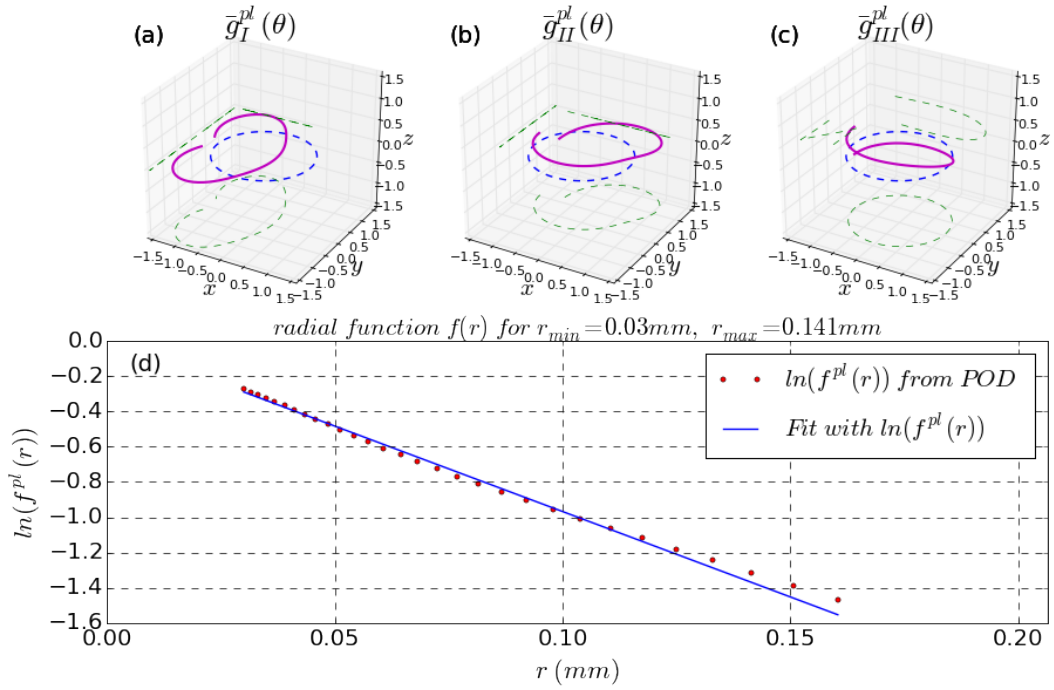


Figure 3.18: Plastic reference field of the isotropic case.

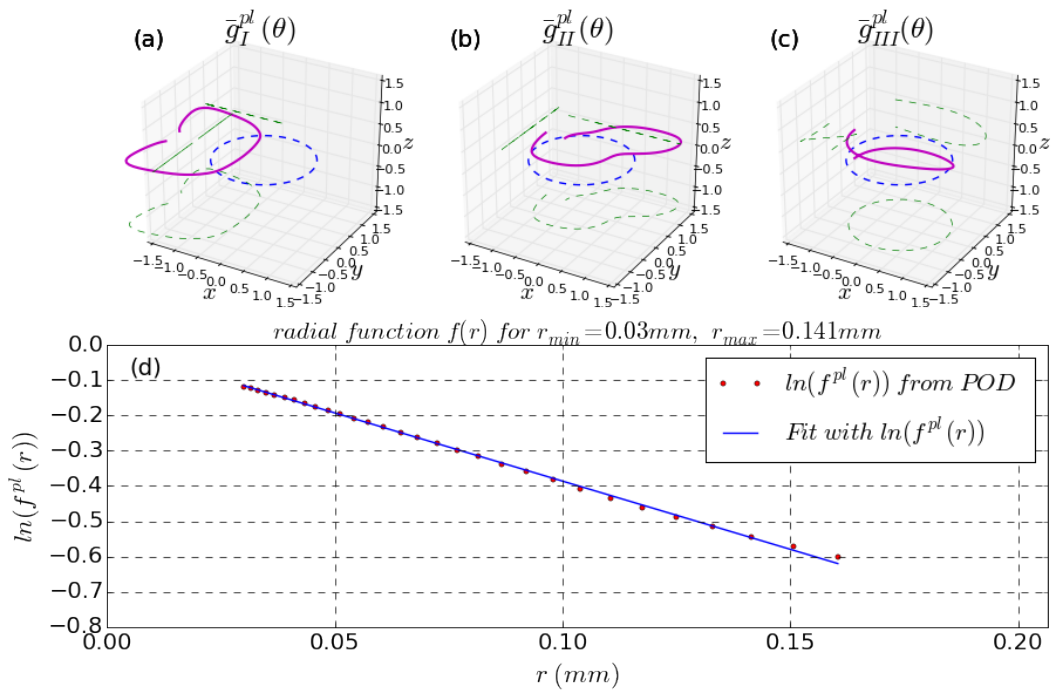


Figure 3.19: Plastic reference field for material orientation $\gamma_{[100]}^{(010)}$.

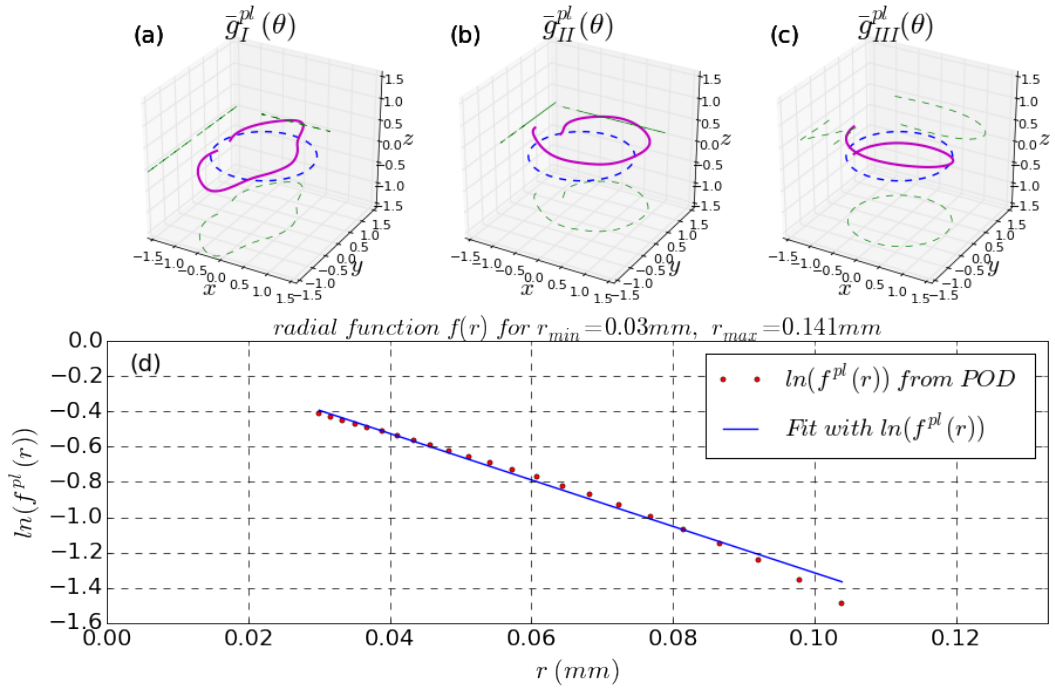


Figure 3.20: Plastic reference field for material orientation $\gamma_{[110]}^{(110)}$.

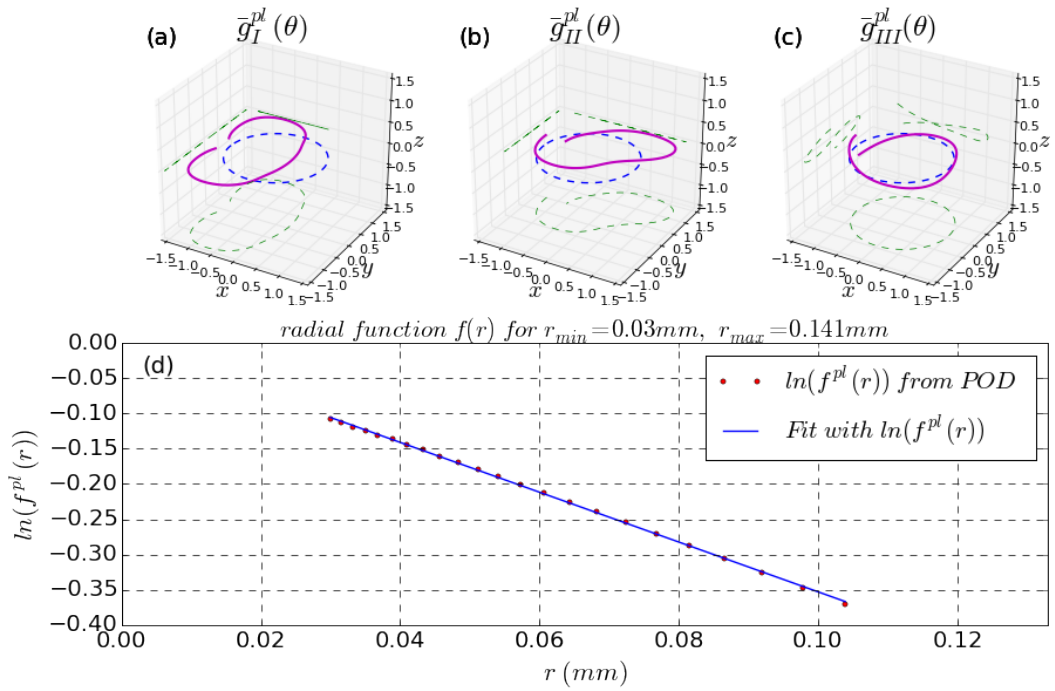


Figure 3.21: Plastic reference field for material orientation $\gamma_{[001]}^{(110)}$.

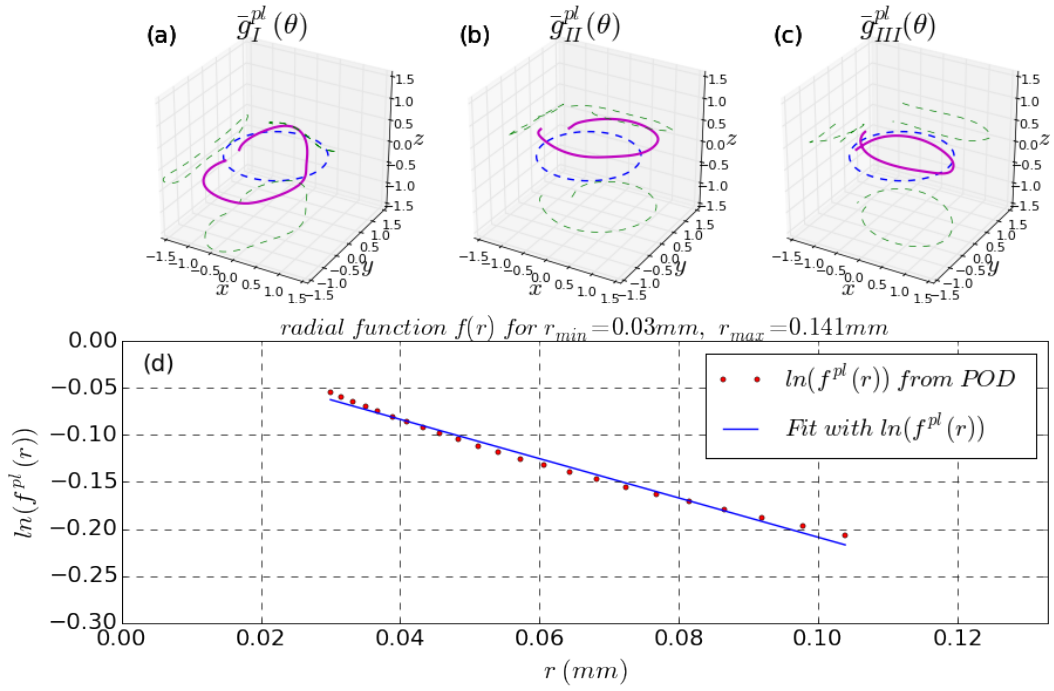


Figure 3.22: Plastic reference field for material orientation $\gamma_{[111]}^{(110)}$.

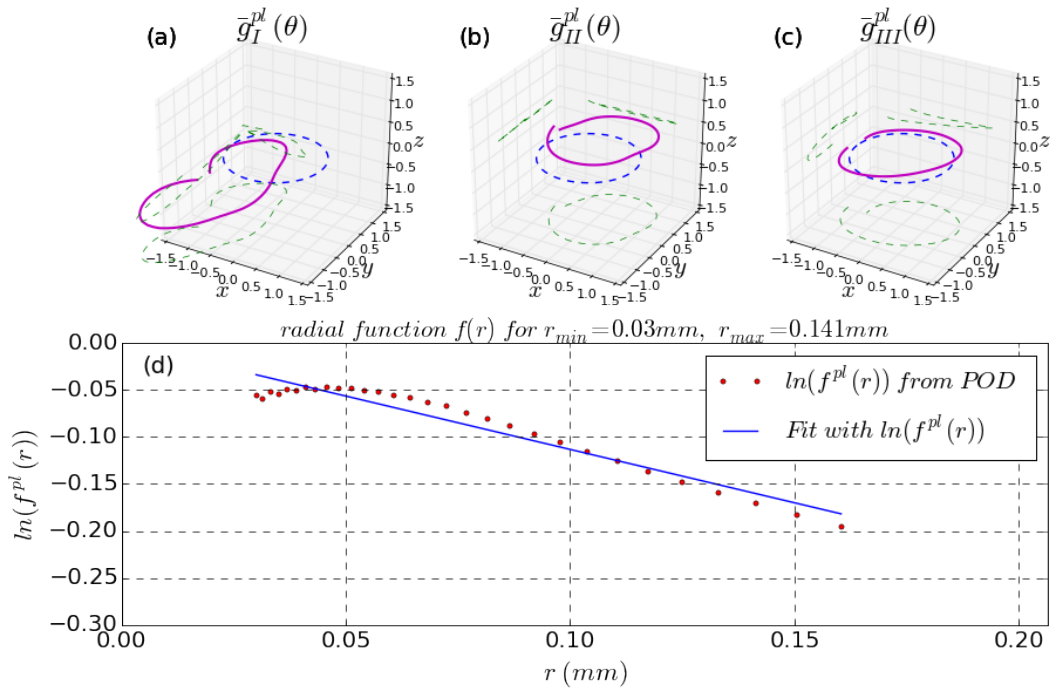


Figure 3.23: Plastic reference field for material orientation $\gamma_{[311]}^{(121)}$.

Orthogonality and reconstruction

Despite not being constructed based on geometrical symmetries, elastic and plastic reference fields were almost orthogonal for all the studied cases. It was verified, for different orientations, that:

$$\left| \sum_{P \in D} \underline{\phi}_i^{el}(P) \cdot \underline{\phi}_j^{el}(P) \right| \leq \varepsilon, \quad \left| \sum_{P \in D} \underline{\phi}_i^{pl}(P) \cdot \underline{\phi}_j^{pl}(P) \right| \leq \varepsilon, \quad \left| \sum_{P \in D} \underline{\phi}_i^{el}(P) \cdot \underline{\phi}_k^{pl}(P) \right| \leq \varepsilon \quad (3.47)$$

with $(i, j, k) \in \{I, II, III\}$ and $i \neq j$. These observations are in coherence with the assumption that elasticity and plasticity are kinematically independent. Thus, it is possible to consider these reference fields as an orthogonal basis to reduce the model.

The plastic kinematic field of an elastic plastic finite element simulation can be finally approximated as follows:

$$\tilde{\underline{v}}^{pl}(\underline{x}, t) \approx \sum_{i=1}^3 \dot{\rho}_i \underline{\phi}_i^{pl}(\underline{x}) \quad (3.48)$$

with:

$$\dot{\rho}_i = \frac{\sum_{P \in D} \underline{v}^{FE}(P, t) \cdot \underline{\phi}_i^{pl}(P)}{\sum_{P \in D} \underline{\phi}_i^{pl}(P) \cdot \underline{\phi}_i^{pl}(P)} \quad (3.49)$$

The total velocity field is reconstructed using the following approximation:

$$\begin{aligned} \underline{v}^{FE}(\underline{x}, t) &\approx \sum_{i=1}^3 \dot{\tilde{K}}_i(t) \underline{\phi}_i^{el}(\underline{x}) + \sum_{i=1}^3 \dot{\rho}_i(t) \underline{\phi}_i^{pl}(\underline{x}) \\ &\approx f^{el}(r) \sum_{i=1}^3 \tilde{K}_i(t) \underline{g}_i^{el}(\theta) + f^{pl}(r) \sum_{i=1}^3 \dot{\rho}_i(t) \underline{g}_i^{pl}(\theta) \end{aligned} \quad (3.50)$$

3.4.3 Reconstruction errors

In order to evaluate the aforementioned decomposition, two reconstruction errors were computed:

$$C_e = \sqrt{\frac{\sum_{P \in D} (\underline{v}^{FE}(P, t) - \tilde{\underline{v}}^{el}(P, t))^2}{\sum_{P \in D} (\underline{v}^{FE}(P, t))^2}} \quad (3.51)$$

$$C_{ep} = \sqrt{\frac{\sum_{P \in D} (\underline{v}^{FE}(P, t) - \tilde{\underline{v}}(P, t))^2}{\sum_{P \in D} (\underline{v}^{FE}(P, t))^2}} \quad (3.52)$$

$\tilde{\underline{v}}^{el}(\underline{x}, t)$ is the kinematic field approximated only with the elastic basis:

$$\tilde{\underline{v}}^{el}(\underline{x}, t) = \sum_{i=1}^3 \dot{\tilde{K}}_i(t) \cdot \underline{\phi}_i^{el}(\underline{x}) \quad (3.53)$$

$\tilde{v}(\underline{x}, t)$ is the kinematic field approximated with both elastic and plastic bases:

$$\tilde{v}(\underline{x}, t) = \sum_{i=1}^3 \dot{\tilde{K}}_i(t) \cdot \underline{\phi}_i^{el}(\underline{x}) + \dot{\rho}_i(t) \cdot \underline{\phi}_i^{pl}(\underline{x}) \quad (3.54)$$

C_e is the relative error of the reconstruction using only the elastic field, C_{ep} is the error using both elastic and plastic fields. The difference between both errors means that the contribution of the plastic field is enhancing the solution. It can be then concluded that plasticity mechanism interferes into the total kinematic field which means also that the crack tip region started to yield. Therefore, the $C_e - C_{ep}$ can be considered as a plasticity indicator.

Note: The difference of volumes of elements relating different nodes P is not considered. This error estimator is more sensitive to the region near the crack tip since the mesh has a higher density in this region, which gives it more weight in the approximation.

Results

For each studied material orientation, a set of elastic plastic simulations were performed under different loading conditions as shown in plots (a) of figures from 3.24 to 3.28:

- Loading in pure *mode I* to $K_I^\infty = 12 \text{ MPa}\sqrt{\text{m}}$ then unloading to 0.
- Loading in pure *mode II* to $K_{II}^\infty = 7 \text{ MPa}\sqrt{\text{m}}$ then unloading to 0 with a slight opening ensured by a $K_I^\infty = 0.5 \text{ MPa}\sqrt{\text{m}}$ to avoid crack faces friction.
- Loading in pure *mode III* to $K_{III}^\infty = 6 \text{ MPa}\sqrt{\text{m}}$ then unloading to 0 with a slight opening ensured by a $K_I^\infty = 0.5 \text{ MPa}\sqrt{\text{m}}$ to avoid crack faces friction.
- A mixed mode loading to reach $\underline{K}^\infty = [4, 2, 1](\text{MPa}\sqrt{\text{m}})$ in a first step then $\underline{K}^\infty = [9, 5, 4](\text{MPa}\sqrt{\text{m}})$ in a second step.

Note: Under elastic-plastic conditions, nominal stress intensity factors K_i^∞ are defined as the stress intensity factors seen by the crack if the structure had a linear elastic response once subjected to the same loading conditions.

Kinematic fields from these simulations were projected on the kinematic basis of the considered material orientation in order to obtain the rates of intensity factors $\dot{\tilde{K}}_i(t)$ and $\dot{\rho}_i(t)$ of different modes. The integration of these stress and blunting intensity factors over the time laps gave \tilde{K}_i and $\tilde{\rho}_i$. Blunting intensity factor is shown for some cases in plots (b) on figures from 3.24 to 3.28.

$$\rho_i(t) = \int_0^t \dot{\rho}_i(x) dx \quad (3.55)$$

$$\tilde{K}_i(t) = \int_0^t \dot{\tilde{K}}_i(x) dx \quad (3.56)$$

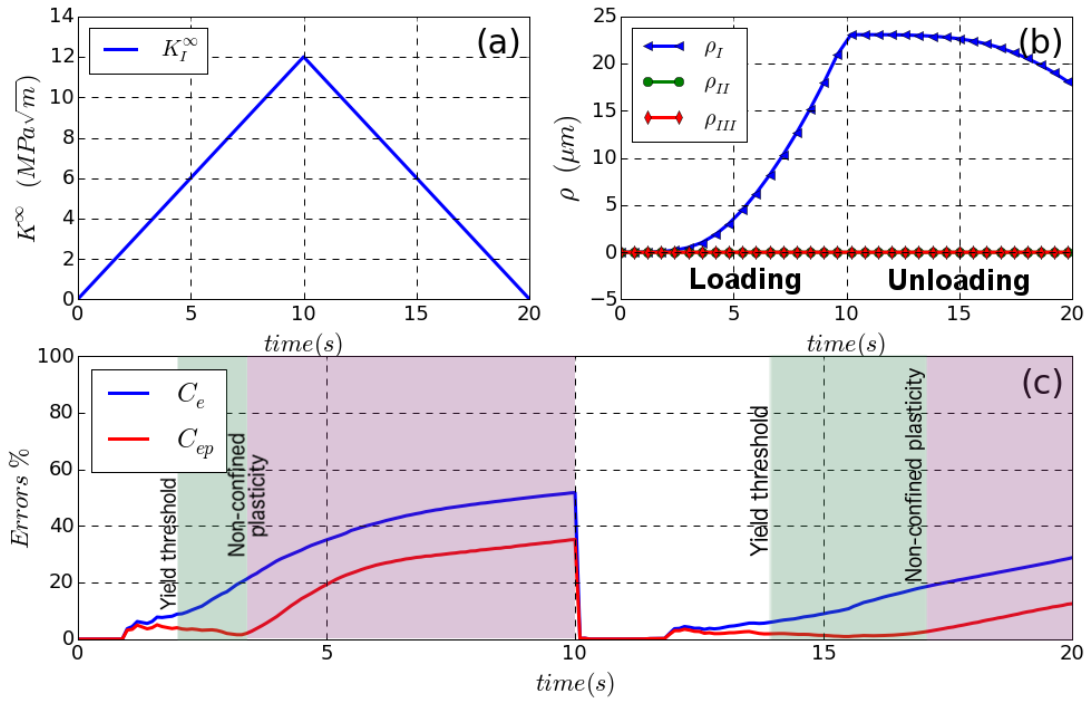


Figure 3.24: Loading and unloading under a pure *mode I* (a) applied nominal SIFs, (b) blunting intensity factors ρ_i and (c) reconstruction errors C_e and C_{ep} for material orientation $\gamma_{\begin{smallmatrix} 010 \\ 100 \end{smallmatrix}}$.

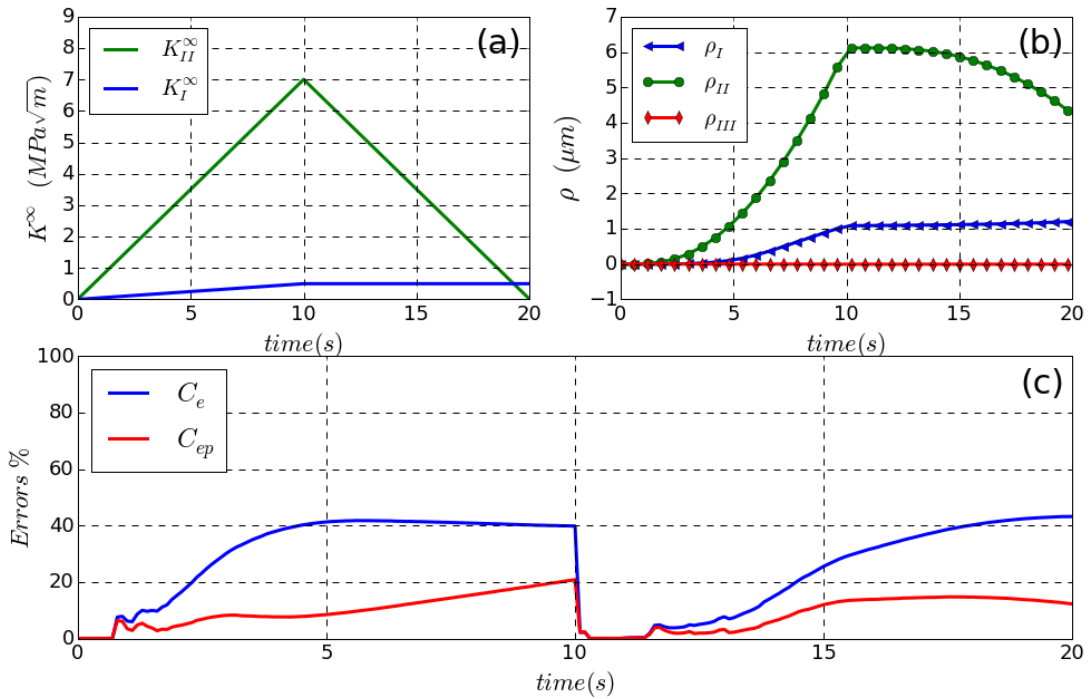


Figure 3.25: Loading and unloading under a pure *mode II* (a) applied nominal SIFs, (b) blunting intensity factors ρ_i and (c) reconstruction errors C_e and C_{ep} for material orientation $\gamma_{\begin{smallmatrix} 010 \\ 100 \end{smallmatrix}}$.

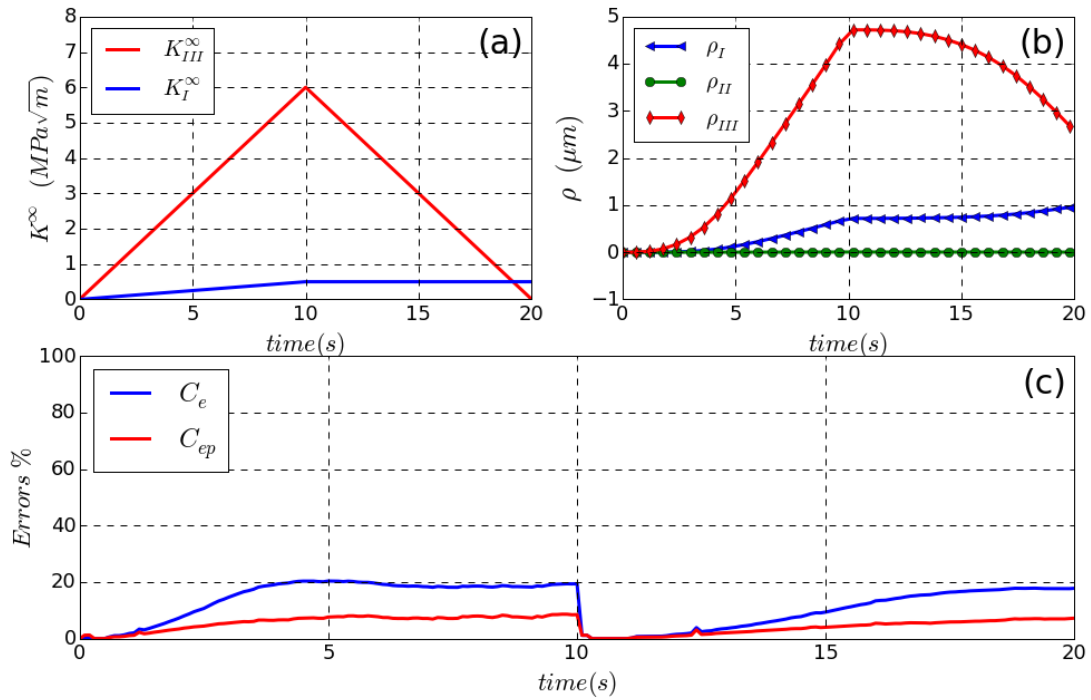


Figure 3.26: Loading and unloading under a pure *mode III* (a) applied nominal SIFs, (b) blunting intensity factors ρ_i and (c) reconstruction errors C_e and C_{ep} for material orientation $\gamma_{\begin{smallmatrix} (010) \\ [100] \end{smallmatrix}}$.

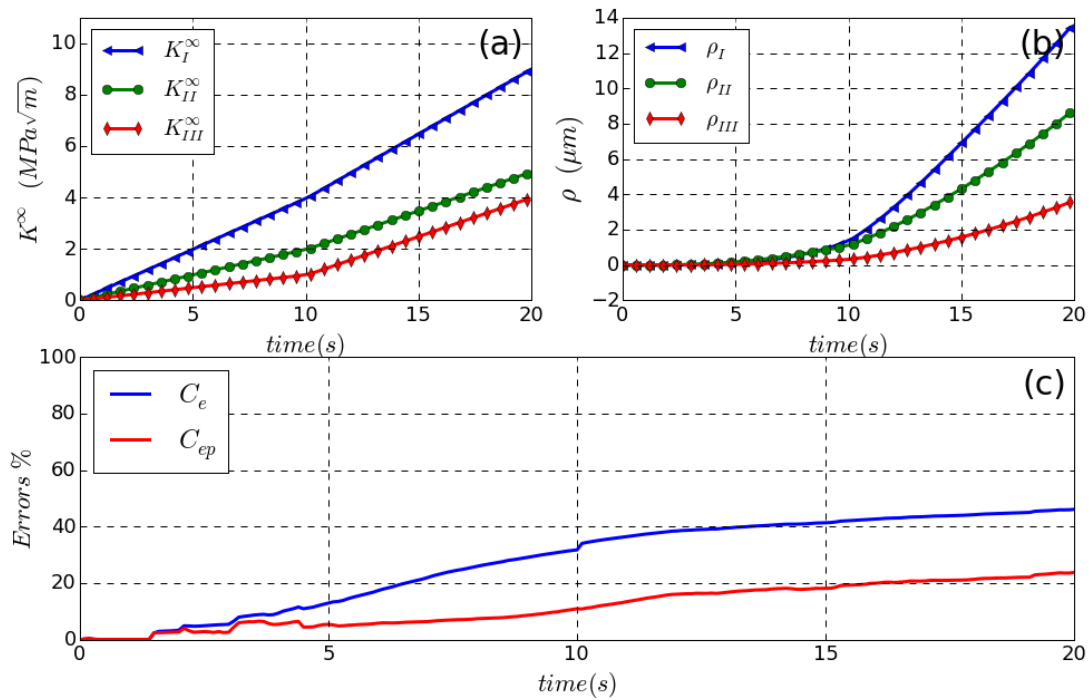


Figure 3.27: Mixed mode loading (a) applied nominal SIFs, (b) blunting intensity factors ρ_i and (c) reconstruction errors C_e and C_{ep} for an isotropic case.

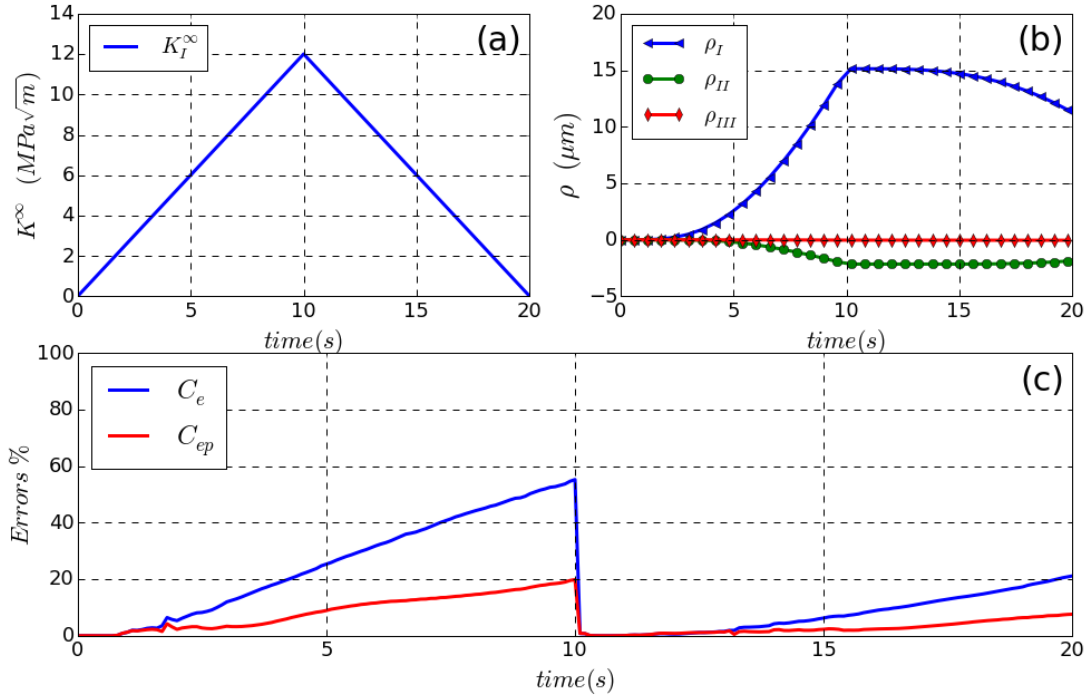


Figure 3.28: Loading and unloading under a pure *mode I* (a) applied nominal SIFs, (b) blunting intensity factors ρ_i and (c) reconstruction errors C_e and C_{ep} for material orientation $\gamma_{[3\bar{1}\bar{1}]}^{(121)}$.

Total kinematic fields were then approximated based on these quantities and reconstruction errors C_e and C_{ep} were computed. Curves (c) of figures from 3.24 to 3.28 show the evolution of these errors for some material orientations and loading conditions.

Reconstruction errors on figure 3.24(c) show different phases during both loading and unloading. At the beginning, both errors remain equal to zero. The behavior of the region near the crack tip is purely elastic. Thus, an elastic reconstruction is sufficient to describe it. Then, during the phase shown in green, the elastic reconstruction error C_e increases and the total reconstruction error remains negligible. It means that the incorporation of the complementary part is useful in the approximation of the total kinematic field. With the increasing loading, the crack tip region continues yielding and the plasticity become no more confined. At this spot, a basic hypothesis of the model is no more valid and the decomposition of kinematic field into an elastic and plastic part is not sufficient. Zhang [Zhang, 2016] had shown that, under large scale yielding, an other term must be added to the decomposition to account for generalized plasticity.

According to reconstruction errors, the accuracy of the decomposition depends on the type of the applied loading and on the material orientation. Nevertheless, these errors remain reasonable even under mixed mode loading (see figure 3.27) and for non symmetric material orientation (see figure 3.28).

As shown on figure 3.28b, under a pure fracture *mode I* loading, material orientation $\gamma_{[3\bar{1}\bar{1}]}^{(121)}$ exhibits a plastic flow in both directions I and II .

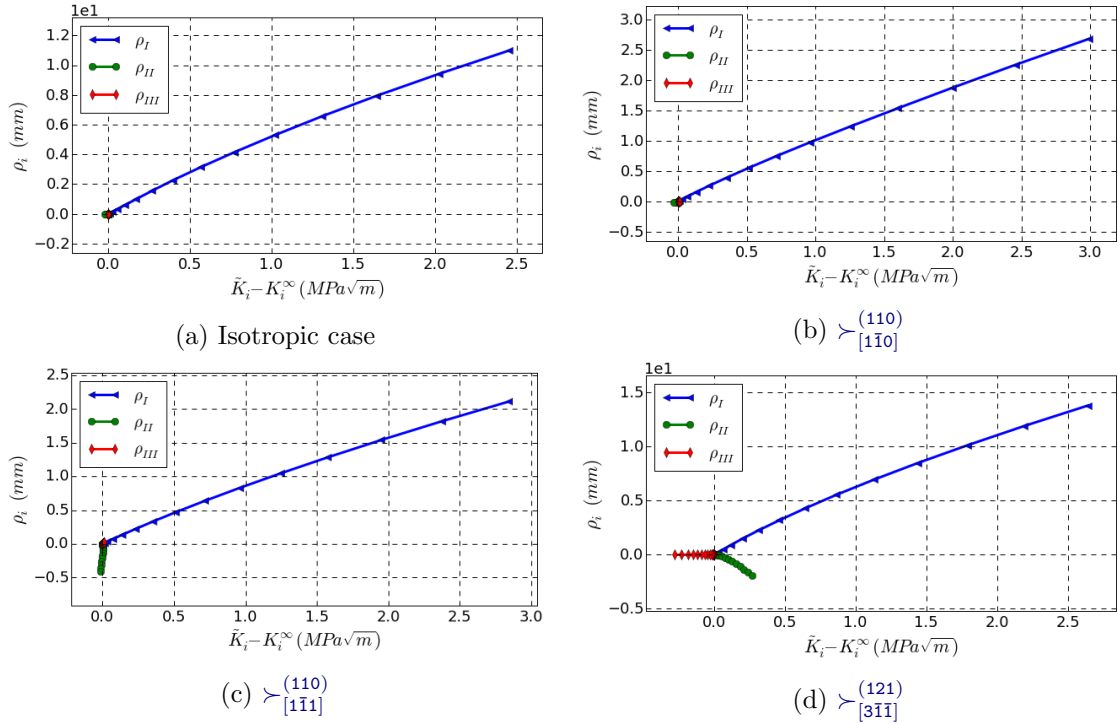


Figure 3.29: Evolution of the blunting intensity factor ρ_i us function of $(\tilde{K}_i - K_i^\infty)$ under pure fracture *mode I*.

Figure 3.29 shows the evolution of different blunting intensity factors ρ_i as function of $(\tilde{K}_i - K_i^\infty)$ for different material orientations under a pure *mode I* loading. It can be noted that these evolutions are linear. In fact, the difference $(\tilde{K}_i - K_i^\infty)$ is related to the “shielding effect” due to the confinement of the plastic zone. For this reason, this difference is proportional to the evolution of the plasticity described by the blunting intensity factor. It can be noted as well that material orientations $\succ_{[110]}$ and $\succ_{[311]}$ are exhibiting a plastic flow in directions *II* and *III* even though the loading is pure fracture *mode I*.

3.4.4 Other yield criteria

As discussed in the previous subsection, the difference between relative errors $C_e - C_{ep}$ can indicate whether the contribution of the complementary part is enhancing the quality of the approximation or not. This indication serves as a criterion to predict the yielding of the crack tip region. Moreover, further indicators based on the aforementioned kinematic basis can be used.

- **Reconstructed complementary field ratio**

Assuming that the quality of the approximation is acceptable, the ratio of the constructed plastic field with respect to the full reconstructed field can give an idea about the plasticity at the crack tip region without counting for the approximation error.

$$C_{corr} = \sqrt{\frac{\sum_{P \in D} (\tilde{v}^{pl}(P, t))^2}{\sum_{P \in D} (\tilde{v}^{el}(P, t) + \tilde{v}^{pl}(P, t))^2}} \quad (3.57)$$

- **Blunting intensity factors**

The Karhunen-Loeve decomposition was performed on the spatial reference fields of all modes combined in one snapshot matrix, therefore, one scale function $f^{pl}(r)$ is obtained for the three fracture modes of the complementary reference field. Besides, the spatial basis was rescaled to obtain a discontinuity between crack faces equal to a unit vector when $r \rightarrow 0$ (equation 3.46). This rescaling process allows introducing intensity factors $\dot{\rho}_I$, $\dot{\rho}_{II}$ and $\dot{\rho}_{III}$ as homogeneous physical quantities that describe the plastic opening of the crack. As a consequence, these quantities are comparable and can be gathered in one equivalent expression that can serve as a yield indicator.

$$\rho_{eq}(t) = \sqrt{\rho_I^2(t) + \rho_{II}^2(t) + \rho_{III}^2(t)} \quad \text{with} \quad \rho_i(t) = \int_0^t \dot{\rho}_i(x) dx \quad (3.58)$$

These yielding indicators will be used in section 3.5.3 to investigate the limits of the yield locus.

3.5 Incremental material model

The next step is to find an extended elastic-plastic material model for the region near the crack tip under mixed fracture modes $I + II + III$ based on the previously identified elastic and plastic frameworks. This modeling requires the identification of an extended yield criterion for the crack region, a plastic flow rule and an evolution law of internal variables such as the yield locus center and size.

3.5.1 Yield locus

A yield criterion for the region near the crack tip can be proposed based on the density of the elastic shear energy and LEFM fields. This criterion was developed for the 3D case for isotropic materials using Westergaard asymptotic solutions in the work of Frémy [Frémy et al., 2012]. The criterion presented previously in 2.4.1 for mixed fracture modes $I + II$ will be extended in this section to the general case of anisotropy under mixed fracture modes $I + II + III$ based on Hoenig's analytical solutions.

For the case of a cracked structure, the idea is to integrate elastic distortional energy density on a domain with radius δ around the crack tip where LEFM fields are still valid. The obtained distortional energy is written as follows:

$$E^D = \int_{\theta=-\pi}^{\pi} \int_{r=0}^{\delta} \frac{1}{2} \underline{\underline{\sigma}}^D : \underline{\underline{\mathbb{S}}} : \underline{\underline{\sigma}}^D r dr d\theta \quad (3.59)$$

The behavior of the material remains elastic as long as loading state remains inside the yield surface, therefore, an assumption is made that Hoenig analytical solutions are valid inside this domain as long as the possible motion of the center of the yield surface is taken into account. Therefore, the position of the yield surface $\underline{K}^X = (K_I^X, K_{II}^X, K_{III}^X)$ is accounted for and subtracted from the applied loading $\underline{K}^\infty = (K_I^\infty, K_{II}^\infty, K_{III}^\infty)$.

The Hoenig solution in stress is written as follows:

$$\begin{aligned}
\sigma_{xx} &= \frac{1}{\sqrt{2\pi r}} \Re \left[\sum_{i=1}^3 \frac{p_i^2 N_{ij}^{-1} K_j^*}{Q_i} \right] & \sigma_{yy} &= \frac{1}{\sqrt{2\pi r}} \Re \left[\sum_{i=1}^3 \frac{N_{ij}^{-1} K_j^*}{Q_i} \right] \\
\sigma_{xy} &= -\frac{1}{\sqrt{2\pi r}} \Re \left[\sum_{i=1}^3 \frac{p_i N_{ij}^{-1} K_j^*}{Q_i} \right] & \sigma_{zx} &= \frac{1}{\sqrt{2\pi r}} \Re \left[\sum_{i=1}^3 \frac{p_i \lambda_i N_{ij}^{-1} K_j^*}{Q_i} \right] \\
\sigma_{zy} &= -\frac{1}{\sqrt{2\pi r}} \Re \left[\sum_{i=1}^3 \frac{\lambda_i N_{ij}^{-1} K_j^*}{Q_i} \right] & \sigma_{zz} &= \frac{1}{\sqrt{2\pi r}} \Re \left[\sum_{i=1}^3 \frac{\alpha_i N_{ij}^{-1} K_j^*}{Q_i} \right]
\end{aligned} \tag{3.60}$$

under plane strain assumption:

$$\alpha_i = -\frac{1}{S_{33}} \left[S_{31} p_i^2 + S_{32} - S_{34} \lambda_i + S_{35} p_i \lambda_i - S_{36} p_i \right] \tag{3.61}$$

with:

$$\underline{K}^* = \begin{pmatrix} K_I^\infty - K_I^X \\ K_{II}^\infty - K_{II}^X \\ K_{III}^\infty - K_{III}^X \end{pmatrix} \tag{3.62}$$

Vectors p_i , λ_i , Q_i and matrix N_{ij} were previously detailed in section 3.2.1.

The deviatoric part of the Hoenig stress is computed then injected into the expression 3.59. It is important to mention that this analysis is made in the crack coordinates system, therefore the compliance tensor $\underline{\underline{S}}$ has to be expressed in this same coordinates system. The technical computing software *Mathematica* was used to ensure these mathematical developments.

The obtained distortional energy is function of the nominal stress intensity factors and the position of the yield surface $E^D(K_I^\infty - K_I^X, K_{II}^\infty - K_{II}^X, K_{III}^\infty - K_{III}^X)$. In analogy with the local Von-Mises criterion, a criterion is set when this energy reaches a pure *mode I* yield threshold K_I^Y so that:

$$E^D(K_I^\infty - K_I^X, K_{II}^\infty - K_{II}^X, K_{III}^\infty - K_{III}^X) = E^D(K_I^Y, 0, 0) \tag{3.63}$$

Thus, the distortional energy is a factor of the radius δ of the integration area. This scale factor can be eliminated from both sides of the equation 3.63 to obtain an expression independent from the integration radius δ which finally gives a scale invariant yield criterion. This yield criterion can be rewritten as a yield function f :

$$f = \frac{(K_I^\infty - K_I^X)^2}{(K_I^Y)^2} + \frac{(K_{II}^\infty - K_{II}^X)^2}{(K_{II}^Y)^2} + \frac{(K_{III}^\infty - K_{III}^X)^2}{(K_{III}^Y)^2} - 1 + \psi(K_I^\infty - K_I^X, K_{II}^\infty - K_{II}^X, K_{III}^\infty - K_{III}^X) \tag{3.64}$$

with

$$\psi = \frac{(K_I^\infty - K_I^X)(K_{II}^\infty - K_{II}^X)}{(K_{I+II}^t)^2} + \frac{(K_I^\infty - K_I^X)(K_{III}^\infty - K_{III}^X)}{(K_{I+III}^t)^2} + \frac{(K_{II}^\infty - K_{II}^X)(K_{III}^\infty - K_{III}^X)}{(K_{II+III}^t)^2} \tag{3.65}$$

K_{II}^Y , K_{III}^Y , K_{I+II}^t , K_{I+III}^t and K_{II+III}^t are intrinsic parameters of the material. They depend on elasticity coefficients, the crystallographic orientation with respect to the crack plane and direction and on the adjustable parameter K_I^Y presented in equation 3.63.

In the $K_I^\infty - K_{II}^\infty - K_{III}^\infty$ diagram, this criterion function represents an ellipsoid slightly tilted from the K_I^∞ axis as shown in figure 3.31. The size of this ellipsoid is given by the adjustable parameter K_I^Y . The shape depends on the elasticity constants through the two fixed ratios $\frac{K_{II}^Y}{K_I^Y}$ and $\frac{K_{III}^Y}{K_I^Y}$. The angles of tilting are functions of K_{I+II}^t , K_{I+III}^t and K_{II+III}^t that depend on elasticity coefficients. In fact, the anisotropy creates the coupling between different fracture modes in the expression of ψ , this coupling manifests in the angle of tilting which makes it directly related to the orientation of the crystal with respect to the crack plane.

When the material is orthotropic and its axes coincide with the crack axes, ψ in equation 3.64 is equal to zero and the major axis of the ellipsoid is parallel to the K_I^∞ axis in the $K_I^\infty - K_{II}^\infty - K_{III}^\infty$ diagram as shown on figure 3.30. For an isotropic case, the ratio between the major axis and the two minor axes is given as follows [Pommier et al., 2009], [Decreuse, 2010], [Frémy, 2012]:

$$\left. \begin{aligned} \frac{K_{II}^Y}{K_I^Y} &= \sqrt{\frac{7-16\nu(1-\nu)}{19-16\nu(1-\nu)}} = 0.48 \\ \frac{K_{III}^Y}{K_I^Y} &= \sqrt{\frac{7-16\nu(1-\nu)}{24}} = 0.39 \end{aligned} \right\} \text{ for } \nu = 0.3 \quad (3.66)$$

In order to write this criterion in a thermodynamic framework, new variables G_i homogeneous to the energy release rate G are introduced, the criterion is then rewritten as follows:

$$f = \frac{|G_I|}{|G_I^Y|} + \frac{|G_{II}|}{|G_{II}^Y|} + \frac{|G_{III}|}{|G_{III}^Y|} - 1 + \varphi(G_I, G_{II}, G_{III}) \quad (3.67)$$

with

$$\varphi = \text{sign}(G_I G_{II}) \frac{\sqrt{|G_I G_{II}|}}{|G_{I+II}^t|} + \text{sign}(G_I G_{III}) \frac{\sqrt{|G_I G_{III}|}}{|G_{I+III}^t|} + \text{sign}(G_{II} G_{III}) \frac{\sqrt{|G_{II} G_{III}|}}{|G_{II+III}^t|} \quad (3.68)$$

$$\begin{aligned} G_i &\propto \text{sign}(K_i^\infty - K_i^X)(K_i^\infty - K_i^X)^2 \\ G_i^Y &\propto (K_i^Y)^2 \\ G_{i+j}^t &\propto (K_{i+j}^t)^2 \end{aligned} \quad (3.69)$$

For instance for the isotropic case, the exact expressions assigned to these quantities are ([Decreuse, 2010], [Frémy, 2012]):

$$\begin{aligned} G_i &= \text{sign}(K_i^\infty - K_i^X) \frac{1-\nu^2}{E} (K_i^\infty - K_i^X)^2, & G_i^Y &= \frac{1-\nu^2}{E} (K_i^Y)^2 \text{ for } i \in \{I, II\} \\ G_{III} &= \text{sign}(K_{III}^\infty - K_{III}^X) \frac{1+\nu}{E} (K_{III}^\infty - K_{III}^X)^2, & G_{III}^Y &= \frac{1+\nu}{E} (K_{III}^Y)^2 \end{aligned} \quad (3.70)$$

For an orthotropic case where the material axes are along the problem coordinates system, an expression of these quantities can be given based on the work done by

[Banks-Sills et al., 2005]:

$$\begin{aligned}
 G_I &= \text{sign}(K_I^\infty - K_I^X) \frac{D_0 \sqrt{S'_{22}}}{2} (K_I^\infty - K_I^X)^2 & , & \quad G_I^Y = \frac{D_0 \sqrt{S'_{22}}}{2} (K_I^Y)^2 \\
 G_{II} &= \text{sign}(K_{II}^\infty - K_{II}^X) \frac{D_0 \sqrt{S'_{11}}}{2} (K_{II}^\infty - K_{II}^X)^2 & , & \quad G_{II}^Y = \frac{D_0 \sqrt{S'_{11}}}{2} (K_{II}^Y)^2 \\
 G_{III} &= \text{sign}(K_{III}^\infty - K_{III}^X) \frac{\sqrt{S'_{44} S'_{55} - S'^2_{45}}}{2} (K_{III}^\infty - K_{III}^X)^2 & , & \quad G_{III}^Y = \frac{\sqrt{S'_{44} S'_{55} - S'^2_{45}}}{2} (K_{III}^Y)^2
 \end{aligned} \tag{3.71}$$

with $D_0 = \sqrt{2\sqrt{S'_{11} S'_{22}} + 2S'_{12} + S'_{66}}$.

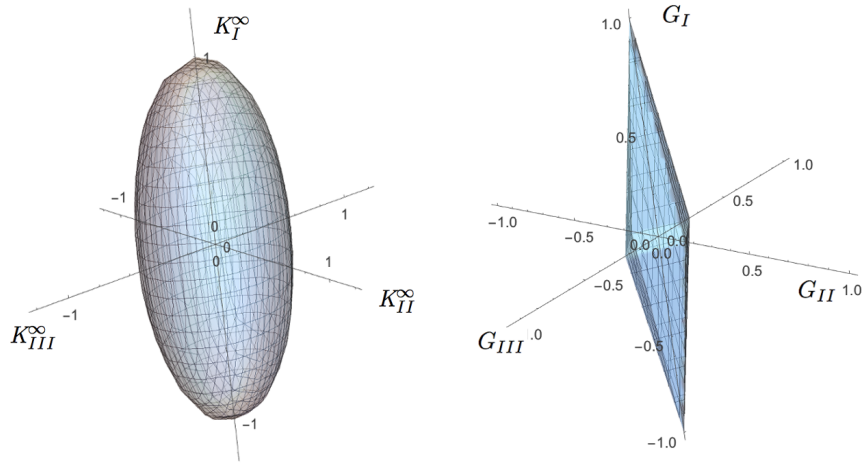


Figure 3.30: Yield domains is an ellipsoid in the $K_I^\infty - K_{II}^\infty - K_{III}^\infty$ space and a twisted octahedron in the $G_I - G_{II} - G_{III}$ space when the anisotropy seen by the crack is orthotropic.

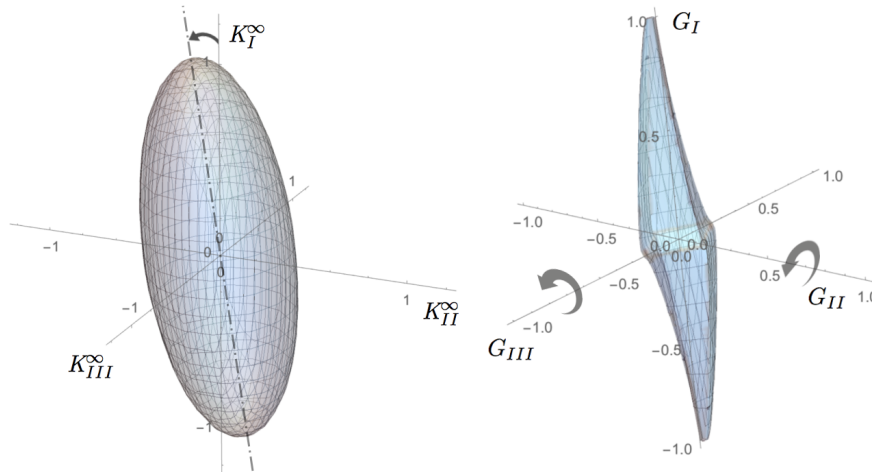


Figure 3.31: Yield domains is an ellipsoid in the $K_I^\infty - K_{II}^\infty - K_{III}^\infty$ space and a twisted octahedron in the $G_I - G_{II} - G_{III}$ space when the anisotropy seen by the crack is not orthotropic.

This new criterion draws an octahedron in the $G_I - G_{II} - G_{III}$ diagram with G_I as a principle axis. As shown on figure 3.30, the octahedron is straight when the material

is orthotropic and when the material axes coincide the crack coordinate system. When it is not the case, the octahedron is slightly twisted around axes G_{II} and G_{III} as shown on figure 3.31. The twisting is given by the function φ and it mainly depends on the crystallographic orientation with respect to the crack plane.

3.5.2 FE simulation: ellipsoid exploration

A method based on finite element simulations and the kinematic bases already defined in section 3.4 is used in this section to identify plastic flow directions.

Ellipsoid loading path

As shown previously in chapter 2, a first attempt was made to explore yield surface by loading in one direction with a given mixed mode ratio, to make a slight elastic comeback inside the yield locus, then to start exploring in different directions with different mixture ratios. In each direction, a plasticity indicator was computed based on the kinematic basis previously found. It was possible to identify the elliptic shape of the yield surface in a $K_I^\infty - K_{II}^\infty$ diagram, however, it was obvious that the initial loading has distorted drastically the shape of the yield surface. This distortion has an effect also on the plastic flow directions. In order to avoid this phenomena or at least to reduce its effects, a new manner of exploration was proposed in order to get closer to the yield surface limits without deforming it. The idea is to follow a loading path similar to the analytically computed yield locus ellipsoid (same ratios), and to increase the size of the ellipsoid step by step by increasing the adjustable parameter K_I^Y . At a certain point, the cracked region starts yielding continually while staying tangent to the yield surface but without drastically deforming it. Plastic flow directions can then be studied without being perturbed. For each

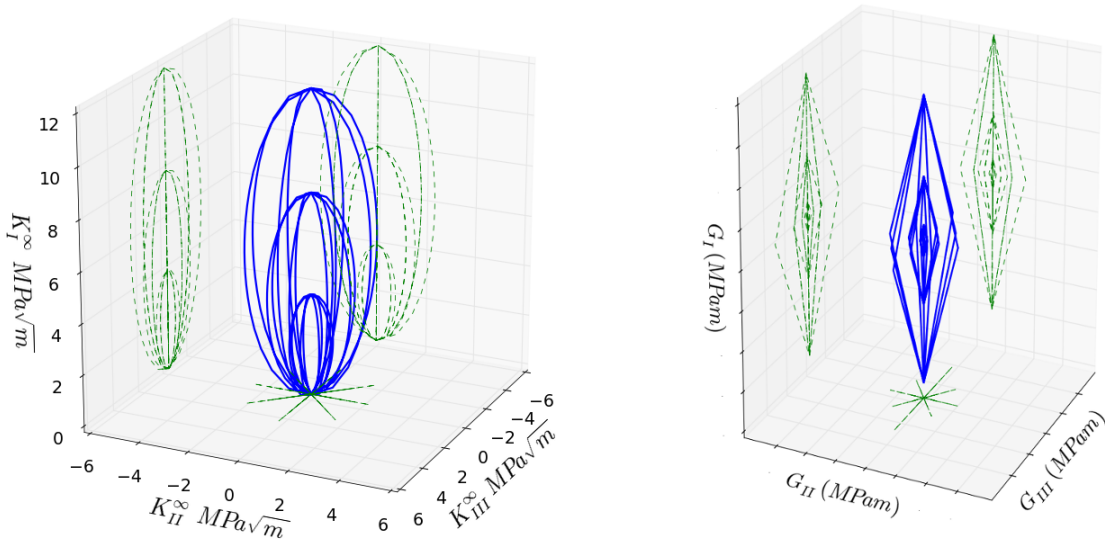


Figure 3.32: Loading path following an ellipsoid in the $K_I^\infty - K_{II}^\infty - K_{III}^\infty$ which gives an octahedron in the $G_I - G_{II} - G_{III}$ diagram.

material orientation, the two ratios of the ellipsoid were analytically computed. Tilting angles were found to be very small, at least for the studied range of material orientations, therefore, the tilting was neglected to simplify the loading path. Three ellipsoids with

different sizes ($K_I^Y = 2 \text{ MPa}\sqrt{\text{m}}$, $K_I^Y = 4 \text{ MPa}\sqrt{\text{m}}$ and $K_I^Y = 6 \text{ MPa}\sqrt{\text{m}}$) but same ratios were explored for each case.

Reconstruction errors

Reconstruction errors of the full loading path (equations 3.51 and 3.52) were computed based on the kinematic bases previously determined for each material orientation. Figure 3.33 shows these errors for the material orientation $\gamma_{[100]}^{(010)}$. Three main phases that correspond to the three explored ellipsoids can be distinguished. A snapshot of the cumulated plastic strain plotted in logarithmic scale is shown in each one of these three phases. According to the difference between C_e and C_{ep} errors and as shown in the cumulated plastic strain plots, the first ellipsoid kept the crack tip region into an elastic regime. The second loading path started to create some yielding in this region and the third ellipsoid is ensuring plasticity at a confined zone near the crack tip. It can be noted that, for

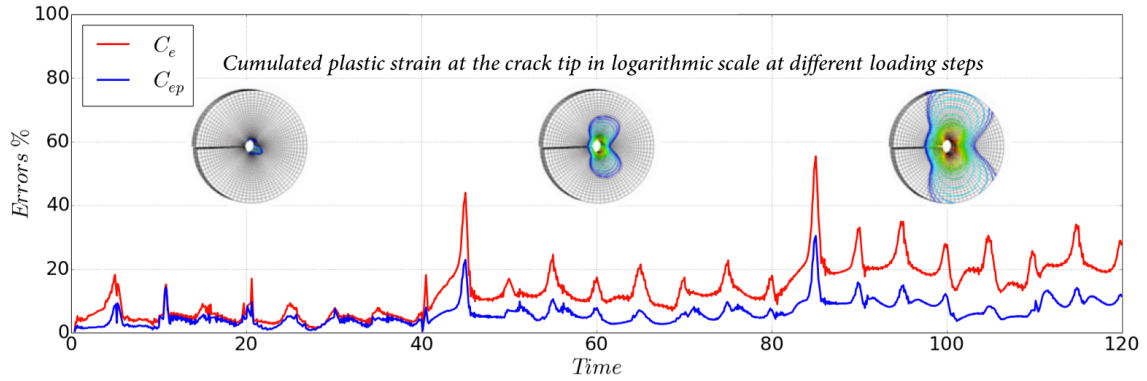


Figure 3.33: Reconstruction errors of the ellipsoid exploration path for material orientation $\gamma_{[100]}^{(010)}$.

this presented material orientation $\gamma_{[100]}^{(010)}$, the applied mixed mode loading during the last ellipsoid has the same order of magnitudes as the ones shown on figures 3.24, 3.25 and 3.26. However, the third phase on figure 3.33 exhibits a smaller difference between C_e and C_{ep} . It can be concluded that staying near the borders of the nominal yield locus needs less correction using the plasticity field.

Plastic flow directions

- **Extended flow rule**

Since the model does not take into account damage, neither strain localization, the only source of dissipation is the plastic blunting of the crack tip. Hence, the dissipated energy density can be written for a volume element as a fraction of the elastic distortional energy per unit volume. The integration over the circular region of radius δ centered at the crack tip gives that the dissipated energy per unit length of crack front is function of the elastic distortional energy of this circular region. As shown in equations 3.59 and 3.63, the yield criterion of the cracked region derives from this elastic distortional energy, as a consequence, the pseudo-potential of dissipation is an expression of the yield criterion $\Omega = \Omega(f(K_i^\infty)) = \Omega(f(G_i))$. Thus, the normality flow rule can be associated to this

extended material model of the cracked region. This statement means that plastic flow directions are considered normal to the yield locus to ensure maximum dissipation as if it was a problem of standard generalized model.

With the approximation of kinematic fields, intensity factors $\dot{\rho}_i$ can be introduced as extensive variables that describe the plastic flow at the crack tip region. These blunting intensity factors, equivalent to the plastic strain in a standard generalized model, are assumed to follow an extended normality flow rule. On the other hand, the incremental model assumes that the crack growth is a geometric consequence of the plastic contribution of different fracture modes. The extension area of the crack is then expressed in terms of blunting intensity factors. Regarding the relation between the cracked area and the energy release rate, it's possible to consider $\dot{\rho}_i$ and G_i as dual variables. The flow rule derives finally from the pseudopotential Ω as a normality rule: $\dot{\rho}_i = \partial\Omega/\partial G_i$. As mentioned before, the pseudopotential of dissipation Ω can be written as function of the yield criterion $f(G_i)$ (equation 3.67). Thus, the normality rule is written as follows:

$$\dot{\rho}_i = \dot{\lambda} \frac{\partial f(G_I, G_{II}, G_{III})}{\partial G_i} \quad (3.72)$$

• Results from FE simulations and kinematic bases

Kinematic fields were extracted from the ellipsoid path simulation. The plastic flow directions are obtained by the projection of these fields on the corresponding basis in order to identify, at each time increment, the vector of blunting intensity factors $\underline{\dot{\rho}} = (\dot{\rho}_I, \dot{\rho}_{II}, \dot{\rho}_{III})$. Figure 3.34 shows these vectors plotted, with the loading path, in the $K_I^\infty - K_{II}^\infty - K_{III}^\infty$ diagram for an isotropic case. As a first observation, the plastic flow directions are totally different from the loading direction.

According to reconstruction errors discussed in 3.5.2, the yielding is well ensured during the last ellipsoid. Therefore, only this last loading sequence is plotted on figures from 3.35 to 3.39 for the clarity of representation and the simplicity of discussion. These figures show the distribution of plastic flow directions plotted in the $G_I - G_{II} - G_{III}$ diagram for different material orientations.

The accuracy of the normality flow rule depends on the anisotropy seen by the crack. For the isotropic case shown in $K_I^\infty - K_{II}^\infty - K_{III}^\infty$ diagram in figure 3.34 and in $G_I - G_{II} - G_{III}$ diagram in figure 3.35, the flow rule occurs in a direction normal to the yield surface described by the loading path. With the anisotropy, the normality rule was verified for some material orientations during some loading sequences and more or less for others. It's then obvious that plastic flow direction highly depends on the elastic anisotropy. Material orientations $\succ_{[100]}^{(010)}$ in figure 3.36 and $\succ_{[001]}^{(110)}$ in figure 3.37 have shown that applying a loading in a given K-nominal plane with only two mixed modes ($G_I - G_{II}$ or $G_I - G_{III}$) will restrain the plastic flow in that loading plane. Once the loading combines the second and third fracture modes together, a plastic flow out of loading plane appears with a privileged flow in the direction *II* for orientation $\succ_{[1\bar{1}0]}^{(110)}$ and in the direction *III* for orientation $\succ_{[001]}^{(110)}$. When loaded in the $G_I - G_{III}$ plane, orientation $\succ_{[1\bar{1}1]}^{(110)}$ (figure 3.38d) exhibits a plastic flow in the direction *II*. This flow direction changes its sign when the loading switch from increasing G_{III} to decreasing one and vice versa. Nevertheless, no out-of-plane plastic flow is observed when loading is in the $G_I - G_{II}$ plane. Figure 3.39d shows that for orientation $\succ_{[3\bar{1}\bar{1}]}^{(121)}$, two in-plane plastic flows occur in a given loading plane (*I - II* or

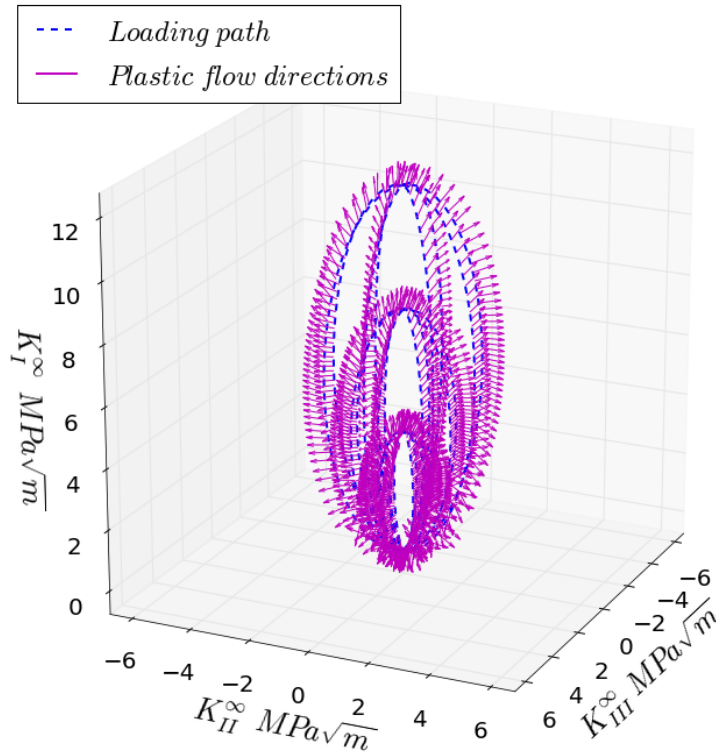


Figure 3.34: Plastic flow directions of the last explored ellipsoid for an isotropic case.

$I - III$), besides, an out-of-plane plastic flow appears systemically. This out of the $I - II$ plane (respectively $I - III$ plane) plastic flow experiences a transient change of direction when the loading G_{III} (respectively G_{II}) changes its variation sign.

It is important to recall that, for the anisotropic case, the tilting of the yield domain was neglected in the loading path since the aim of these loading sequences is to approach the maximum the borders of the yield locus without distorting it and not identifying these borders. Knowing that the values of these tilting angles in the K-nominals space (the twisting angle in the $G_I - G_{II} - G_{III}$ space) vary from an orientation to another, the imposed shape of the exploration path may cause the yielding of the crack tip region for some material orientations during some loading phases more than others. As a consequence, the yield domain may experience more distortion in these phases compared to others, which can explain the perturbation in the normality flow rule for some symmetric faces of the octahedron more than others (see plots (b) and (c) of figures 3.38 and 3.39). Moreover, the twisting can be clearly observed on the edges and around the vertices of some crystallographic orientations (figures 3.38 and 3.39) and the magnitude of this twisting varies from one orientation to another.

- **Discussion about the convexity of the yield domain and the choice of G_i as dual variables for ρ_i**

Ishikawa and co-workers [Ishikawa, 1980] had shown that, under mixed fracture modes I and II , it is possible to separate the J-integral into two path independent integrals per mode (J_I and J_{II}) as long as the material is isotropic. This conclusion was established

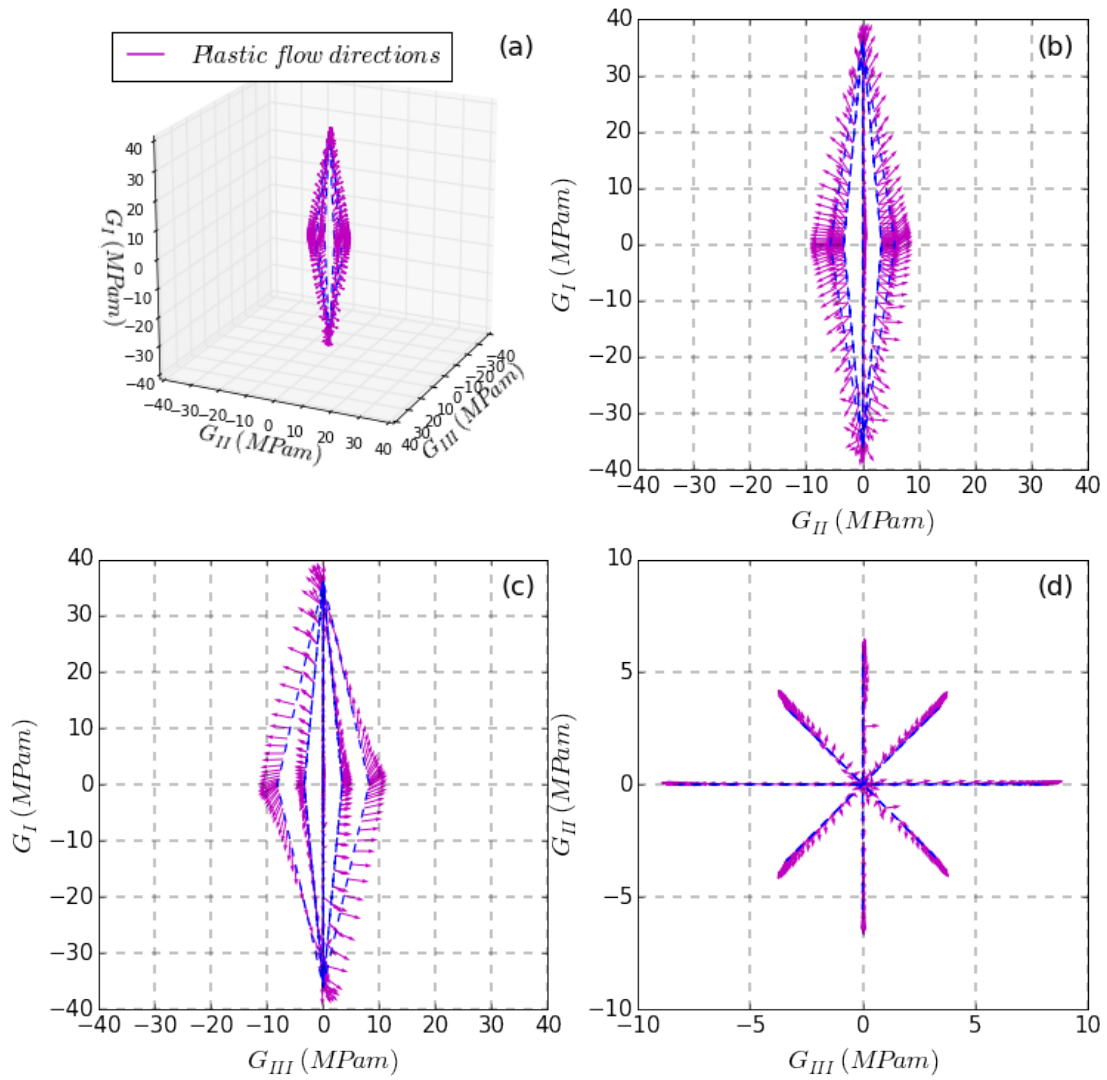


Figure 3.35: Plastic flow directions of the last explored ellipsoid for an isotropic case (a) in the $G_I - G_{II} - G_{III}$ diagram and their projections on the (b) $G_I - G_{II}$, (c) $G_I - G_{III}$ and (d) $G_{II} - G_{III}$ planes.

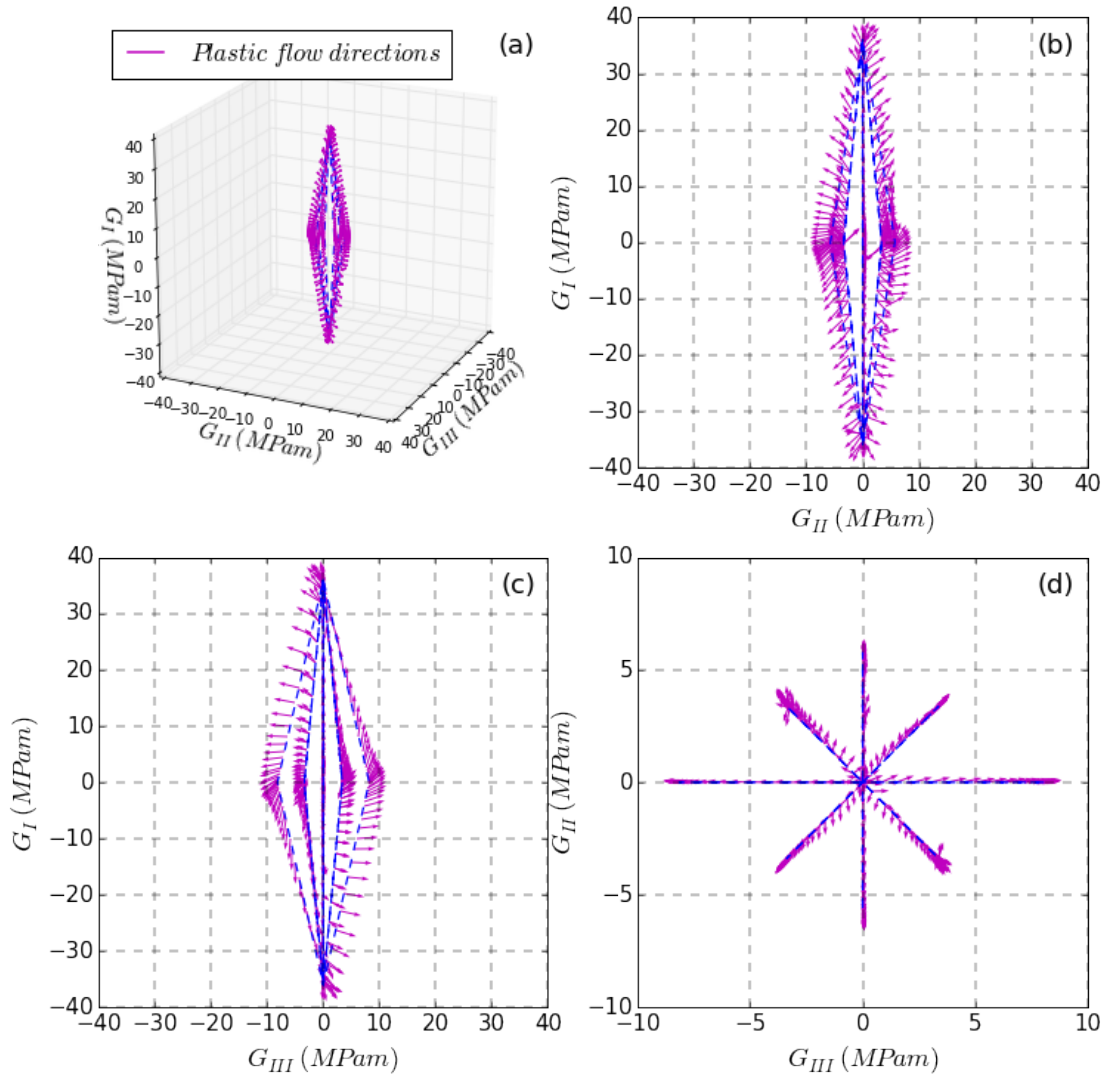


Figure 3.36: Plastic flow directions of the last explored ellipsoid for material orientation $\chi_{[100]}^{(010)}$ (a) in the $G_I - G_{II} - G_{III}$ diagram and their projections on the (b) $G_I - G_{II}$, (c) $G_I - G_{III}$ and (d) $G_{II} - G_{III}$ planes.

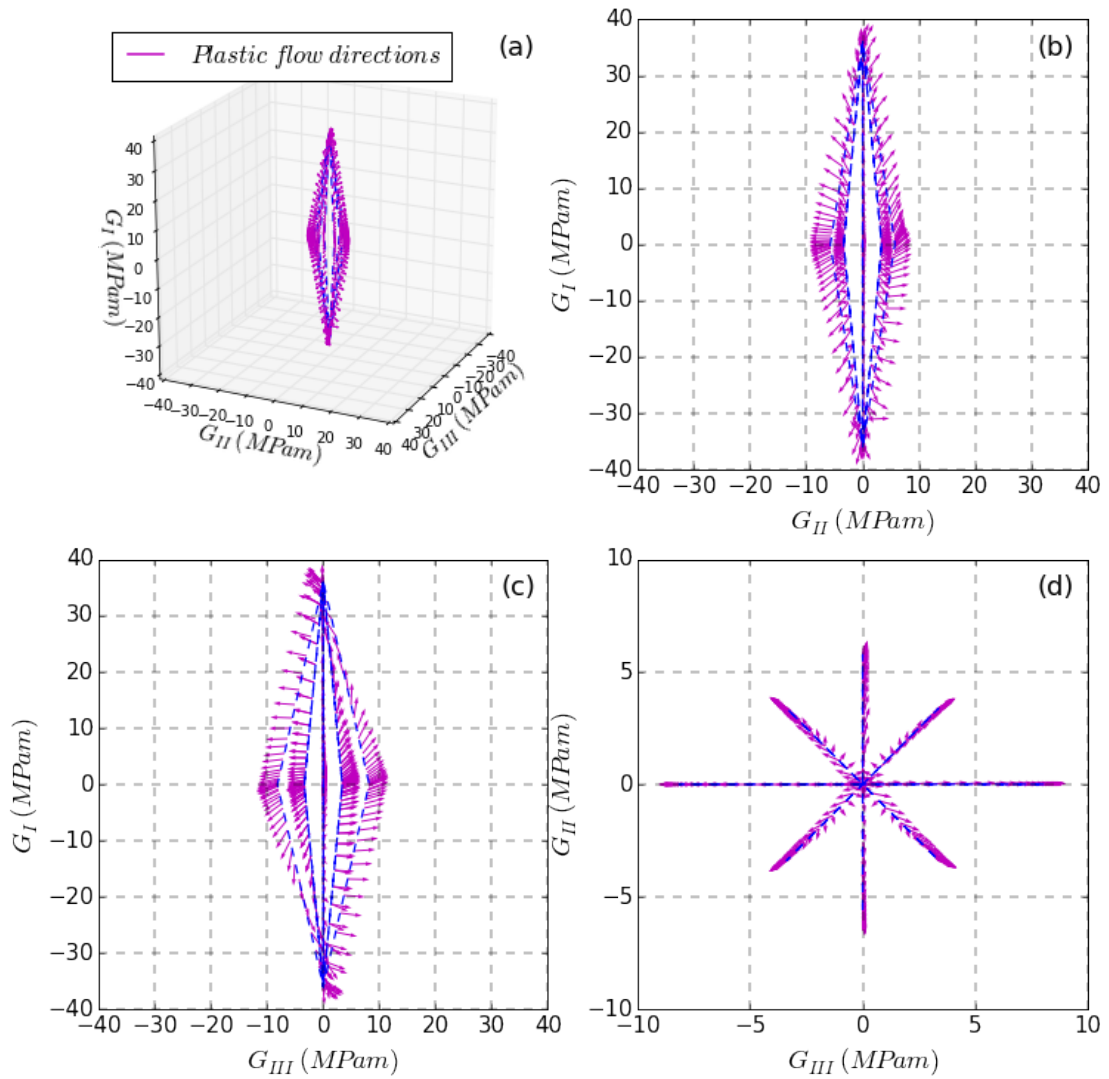


Figure 3.37: Plastic flow directions of the last explored ellipsoid for material orientation $\chi_{[001]}^{(110)}$ (a) in the $G_I - G_{II} - G_{III}$ diagram and their projections on the (b) $G_I - G_{II}$, (c) $G_I - G_{III}$ and (d) $G_{II} - G_{III}$ planes.

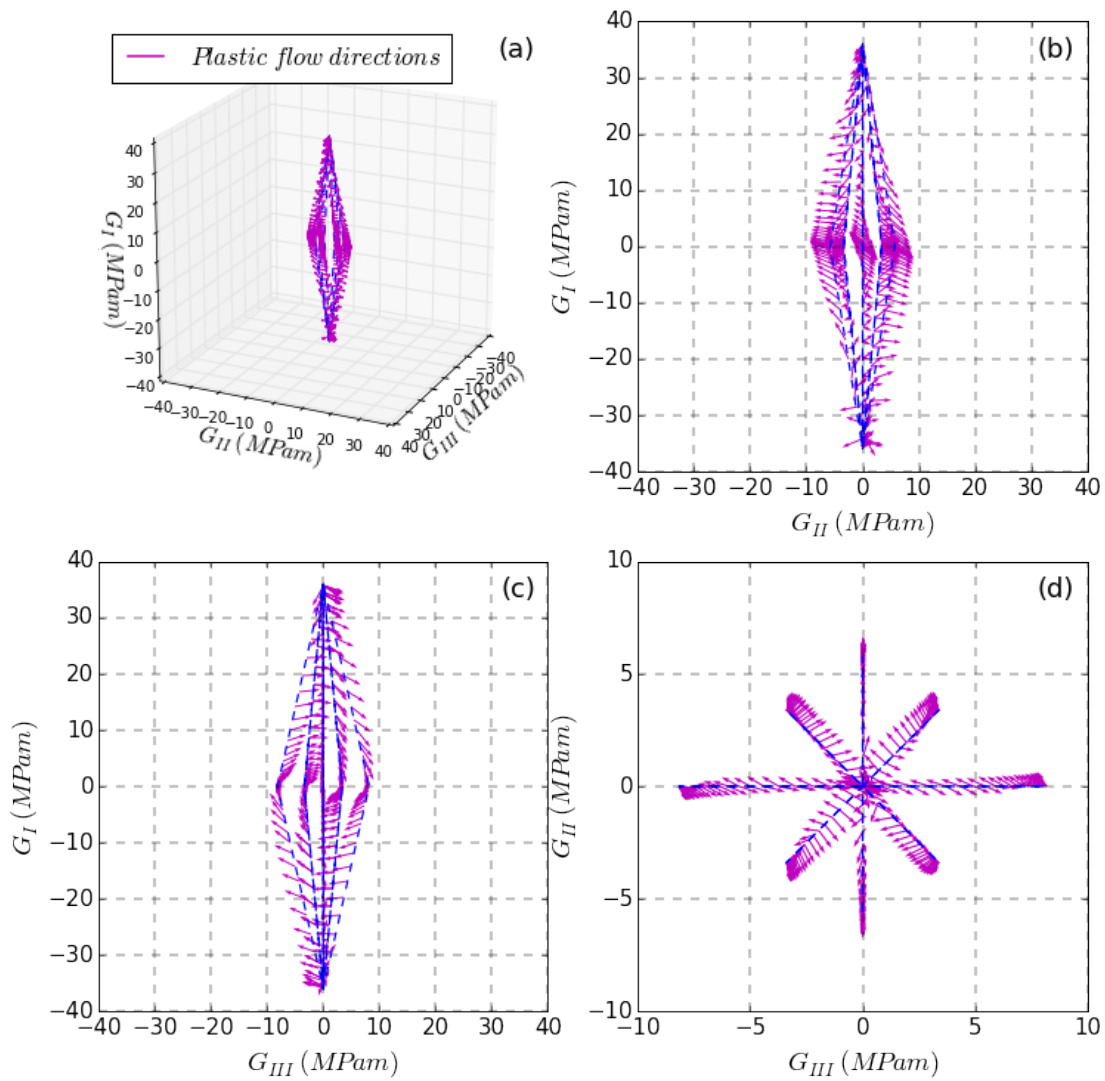


Figure 3.38: Plastic flow directions of the last explored ellipsoid for material orientation $\chi_{[111]}^{(110)}$ (a) in the $G_I - G_{II} - G_{III}$ diagram and their projections on the (b) $G_I - G_{II}$, (c) $G_I - G_{III}$ and (d) $G_{II} - G_{III}$ planes.

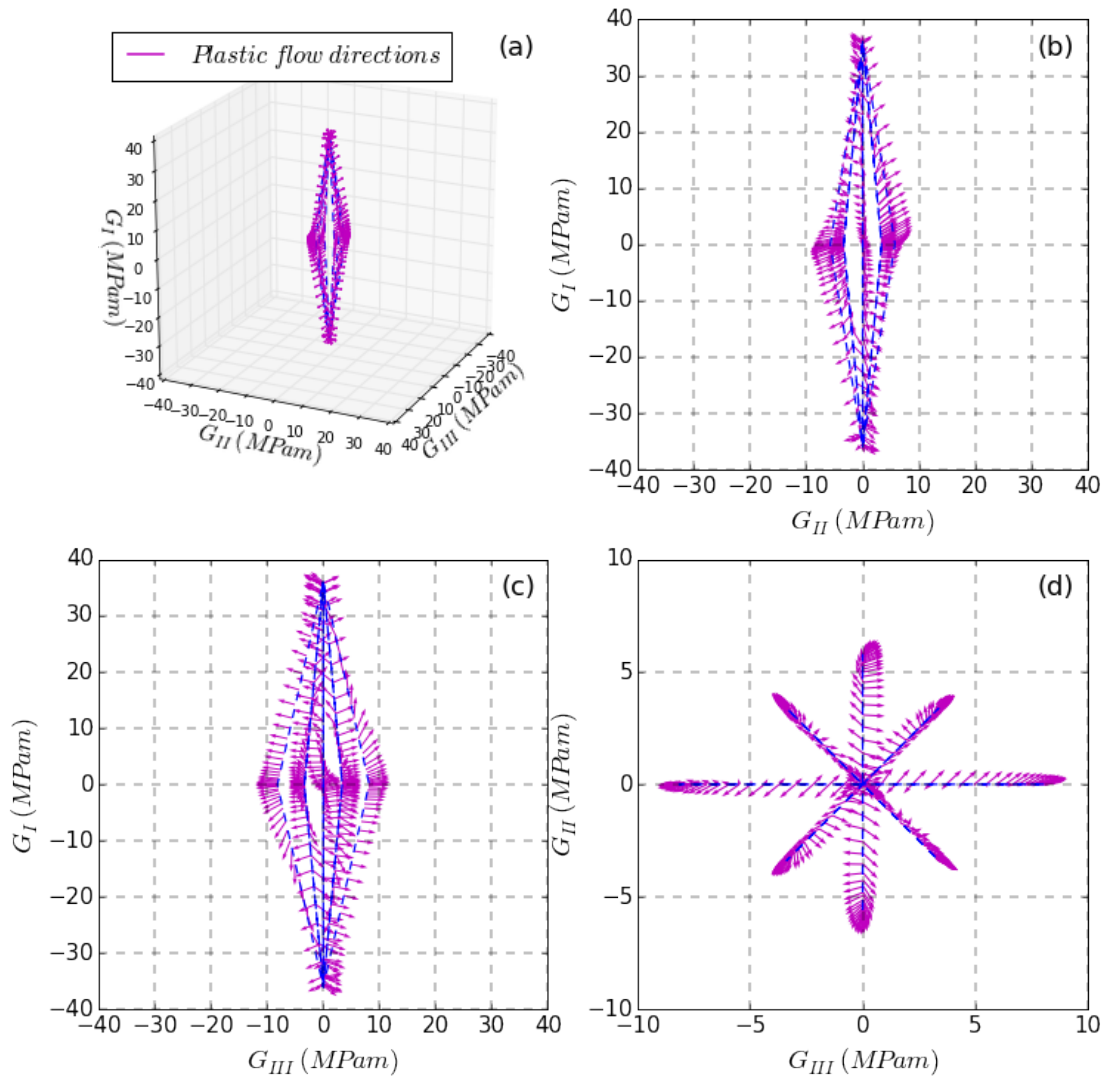


Figure 3.39: Plastic flow directions of the last explored ellipsoid for material orientation $\gamma_{[311]}^{(121)}$ (a) in the $G_I - G_{II} - G_{III}$ diagram and their projections on the (b) $G_I - G_{II}$, (c) $G_I - G_{III}$ and (d) $G_{II} - G_{III}$ planes.

independently by [Sun and Jih, 1987], [Raju et al., 1988] for interfacial cracks. Banks-Sills and co-workers [Banks-Sills et al., 2005] have shown that this separation is possible for an orthotropic material with a coincidence between the material axes and the crack coordinates system, which is the case of orientations $\succ_{[100]}^{(010)}$ and $\succ_{[001]}^{(110)}$ in this work. The demonstration was done using two different methods. A first one is using the alternative definition of the J-integral known as the crack closure integral. A second method is computing analytically the known expression of the J-Integral while separating stress, strain and displacement fields into symmetric and asymmetric parts. The following J_I and J_{II} were obtained (no distinction was made in this work between Rice's J-integral and the energy release rate G):

$$\begin{aligned} G_I &= J_I = C_1^{(I)} K_I^2 + C_2^{(I)} K_I K_{II} + C_3^{(I)} K_{II}^2 \\ G_{II} &= J_{II} = C_1^{(II)} K_I^2 + C_2^{(II)} K_I K_{II} + C_3^{(II)} K_{II}^2 \end{aligned} \quad (3.73)$$

Despite the coefficients of mixture $C_2^{(I)}$, $C_3^{(I)}$, $C_1^{(II)}$ and $C_2^{(II)}$ are present in the analytical formulation of the J-integrals J_I and J_{II} , authors have shown numerically that these coefficients are nine orders of magnitude smaller than the coefficients $C_1^{(I)}$ of the pure *mode I* for J_I and $C_3^{(II)}$ pure *mode II* for J_{II} . Associating an energy release to each fracture mode is then possible. The fact that G_I , G_{II} and G_{III} can be defined without mixing fracture modes for the isotropic case and for orientations $\succ_{[100]}^{(010)}$ and $\succ_{[001]}^{(110)}$ explains why the plastic flow directions in the diagram $G_I - G_{II} - G_{III}$ do not exhibit any mixture when loaded in planes $I - II$ and $I - III$ in figures 3.35, 3.36 and 3.37. The choice of the conventional G_i as a dual variable to $\dot{\rho}_i$ is adequate and the normality rule is accurate for these cases.

For other orientations $\succ_{[111]}^{(110)}$ and $\succ_{[3\bar{1}\bar{1}]}^{(121)}$, the “wavy” behavior observed along the borders of the loading path on figures 3.38 and 3.39 is in concordance with the twisted octahedron shape found analytically in the diagram of energy release rates (equation 3.67 and figure 3.31). However, we recall that, in this work, the building of the model is monitored by the kinematics. Thus, the choice of variables of the thermodynamic framework is monitored by the kinematics as well. Therefore, it is important to chose a dual variable for $\dot{\rho}_i$ that is responsible only for the plastic flow in direction i .

These observations indicate that variables G_i are not a convenient choice for crystallographic orientations that are not seen as orthotropic anisotropy by the crack. A good choice of dual variables \tilde{G}_i taking into account the mixture of fracture modes can exhibit a good flow rule and a regular convex shape of the yield domain in the diagram of these new variables. Since the final aim of this thesis is to work with a crystal plasticity model, this approach was not pursued in this work, it can be discussed in a further work.

• Discussion about the distortion of the yield domain

The motion of the center of the macroscopic yield domain is already taken into account in the model via the back-stress variable (kinematic hardening), the growing of this domain is less apparent since the used isotropic hardening is not important (see table 3.1). However, the distortion of the yield surface under nonproportional loadings is not taken into account. Therefore, the assumption that the yield domain will preserve its shape and

fixed size is not always valid regarding the yielding effects and the over-hardening induced by nonproportional loadings.

In fact, many works ([Abdul-Latif et al., 1994], [Aubin, 2001],[Aubin et al., 2002], etc.) had shown that, the over-hardening is not directly and only correlated to isotropic hardening as it was commonly known. Therefore, even though the isotropic hardening is not important in the used behavior law in this work, the over-hardening may occur in relation with the kinematic component of the hardening. The distortion of the yield locus can be modeled by taking into account the over-hardening [Benallal and Marquis, 1987], [Calloch, 1997], [Tanaka, 1994], [Abdul-Latif et al., 1994].

3.5.3 FE simulation: Ramified exploration

Previous analyses gave an idea about plastic flow directions. Another main ingredient of the model is the evolution of the elastic domain of a representative section of the crack front. In an analogy with the kinematic hardening in an elastic-plastic behavior, a variable $\underline{K}^X = (K_I^X, K_{II}^X, K_{III}^X)$ can be assigned to the position of the center of the elastic domain. Moreover, in an analogy with an isotropic hardening, the size of this domain can be described using $\underline{K}^R = (K_I^R, K_{II}^R, K_{III}^R)$.

Note: In fact, as long as the loading point is inside the elastic domain, no blunting occurs at the crack tip region. Besides, the crack growth rate is proportional to the blunting rate. Therefore, the crack will not grow as long as the effective amplitude of the stress intensity factor is below the size of the elastic domain. In other words, defining the size of an elastic domain is equivalent to introducing into the model an intrinsic parameter that defines the nonpropagation threshold ΔK_{th}^{int} [Ruiz-Sabariego and Pommier, 2009]. As a consequence, the size of the elastic domain is crucial and needs to be integrated in the incremental plasticity model of the region near the crack tip.

The size of the yield domain and the position of its center can be obtained based on a set of finite element simulations by exploring the $K_I^\infty - K_{II}^\infty - K_{III}^\infty$ space. A strategy to assess these quantities is discussed in this section.

Loading path

As shown in the previous part, the ellipsoidal loading did ensure the yielding of the crack tip region without drastically deforming it. The last time increment of the ellipsoidal loading corresponds to zero nominal stress intensity factors: $\underline{K}^\infty = \underline{0}$. Starting from this last increment, different simulations were performed by loading with different mixture ratios in the $K_I^\infty - K_{II}^\infty - K_{III}^\infty$ space. Simulations are independent and as shown in figure 3.40, each branch of the ramified loading corresponds to an elastic-plastic simulation.

Note: Each simulation of this exploration has, as an initial condition, the state of fields at the last time increment of the previous ellipsoidal simulation. In fact, an assumption is made that the previous simulation had already caused the motion of the yield domain toward a positive value of K_I^∞ . Thus, it became possible to explore the full yield domain without being opposed to the crack closure when exploring in different directions.

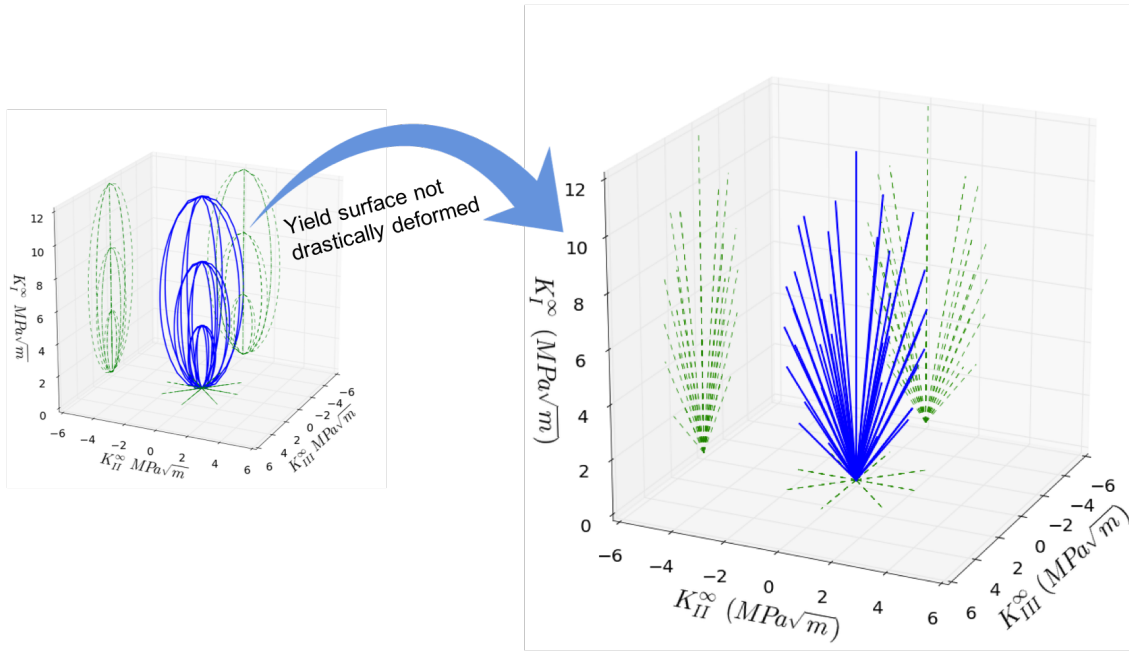


Figure 3.40: From an ellipsoid to a ramified exploration path in the $K_I^\infty - K_{II}^\infty - K_{III}^\infty$ diagram.

3.5.4 Plastic flow directions

On each loading branch, these criteria were computed based on the kinematic basis of the corresponding crystallographic orientation. A threshold value was assigned to each one of these yielding indicators. An assumption is made that the crack tip region starts to yield when the computed indicator reaches this threshold value. Different yield criteria previously discussed in subsection 3.4.4 were used to assess the borders of the yield domain. Figure 3.41 shows the results of the ramified loading in the plane $K_I^\infty - K_{II}^\infty$ and the plastic flow directions for the isotropic case. The results of the different criteria are quite close to each others. They are all showing a good agreement with the elliptical shape of the yield domain predicted by the extended Von-Mises criterion for the region near the crack tip.

For the following study, the equivalent blunting intensity factor ρ_{eq} presented in equation 3.58 was chosen as a criterion for yielding. Figures 3.42, 3.43 and 3.44 show the obtained yield domains for the isotropic case and for material orientations $\gamma_{[100]}^{(010)}$ and $\gamma_{[001]}^{(110)}$ respectively. Plots (a) and (b) present the yield surfaces computed in the $K_I^\infty - K_{II}^\infty$ and the $K_I^\infty - K_{III}^\infty$ planes respectively.

It is obvious, from the obtained results, that the shape of the yield domain did not experience a drastic distortion caused by the initial ellipsoidal loading. Plastic flow directions are determined at every time increment through the vector $\hat{\rho}$. The normality flow rule seems to be respected for these studied cases and plastic flow directions are not perturbed by the loading history. Based on the fitted ellipse, the size and the center of the yield domain can be determined. The center is shown on the graphs as the pentagon symbol.

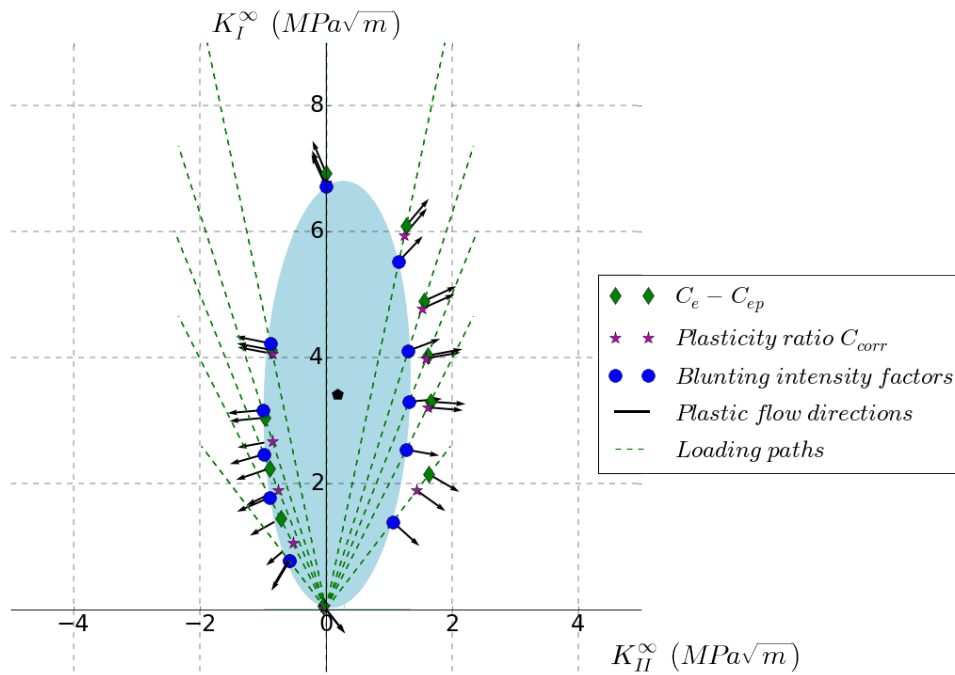


Figure 3.41: A section of ramified loading path in the $K_I^\infty - K_{II}^\infty$ plane, the yield surface is given by three different yielding estimators.

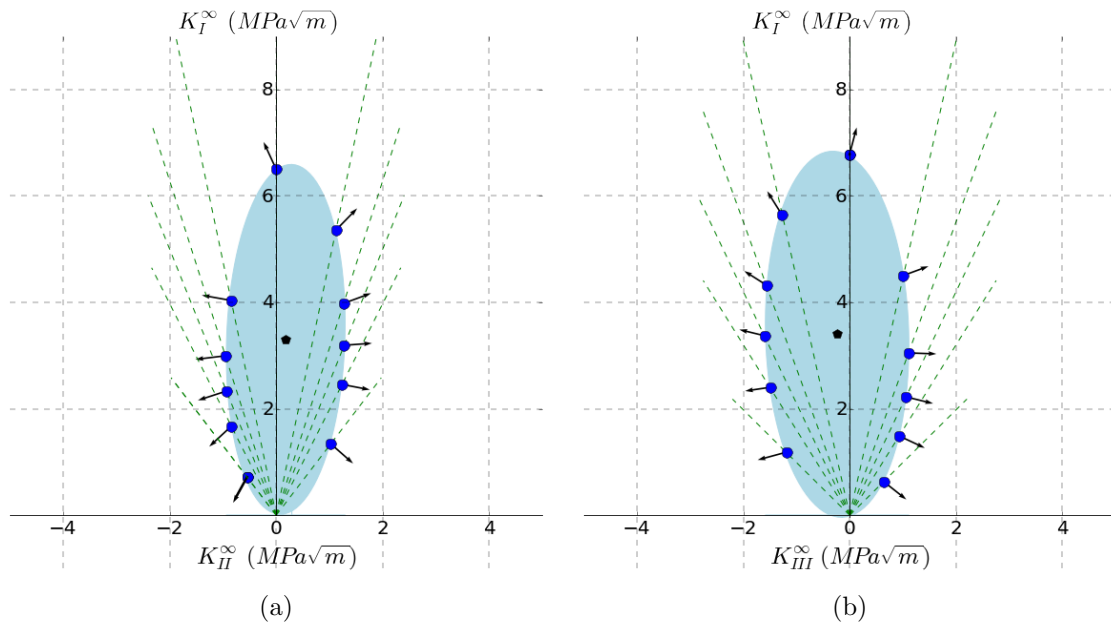


Figure 3.42: Yield locus in (a) the $K_I^\infty - K_{II}^\infty$ and (b) the $K_I^\infty - K_{III}^\infty$ diagrams for a ramified exploration and after an ellipsoidal exploration for the isotropic case.

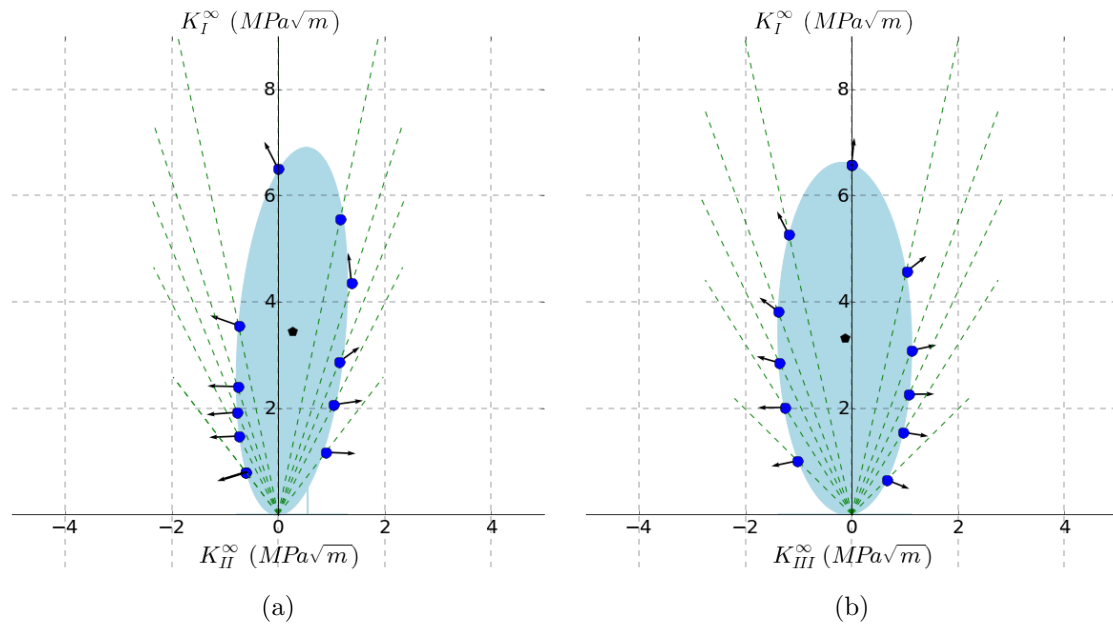


Figure 3.43: Yield locus in (a) the $K_I^\infty - K_{II}^\infty$ and (b) the $K_I^\infty - K_{III}^\infty$ diagrams for a ramified exploration and after an ellipsoidal exploration for orientation $\gamma_{[100]}^{(010)}$.

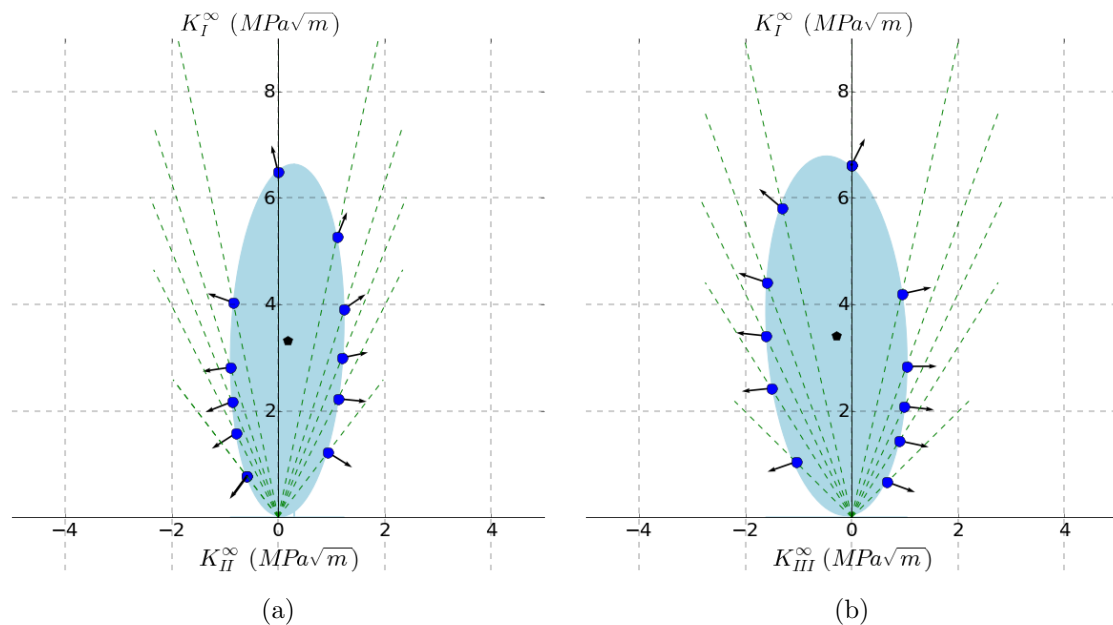


Figure 3.44: Yield locus in (a) the $K_I^\infty - K_{II}^\infty$ and (b) the $K_I^\infty - K_{III}^\infty$ diagrams for a ramified exploration and after an ellipsoidal exploration for orientation $\gamma_{[001]}^{(110)}$.

A more refined quantitative analysis for each material orientation and under different loading cases permits the study of the evolution of the center and the size of the yield domain as function of the blunting of the crack tip. An empirical evolution equation can be assigned to each variable.

These equations, obtained numerically for a stationary crack problem, can be incorporated in the reduced model as the evolution laws of the internal variables $\partial V_{int}/\partial \rho$. In an advanced study, the crack can be “grown” numerically without allowing the plastic strain. Thus, it become possible to assess the evolution equations of internal variables with respect to the crack length $\partial V_{int}/\partial a$. Finally, an evolution equation can be determined independently for each internal variable, due to plasticity and due to crack propagation under different crystallographic orientations with respect to the crack plane and front.

3.6 Conclusion

The confinement of the plastic zone in a K-dominance elastic bulk creates a high dependency between the evolution of plasticity near the crack tip region and the elastic anisotropy, i.e. the crystal orientation with respect to the crack.

The elastic and plastic reference fields are determined for different crystallographic orientations with respect to the crack plane and direction. The elastic basis obtained using the Proper Orthogonal Decomposition shows good agreement with Hoenig’s elastic solutions for all cases of material orientations presented in this work.

These frameworks helped reducing the number of degrees of freedom of the problem as the crack tip plasticity is reduced to a set of nonlocal variables. The loading applied on the crack is described using the stress intensity factors of the three fracture modes $K_I^\infty, K_{II}^\infty, K_{III}^\infty$ whereas the blunting of the crack tip region is described using the blunting intensity factors $\dot{\rho}_I, \dot{\rho}_{II}, \dot{\rho}_{III}$.

An extended Von-Mises criterion for the region near the crack tip is determined based on Hoenig’s elastic solutions. A nonlocal yield criterion of this region can be written. A qualitative study of the plastic flow directions is performed under different crystallographic orientations based on the kinematic basis already presented. The study showed the sensitivity of the reduced plasticity model to the crystallographic orientation with respect to the crack.

A strategy to assess internal variables of the model based on the kinematic bases is presented as well. The evolution laws of these variables are crucial in the modeling of cyclic plasticity. They describe the existence of material hardening, internal stresses and other effects of the nonlinear behavior of the material that can be seen as history effects.

However, this first analysis shows that the formulation of the model, and in particular the suitable choice of the thermodynamics driving force associated with $\dot{\rho}_i(t)$, remains difficult, in particular when the crack plane and front do not coincide with one of the symmetry planes of the elastic anisotropy law.

Reduced basis of a crystal plasticity model

In this chapter, the three-dimensional problem of a crack under mixed fracture modes $I + II + III$ is studied with a material behavior described by a cubic elasticity and a crystal plasticity model. This model urged the study to explore some new strategies in the partition of kinematic fields and in the model reduction procedure. Moreover, the yield domain of the near crack tip region is explored numerically. Finally, a procedure was proposed to transpose the local model of crystal plasticity to the scale of the crack tip region.

4.1 State of the art

Computations tools nowadays are well developed which allows the study of complex three-dimensional cracks and the evaluation of LEM quantities under a linear elastic behavior. These tools vary from the XFEM [Belytschko and Black, 1999] [Moës et al., 1999] [Moës et al., 2002] to the Hybrid analytical/XFEM method [Réthoré et al., 2010] or the Thick Level Set method coupled with XFEM [Moës et al., 2011] [Bernard et al., 2012], etc. However, finite element simulations of fatigue growth of three-dimensional cracks under nonproportional mixed fracture modes with a nonlinear behavior are still not reachable with the available resources. Within this context, this work deals with the modeling of fatigue crack propagation with the assumption that crack tip plasticity is the main mechanism at the origin of crack growth. The plasticity is finally modeled with a reduced number of degrees of freedom which allows its integration in an incremental crack propagation approach.

High pressure turbine blades can be made out of polycrystalline materials, directionally solidified or single crystal superalloys which will influence a lot the mechanical behavior and consequently the model used to design and validate such component. In this work, we are interested in the study of Nickel base single crystals as a first step to develop a model reduction strategy for crack propagation in anisotropic materials. Further work is needed to predict the growth plane and to integrate the approach in linear elastic FE codes. This strategy could be extended in the future so that it can be applied to the case of composite and polycrystalline materials.

4.1.1 Material and microstructure

Due to its mechanical properties, the element Nickel had shown its efficiency as a base material for superalloys used at high temperatures especially for high pressure turbine blades. The micro-structure of Nickel base superalloys consists of two phases, a γ austenitic matrix and cubic γ' precipitates Ni_3Al . These two phases have both a FCC lattice structure. A misfit in lattice parameter between these two phases creates a local coherence stress. This small misfit is accommodated by the elastic straining between lattices of different phases. The elastic coherence strains give the material a higher strength. For plasticity mechanism, the γ' precipitates are an obstacle for dislocations which concentrate their motion in the γ matrix channel. Thus, these precipitates have a strengthening effect that results in a structural hardening of nickel base superalloys.

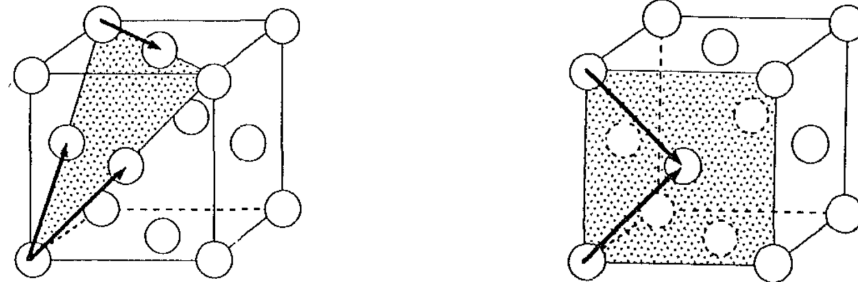
Materials with FCC structure contain 4 densely packed octahedral planes $\{111\}$ with 3 closely packed directions $\langle 110 \rangle$ on each plane and 3 less dense cube planes $\{001\}$ with 2 dense directions by plane $\langle 011 \rangle$. The combination of these easy slip directions constitute the 12 octahedral and 6 cubic slip systems of a Face Centered Cubic FCC lattice structure (see Table 4.1 and Figure 4.1).

Bettge [Bettge and Österle, 1999] made tensile tests on single crystal nickel base superalloy with specimens orientations near the direction $[111]$. Despite this direction is the most favorable to activate cube slip systems since their Schmid factors are higher than the octahedral ones, results showed that cube slip systems are activated as a result of the interaction of a vast amount of octahedral ones. Besides, due to their high planar density, octahedral slip systems have a favorable energy to be activated compared to the activation energy of cubic slip systems. Considering the aforementioned observations, we only

consider in the following work the activation of octahedral slip systems, the activation of the cubic ones is not taken into account.

The crack initiation and propagation mechanisms are dominated by the localization of plastic strain in slip bands. Besides, under fatigue loading, the emergence of slip bands induces extrusions and/or intrusions on the material surface. This phenomenon is a consequence of the localization of plastic deformation [Suresh, 1998] [Risbet and Feaugas, 2008] and [Vilchaise et al., 2002]. These surface roughness sites develop a notch-peak geometry which favor the initiation of fatigue cracks [Risbet et al., 2018].

On the one hand, development of cracks in a stable crack growth regime is mainly plasticity-induced. On the other hand, the presence of specific slip systems that constitute privileged planes and directions for dislocation movement induces a sort of plastic anisotropy. Thereby, it is important to take into account this anisotropy in the study of crack propagation in FCC single crystals.



Slip systems $1/2 \langle 011 \rangle \{111\}$.

(a) One octahedral slip plane with the three possible slip directions.

Slip systems $1/2 \langle 011 \rangle \{001\}$.

(b) One cubic slip plane with the two possible slip directions.

Figure 4.1: Slip systems in an FCC single crystal (figure from [Méric et al., 1991]).

4.1.2 The Schmid law

In 1924, Schmid introduced the concept of the resolved shear stress τ^s as the projection of the stress tensor on a given slip system. He suggested that dislocation motion and hence the plastic strain occurs on a given slip system when the corresponding resolved shear stress reaches a critical value known as the critical resolved shear stress (CRSS or τ_c). This intrinsic parameter of the material takes into account the barriers that can oppose to the dislocation motion along slip systems and the ability to overcome these barriers.

Table 4.1: Slip systems in an FCC crystal.

Slip system family	Slip system number	[Schmid and Boas, 1935] notation	Slip plane n^s	Slip direction l^s
Octahedral	1	B4	(111)	$[\bar{1}01]$
	2	B2		$[0\bar{1}1]$
	3	B5		$[\bar{1}10]$
	4	D4	$(1\bar{1}1)$	$[10\bar{1}]$
	5	D1		$[01\bar{1}]$
	6	D6		$[\bar{1}10]$
	7	A2	$(\bar{1}11)$	$[0\bar{1}1]$
	8	A6		$[\bar{1}10]$
	9	A3		$[\bar{1}01]$
	10	C5	$(11\bar{1})$	$[\bar{1}10]$
	11	C3		$[\bar{1}01]$
	12	C1		$[0\bar{1}1]$
Cubic	13	E5	(001)	$[\bar{1}10]$
	14	E6		$[\bar{1}10]$
	15	F1	(100)	$[0\bar{1}1]$
	16	F2		$[0\bar{1}1]$
	17	G4	(010)	$[\bar{1}01]$
	18	G3		$[\bar{1}01]$

4.1.3 Models

Considering its importance in the manufacturing of high pressure turbine blades, single crystals were the subject of many studies. Researchers have proposed many models in an attempt to describe the physical phenomena and their interactions on different scales. Models, present today to reproduce the cyclic behavior of nickel base single crystals, can be categorized on three main approaches:

- Crystallographic micromechanical models developed at the scale of the slip system and based on internal variables that describe explicitly the mechanism of deformation at the level of dislocations. This type of models may introduce dislocation density as an interest quantity characterizing explicitly the irreversible mechanical behavior of crystals. Added to dislocation density, Fedelich used the length of matrix channels to model rafting [Fedelich, 1999], [Fedelich, 2002]. These variables give the model a quasi-physical aspect that can enhance its predictive character once the model is implemented in a simulation code.

- A phenomenological approach at the macroscopic scale based on the theory of invariants. The anisotropy is taken into account by a simple modification of the Von Mises criterion, for instance, a quadratic Hill criterion can be considered in the case of cubic symmetry [Nouailhas, 1990], [Nouailhas and Culié, 1991]. However, this approach is not efficient enough to describe material behavior for single crystal with a cubic symmetry under complex tensile-torsion loadings or internal pressure [Bonnand, 2006].

- A phenomenological crystallographic approach where constitutive equations, usually

found in macroscopic models, are developed starting from the microscopic scale of slip systems. This model uses internal variables that have no direct and explicit physical signification. Nevertheless, the evolution of internal variables can be linked to dislocation density.

For the case of a single crystal, this type of models is built over two levels of heterogeneity following three distinct steps. A first step relying the macroscopic scale to the scale of slip systems through a projection process. It consists in determining the resolved shear stress on each slip system s from the stress tensor. Then, applying the behavior law to obtain the slip rate always on the scale of the slip system. The third step is the weighted sum of slip rates of different slip systems to obtain finally the macroscopic visco-plastic strain rate (see figure 4.2).

The difference between models that follow this approach lays in the choice of the hardening in the behavior law step. In this chapter, the small strain formulation of the Méric & Cailletaud model [Méric et al., 1991], [Méric and Cailletaud, 1991] was exclusively used.

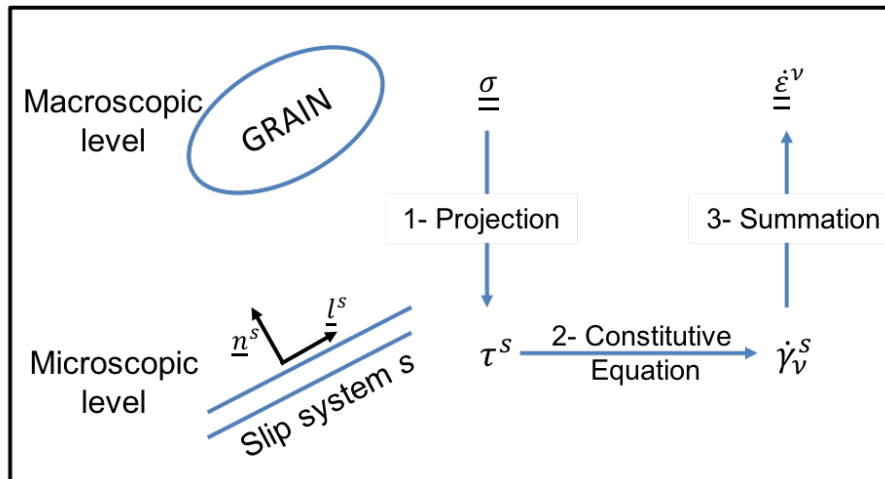


Figure 4.2: Different steps and levels of the model [Méric et al., 1991].

4.2 Material model and finite element computational tools

4.2.1 Crystallographic phenomenological model

The model, proposed by Méric and Cailletaud and validated by many studies on different alloys [Méric et al., 1991], is already implemented in material subroutines. Besides the coefficients of this model for the AM1 single crystal superalloy are already identified and discussed in literature. Therefore, this model seems to be a convenient choice to be used as a starting point to model the anisotropic plastic behavior near the crack tip region. Other models can be used while the strategy to reduce the crack tip region behavior to a condensed plasticity model will remain the same.

This model is characterized by unified internal variables with multiple criteria defined per slip system. Two internal variables are introduced to account for the hardening effect stemming from the interactions between dislocations at the scale of slip systems. The

model describes implicitly these interactions by using a backstress and a threshold stress for each slip system.

Hypotheses

This model assumes that the deformation process is mainly caused by the crystallographic dislocation slip. Other phenomena such as twinning and diffusion are not taken into account. The model is developed in the framework of anisothermal and infinitesimal thermodynamic transformations. The used state variables are the elastic strain, the kinematic and the isotropic hardening variables. In this work, we only take into account the 12 octahedral slip systems $\{111\}\langle 110\rangle$.

Formulation of the model

For the projection step, the resolved shear stress experienced by a slip system is obtained by the projection of the macroscopic stress on the generalized Schmid factor of this slip system:

$$\tau^s(r, \theta) = \underline{\underline{m}}^s : \underline{\underline{\sigma}}(r, \theta) \quad (4.1)$$

with:

$$\underline{\underline{m}}^s = \frac{1}{2}(\underline{\underline{l}}^s \otimes \underline{\underline{n}}^s + \underline{\underline{n}}^s \otimes \underline{\underline{l}}^s) \quad (4.2)$$

The total strain is decomposed into an elastic part and a plastic one:

$$\underline{\underline{\varepsilon}} = \underline{\underline{\varepsilon}}^e + \underline{\underline{\varepsilon}}^p \quad (4.3)$$

Regarding the FCC lattice structure of the single crystal, cubic anisotropy is used to model elasticity. The stiffness tensor C_{ijkl} is then characterized by three elastic parameters at a given temperature. The linear elastic behavior of the single crystal is modeled as follows:

$$\underline{\underline{\sigma}} = \underline{\underline{\mathbb{C}}} : \underline{\underline{\varepsilon}}^e \quad (4.4)$$

The Voigt notation is used:

$$\underline{\underline{\sigma}} = \begin{pmatrix} \sigma_{11} \\ \sigma_{22} \\ \sigma_{33} \\ \sigma_{23} \\ \sigma_{13} \\ \sigma_{12} \end{pmatrix} \quad \underline{\underline{\varepsilon}} = \begin{pmatrix} \varepsilon_{11} \\ \varepsilon_{22} \\ \varepsilon_{33} \\ 2\varepsilon_{23} \\ 2\varepsilon_{13} \\ 2\varepsilon_{12} \end{pmatrix} \quad \underline{\underline{\mathbb{C}}} = \begin{pmatrix} C_{11} & C_{12} & C_{12} & 0 & 0 & 0 \\ C_{12} & C_{11} & C_{12} & 0 & 0 & 0 \\ C_{12} & C_{12} & C_{11} & 0 & 0 & 0 \\ 0 & 0 & 0 & C_{44} & 0 & 0 \\ 0 & 0 & 0 & 0 & C_{44} & 0 \\ 0 & 0 & 0 & 0 & 0 & C_{44} \end{pmatrix} \quad (4.5)$$

Viscoplastic constitutive equations are written on each slip system. To formulate these equations, the following state variables are used:

- A vector of backstresses $\{x^s, s = 1..N\}$ characterizing the displacement of the elastic domain for each slip system, and associated with their counterparts, the vector $\{\alpha^s, s = 1..N\}$ used as kinematics hardening internal variables in the model (see Figure 4.3).
- A vector of plastic slip threshold stresses $\{r^s, s = 1..N\}$ associated with their counterparts $\{q^s, s = 1..N\}$ used as internal variables in the model (see Figure 4.3).

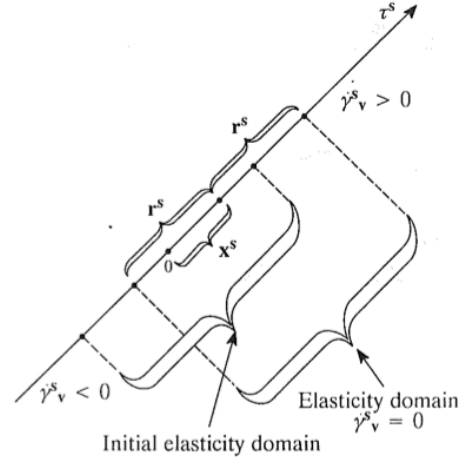


Figure 4.3: Illustration of the local elasticity domain of a given slip system [Méric et al., 1991].

The plastic strain is the result of the activation of one or multiple slip systems. Since we only consider in this work octahedral slip systems, we obtain:

$$\underline{\underline{\dot{\epsilon}^p}} = \sum_{s=1}^{12} \underline{\underline{m}}^s \dot{\gamma}_{oct}^s \quad (4.6)$$

where $\dot{\gamma}_{oct}^s$ is the slip rate of the octahedral slip systems s .

The flow rule is written based on a classical macroscopic Norton law with a threshold.

$$\dot{\gamma}^s = \left\langle \frac{|\tau^s - x^s| - r^s}{k} \right\rangle^n \text{sign}(\tau^s - x^s) \quad (4.7)$$

$\langle x \rangle$ takes only the positive part of x

Dislocation density is known to saturate upon continued plastic yielding for many crystalline materials. This saturation modeling is achieved in the case of single crystals by the use of a non linear threshold stress, Méric and Cailletaud presented it as follows:

$$r^s = r_0 + Q \sum_r H^{rs} (1 - e^{b\nu^r}) \quad (4.8)$$

where ν^r the cumulative slip defined by $\dot{\nu}^r = |\dot{\gamma}^r|$, Q and b characterize respectively the asymptotic stabilized value and the rapidity of this stabilization. r_0 is the initial plastic slip threshold of the octahedral slip system family. The term $(1 - e^{b\nu^r})$ represents the exponential saturation of dislocation density. H^{rs} is the “interaction matrix” between different slip systems. In fact, the plastic slip on a given slip system induces hardening on this slip system (self-hardening), but it can also promote hardening on other slip system

(latent hardening). For the case of AM1 Nickel base superalloy, many authors have shown that the phenomenon of self-hardening is so pronounced that the latent hardening caused by this interaction can be neglected [Méric et al., 1991], [Méric and Cailletaud, 1991], [Hanriot, 1993], [Nouailhas and Cailletaud, 1995]. The interaction matrix is then taken equal to the identity.

The evolution law of the kinematic hardening term is non linear. Its aim is essentially to represent the cyclic behavior of the single crystal by describing the displacement of the center of the yield surface.

$$x^s = c\alpha^s \quad , \quad \dot{\alpha}^s = \dot{\gamma}^s - d \dot{\nu}^s \alpha^s \quad (4.9)$$

where c and d are material parameters that may depend on temperature, they are calibrated by experimental studies. The recall term $d \dot{\nu}^s \alpha^s$ provides a fading memory effect of the deformation path. The integration of equation 4.9 for a symmetrical isothermal fatigue loading gives:

$$x^s = \pm \frac{c}{d} (1 - e^{\pm d \gamma^s}) \quad (4.10)$$

The plasticity yield criterion is finally written for a given slip system r :

$$f^r = |\tau^r - x^r| - r^r \quad (4.11)$$

4.2.2 Numerical model

The geometry used for simulations in this chapter is the same used in the previous one; a 3D thin plate model (2 m × 2 m) with a 20 mm through thickness crack (see figure 4.4). A periodic boundary condition was imposed on two parallel faces of the FE model to ensure the plane strain condition.

The displacement of the crack front line was blocked in the plane $z = 0$. The four corners of the model were tied to four discrete rigid bodies. In-plane and out-of-plane forces were applied on the reference points of these rigid bodies in order to obtain different stress states at the crack tip region.

The interest region near the crack tip is the middle section of a disc with a hole. The inner radius is big enough to exclude all singularities at the vicinity of the crack tip ($r_{min} = 30 \mu\text{m}$) and the outer radius is small enough to remain into the Irwin plastic zone ($r_{max} = 250 \mu\text{m}$).

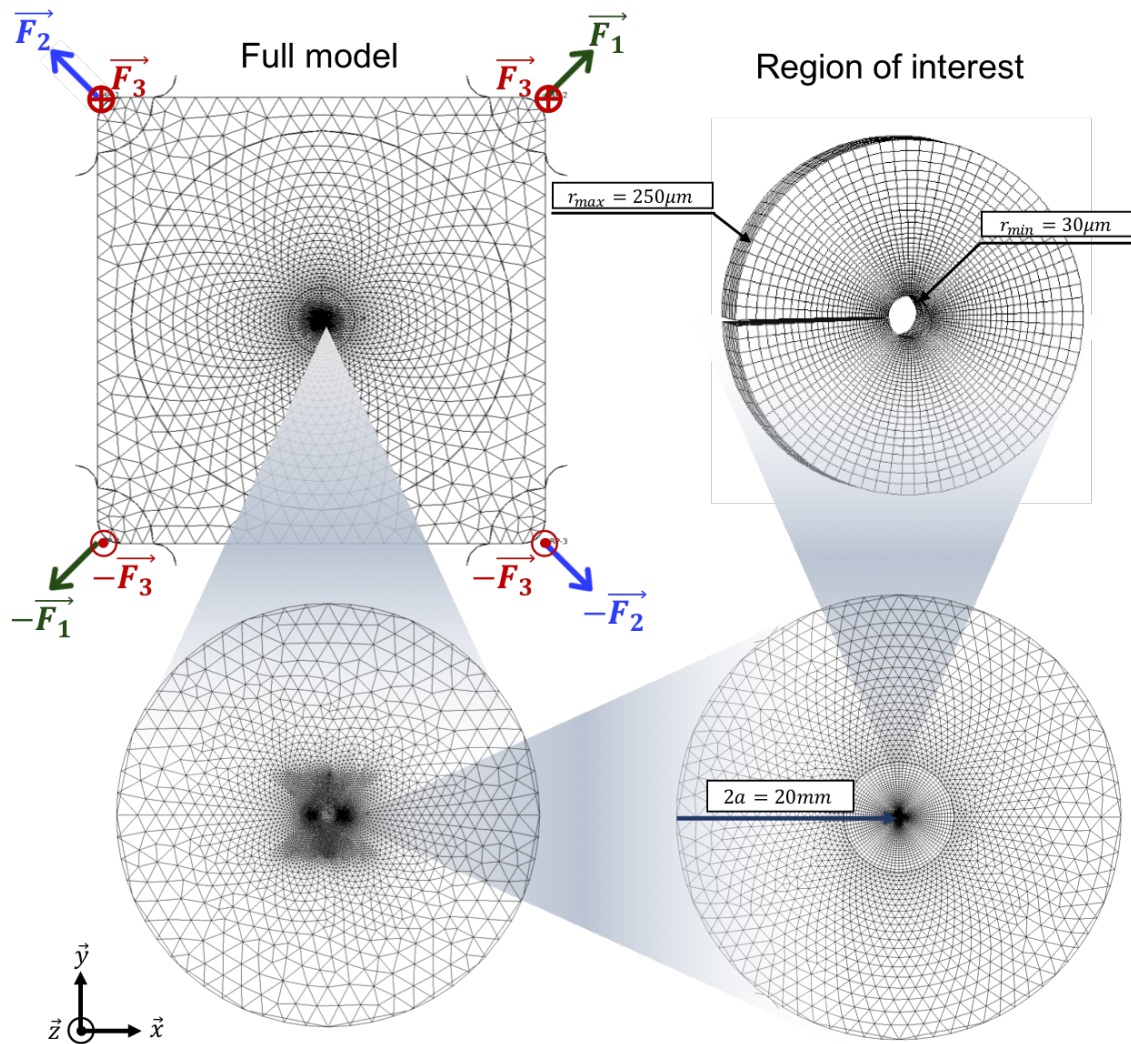


Figure 4.4: Full geometry of the finite element model and a zoom on the region of interest surrounding the crack tip.

4.2.3 Cubic elasticity and crystal plasticity

For both elasticity and plasticity, we used material parameters of the AM1 at 20 °C presented in the work of [Hanriot, 1993]. These parameters were identified on AM1 single crystals for different orientations. Hanriot performed tensile tests at different rates (from 10^{-5} s to 10^{-3} s) and cyclic hardening tests.

Cubic elasticity is described by the three stiffness constants presented in table 4.2. Typically, these material parameters are measured for single crystals along the orientation [001].

Table 4.2: Coefficients of the cubic elasticity of the AM1 at 20 °C [Hanriot, 1993].

C_{11} (GPa)	C_{12} (GPa)	C_{44} (GPa)
296	204	125

The ratio $(C_{11} - C_{12})/(2C_{44})$ is used to characterize the intensity of the anisotropy of cubic crystals. A value of one is found for an isotropic behavior. The anisotropy ratio of the AM1 alloy at 20 °C is equal to 0.368, indicating a pronounced elastic anisotropy. For copper, which has also a pronounced elastic anisotropy, this ratio is equal to 0.337 and for aluminum, which is nearly isotropic, this ratio is equal to 0.81.

A set of crystallographic orientations of the crystal lattice with respect to the crack coordinates was explored in this chapter. Figure 4.5 shows the orientations initially studied.

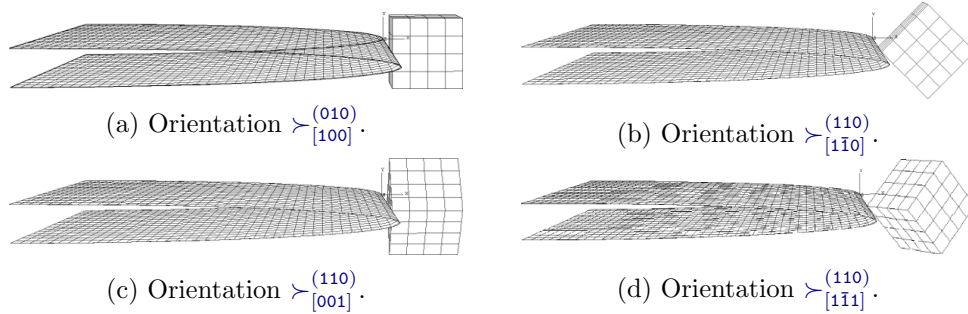


Figure 4.5: Illustrations of the crystallographic orientations with respect to the crack coordinate system.

For the inelastic part of the model, parameters are presented in the table 4.3. For the sake of simplicity, the coefficient Q was taken equal to 0 (see [Hanriot, 1993]).

Table 4.3: Parameters of the hardening model corresponding to octahedral slip systems of the AM1 at 20 °C [Hanriot, 1993].

Isotropic hardening		Kinematic hardening		Viscosity		
r_0 (MPa)	Q (MPa)	b	c (MPa)	d	k (MPa s $^{\frac{1}{n}}$)	n
245	0	0	73400	3270	90	15

4.2.4 Z-mat (Integration method, material orientation and stress intensity factors (SIF) determination)

ABAQUS/Standard (implicit) solver was used for finite element simulations. The aforementioned crystal plasticity model is not supported by the *ABAQUS* predefined material library, therefore, *Z-mat* subroutine was used to define the behavior law. This user defined “extension set” was initially developed by “Centre des Matériaux de l’Ecole des Mines de Paris”, the “ONERA” and “Northwest Numerics”. This material simulation program is natively implemented in Z-set, but it can be interfaced with other finite element codes. In our case, we used it as an extension set to the *ABAQUS/Standard* finite element software.

The high stress concentration near the crack tip is susceptible to create zero energy modes that may lead to massive “Hourglassing”. To avoid this kind of problems, eight-node brick elements with linear interpolation and full integration were used in this region.

To integrate the material response law, an implicit generalized integration method known as “ θ -Integration” method was used. It’s an Euler method with a parameter θ between 0 and 1:

$$x(t + \Delta t) - x(t) = \dot{x}(t + \theta\Delta t)\Delta t \quad (4.12)$$

With this integration scheme, internal variable x is initially evaluated at a time $t_\theta = t + \theta\Delta t$ in between the time increment size. The parameter θ was taken equal to 0.5 to get an optimized convergence rate.

Stress intensity factors

As mentioned in the previous chapter, the stress intensity factors can be determined directly using the interaction integral method (see Appendix B) already implemented in *ABAQUS*. However, the use of *Z-mat* subroutine prevented *ABAQUS* from accessing to material parameters and assessing the interaction integral.

To overcome this technical issue, a routine was added in order to determine stress intensity factors based on the displacement extrapolation [Banks-Sills et al., 2005], [Banks-Sills et al., 2007]. The displacement discontinuity vector that derives from the Hoenig’s asymptotic solutions is written as follows:

$$\Delta u_i = \sqrt{\frac{2r}{\pi}} \sum_{j=1}^3 \Delta g_i^j K_j^\infty \quad (4.13)$$

which can be written as:

$$\underline{\Delta u} = \sqrt{\frac{2r}{\pi}} \underline{\underline{G}} \cdot \underline{\underline{K}}^\infty \quad (4.14)$$

with

$$\underline{\underline{G}} = \begin{pmatrix} \Delta g_x^I & \Delta g_x^{II} & \Delta g_x^{III} \\ \Delta g_y^I & \Delta g_y^{II} & \Delta g_y^{III} \\ \Delta g_z^I & \Delta g_z^{II} & \Delta g_z^{III} \end{pmatrix} \quad \underline{\underline{K}}^\infty = \begin{pmatrix} K_I^\infty \\ K_{II}^\infty \\ K_{III}^\infty \end{pmatrix} \quad (4.15)$$

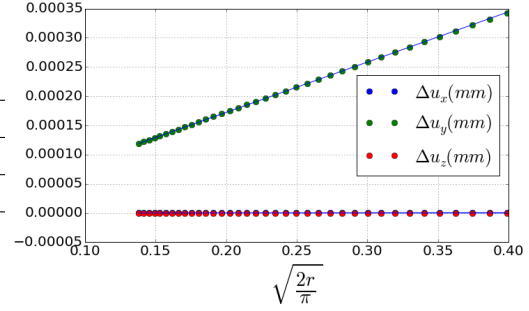
and

$$\Delta g_i^j = g_i^j(\pi) - g_i^j(-\pi) \quad (4.16)$$

The displacement discontinuity vector between both crack faces $\underline{\Delta u}$ was extracted from a linear elastic computation with a material behavior defined by a *Z-mat* subroutine. These fields were then post-processed using equation 4.13. Figure 4.6 show the linear evolutions of this displacement discontinuity vector components as function of $\sqrt{\frac{2r}{\pi}}$ for crystallographic orientation $\succ_{[100]}^{(010)}$. Let \underline{A} be the vector composed of the three slopes of these evolutions (a_x, a_y, a_z). Nominal stress intensity factors are then computed as follows:

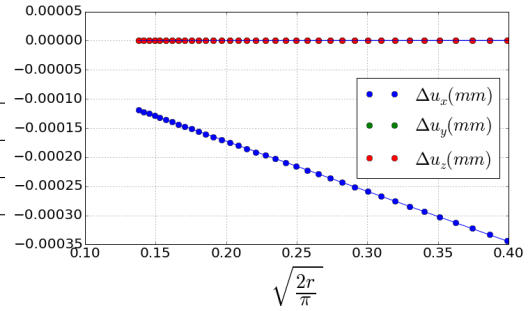
$$\underline{K}^\infty = \underline{G}^{-1} \cdot \underline{A} \quad (4.17)$$

	Interaction integral (MPa \sqrt{m})	Displacement extrapolation (MPa \sqrt{m})
K_I^∞	1	1.00176
K_{II}^∞	0	0.00179
K_{III}^∞	0	-0.0001



(a) mode I of the orientation $\succ_{[100]}^{(010)}$.

	Interaction integral (MPa \sqrt{m})	Displacement extrapolation (MPa \sqrt{m})
K_I^∞	0	0.0001
K_{II}^∞	1	1.00313
K_{III}^∞	0	0.001



(b) mode II of the orientation $\succ_{[100]}^{(010)}$.

Figure 4.6: The table on the left gives nominal stress intensity factors computed using both the interaction integral and the displacement extrapolation methods from a *Z-mat* based computation, the plot on the right gives the evolution of displacement discontinuity components along the crack faces.

The loading to apply is calibrated with the stress intensity factors computed using the interaction integral contour. As shown on tables of figure 4.6, results show a good agreement between the expected values of stress intensity factors and the computed values using the displacement extrapolation technique. The control of loading using stress intensity factors is then ensured.

4.3 Kinematic basis

The general aim of this work is to find a global description of plastic flow nearby the crack front, when confined plasticity conditions are met. The final reduced model of the confined plasticity is based on intensity factors, used as nonlocal quantities, and a basis of reference kinematic fields. As mentioned in previous parts of this work, the main step in this model reduction strategy is to find a suitable kinematic basis.

Following the standard methodology, and based on the self-similarity and small strain hypotheses, kinematic fields extracted from the region near the crack tip are decomposed into a linear elastic part, and a nonlinear complementary part [Pommier et al., 2009], [Decreuse, 2010], [Frémy, 2012].

$$\underline{v}^{FE}(\underline{x}, t) \approx \sum_{i=1}^3 \dot{K}_i(t) \underline{\phi}_i^{el}(\underline{x}) + \sum_{i=1}^3 \dot{\rho}_i(t) \underline{\phi}_i^{pl}(\underline{x}) \quad (4.18)$$

The scale transition process consists in describing confined plasticity near the crack tip region using nonlocal time-dependent quantities $K_i^\infty(t)$ and $\rho_i(t)$ and getting rid of spatial distributions. As a matter of fact, in confined plasticity conditions, under infinitesimal strain conditions and for a locally self-similar geometry, those spatial distributions are constrained and can be defined once for all. The intensity factors hence represent the only degrees of freedom for the problem. They are obtained by projecting elastic-plastic kinematic field on the reference elastic and plastic bases. For a given point P in the region near the crack tip, these quantities are defined as follows:

$$\dot{K}_i(t) = \frac{\sum_{P \in D} \underline{v}^{FE}(P, t) \cdot \underline{\phi}_i^{el}(P)}{\sum_{P \in D} \underline{\phi}_i^{el}(P) \cdot \underline{\phi}_i^{el}(P)} \quad (4.19)$$

$$\dot{\rho}_i(t) = \frac{\sum_{P \in D} \underline{v}^{FE}(P, t) \cdot \underline{\phi}_i^{pl}(P)}{\sum_{P \in D} \underline{\phi}_i^{pl}(P) \cdot \underline{\phi}_i^{pl}(P)} \quad (4.20)$$

For a linear elastic behavior, the quantity $\dot{K}_i(t)$ represents the rate of the nominal applied stress intensity factor K_i^∞ . When the behavior is nonlinear, a plastic region is developed at the crack tip. The confinement of this plastic zone creates internal stresses that are known as the “shielding effect” of the crack tip plastic zone [Rice and Thomson, 1974]. For this reason, the intensity factor of the elastic reference field $\dot{K}_i(t)$, which includes internal stresses, is different from the nominal stress intensity factor K_i^∞ .

Next parts discuss some methodologies and procedures followed in order to obtain the kinematic bases. Results of these elastic and plastic reference fields are shown for a range of crystallographic orientations with respect to the crack plane and direction. One of the main challenges is to find a good description of the slip mechanisms near the crack tip region. For this reason, different methodologies of decomposition of the complementary plastic fields are presented and discussed.

4.3.1 Elastic reference fields

Elastic reference fields related to the three fracture modes are obtained from pure elastic computations. For each mode, a monotonic loading is applied to obtain a unit stress intensity factor of the corresponding mode. For instance, to obtain $\phi_I^{el}(\underline{x})$, a loading ramp is applied so that $K_I^\infty = 1 \text{ MPa}\sqrt{\text{m}}$, $K_{II}^\infty = 0 \text{ MPa}\sqrt{\text{m}}$ and $K_{III}^\infty = 0 \text{ MPa}\sqrt{\text{m}}$. The resulting finite element field can be read directly as the elastic reference field:

$$\underline{v}^{FE}(\underline{x}, t) = \underline{\phi}^{el}(\underline{x}) \quad (4.21)$$

As shown in equation 4.22, the reference field can be decomposed by a Proper Orthogonal Decomposition into an angular distribution and a scale radial function. These functions are shown in figures 4.7, 4.8, 4.9 for material orientations $\gamma_{[100]}^{(010)}$, $\gamma_{[110]}^{(110)}$ and $\gamma_{[110]}^{(111)}$ respectively.

$$\underline{\phi}_i^{el}(\underline{x}) = f_i^{el}(r) \cdot \underline{g}_i^{el}(\theta) \quad (4.22)$$

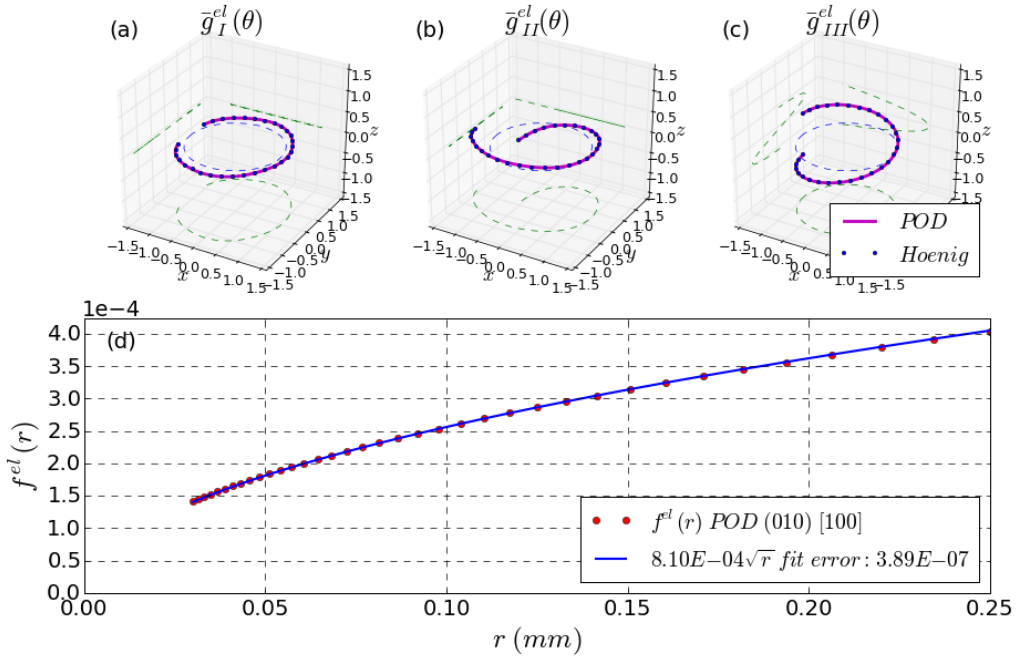


Figure 4.7: $\underline{g}^{el}(\theta)$ functions for (a) mode I, (b) mode II and (c) mode III and (d) radial function $f^{el}(r)$ for material orientation $\gamma_{[100]}^{(010)}$.

$\underline{g}^{el}(\theta)$ functions identified by the POD show good agreement with Hoenig's analytical solutions. The radial function, as predicted by the analytical solution, is fitted to a square root function. It was also an opportunity to verify the well definition of material orientation with respect to the crack plane and direction in the *Z-mat* subroutine.

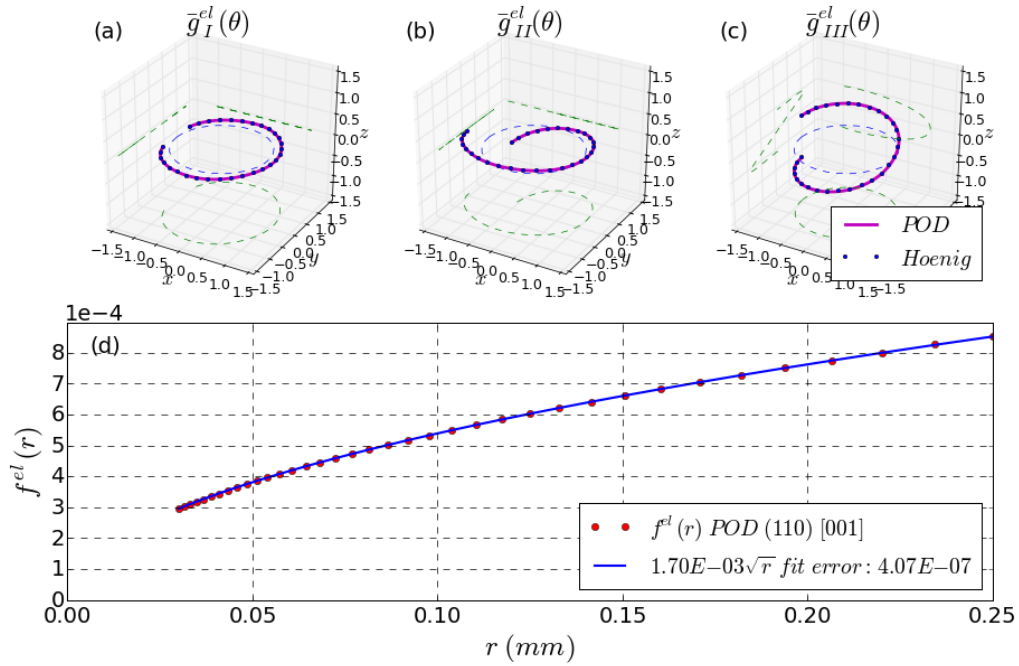


Figure 4.8: $\underline{g}^{el}(\theta)$ functions for (a) mode I, (b) mode II and (c) mode III and (d) radial function $f^{el}(r)$ for material orientation $\succ_{[001]}^{(110)}$.

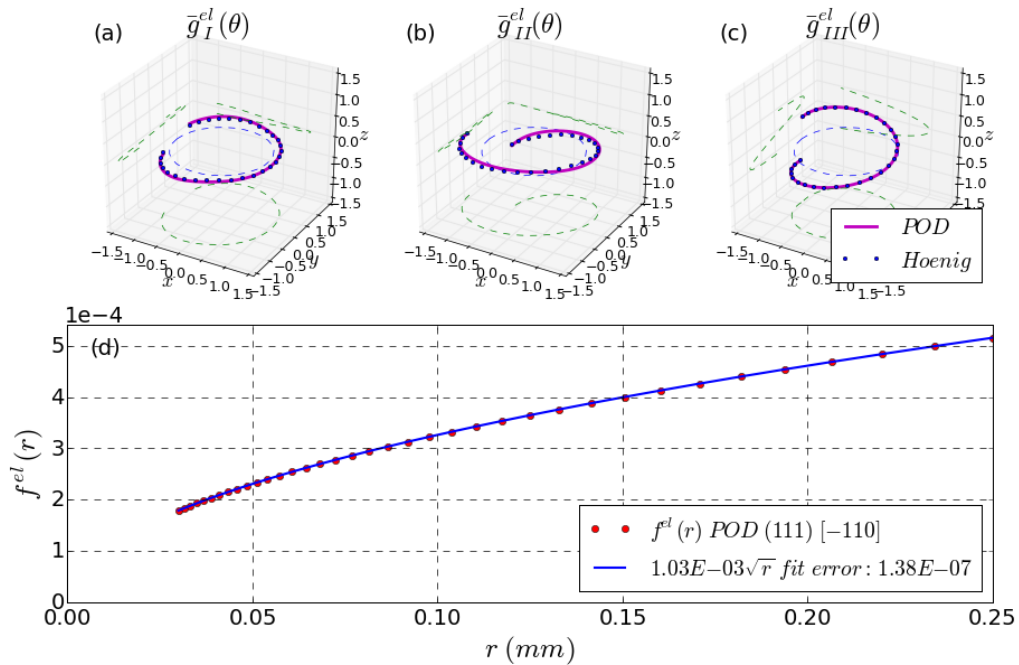


Figure 4.9: $\underline{g}^{el}(\theta)$ functions for (a) mode I, (b) mode II and (c) mode III and (d) radial function $f^{el}(r)$ for material orientation $\succ_{[110]}^{(111)}$.

4.3.2 Complementary reference fields: Geometric decomposition by fracture modes

To obtain complementary reference fields, an elastic-plastic analysis is performed. The Méric-Cailletaud model was implemented in *Z-mat* using the parameters presented on table 4.3. Three monotonic loadings are applied in order to enhance in each time the appearance of the fracture mode in consideration. For each computation, the elastic part is computed as the product of the intensity factor $\dot{K}_i(t)$ (see equation 4.19) and the corresponding reference field $\underline{\phi}_i^{el}(\underline{x})$. This quantity is then subtracted from the total finite element field in order to obtain the complementary part.

$$\tilde{v}^{pl}(\underline{x}, t) = \underline{v}^{FE}(\underline{x}, t) - \sum_{i=1}^3 \dot{K}_i(t) \cdot \underline{\phi}_i^{el}(\underline{x}) \quad (4.23)$$

The residual field, considered as the plastic kinematic field, is partitioned into time and space using a Proper Orthogonal Decomposition POD as the product of an intensity factor $\rho_i(t)$ and a spatial reference field. The intensity factor represents the intensity of plastic flow in the crack tip region and the complementary reference field $\underline{\phi}_i^{pl}(\underline{x})$ its spatial distribution. This reference field is resized so that ρ_i can directly be read as the crack tip plastic opening displacement, i.e. crack tip blunting. A second POD (radial-angular decomposition) can be applied on the reference field $\underline{\phi}_i^{pl}(\underline{x})$ to obtain:

$$\underline{\phi}_i^{pl}(\underline{x}) = f_i^{pl}(r) \cdot g_i^{pl}(\theta) \quad (4.24)$$

Validity of the approach

The incremental model is based on a set of hypotheses and assumptions. One basic hypothesis is the locally self-similar geometry near the crack tip region. This hypothesis, among others, leads to a more basic assumption of the model which is the decomposition of kinematic fields into intensity factors, scale functions and spatial distributions. This hypothesis remains available as long as the scale function, in a local reference attached to the crack plane and front, can be fitted to an evolution that satisfies: $f(\alpha r) - f(0) = \beta(f(r) - f(0))$.

Concerning the complementary part, this field presents a sharp decay since plasticity vanishes when getting away from the Irwin plastic zone to the K-dominance elastic zone. An assumption can be made describing this behavior with an exponential decay.

$$f^{pl}(r) \approx A e^{-r/p} \quad (4.25)$$

In order to maintain this assumption, a procedure of verification was set. Two main tuning factors are considered in this process, the loading range and the size of the extraction zone. For each loading case (*mode I*, *mode II* or *mode III*), complementary fields were extracted from extraction zones with different external radii and then post-processed over different loading ranges.

Figures 4.10 and 4.11 show the magnitude of the coefficient p on a map of loading ranges obtained for the best extraction zone radius. For a fracture mode i , the x-axis and

y-axis present the square of the loading amplitude $\Delta K_i = K_i^{max} - K_i^{min}$ and the square of the maximum loading K_i^{max} respectively. The square of the maximum loading is linearly related to the size of the monotonic plastic zone while the square of the loading amplitude refers to the size of the cyclic plastic zone.

Each spot on the graph is obtained by extracting finite element elastic-plastic kinematic fields from the loading range $[K_i^{min}, K_i^{max}]$. These fields were then post-processed in order to obtain the exponential decay coefficient p .

This procedure was performed for all studied material orientations. For instance, figure 4.10 shows, for the three fracture modes and for material orientation $\gamma_{[110]}$, the evolution of the coefficient p over different loading ranges for an external radius of the extraction zone $r_{max} = 0.104$ mm.

Note: By assuming that the plastic zone is circular, Irwin [Irwin, 1960a] evaluated the radius of the monotonic plastic zone under plane strain conditions as:

$$Z_{pm} = \frac{1}{3\pi} \left(\frac{K}{R_e} \right)^2 \quad (4.26)$$

The repetition of loading and unloading process causes the apparition, inside the monotonic zone, of a cyclic plastic deformation region called the cyclic plastic zone. The radius of this zone is evaluated as function of the loading amplitude. It is written for plane strain as follows:

$$Z_{pc} = \frac{1}{3\pi} \left(\frac{\Delta K}{2R_e} \right)^2 \quad (4.27)$$

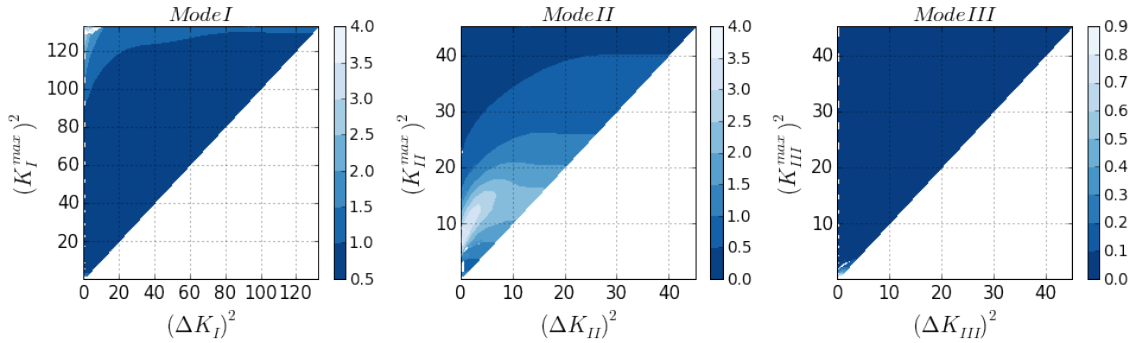


Figure 4.10: Exponential decay coefficient p for an interest region external radius $r_{max} = 0.104$ mm for the material orientation $\gamma_{[110]}$.

It can be noted that the coefficient p do not vary drastically from one loading range to another. This observation approves the assumption that the crack tip plasticity under different loading cases can be represented by one exponential decay function.

A loading range is finally chosen for each fracture mode and for each material orientation. Reference fields will be extracted, is chosen from a region of the map where the exponential coefficient p remains constant.

The external radius of the chosen interest region r_{max} varies from one material orientation to another. In fact, this zone should include the total plastic region. However, the evolution of plasticity near the crack tip region and hence the size of the plastic zone, depends on the elastic anisotropy and the crystallographic orientation with respect to the crack plane [Arakere et al., 2009].

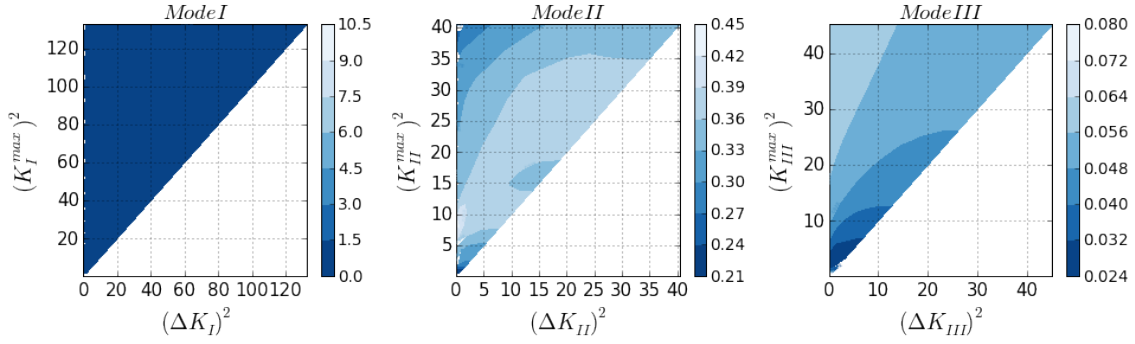


Figure 4.11: Exponential decay coefficient p for an interest region external radius $r_{max} = 0.087$ mm for the material orientation $\chi_{[001]}^{(110)}$.

Radial and angular functions

Once the interest region size and the loading range are fixed for the best exponential decay coefficient, reference fields of different fracture modes are extracted through a POD that separate time and space dependencies. These fields were then grouped together and another POD was performed to decompose radial and angular dependencies. Hence, three angular shape functions $\underline{g}_i^{pl}(\theta)$ and one common radial scale function $f^{pl}(r)$ are identified.

Figures 4.12, 4.13 and 4.14 show the maximum principal plastic strain distribution within the crack tip region for different fracture modes. Angular distributions are shown in (a), (b) and (c) respectively. The radial scale function is shown in (d). According to the aforementioned hypotheses, these functions exhibited an exponential decay with the distance from the crack front.

The deformed surface of the unit circle submitted to the transformation $\underline{g}^{pl}(\theta)$ remains unchanged when compared to the undeformed one. In fact, plastic strain in metals is isochoric because it stems from a combination of slip along slip planes and slip directions.

As it can be noted for some material orientations, for instance for *mode II* and *mode III* in figures 4.13 and 4.14, the obtained reference fields show a strong localization of plastic field near the crack tip region. This localization is mainly associated to the activation of few octahedral slip systems. The activation of more slip systems is associated to a more diffused and spread out shape of angular distribution.

These observations raised questions about the importance of taking into account these mechanisms in the modeling of crack tip plasticity using kinematic fields. In fact, building a complementary reference field for a each fracture mode with few activated slip systems may not be generic and representative of what happens under more complex mixed mode loadings.

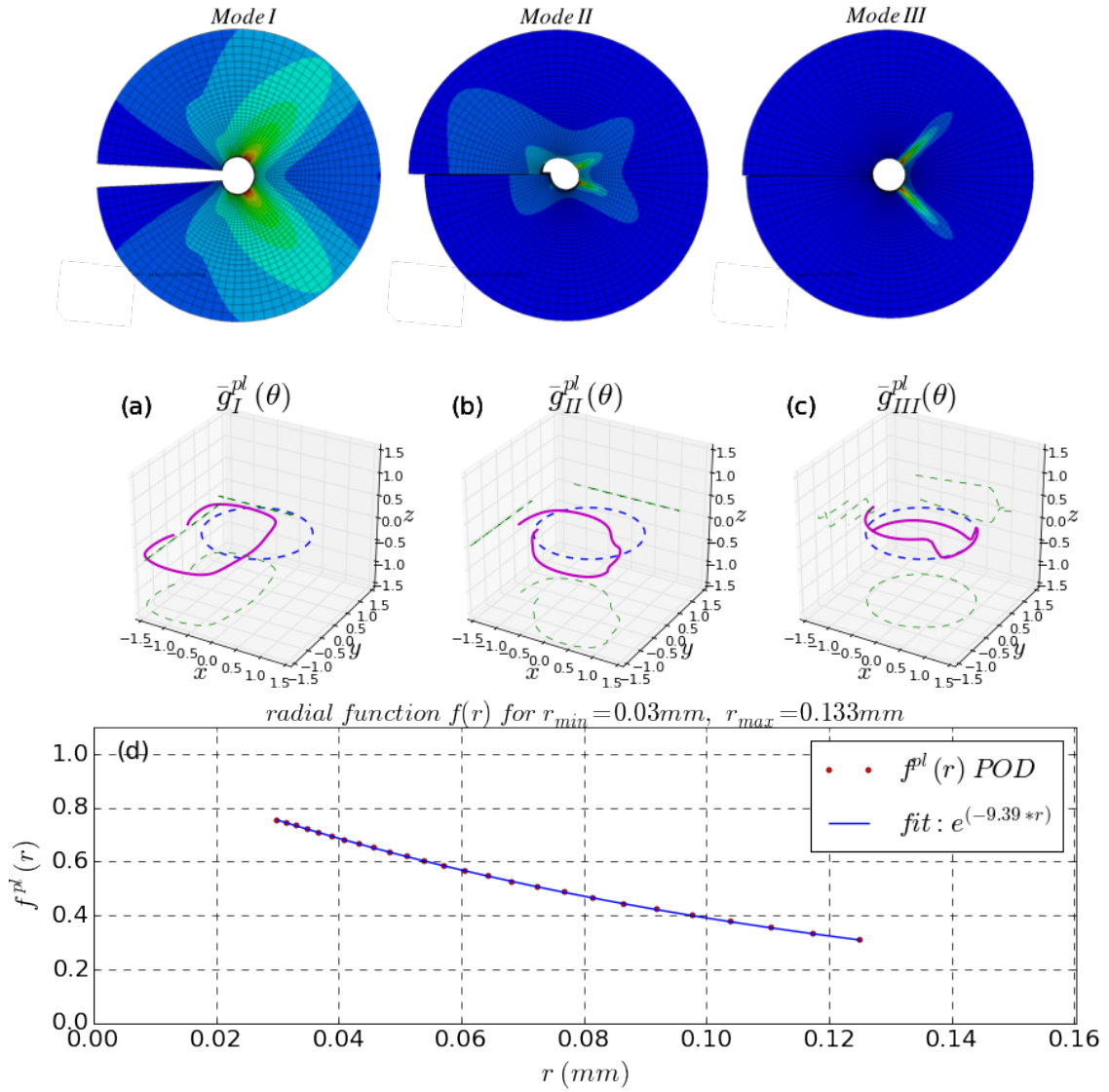


Figure 4.12: Maximum principal plastic strain in the crack tip region under three fracture modes, angular distributions (a) $\underline{g}_I^{pl}(\theta)$, (b) $\underline{g}_{II}^{pl}(\theta)$ and (c) $\underline{g}_{III}^{pl}(\theta)$ and (d) radial function $f^{pl}(r)$ for material orientation $\gamma_{[100]}^{(010)}$.

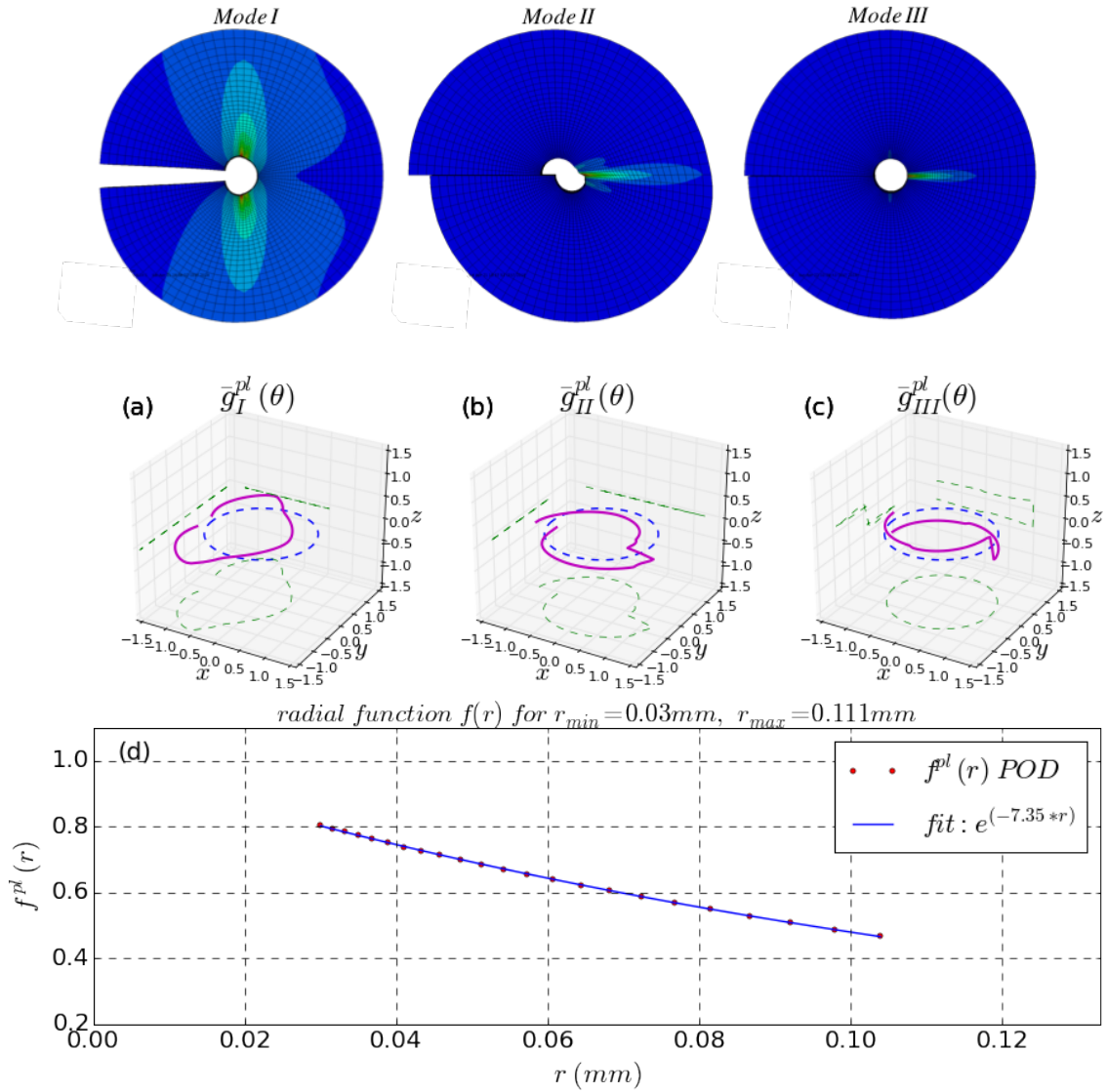


Figure 4.13: Maximum principal plastic strain in the crack tip region under three fracture modes, angular distributions (a) $\bar{g}_I^{pl}(\theta)$, (b) $\bar{g}_{II}^{pl}(\theta)$ and (c) $\bar{g}_{III}^{pl}(\theta)$ and (d) radial function $f^{pl}(r)$ for material orientation $\gamma \succ \begin{smallmatrix} (110) \\ [1\bar{1}0] \end{smallmatrix}$.

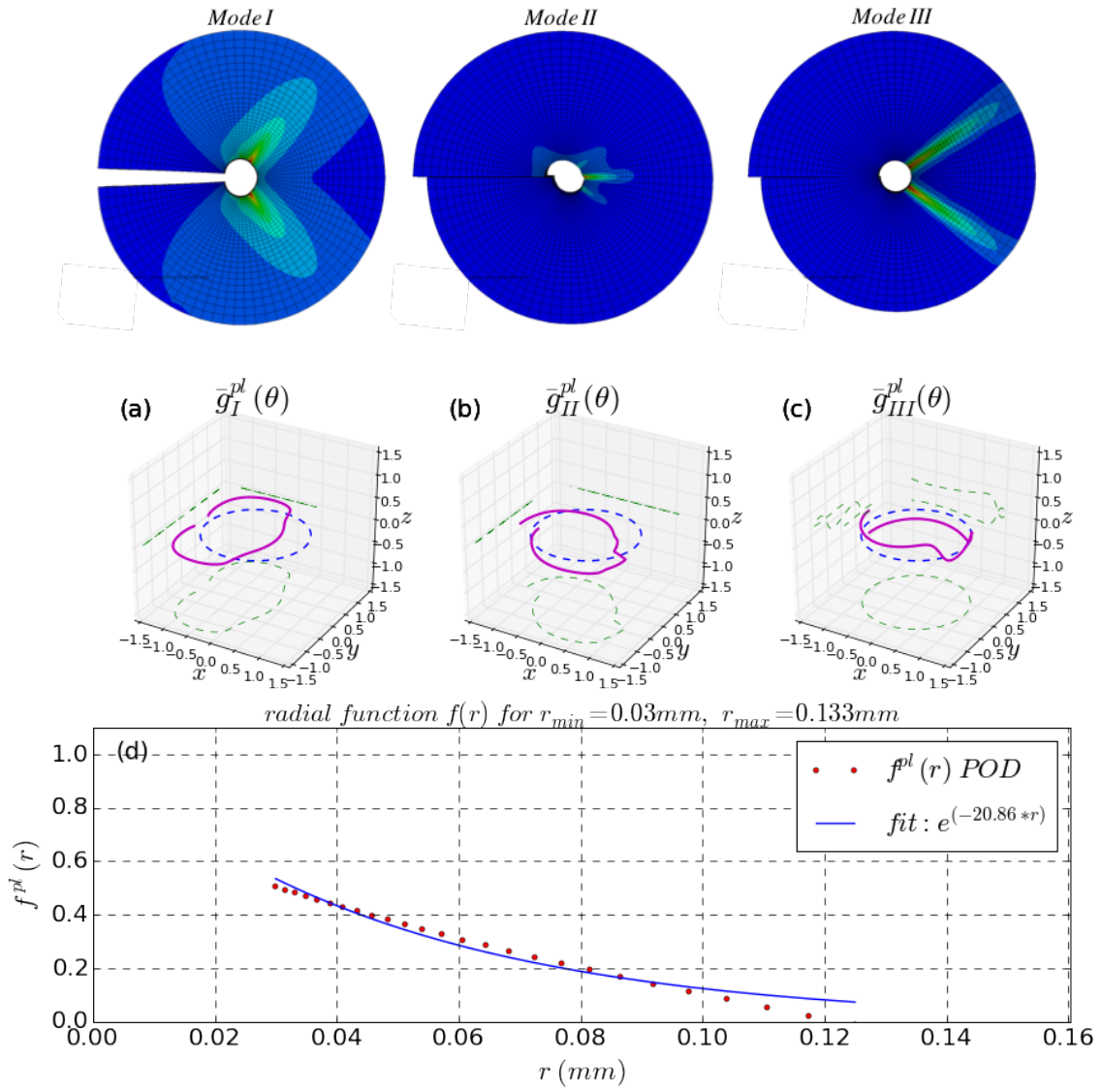


Figure 4.14: Maximum principal plastic strain in the crack tip region under three fracture modes, angular distributions (a) $\underline{g}_I^{pl}(\theta)$, (b) $\underline{g}_{II}^{pl}(\theta)$ and (c) $\underline{g}_{III}^{pl}(\theta)$ and (d) radial function $f^{pl}(r)$ for material orientation $\gamma_{\begin{smallmatrix} (110) \\ [001] \end{smallmatrix}}$.

Reconstruction errors

To control the quality of the approximation, two reconstruction relative errors are systematically computed:

- The relative quadratic error C_e when approximating the total elastic-plastic field $\underline{v}^{FE}(\underline{x}, t)$ by the reconstruction of its projection on the three elastic reference fields.

$$C_e = \sqrt{\frac{\sum_{P \in D} (\underline{v}^{FE}(P, t) - \tilde{\underline{v}}^{el}(P, t))^2}{\sum_{P \in D} (\underline{v}^{FE}(P, t))^2}} \quad (4.28)$$

with

$$\tilde{\underline{v}}^{el}(\underline{x}, t) = \sum_{i=1}^3 \dot{K}_i(t) \cdot \underline{\phi}_i^{el}(\underline{x}) \quad (4.29)$$

- The relative quadratic error C_{ep} when approximating the total elastic-plastic field $\underline{v}^{FE}(\underline{x}, t)$ by the reconstruction of its projection on the total kinematic basis (elastic and plastic).

$$C_{ep} = \sqrt{\frac{\sum_{P \in D} (\underline{v}^{FE}(P, t) - \tilde{\underline{v}}(P, t))^2}{\sum_{P \in D} (\underline{v}^{FE}(P, t))^2}} \quad (4.30)$$

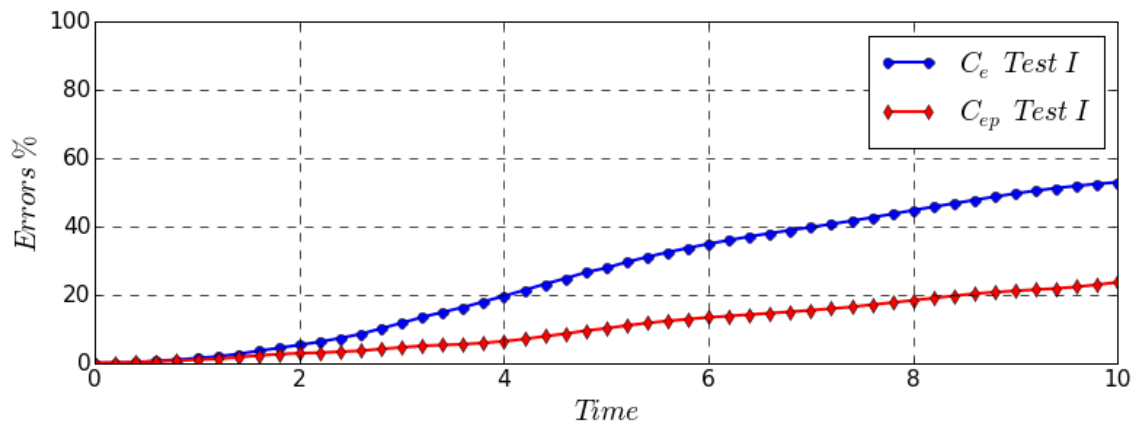
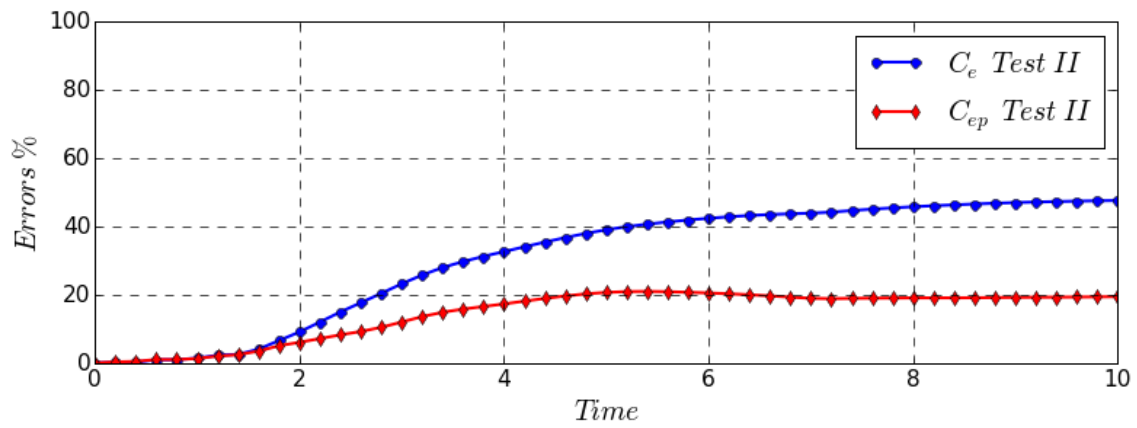
with

$$\tilde{\underline{v}}(\underline{x}, t) = \sum_{i=1}^3 \dot{K}_i(t) \cdot \underline{\phi}_i^{el}(\underline{x}) + \dot{\rho}_i(t) \cdot \underline{\phi}_i^{pl}(\underline{x}) \quad (4.31)$$

These relative errors are shown in figures 4.15a and 4.15b for material orientation $\succ_{[100]}^{(010)}$ for two different tests:

- *Test I* designates a monotonic loading case in pure fracture *mode I* with $K_I^\infty = 12 \text{ MPa}\sqrt{\text{m}}$.
- *Test II* designates a monotonic loading case in pure fracture *mode II* with $K_{II}^\infty = 7 \text{ MPa}\sqrt{\text{m}}$.

The approximated kinematic field represents less error when the complementary part is taken into consideration. The difference between the two reconstruction errors can be interpreted as a yield indicator (see section 2.3.7).

(a) Reconstruction of a pure *mode I* test.(b) Reconstruction of a pure *mode II* test.Figure 4.15: Errors C_e and C_{ep} for material orientation $\gamma \begin{smallmatrix} (010) \\ [100] \end{smallmatrix}$.

4.3.3 Complementary reference fields: Decomposition into fracture modes and into slip systems

In the previous chapter (chapter 3) where material behavior was represented by a cubic elasticity and Von Mises plasticity, the decomposition of reference fields was based on geometrical considerations regarding the symmetry with respect to the crack plane. In fact, the anisotropy induced by the presence of the crack is so large that it can be considered to annihilate the effect of the cubic anisotropy on the complementary part decomposition. In the current case, the presence of an additional source of anisotropy modeled by the crystal plasticity requires a new methodology for partitioning the displacement field using reference fields that take into account this new material model.

In the considered crystallographic phenomenological model, macroscopic visco-plastic strain rate is a linear combination of slip rates of different slip systems weighted by the corresponding orientation tensor (Schmid factor \underline{m}^s).

$$\underline{\dot{\epsilon}}^v = \sum_{s \in G} \dot{\gamma}_v^s \underline{m}^s \quad (4.32)$$

A degree of freedom $\dot{\gamma}_v^s$ is assigned to each slip system in its kinematic tensorial representation. In an analogy with this concept, while always considering the crack geometry, the following decomposition of complementary reference fields was proposed:

$$\underline{v}^{FE}(\underline{x}, t) = \sum_{i=1}^3 \dot{K}_i(t) \underline{\phi}_i^{el}(\underline{x}) + \sum_{s \in G} \sum_{i=1}^3 \dot{\rho}_i^s(t) \underline{\phi}_i^{pl,s}(\underline{x}) \quad (4.33)$$

where $\underline{\phi}_i^{pl,s}(\underline{x})$ is the complementary reference field that corresponds to the fracture mode i and the slip system s .

To obtain these reference fields, different finite element simulations of the three fracture modes were performed while implementing for each one a crystal plasticity model with one slip system. It means that for each set of computations of a slip system r , we assume that plastic slip can occur only when the resolved shear stress τ^r , of that slip system r , reaches the critical resolved shear stress value τ^c . If it is not the case, no plasticity takes place. Thus, twelve sets of computations corresponding to the twelve octahedral slip systems were performed. For each slip system, one computation was performed for each fracture mode.

Results

Computations were conducted for material orientation $\succ_{[100]}^{(010)}$.

- For *mode I* reference fields, an equi-biaxial loading was applied to obtain $K_I^\infty = 50 \text{ MPa}\sqrt{\text{m}}$.
- For *mode II*, a pure in plane shear loading is performed, the stress intensity experienced by the crack is $K_{II}^\infty = 25 \text{ MPa}\sqrt{\text{m}}$.
- For *mode III*, reference fields are obtained from a pure out of plane shear test with $K_{III}^\infty = 25 \text{ MPa}\sqrt{\text{m}}$.

Note: For mode II and mode III, the elastic anisotropy may cause a crack closure, therefore a small crack opening was applied in both cases ($K_I^\infty = 0.5 \text{ MPa}\sqrt{\text{m}}$) to avoid contact and friction between crack faces. An assumption was made that complementary nonlinear fields describe plasticity. Therefore, no source of dissipation, other than plasticity, should exist in the model.

Figures 4.16, 4.17 and 4.18 show a capture of the cumulated slip of the selected slip systems ($D4$, $B5$ and $C1$ respectively). Only results in the region of interest are shown and plotted in a logarithmic scale for the fracture modes.

Note: The notation used for slip systems is the Schmid and Boas notation [Schmid and Boas, 1935] presented in table 4.1. The letter designates the plane and the number is for the direction.

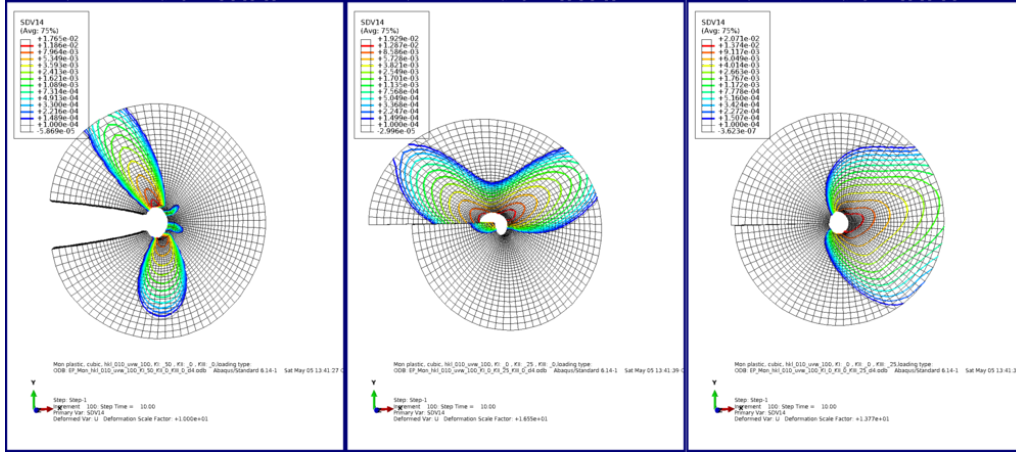


Figure 4.16: Cumulated plastic strain maps at the region of interest plotted in a logarithmic scale for (from left to right) *mode I*, *mode II* and *mode III*, with a single slip system $D4$ available in the crystal plasticity model for material orientation $\succ \begin{smallmatrix} (010) \\ [100] \end{smallmatrix}$.

For a given slip system and a given fracture mode, the plot of the cumulated slip systems in a logarithmic scale displays a series of homothetic isocontours, with a regular spacing. This observations support the hypothesis of the self-similarity of plastic flow in the crack tip regions and its representation with an exponential decay.

In order to compare the quantity of slip occurring on different slip systems, we proposed to compute, for each implemented slip system, the average cumulated slip. The root mean square of the cumulated slip rate is computed over all the region of interest.

$$\gamma_{rms}^s(t) = \sqrt{\frac{1}{N} \sum_{P \in D} \left(\int_0^t |\dot{\gamma}^s(P, x)| dx \right)^2} \quad (4.34)$$

The evolution of $\gamma_{rms}^s(t)$ was extracted from the first set of computations already performed where a single (“Separate”) slip system is implemented each time.

A second set of computations was performed where all slip systems are implemented together (“Combined”) in order to put them in competition. In fact, despite the latent

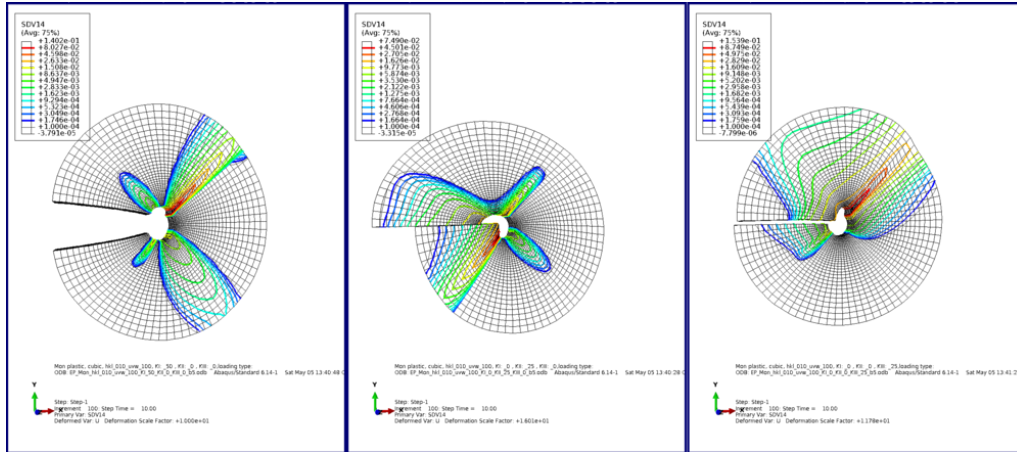


Figure 4.17: Cumulated plastic strain maps at the region of interest plotted in a logarithmic scale for (from left to right) *mode I*, *mode II* and *mode III*, with a single slip system $B5$ available in the crystal plasticity model for material orientation $\gamma_{[100]}^{(010)}$.

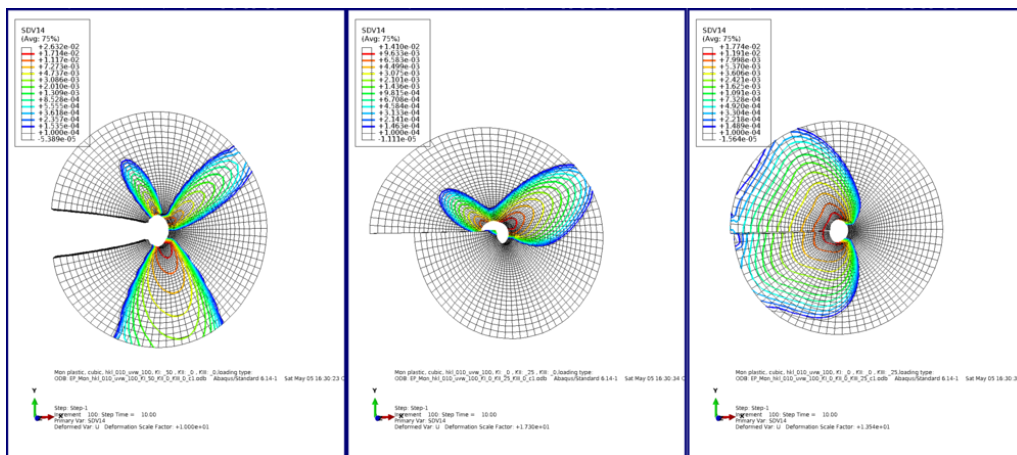


Figure 4.18: Cumulated plastic strain maps at the region of interest plotted in a logarithmic scale for (from left to right) *mode I*, *mode II* and *mode III*, with a single slip system $C1$ available in the crystal plasticity model for material orientation $\gamma_{[100]}^{(010)}$.

hardening is neglected and only self-hardening is considered in the interaction matrix H^{rs} , a slip system activation do affect the activation of other slip systems. It may inhibit the activation of new slip systems [Arakere et al., 2009]. This implies that when plasticity occurs on a dominant slip system at a given position (r, θ) , it persists and no other slip systems are activated in that region. The persistence of slip can be explained by the softening effect [Ebrahimi et al., 2006], [Westbrooke, 2005], the uniqueness of slip system activity at a given position is attributed to plasticity that causes a significant drop in resolved shear stress on other slip systems.

The evolution of the γ_{rms}^s is plotted in figures 4.19, 4.20 and 4.21 for crystallographic orientation $\succ_{[100]}^{(010)}$. Both ‘‘Separate’’ and ‘‘Combined’’ cases are shown. The legend indicates the normalized maximum value of the γ_{rms}^s for each slip system. Thus, slip systems that have the same evolution can be identified from the legend since they have the same maximum normalized value of γ_{rms}^s . For instance, for *mode I*, B5 and C5 slip systems have the same evolution. Besides, these two systems are ‘‘dominant’’ [Arakere et al., 2004], [Arakere et al., 2009]. It means that they experience the highest resolved shear stress. For our case, the γ_{rms}^s is considered as an indicator of slip system activation.

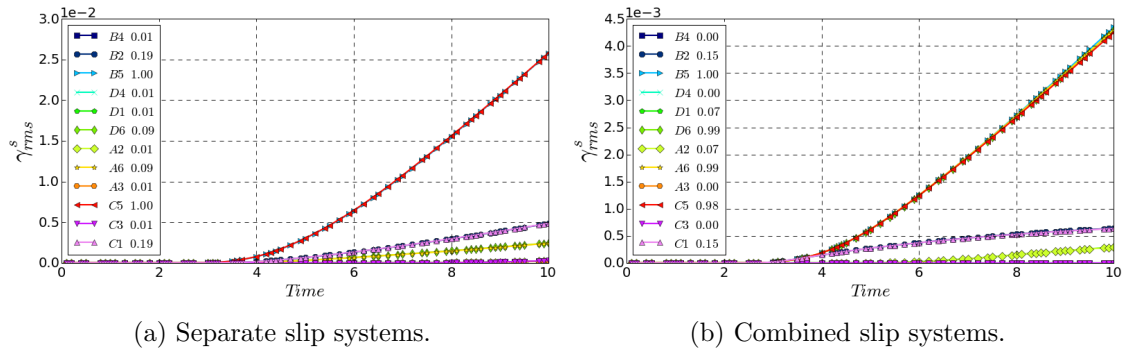


Figure 4.19: Normalized quadratic mean value of the cumulated plastic strain at the region near the crack tip for *mode I* for material orientation $\succ_{[100]}^{(010)}$, (a) separate single slip systems, (b) combined slip systems.

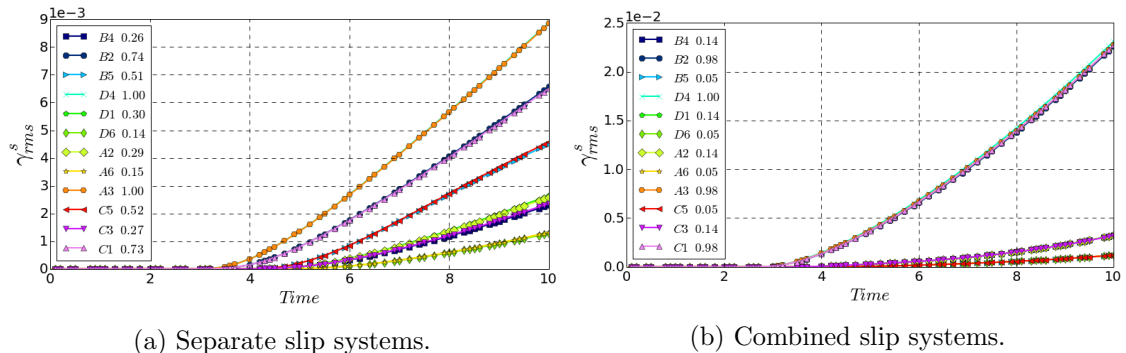
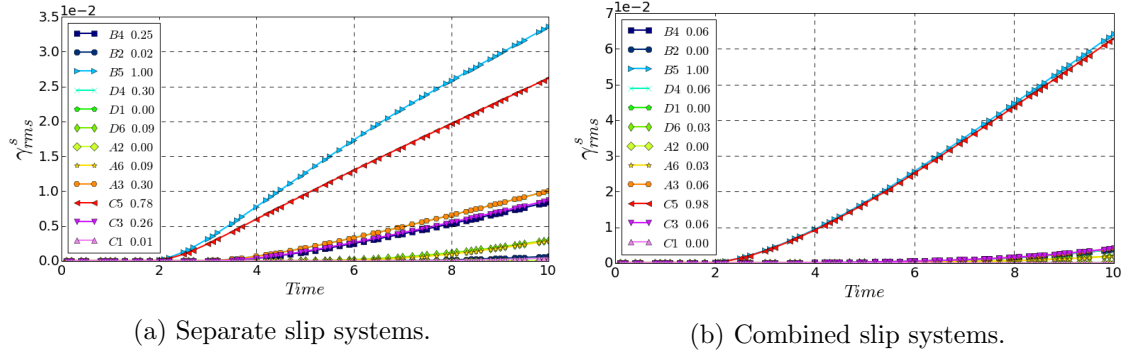


Figure 4.20: Normalized quadratic mean value of the cumulated plastic strain at the region near the crack tip for *mode II* for material orientation $\succ_{[100]}^{(010)}$, (a) separate single slip systems, (b) combined slip systems.



(a) Separate slip systems.

(b) Combined slip systems.

Figure 4.21: Normalized quadratic mean value of the cumulated plastic strain at the region near the crack tip for *mode III* for material orientation $\gamma_{[100]}^{(010)}$, (a) separate single slip systems, (b) combined slip systems.

Table 4.4 summarizes the degree of activation of each slip system for orientations $\gamma_{[100]}^{(010)}$ and $\gamma_{[001]}^{(110)}$. We note that slip systems behave identically two by two for all studied cases except for slip systems *B5* and *C5* under the third fracture mode for orientation $\gamma_{[001]}^{(110)}$. Couples of slip systems that have the same behavior are grouped together between parentheses.

Table 4.4: Slip systems activities in a “separate” case where only one slip system is implemented in the behavior law and for a “combined” case where all octahedral slip systems are implemented together. Results are shown for material orientations $\gamma_{[100]}^{(010)}$ and $\gamma_{[001]}^{(110)}$.

Orientation	Mode	Implementation type	Slip system activation			
			Intense	Medium	Low	Not active
$\gamma_{[100]}^{(010)}$	<i>mode I</i>	Separate	(B5, C5)	(C1, B2)	(D6, A6)	(A3, D4) (C3, B4) (A2, D1)
		Combined	(B5, C5) (D6, A6)	(C1, B2)	(A2, D1)	(A3, D4) (C3, B4)
	<i>mode II</i>	Separate	(A3, D4) (C1, B2)	(C5, B5)	(A2, D1) (C3, B4) (A6, D6)	
		Combined	(A3, D4) (C1, B2)		(A2, D1) (C3, B4)	(A6, D6) (C5, B5)
	<i>mode III</i>	Separate	(B5, C5)	(A3, D4) (C3, B4)	(A6, D6)	(C1, B2) (A2, D1)
		Combined	(B5, C5)		(C3, B4) (A3, D4)	(A6, D6) (C1, B2) (A2, D1)
$\gamma_{[001]}^{(110)}$	<i>mode I</i>	Separate	(C3, C1)		(B4, B2) (A3, D1)	(A2, D4) (A6, D6) B5, C5
		Combined	(C3, C1)	(B4, B2)		(A3, D1) (A2, D4) (A6, D6) B5, C5
	<i>mode II</i>	Separate	(A6, D6)	(C1, C3)	(A2, D4)	B5, C5 (B4, B2) (A3, D1)
		Combined	(A6, D6)	(C1, C3)		B5, C5 (B4, B2) (A3, D1) (A2, D4)
	<i>mode III</i>	Separate	C5 (A6, D6)	(C1, C3)	(A2, D4)	B5 (B4, B2) (A3, D1)
		Combined	C5		(A6, D6) B5	(C1, C3) (B4, B2) (A3, D1) (A2, D4)

These analyses serve to identify which slip systems are the more active in each fracture mode. This helps to reduce the number of reference fields used to create the kinematic basis. Only reference fields from active slip systems are used in each fracture mode. For instance, for *mode I*, six complementary reference fields are extracted from the elastic-plastic analysis instead of twelve. These reference fields are $\underline{\phi}_I^{pl,s}(\underline{x})$ with $s \in \{B5, C5, C1, B2, A6, D6\}$. Since they are not active at all, the remaining slip systems have no contribution in the kinematic field near the crack tip region for crack *mode I*, thus, they are not taken into consideration. The extraction method is the same method usually used for complementary fields.

Reconstruction errors

The quality of the approximated kinematic field was evaluated using both C_e and C_{ep} errors. The elastic reconstruction error C_e remains the same presented before in equation 4.28. The total reconstruction error C_{ep} is updated with new decomposition method:

$$C_{ep} = \sqrt{\frac{\sum_{P \in D} (\underline{v}^{FE}(P, t) - \tilde{\underline{v}}(P, t))^2}{\sum_{P \in D} (\underline{v}^{FE}(P, t))^2}} \quad (4.35)$$

with

$$\tilde{\underline{v}}(\underline{x}, t) = \sum_{i=1}^3 \dot{K}_i(t) \cdot \underline{\phi}_i^{el}(\underline{x}) + \sum_{s \in G} \sum_{i=1}^3 \dot{\rho}_i^s(t) \cdot \underline{\phi}_i^{pl,s}(\underline{x}) \quad (4.36)$$

$\dot{\rho}_i^s(t)$ is the blunting intensity factor rate of the slip system s caused by the fracture mode i . This quantity is obtained by projection as follows:

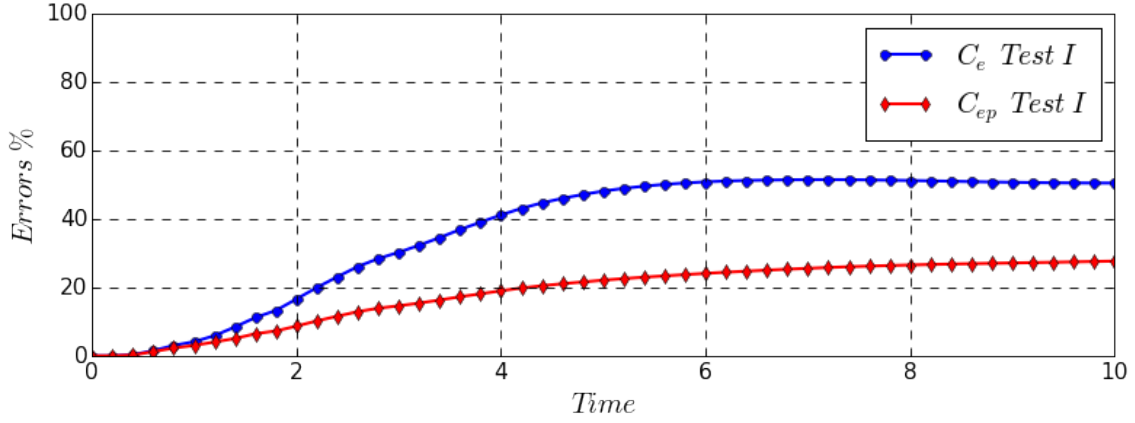
$$\dot{\rho}_i^s(t) = \frac{\sum_{P \in D} \underline{v}^{FE}(P, t) \cdot \underline{\phi}_i^{pl,s}(P)}{\sum_{P \in D} \underline{\phi}_i^{pl,s}(P) \cdot \underline{\phi}_i^{pl,s}(P)} \quad (4.37)$$

Errors are presented in figure 4.22 for different loading cases under pure crack *mode I*, *mode II* and *mode III* for material orientation $\succ_{[100]}^{(010)}$:

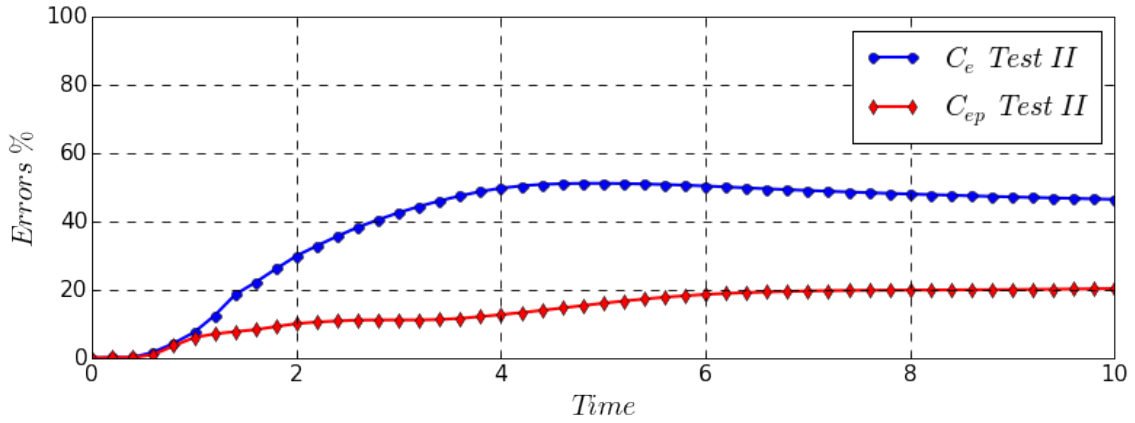
- *Test I* designates a monotonic loading case in pure fracture *mode I* with $K_I^\infty = 50 \text{ MPa}\sqrt{\text{m}}$.
- *Test II* designates a monotonic loading case in pure fracture *mode II* with $K_{II}^\infty = 25 \text{ MPa}\sqrt{\text{m}}$.
- *Test III* designates a monotonic loading case in pure fracture *mode III* with $K_{III}^\infty = 25 \text{ MPa}\sqrt{\text{m}}$.

As mentioned before, only reference fields corresponding to active slip systems were used in the reconstruction procedure.

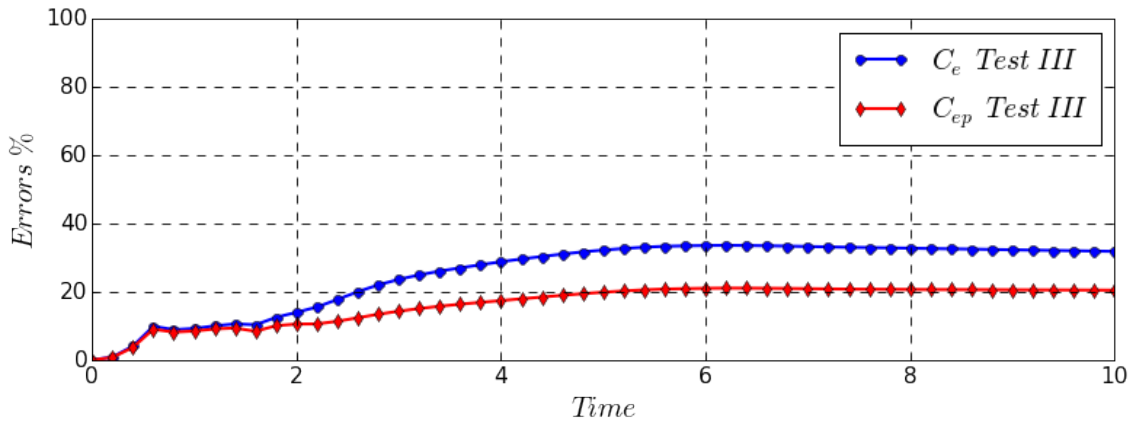
It is obvious from the reconstruction errors that complementary fields ameliorate the quality of the approximation of kinematic fields. The difference between the two errors serves as an indicator of plasticity.



(a) Reconstruction of pure *mode I* test.



(b) Reconstruction of pure *mode II* test.



(c) Reconstruction of pure *mode III* test.

Figure 4.22: Errors C_e and C_{ep} for material orientation $\gamma_{[100]}^{(010)}$.

4.4 Yield surface

The aim of this section is to construct the yield domain of the crack tip region. As a matter of fact, in this region, slip systems are activated in order to relax the crack tip stress concentration and the material undergo plastic deformation. Rice [Rice, 1987] investigated crack tip fields in an elastic-ideally plastic single crystal. His analytical solutions indicated the presence of different constant stress sectors near the crack tip region. The stress state jumps discontinuously at boundaries between these sectors.

A yield domain can be constructed in the stress space. Rice [Rice, 1987] showed that for an elastic-ideally plastic single crystal under plane strain conditions, the yield surface can be constructed in the $(\sigma_{11} - \sigma_{22})/2$ versus σ_{12} stress space. The shape of this surface is a polygon that depends on the crystallographic orientation. The vertexes of this polygon correspond to constant stress sectors observed at the near crack tip region.

Figure 4.23(a) [Crone and Shield, 2001] illustrates three families of slip plane traces near the crack tip region of a FCC crystal with an orientation $\gamma_{[101]}^{(010)}$ with respect to the crack. Every slip family is shown with a type of lines (solid, dashed and dot-dashed lines). As shown on figure 4.23(b), each slip family corresponds to two parallel lines that construct the yield domain in the stress space. For instance, for the family of dashed lines, the effective slip direction is $[101]$. These slip traces are oriented at an angle equal to 180° with the x axis. On the yield surface, these slip traces correspond to the dashed line segments BC and FE.

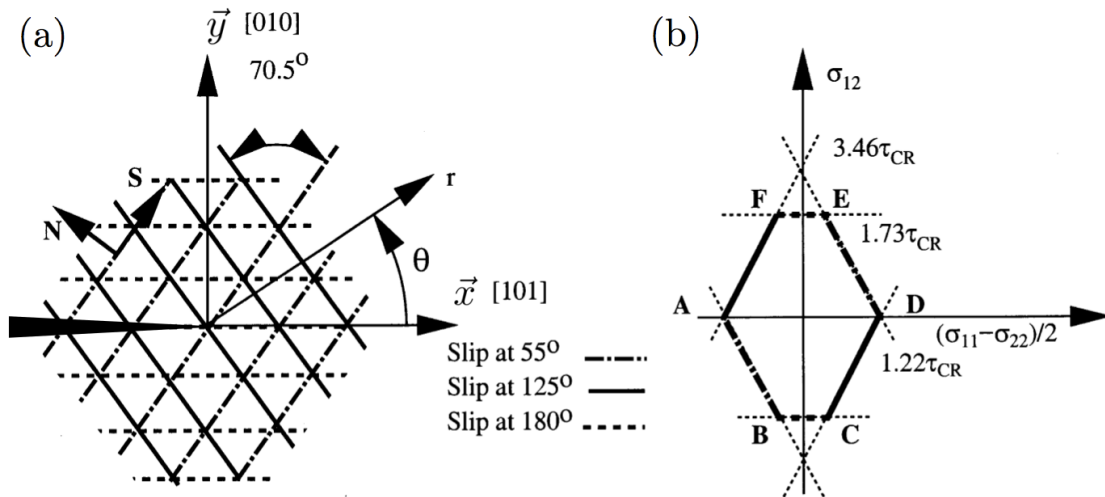


Figure 4.23: The diagram on (a) shows the orientation of slip plane traces on a specimen surface for an FCC material of orientation $\gamma_{[101]}^{(010)}$. The slip systems correspond to lines on the yield surface on (b). For example, the slip in the $[101]$ direction (shown as dashed lines) at 180° from the x axis corresponds to the dashed line segments BC and FE on the yield surface shown on the right. Figure modified from [Crone and Shield, 2001] and adapted from [Rice, 1987].

For the present work, finite element simulations were conducted in order to construct a yield domain for the region near the crack tip. The implemented crystallographic model is a multiple slip systems model with a yield function defined on each one of them. Therefore, we decided to explore a yield surface for each one of these slip systems separately. Thus, a unique slip system model was implemented for every set of simulations. Then, an exploration process is performed in order to identify the yield domain of the corresponding slip system.

A preliminary exploration was performed on different planes of the K-nominals space. For every plane, the crack is loaded in two fracture modes. We refer to this exploration process as “In-plane exploration”. In a second step, more complicated and time consuming computations were performed. They consist in exploring the 3D K-nominals space by mixing the three fracture modes. We refer to it as the “3D exploration” or the “spiked sphere” exploration path.

4.4.1 In-plane exploration

Exploration path

As mentioned before, only one slip system is implemented and allowed to activate in each set of simulations. For each slip system, three computation campaigns were initially conducted over the three planes of the K-nominals space. On each plane, the crack is submitted to an initial loading important enough to create a plastic zone in the studied region. Then a small back-loading, assumed to be purely elastic, is applied to move the loading point away from the yield domain borders. From this point, an exploration is applied with different mixture ratios inside the corresponding plane. Figure 4.24 shows the in-plane loading path in the 3D K-nominals space and in the three planes of the coordinates system. Previous analyses of reference fields (see table 4.4) have shown that not all slip systems are always activated when loading in a pure mode *I*, *II* or *III*. For this reason and to simplify the exploration, only slip systems present in the union of the activation lists of both fracture modes in question are studied. For instance, if a slip system is exclusively activated in *mode II*, no need to explore it in the $K_{III}^{\infty} - K_I^{\infty}$ plane.

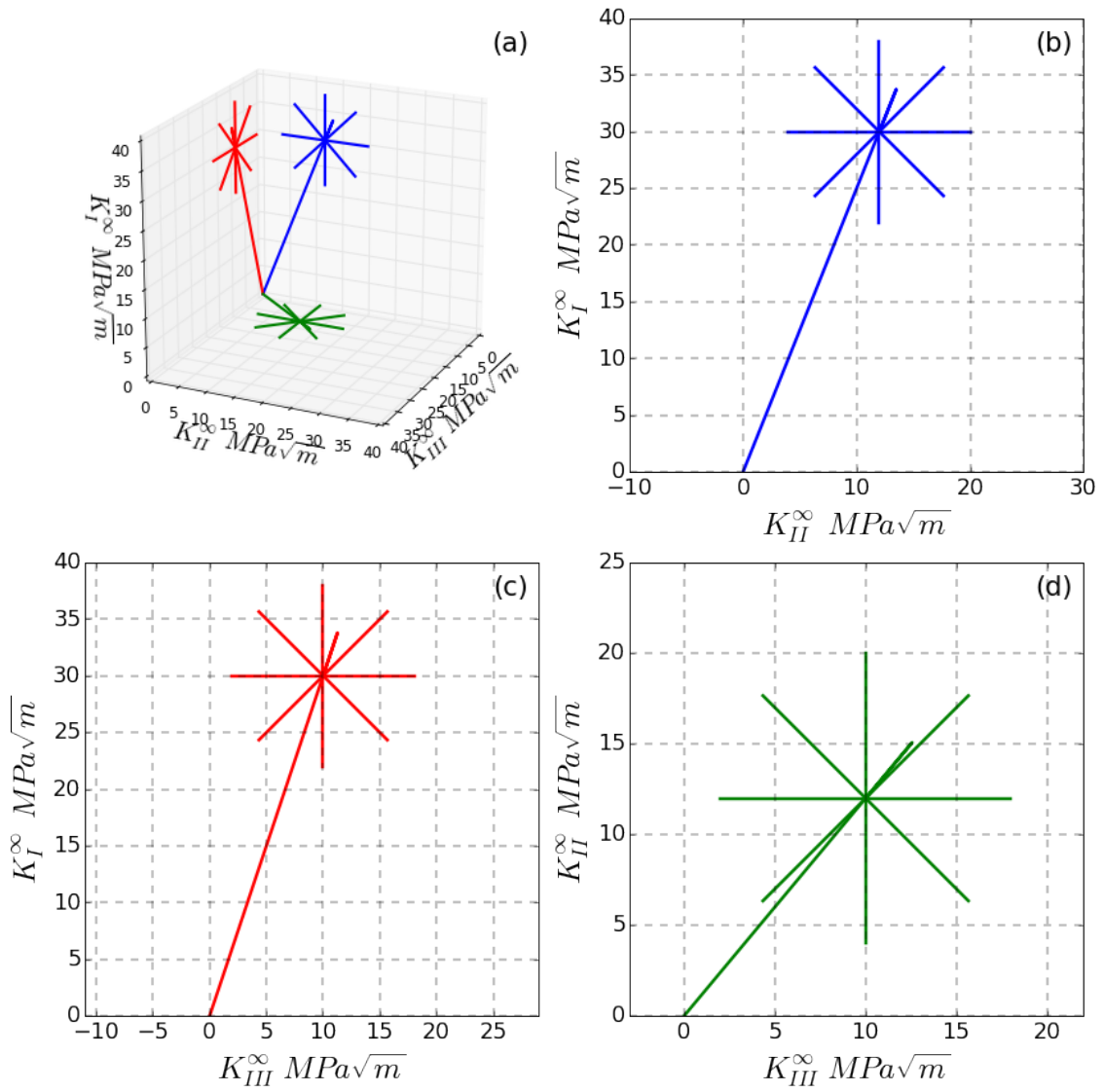


Figure 4.24: Yield surface exploration path in $K_I^\infty - K_{II}^\infty$ plane (b), in $K_I^\infty - K_{III}^\infty$ plane (c) and in $K_{II}^\infty - K_I^\infty$ plane (d)

Simulations and results

The quadratic mean value of the cumulated slip rate $\gamma_{rms}^s(t)$ previously defined in equation 4.34 seems to be a convenient indicator of the material state at the crack tip region. This quantity was computed on each branch of the exploration star. The evolution cards of the $\gamma_{rms}^s(t)$ are shown in figure 4.25 for some slip systems under material orientation $\gamma_{[100]}^{(010)}$.

Results of this preliminary exploration can be interpreted as the intersection between the yield surface of the slip system in consideration and the three loading planes $K_{II}^\infty - K_I^\infty$, $K_{III}^\infty - K_I^\infty$ and $K_{III}^\infty - K_{II}^\infty$. These yield maps show that this intersection is a straight line. Besides, the model assumes that slip is occurring on a giving plane. Thus, we postulate that the yield surface of a given slip system is one or multiple planes in the K-nominals domain. A second computation campaign is performed with a finer exploration in the 3D space in order to identify these yield planes.

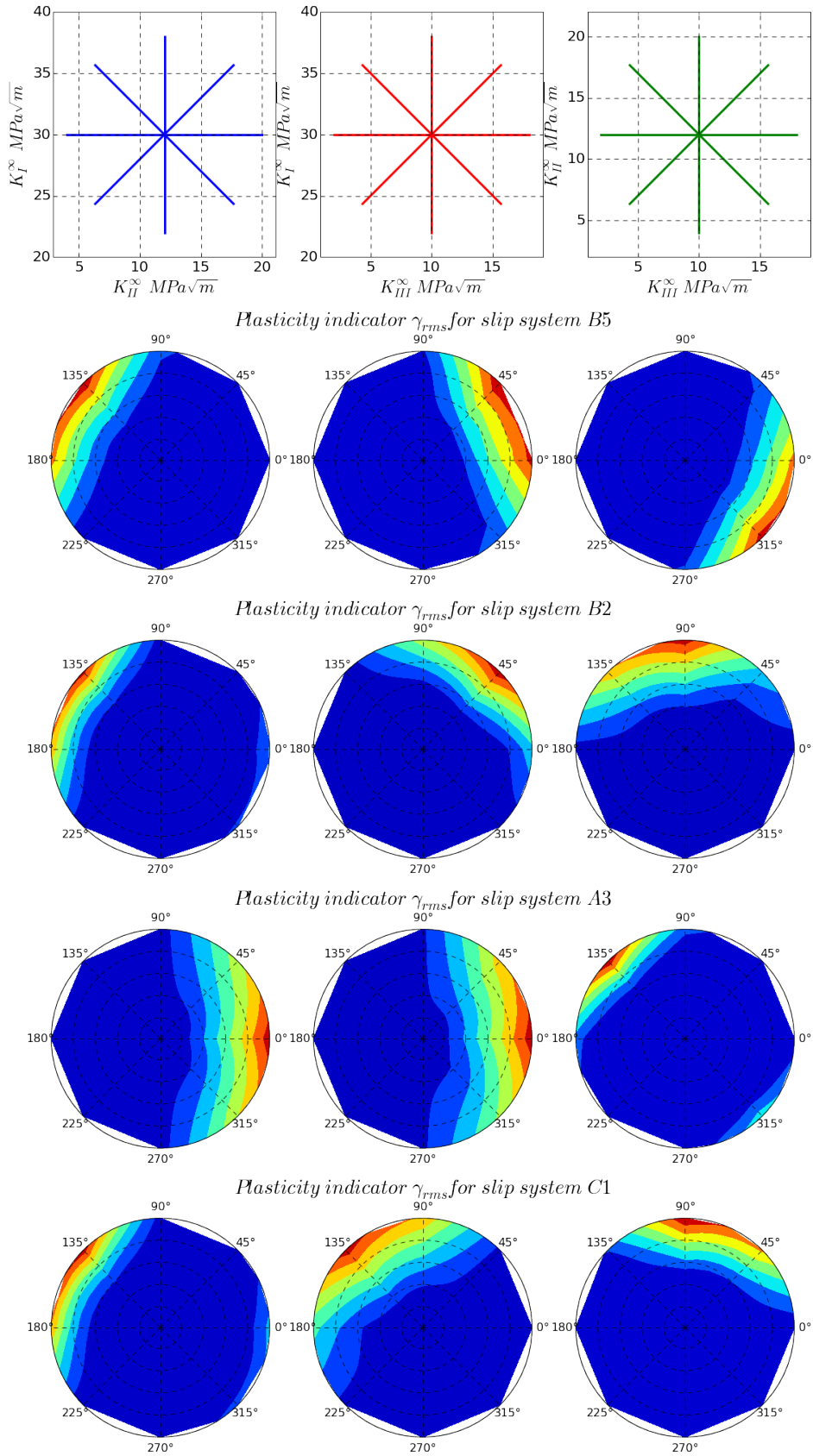


Figure 4.25: Yield indicator cartography for different slip systems and in different planes for orientation $\gamma_{\begin{smallmatrix} 010 \\ 100 \end{smallmatrix}}$

4.4.2 3D exploration

Exploration path and speedup analysis

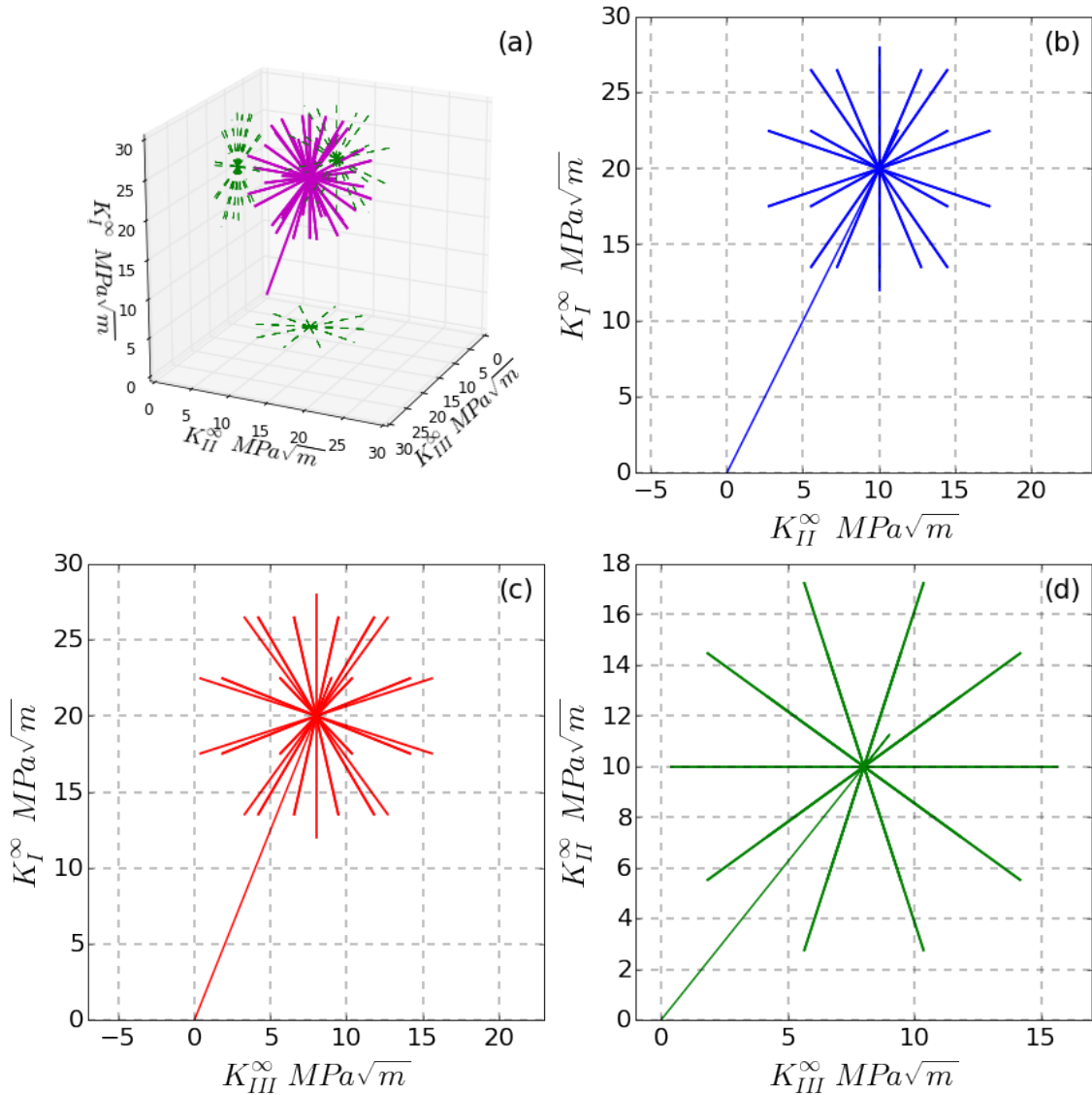


Figure 4.26: (a) Yield surface exploration path in the $K_I^\infty - K_{II}^\infty - K_{III}^\infty$ space and its projections on (b) $K_I^\infty - K_{II}^\infty$, (c) $K_I^\infty - K_{III}^\infty$ and (d) $K_{II}^\infty - K_I^\infty$ planes

One initial computation was performed with a given mixture ratio between the three fracture modes. An elastic back-loading is performed in order to take a distance from the yield limits. Then, 42 exploration computations were performed for each one of the 12 slip systems restarting from the last time increment of initial analysis which create a loading path similar to the shape of a spiked sphere. All this makes a total of 516 simulations to perform and then to post-process. Regarding this big number of elastic-plastic simulations over a 3D structure, an *ABAQUS* speedup analysis was initially performed on a representative simulation case in order to identify the optimum number of parallelization processors. As shown in figure 4.27, 8 CPUs seemed to present a good compromise be-

tween the gain in simulation time and the available resources at the LMT computation Cluster (CPUs and *ABAQUS* licenses).

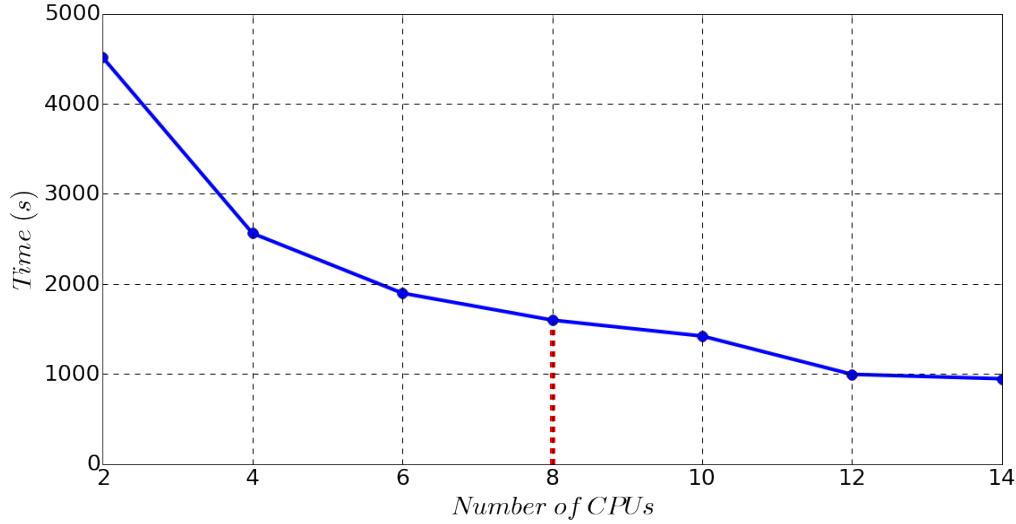


Figure 4.27: *ABAQUS* speedup analysis

Simulations and results

The root mean square value of the cumulated slip rate computed over the region of interest $\gamma_{rms}^s(t)$, defined in equation 4.34, is again used as a yield criterion. This quantity was computed on each branch of the exploration star. A threshold value γ_{rms}^c is set as an elasticity limit. We assume that below this value, no plasticity takes place at the region near the crack tip. When loading changes while exploring, the slip system is assumed to be activated as soon as the $\gamma_{rms}^s(t)$ reaches the critical value γ_{rms}^c . In that loading spot, a point is plotted in the K-nominals space.

Figure 4.28 shows that, for each one of the twelve octahedral slip systems studied in this work, these loading threshold points can be fitted to a plane, representing the yield surface of the corresponding slip system. Table 4.5 sums up the list of unit normal vectors to yield planes for different slip systems. The standard deviation of the residuals was computed as an indicator of the least squares fit quality. In an analogy with a standard generalized model and based on the assumption of normal dissipation, these normals represent the plastic flow that occurs in a direction normal to this yield plane.

We recall that these results were conducted with a single slip system implemented per set of computations. In order to verify the effect of the presence of other slip systems in the model, we conducted another exploration campaign where all octahedral slip systems were implemented together. On each loading branch of the spiked sphere, the twelve slip rates were extracted and the same yield criterion $\gamma_{rms}^s(t)$ was computed. Results show that not all slip systems were activated because of the dominance effect of some slip systems. However, for the activated ones, yield surfaces have almost the same normals found in the case of a separate implementation. This means that putting slip systems in competition does not affect the orientations of yield planes. Therefore, yield planes of each slip system

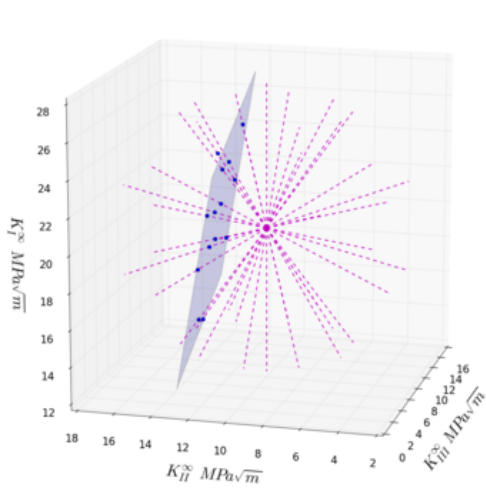
Table 4.5: Normals of yield planes and the fit root mean square errors for different octahedral slip systems for material orientation $\succ_{[100]}^{(010)}$

Slip system		normal $[K_{III}^\infty, K_{II}^\infty, K_I^\infty]$	Fit RMS Error
1	B4	[-0.84 , -0.52 , 0.16]	0.03
2	B2	[0.39 , -0.78 , 0.45]	0.015
3	B5	[0.83 , -0.48 , 0.27]	0.031
4	D4	[-0.74 , -0.66 , 0.04]	0.018
5	D1	[0.25 , 0.95 , 0.17]	0.098
6	D6	[-0.98 , -0.20 , 0.05]	0.08
7	A2	[-0.09 , 0.98 , 0.16]	0.062
8	A6	[0.46 , -0.74 , 0.48]	0.12
9	A3	[0.81 , -0.55 , 0.21]	0.23
10	C5	[-0.89 , -0.32 , 0.32]	0.21
11	C3	[0.89 , -0.41 , 0.17]	0.066
12	C1	[-0.10 , -0.92 , 0.37]	0.188

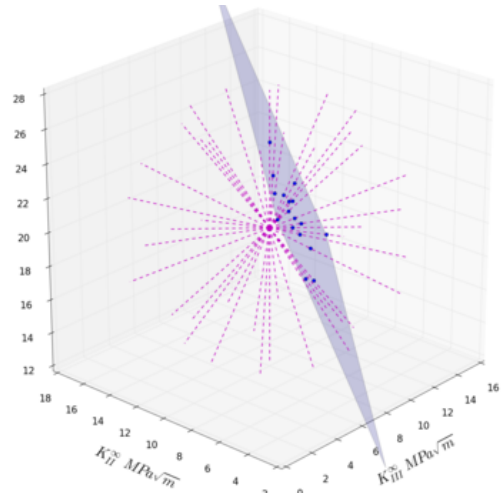
can be investigated independently and then put together following a dominance criterion in order to create a yield domain.

The reconstruction error criterion $C_e - C_{ep}$ was also implemented and computed on each loading branch and for each slip system. Kinematic fields of a given slip system $\underline{v}_s^{FE}(\underline{x}, t)$ were extracted from the region near the crack tip then projected on elastic reference fields $\underline{\phi}_i^{el}(\underline{x})$ to obtain the elastic intensity factors $\dot{K}_i(t)$, the residual field was projected on the corresponding complementary reference fields $\underline{\phi}_i^{pl,s}(\underline{x})$ in order to obtain the blunting intensity factors $\dot{\rho}_i^s(t)$ of the fracture mode i and slip system s .

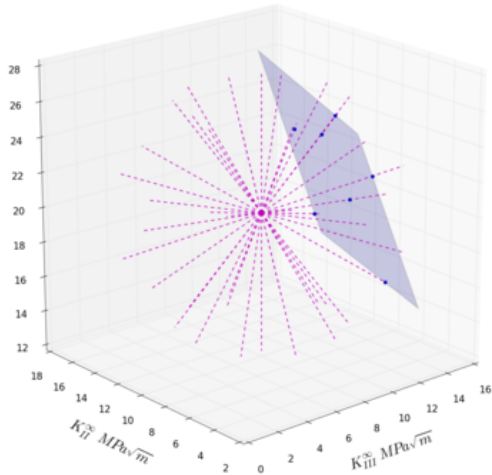
We note that for slip system $B5$, a good agreement was found between yield planes obtained by the reconstruction error as a yield criterion and the γ_{rms} criterion. For other slip systems, despite a convenient fit with planes using the $C_e - C_{ep}$ criterion is found, those planes were different from those found using the γ_{rms} criterion.



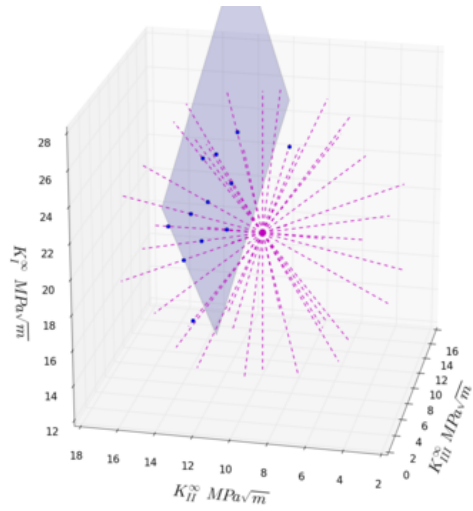
(a) Yield plane for slip system $A2$



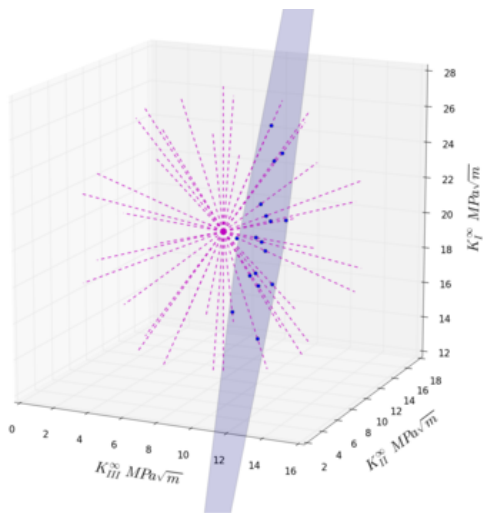
(b) Yield plane for slip system $B5$



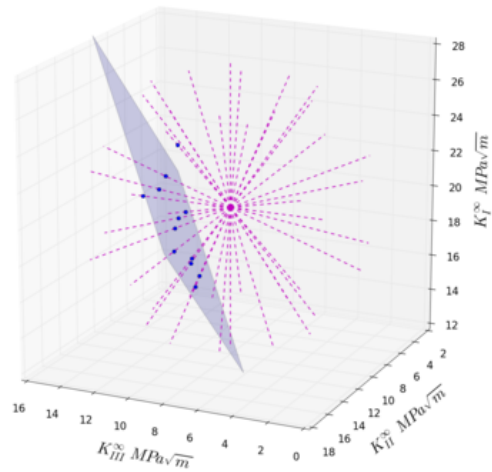
(c) Yield plane for slip system $B2$



(d) Yield plane for slip system $D1$



(e) Yield plane for slip system $B4$



(f) Yield plane for slip system $C5$

Figure 4.28: Yield planes in $K_I^\infty - K_{II}^\infty - K_{III}^\infty$ space for crystallographic orientation $\gamma_{\begin{smallmatrix} 010 \\ 100 \end{smallmatrix}}$

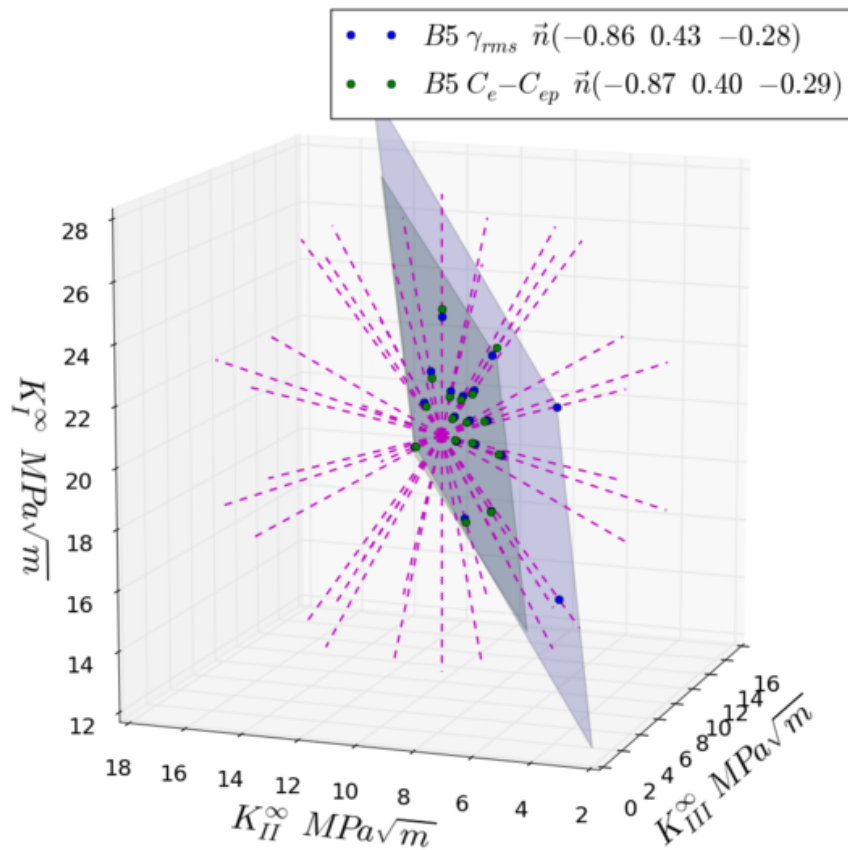


Figure 4.29: Yield plane in $K_I^\infty - K_{II}^\infty - K_{III}^\infty$ space for slip system $B5$, comparison between γ_{rms} criterion and the reconstruction error ($C_e - C_{ep}$) criterion

Exploration of other yield planes

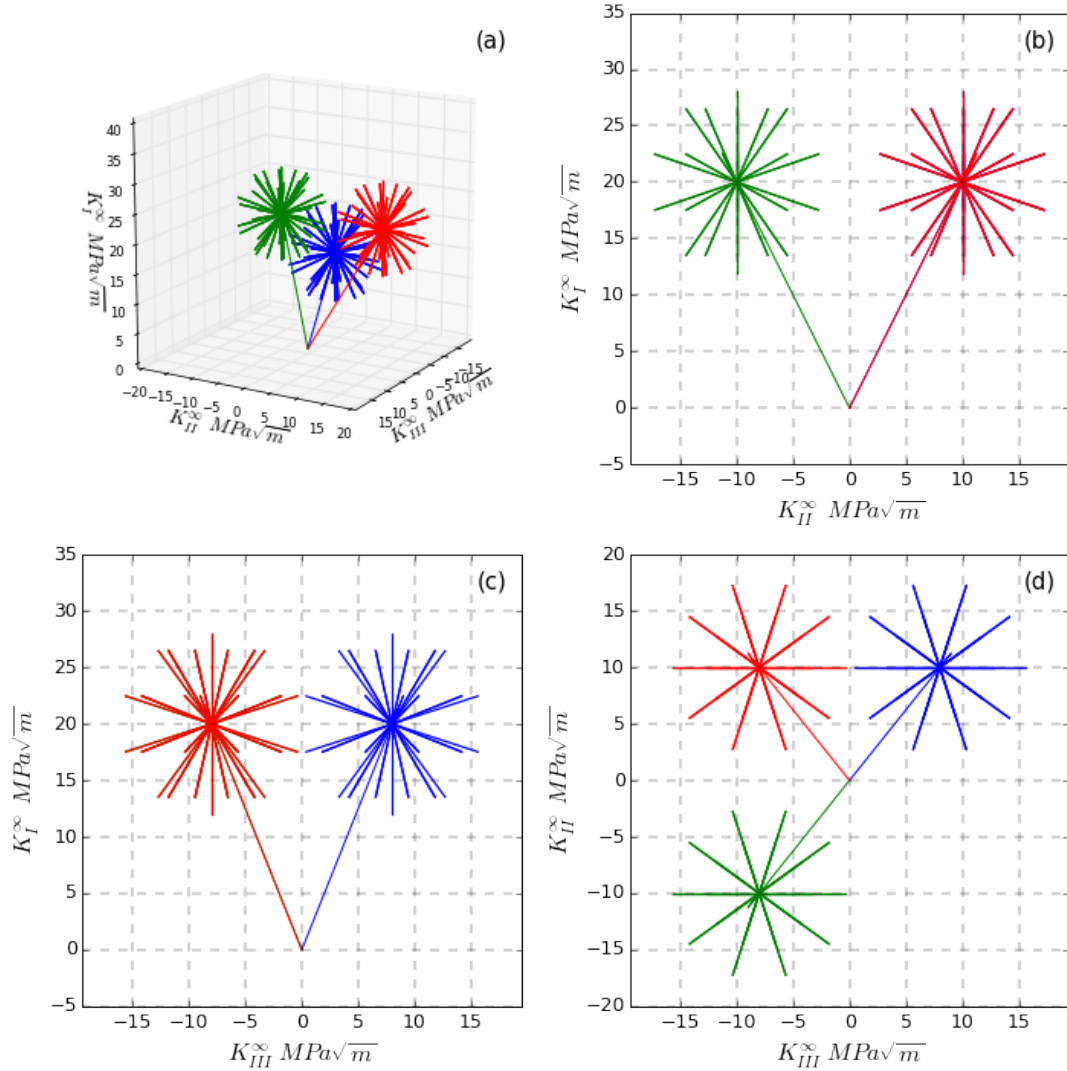


Figure 4.30: Yield surface exploration path in the $K_I^\infty - K_{II}^\infty - K_{III}^\infty$ space with different initial loading directions.

Previous loading campaigns were conducted with an initial mixture ratio where the position of the spiked sphere center is at $K_{IIIc}^\infty = 8 \text{ MPa}\sqrt{\text{m}}$, $K_{IIc}^\infty = 10 \text{ MPa}\sqrt{\text{m}}$ and $K_{Ic}^\infty = 20 \text{ MPa}\sqrt{\text{m}}$ (Blue loading path in figure 4.30). These analyses gave one plane per slip family as a yield surface. According to Rice's work [Rice, 1987] and as shown on figure 4.23, each slip system corresponds to two parallel segments of the yield surface in the stress space. One can assume that each segment refers to a plane in the K-nominals 3D space. Thus, it is important to investigate the eventual presence of other yield planes per slip system. The idea is to explore different initial directions.

Only slip systems of normal $\vec{n} = (111)$ were implemented. For $B4$, $B2$ and $B5$, an initial mixture ratio was performed so that $K_{IIIc}^\infty = -8 \text{ MPa}\sqrt{\text{m}}$, $K_{IIc}^\infty = -10 \text{ MPa}\sqrt{\text{m}}$ and $K_{Ic}^\infty = 20 \text{ MPa}\sqrt{\text{m}}$ (Green loading path in figure 4.30). For both $B4$ and $B2$, opposite

planes were found. As shown in table 4.6, these yield surfaces have almost the same normals as the first yield planes but are located in the opposite side with respect to the center of loading sphere. For slip family $B5$, the same yield surface initially described by the first loading campaign was found. Figure 4.31 shows these two planes in blue and green in multiple views. Therefore, a third exploration was performed with an initial loading $K_{IIIc}^\infty = -8 \text{ MPa}\sqrt{\text{m}}$, $K_{IIc}^\infty = 10 \text{ MPa}\sqrt{\text{m}}$ and $K_{Ic}^\infty = 20 \text{ MPa}\sqrt{\text{m}}$ (Red loading path in figure 4.30). This third loading campaign led to an opposite yield plane parallel to the ones initially found. This yield surface is represented in red in figure 4.31.

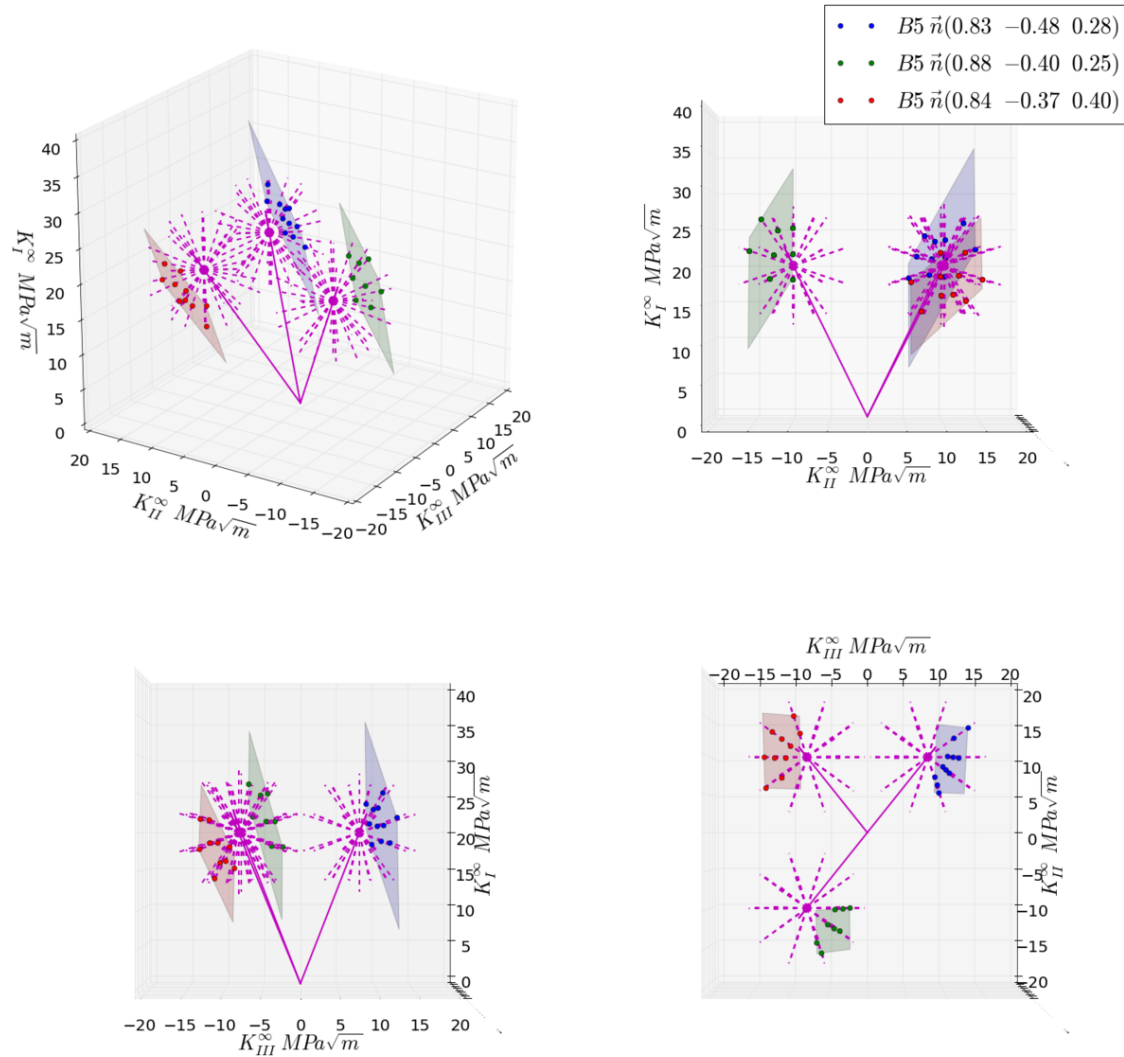


Figure 4.31: Yield planes of the slip system $B5$ obtained from different initial loading ratios. Two yield planes can be identified, the first is represented by the red plane and the second is represented by both the blue and the green planes

We made a generalization from these explored cases that each slip system has two parallel yield planes. Regarding the kinematic hardening effect, the position of the yield plane changes with the loading history. This position should be determined for each center of the spiked sphere loading path. The position of the second yield plane for a given

Table 4.6: Normals of yield planes with different initial loading mixture ratios for slip systems of normal (111) for orientation $\gamma_{[100]}^{(010)}$.

Slip system	$[K_{III}^\infty, K_{II}^\infty, K_I^\infty]$ (MPa \sqrt{m})	normal $[K_{III}^\infty, K_{II}^\infty, K_I^\infty]$	Fit RMS Error
1	[8, 10, 20]	[-0.84 , -0.52 , 0.16]	0.03
	[-8, -10, 20]	[-0.86 , -0.47 , 0.16]	0.023
2	[8, 10, 20]	[0.39 , -0.78 , 0.45]	0.015
	[-8, -10, 20]	[0.28 , -0.88 , 0.37]	0.061
3	[8, 10, 20]	[0.83 , -0.48 , 0.27]	0.031
	[-8, -10, 20]	[0.88 , -0.40 , 0.25]	0.006
	[-8, 10, 20]	[0.84 , -0.37 , 0.39]	0.147

initial loading ratio is simply found by loading, from the center of the “spiked sphere”, in a direction normal but from the opposite side of the initial yield plane. The $\gamma_{rms}^s(t)$ is determined on this loading branch. When this yield criterion reaches the critical value γ_{rms}^c , a point is plotted in the K-nominals space as a position of the second yield plane.

4.4.3 Yield domain

As discussed before, a yield convex domain can be constructed by combining yield surfaces of different slip systems [Rice, 1987]. This elasticity domain is represented by the minimum convex volume found as the intersection between different yield surfaces. We decided to use yield surfaces found in a separate implementation when each slip family is investigated independently. These analyses give the same yield surfaces found when combining all octahedral slip systems whereas they provide a finer exploration with more precision.

According to computations from the previous subsection, two yield planes are assigned to each slip system. The minimum convex volume obtained from the combination of these yield planes is a polyhedron as shown in figure 4.32. The shape and size of this polyhedron depend on the value of the critical value γ_{rms}^c chosen as a yield limit. Each vertex of the obtained yield domain corresponds to a constant stress state on a given sector near the crack tip region.

Note: Strain hardening was neglected in Rice’s work with elastic-ideally plastic crystal but in our case, with the presence of a kinematic hardening, it was not neglected. Therefore, the yield locus depends on the plastic deformation.

Note: The crystal slip systems rotations with respect to the material axes can cause a “geometric” hardening or softening [Rice, 1987]. This behavior was neglected since this work is formulated within the small strain approximation.

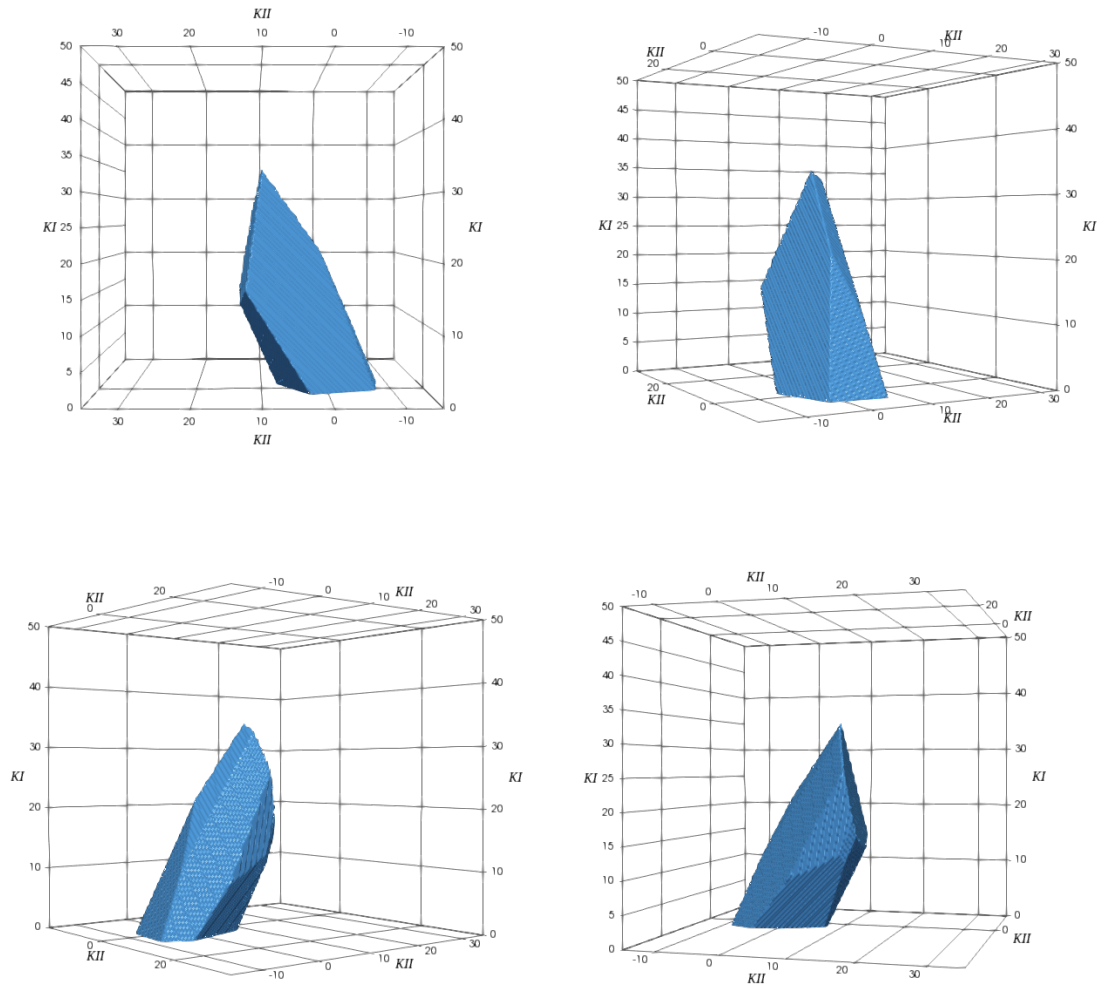


Figure 4.32: Yield domain of the region near the crack tip in the K -nominals space for material orientation $\gamma_{\begin{smallmatrix} (010) \\ [100] \end{smallmatrix}}$.

4.5 Updated reference fields

4.5.1 Decomposition principle

Under the assumption of a standard generalized model and according to normal dissipation principle, plastic flow and hence dissipation is maximum in a direction normal to the yield locus. The idea here is to maximize the plastic strain flow on a given slip system in order to obtain a significant plastic field that can be considered as a reference and representative field of the slip system in consideration. For this reason, a unique slip system is implemented each time and a loading in the direction normal to the yield plane of that slip system is performed. Kinematic fields are then extracted from the region of interest near the crack tip. After subtracting elastic fields of the three fracture modes from these elastic-plastic fields, the remaining quantity represents the plastic kinematic field caused by the plastic strain flow on the implemented slip system. A time-space decomposition is then applied on this field through a POD in order to obtain the reference plastic field corresponding to the slip system in consideration.

$$\tilde{\underline{v}}_s^{pl}(\underline{x}, t) = \dot{\rho}^s(t) \underline{\phi}^{pl,s}(\underline{x}) = \underline{v}_s^{FE}(\underline{x}, t) - \sum_{i=1}^3 \dot{K}_i(t) \underline{\phi}_i^{el}(\underline{x}) \quad (4.38)$$

where $\underline{v}_s^{FE}(\underline{x}, t)$ is the elastic-plastic kinematic field at the region near the crack tip of a unique implemented slip system s . This field is obtained from a monotonic loading in a direction normal to the yield planes of the slip system in consideration.

For a given crystallographic orientation, twelve plastic reference fields corresponding to the twelve octahedral slip systems have to be defined. These fields, with elastic reference fields, will represent the kinematic basis of the nonlocal approach. This procedure is based on the knowledge of normals to yield planes of different slip systems previously investigated. Finally, kinematic field at the region of interest of a cracked single crystal with all of its octahedral slip systems can be approximated as follows:

$$\underline{v}^{FE}(\underline{x}, t) \approx \sum_{i=1}^3 \dot{K}_i(t) \underline{\phi}_i^{el}(\underline{x}) + \sum_{s \in G} \dot{\rho}^s(t) \underline{\phi}^{pl,s}(\underline{x}) \quad (4.39)$$

where $\underline{v}^{FE}(\underline{x}, t)$ is the total kinematic field of an elastic-plastic finite element simulation and $\underline{\phi}^{pl,s}(\underline{x})$ is the plastic reference field of the slip family s . These fields are presented and discussed in the next paragraph.

4.5.2 Reference fields

Yield planes for the crystallographic orientation $\succ_{[100]}^{(010)}$ had been already identified in a section 4.4.2. Based on these analyses, a simulation campaign was conducted in order to identify plastic reference fields for this orientation.

For a given implemented slip system s , a monotonic loading was performed in the direction normal to the yield surface of the slip system s . These directions are summed

up in table 4.5. The equivalent loading K_{eq}^∞ was kept always the same for all simulations $K_{eq}^\infty = \|\underline{K}^\infty\| = 40 \text{ MPa}\sqrt{\text{m}}$. For each monotonic loading, the quadratic mean of the cumulated slip rate $\gamma_{rms}^s(t)$ was computed. Figure 4.33 shows the normalized evolution of these quantities.

On the one hand, it was observed that, for material orientation $\succ_{[100]}^{(010)}$, slip systems behaved identically two by two when the same applied loading is symmetric with crack coordinate system (pure *mode I*, pure *mode II* or pure *mode III*). On the other hand, the observed results of a loading in a random direction with no symmetry with the crack plane would not give this two by two behavior.

For the present case, loadings were performed in different directions since every slip family has a different normal to yield surface. Besides, these loading directions have no symmetry with the crack. However, the two by two behavior of different slip systems is still observed.

Moreover, figure 4.33 shows that, unlike what was observed when loading in a pure fracture mode (see figures 4.19, 4.20 and 4.21), loading in normal directions had activated all slip systems with different magnitudes.

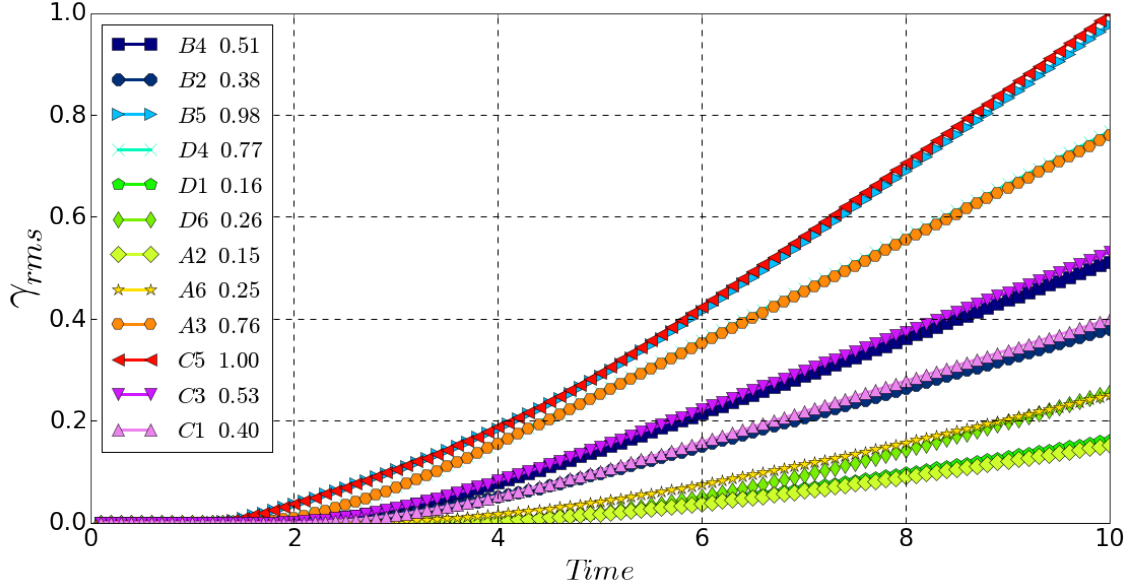


Figure 4.33: γ_{rms} computed from different slip systems and different loading directions (normal to the yield surface).

Fields from these simulations were extracted from the region of interest then post-processed to obtain complementary reference fields. Then, these fields were assembled together in the same snapshot matrix and a Proper Orthogonal Decomposition is applied in order to obtain the same radial function. Radial function $f^{pl}(r)$ and angular functions $\underline{g}_s^{pl}(\theta)$ are shown in figure 4.34.

$$\underline{\phi}^{pl,s}(\underline{x}) = f^{pl}(r) \cdot \underline{g}_s^{pl}(\theta) \quad (4.40)$$

$f^{pl}(r)$ represents the exponential decay in the scale of magnitude of complementary fields while shifting away from the crack tip. Angular functions $\underline{g}_s^{pl}(\theta)$ were applied to a trigonometric circle and sized to have the same norm of the opening vector $\|\underline{g}_s^{pl}(\pi) - \underline{g}_s^{pl}(-\pi)\|$.

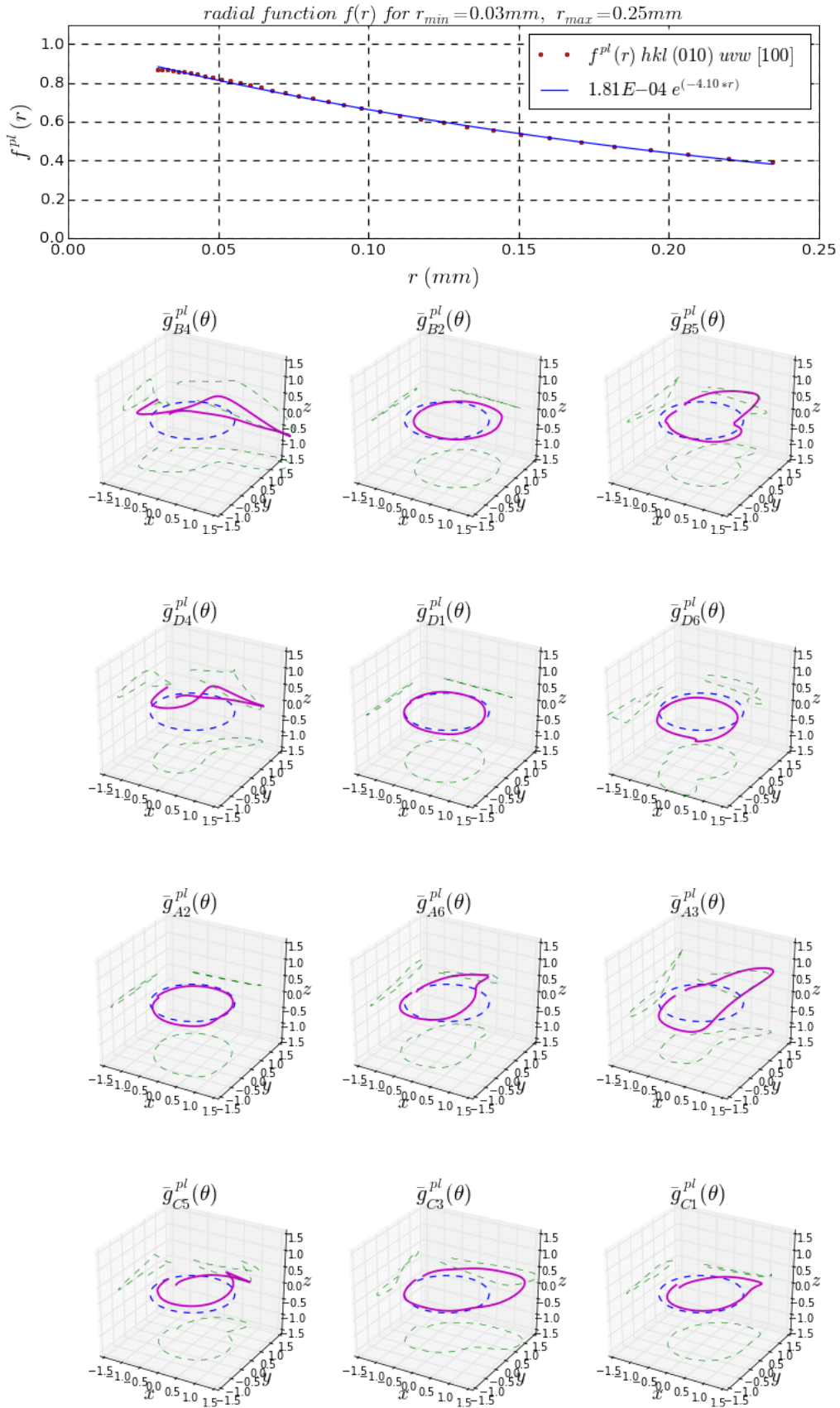


Figure 4.34: Radial function $f^{pl}(r)$ and angular distributions $\bar{g}_s^{pl}(\theta)$ of different complementary reference fields $\underline{\phi}_s^{pl}(\underline{x})$ for crystallographic orientation $\gamma_{[100]}^{(010)}$.

Linear plots of the components of some angular functions $g_s^{pl}(\theta)$ are shown in figures 4.35 and 4.36. Due to symmetry considerations of the crystallographic orientation $\gamma_{[100]}^{(010)}$ with respect to the crack plane and direction, complementary reference fields are found to be similar two by two in absolute value since components on \vec{x} and \vec{y} axes are the same and components on \vec{z} axis are of opposite sign.

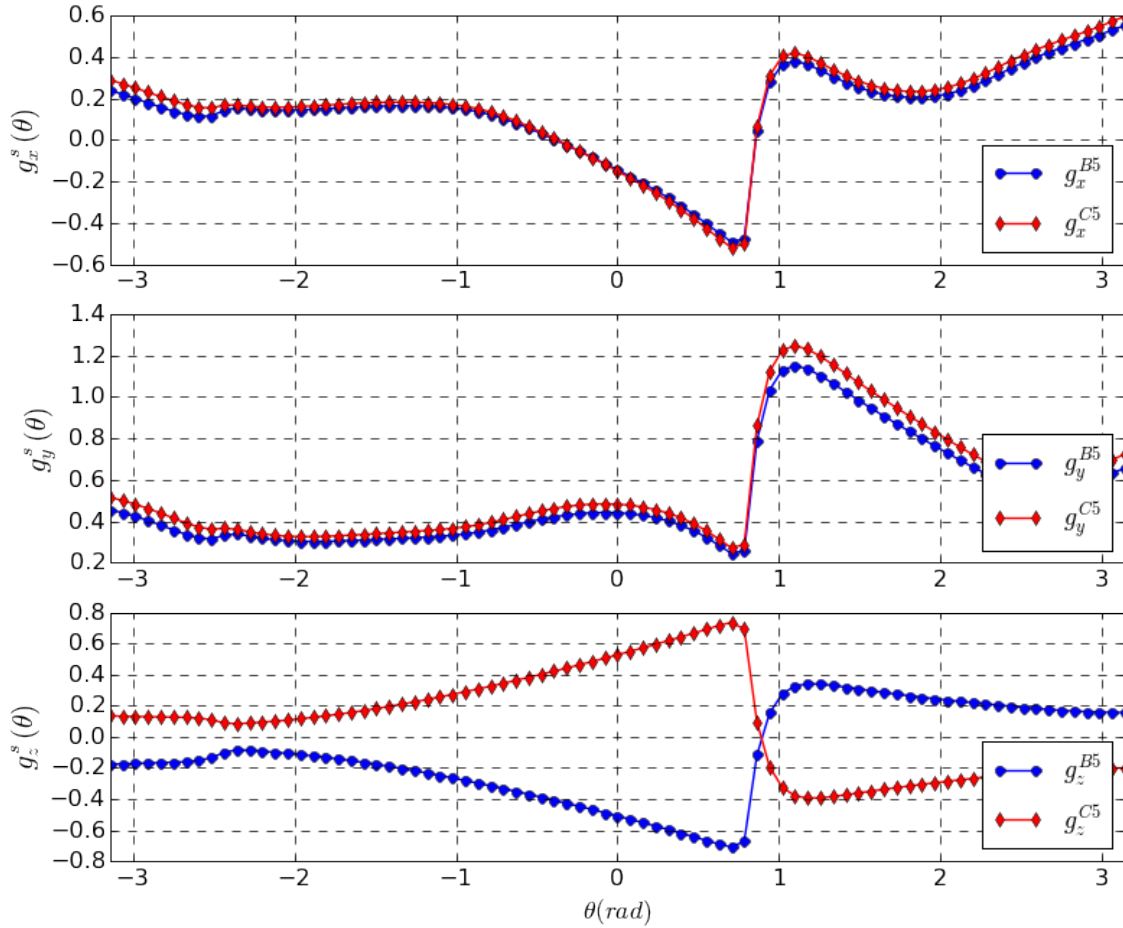


Figure 4.35: Linear plots of $\underline{\phi}^{pl,s}(\underline{x})$ components of slip systems $B5$ and $C5$ for crystallographic orientation $\gamma_{[100]}^{(010)}$.

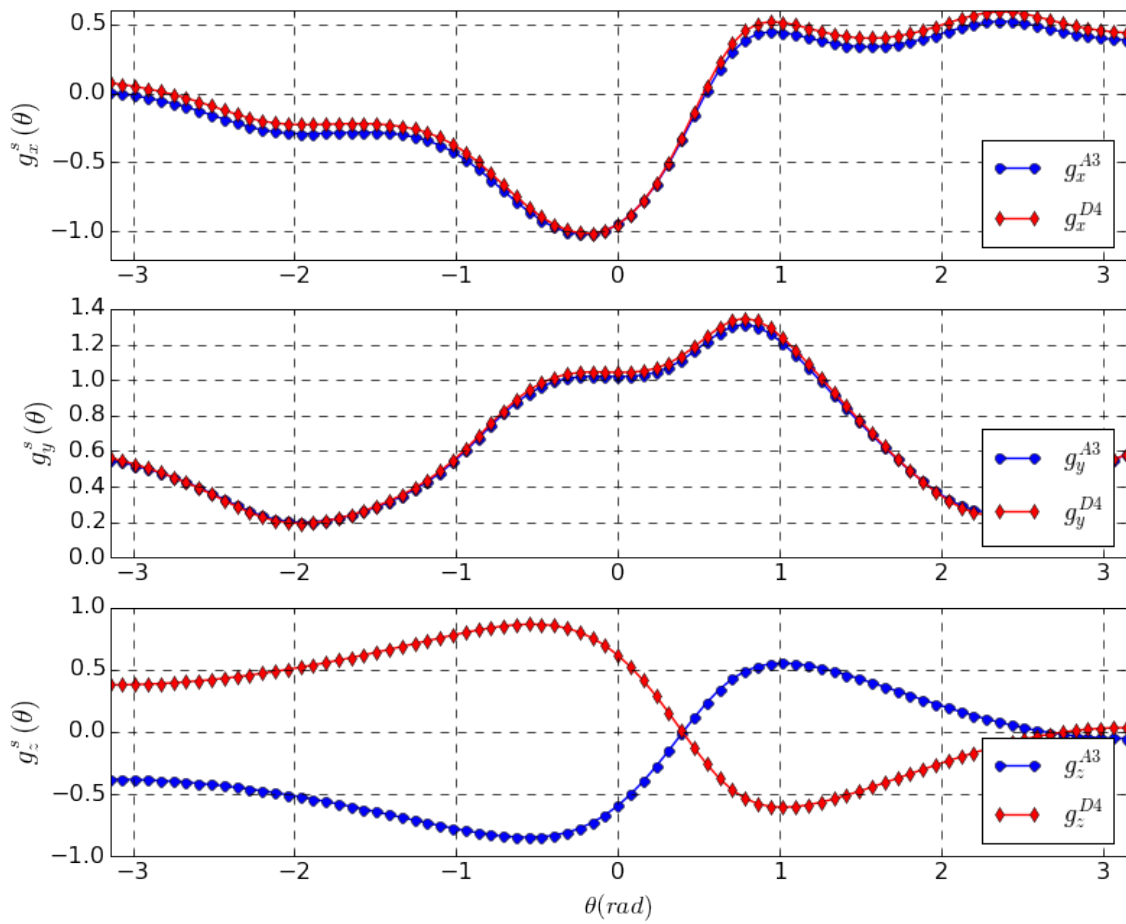


Figure 4.36: Linear plots of $\underline{\phi}^{pl,s}(\underline{x})$ components of slip systems $A3$ and $D4$ for crystallographic orientation $\gamma_{\begin{smallmatrix} 010 \\ 100 \end{smallmatrix}}$.

4.5.3 Schmid factor based on Hoenig analytical solutions and slip systems “non-local” dominance criterion

Reference fields discussed before will serve as a projection basis for elastic-plastic kinematic fields in order to extract nonlocal quantities $\dot{\rho}^s(t)$. However, unlike previous complementary fields based on crack symmetries, reference fields $\underline{\phi}^{pl,s}(\underline{x})$ are not orthogonal by construction. Therefore, it is important to investigate the effect of each slip system on the evolution of plasticity near the crack tip region. This will help quantifying the contribution of each slip system in the nonlinear part of the kinematic field. The activity of a slip system is effective when it is dominant on a given sector due to its persistence and uniqueness characters. For this reason, the concept of dominant slip system needs to be studied and discussed.

Dominant slip system

The yielding of single crystals takes place on a given slip system when the resolved shear stress $\tau^s(r, \theta)$ reaches a critical value τ^c . When loading increases, the plastic slip at a given location (r, θ) occurs on the plane and in the direction that have the highest resolved shear stress. The slip system that experienced this plastic slip straining is called the “dominant” (or primary) slip system at that location [Arakere et al., 2009]. This dominance persists with higher loadings and no other slip systems take place at that location (r, θ) [Westbrooke, 2005], [Ebrahimi et al., 2006], [Arakere et al., 2009]. As mentioned in subsection 4.3.3, the softening effect and slip localization can explain the persistence of this slip. Besides, the occurrence of plasticity causes a significant drop in the resolved shear stress on other slip systems which explains the uniqueness of the slip system in consideration.

Based on this definition, the region near the crack tip can be divided into spatial sectors of constant stress in which a slip system is dominant. Boundaries between sectors represent the transition from a dominant slip system to another. Rice [Rice, 1987] had shown that the stress state near the crack tip remains uniform within small ranges of theta then it varies discontinuously when crossing sector boundaries. He mentioned that, for crystallographic orientations $\succ_{[101]}^{(010)}$ and $\succ_{[010]}^{(101)}$ of an FCC cracked single crystal, the stress state evaluated on a given sector corresponds to a vertex on the yield surface plotted on the stress space with $\frac{1}{2}(\sigma_{11} - \sigma_{22})$ and σ_{12} axes (see figure 4.23). Regarding the symmetries of these two orientations with respect to the crack, Rice found that each sector corresponds to the yielding of two families of slip systems. Which corresponds to the two by two behavior previously mentioned in this work for material orientation $\succ_{[100]}^{(010)}$.

Dominance criterion

Arakere and co-workers [Arakere et al., 2009] had shown that the “*elastic anisotropy governs the development of the elastic stress field and controls which slip systems become initially dominant/activated*”. They showed experimentally that the initiation of plasticity does not change significantly the state of stress calculated based on the linear elastic approach. This means that a linear anisotropic elastic analysis is sufficient to predict the stress field evolution and distribution near the crack tip of a single crystal even with the presence of yielding. This prediction can stay valid even at higher applied loadings due to the persistence in the dominance of slip systems. It is obvious that the elastic solution will

miss some nonlinear effects because of plasticity. However, it serves in the development of a dominance criterion since it can identify which slip system is initially activated at a given location. The nonlinear effect is taken into account into the model developed in this work since informations about plasticity are already included in the complementary reference fields.

The idea is to obtain a dominance criterion based on the theoretical analysis of the elastic anisotropic stress solution. Many experimental studies were conducted based on the footsteps of Rice and co-workers ([Rice, 1987], [Rice and Saeedvafa, 1987], [Saeedvafa and Rice, 1989], [Rice et al., 1990]). In his original work, Rice developed an asymptotic analysis of stress and strain at the crack tip region of an FCC and BCC elastic-ideally plastic single crystals under 2D plane-strain assumption.

Arakere and co-workers ([Arakere et al., 2009], [Ebrahimi et al., 2006], [Sabnis et al., 2012]) have shown considerable disagreement between activated slip systems and sectors predicted by Rice's analytical solutions and slip traces observed experimentally. However, they found a satisfactory matching between experiments and three-dimensional finite element simulations that incorporate an elastic anisotropic material behavior. Crone and Shield [Crone and Shield, 2001] , [Crone and Shield, 2003] experimentally investigated strain fields near a notch tip in Copper and Copper-Beryllium single crystals for the same crystallographic orientations explored by [Rice, 1987]. Although results validated the existence of constant stress sectors with discontinuity along sector boundaries, they disagreed with the sector boundary angles predicted theoretically by Rice.

Hoening's stress solution and corresponding Shmid factor

As shown in chapter 3, Hoening's analytical solution is accurate when it comes to predicting elastic displacement and stress fields at the vicinity of the crack tip. Based on the Lekhnitskii formalism, [Hoening, 1982] presented the general elastic analytical solution of stress near the crack tip of an anisotropic body as follows:

$$\begin{aligned}
 \sigma_{xx} &= \frac{1}{\sqrt{2\pi r}} \Re \left[\sum_{i=1}^3 \frac{p_i^2 N_{ij}^{-1} K_j^\infty}{Q_i} \right] & \sigma_{yy} &= \frac{1}{\sqrt{2\pi r}} \Re \left[\sum_{i=1}^3 \frac{N_{ij}^{-1} K_j^\infty}{Q_i} \right] \\
 \sigma_{xy} &= -\frac{1}{\sqrt{2\pi r}} \Re \left[\sum_{i=1}^3 \frac{p_i N_{ij}^{-1} K_j^\infty}{Q_i} \right] & \sigma_{zx} &= \frac{1}{\sqrt{2\pi r}} \Re \left[\sum_{i=1}^3 \frac{p_i \lambda_i N_{ij}^{-1} K_j^\infty}{Q_i} \right] \\
 \sigma_{zy} &= -\frac{1}{\sqrt{2\pi r}} \Re \left[\sum_{i=1}^3 \frac{\lambda_i N_{ij}^{-1} K_j^\infty}{Q_i} \right] & \sigma_{zz} &= \frac{1}{\sqrt{2\pi r}} \Re \left[\sum_{i=1}^3 \frac{\alpha_i N_{ij}^{-1} K_j^\infty}{Q_i} \right]
 \end{aligned} \tag{4.41}$$

under plane strain assumption:

$$\alpha_i = -\frac{1}{S_{33}} \left[S_{31} p_i^2 + S_{32} - S_{34} \lambda_i + S_{35} p_i \lambda_i - S_{36} p_i \right] \tag{4.42}$$

Taking θ as the angular position around the crack, vector Q_i is defined as follows:

$$Q_i = \sqrt{\cos \theta + p_i \sin \theta} \tag{4.43}$$

K_i is the vector of stress intensity factors:

$$K_i^\infty = \begin{pmatrix} K_I^\infty \\ K_{II}^\infty \\ K_{III}^\infty \end{pmatrix} \quad (4.44)$$

The matrix N_{ij} and vectors p_i and λ_i are previously presented in [chapter 3](#) section [3.2.1](#) and in [Appendix A](#).

We recall that there are some special cases of anisotropy that lead to a mathematically degenerate development. Further details about these cases are provided in [Appendix A](#).

Based on this analytical development, the resolved shear stress can be obtained theoretically by projecting the stress tensor solution on the Schmid factor \underline{m}^s :

$$\begin{aligned} \tau^s(r, \theta) &= \underline{m}^s : \underline{\sigma}(r, \theta) \\ &= \frac{1}{\sqrt{2\pi r}} \Re \left[\sum_{i=1}^3 \frac{N_{ij}^{-1} K_j^\infty}{Q_i} (p_i^2 m_{11}^s + m_{22}^s + \alpha_i m_{33}^s - 2p_i m_{12}^s + 2p_i \lambda_i m_{13}^s - 2\lambda_i m_{23}^s) \right] \end{aligned} \quad (4.45)$$

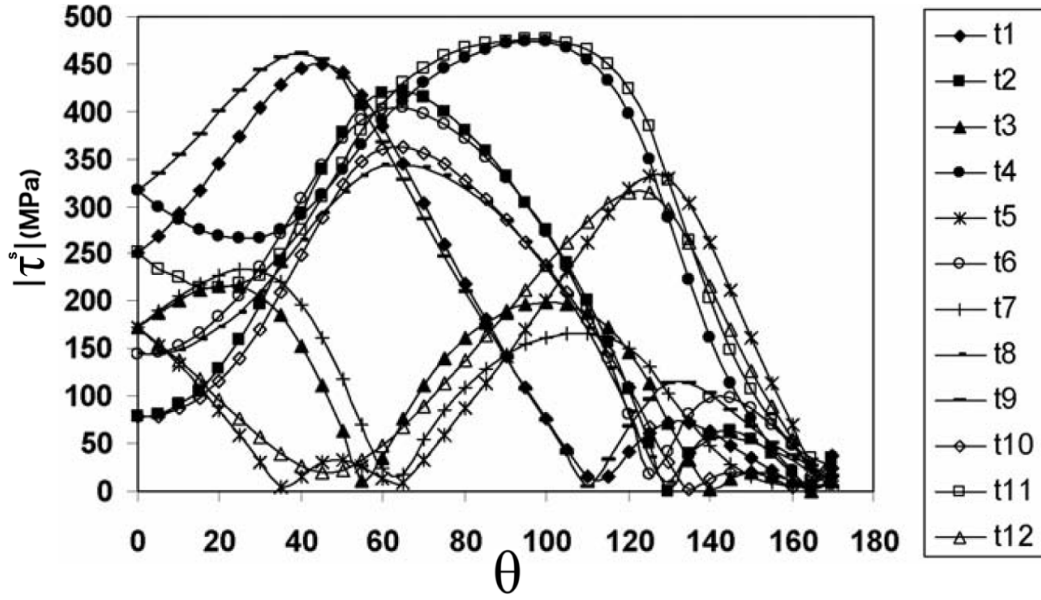
Note: Since the stress solution is expressed in the crack reference, \underline{m}^s , usually expressed in the crystal coordinates system, should be also expressed in this same coordinates system of the crack.

These theoretical developments were implemented in the technical computing software *Mathematica*. As a primary observation, analytical results confirmed that each sector represents the activation of two slip systems and some times four for some orientations that have a symmetry with the crack plane and direction.

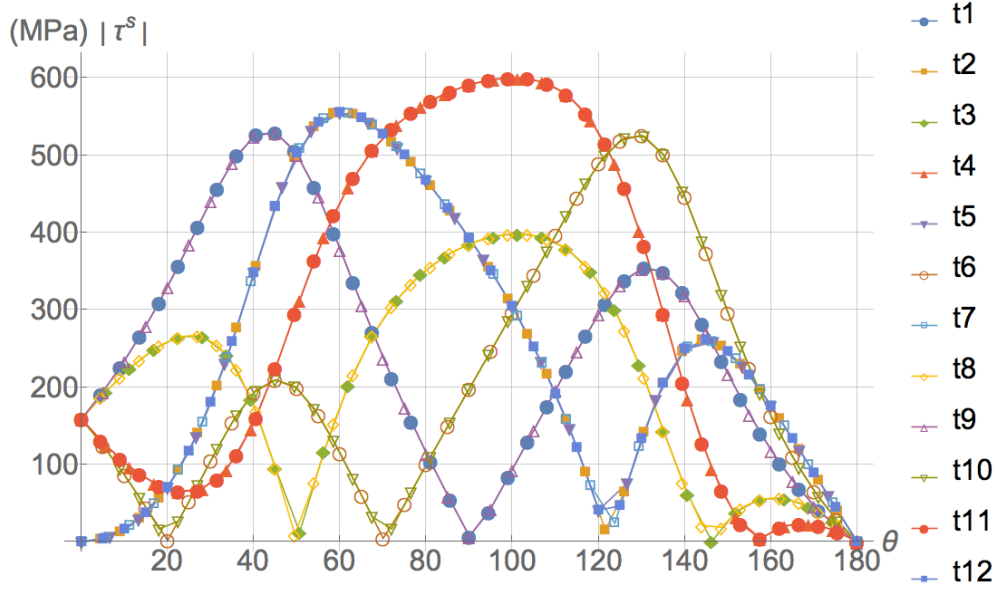
Comparison between theoretical, numerical and experimental analyses

Ebrahimi and co-workers ([\[Ebrahimi et al., 2006\]](#)) studied the plasticity near the notch in a Ni-base superalloy single crystal. Experimental results were compared to those from finite element simulations of a double-notched specimens under tensile loading. A good agreement between both results was concluded. [Figure 4.37a](#) shows numerical results of the distribution of different resolved shear stresses for the material orientation $\succ_{[010]}^{(001)}$ at a radius $r = 5\rho$, with ρ is the notch height. [Figure 4.37b](#) shows this same distribution computed analytically based on the expression presented in [equation 4.45](#) at the same distance r from the crack tip and the same applied loading $K_I^\infty = 45 \text{ MPa}\sqrt{\text{m}}$. These results show a reasonable agreement in the stress distribution and in the dominant slip system corresponding to each angular sector.

The geometry responsible for the stress concentration in [\[Ebrahimi et al., 2006\]](#) is a double notched specimen with a quite short length while the asymptotic solutions of Hoenig [\[Hoenig, 1982\]](#) were developed for the case of a straight crack subjected to a uniform far stress. This major differences may explain the difference between both results. Besides, secondary orientations measured on the experimentally tested samples were some times off by small angles (less than 8°). It seems that authors took into account this small twist of



(a)



(b)

Figure 4.37: Resolved shear stresses distribution at $r = 5\rho$ for material orientation $\gamma_{[010]}^{(001)}$ τ^s , (a) Finite element simulations ([Ebrahimi et al., 2006]), (b) analytical results based on Hoenig's solutions

the secondary orientation of the crystal in the simulation part. This small twist explains the small difference between some slip system couples that exhibit analytically the same behavior, i.e. between slip systems $B4(\tau^1)$ and $A3(\tau^9)$.

Another comparison was made between experimental, numerical and theoretical results. In the work done by [Sabnis et al., 2012], the notch-tip plasticity was investigated in superalloy single crystals. Considering the crystal growth direction $[001]$ as a primary orientation, authors represented the effect of secondary orientation on the evolution of plastic fields near the notch. A tensile loading was applied with a magnitude of $K_I^\infty = 50 \text{ MPa}\sqrt{\text{m}}$ on a single crystal oriented $\succ_{[\bar{1}10]}^{(001)}$ with respect to the notch. Figure 4.38a shows the slip sectors at the region near the notch found with cubic elasticity computations and superposed to experimentally observed slip traces. Figure 4.38b shows experimentally obtained slip bands. Figure 4.38c shows the distribution of analytical resolved shear stresses (see equation 4.45) at the region near the crack tip for the same material orientation $\succ_{[\bar{1}10]}^{(001)}$. Taking into account that these results correspond to two different geometrical defaults, one can conclude that a reasonable agreement is observed between both results.

As observed experimentally and as predicted by the Crystal Plasticity Finite Element Analysis (CPFEA) done by [Sabnis, 2012] for this material orientation $\succ_{[\bar{1}10]}^{(001)}$, slip systems B4, B2, D1, A2, C3 and C1 are the most active ones. In a second row, B5, D4, A3 and C1 are less activated and finally, A6 and D6 are not activated at all. These observations can be interpreted also from theoretical distributions of stresses. Theoretical results exhibit a two by two behavior of slip systems due to symmetry of the crystal with respect to crack plane. This behavior is hard to be observed in experiments since the secondary material orientation is not perfectly controlled, therefore no perfect symmetry can be obtained. The lack of perfect symmetry in the stress distribution near the crack tip region prevents the simultaneous yielding of two slip systems in a given sector.

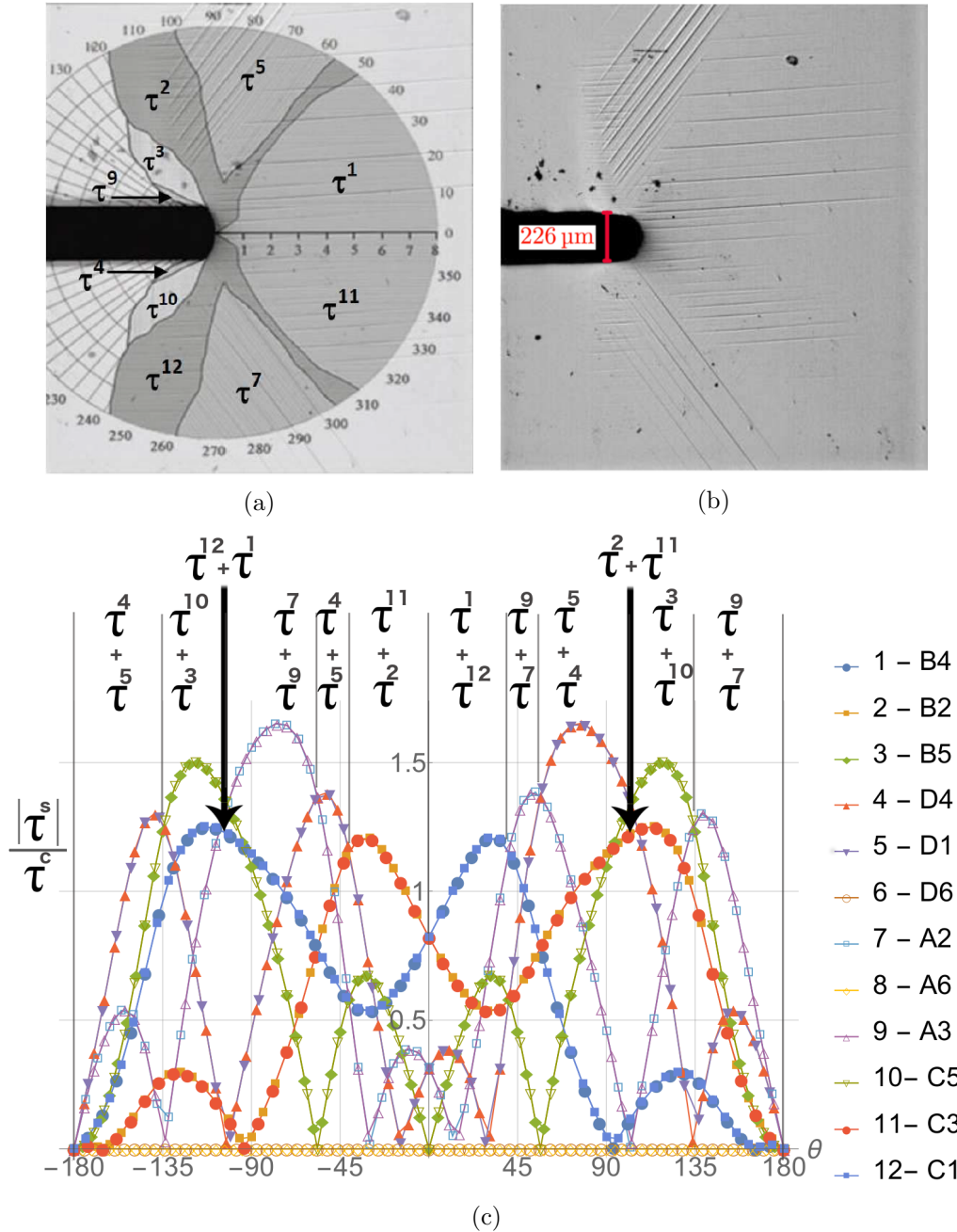


Figure 4.38: Resolved shear stresses for material orientation $\gamma_{[110]}^{(001)}$ under a tensile test with $K_I^\infty = 50 \text{ MPa}\sqrt{\text{m}}$ (a) Numerical slip sectors superposed to experimental slip traces, (b) experimental slip bands [Sabnis et al., 2012] and (c) resolved shear stress distributions at the region near the crack tip based on Hoenig's analytical solutions

Non linear basis

As shown in the previous part, the distribution of resolved shear stresses can be identified theoretically with a quite good precision. This identification can be used as a criterion to tell which complementary reference field $\underline{\phi}^{pl,s}(\underline{x})$ can be firstly used in the kinematic basis. In the following work, some methods were explored in the processing of the complementary fields:

- **Method 1:**

The geometrical symmetry of the crack can be taken into account by constructing a complementary field for each fracture mode through a patchwork of complementary reference fields of every slip system. The idea is to extract the sectors distribution for three loadings corresponding to the three fracture modes *I*, *II* and *III*. Based on these distributions and on complementary fields of each slip system, a reference field is constructed for each fracture mode. The resulting complementary reference field can be finally written as follows:

$$\tilde{\underline{u}}_i^{pl}(r, \theta) = \underline{u}^{pl,s}(r, \theta) \quad (4.46)$$

with *s* is dominant in the location (r, θ) under a *mode i* loading, $i \in \{I, II, III\}$. Concerning fields that have the same evolution of the resolved shear stress, they have the same angular distribution of the complementary reference field (see figures 4.35, 4.36).

Figures 4.39, 4.40, and 4.41 show the distribution of resolved shear stresses $|\tau^s|$ for a crystal with $\gamma_{[100]}^{(010)}$ orientation under loadings in *mode I*, *mode II* and *mode III* respectively. These distributions were computed at the same distance δ from the crack tip. Tables 4.7, 4.8, and 4.9 summarize dominant slip systems and their dominance θ -ranges.

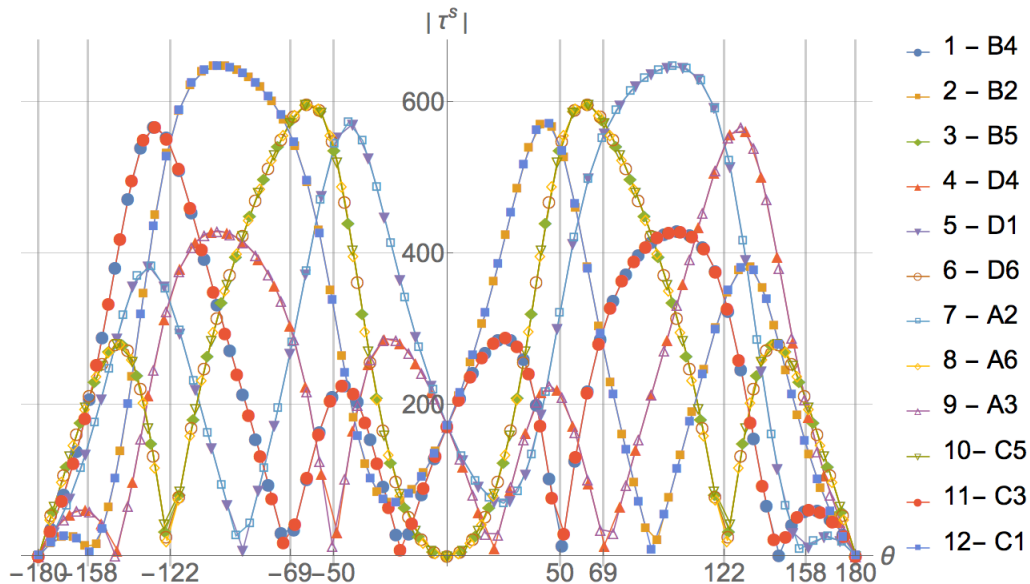


Figure 4.39: Resolved shear stresses distributions $|\tau^s|$ (MPa) of different slip systems at the region near the crack tip based on Hoenig's analytical solutions for material orientation $\gamma_{[100]}^{(010)}$ under pure *mode I* $K_I^\infty = 25 \text{ MPa}\sqrt{\text{m}}$ at a distance δ from the crack tip.

Table 4.7: Sectors of dominant slip systems for material orientation $\gamma_{[100]}^{(010)}$ under *mode I* at a distance δ from the crack tip.

Angle θ	$[-180^\circ, -158^\circ]$	$[-158^\circ, -122^\circ]$	$[-122^\circ, -69^\circ]$	$[-69^\circ, -50^\circ]$	$[-50^\circ, 0^\circ]$
Dominant systems	$B5, C5$ $A6, D6$	$B4, C3$	$B2, C1$	$B5, C5$ $A6, D6$	$A2, D1$
Angle θ	$[0^\circ, 50^\circ]$	$[50^\circ, 69^\circ]$	$[69^\circ, 122^\circ]$	$[122^\circ, 158^\circ]$	$[158^\circ, 180^\circ]$
Dominant systems	$B2, C1$	$B5, C5$ $A6, D6$	$A2, D1$	$D4, A3$	$B5, C5$ $A6, D6$

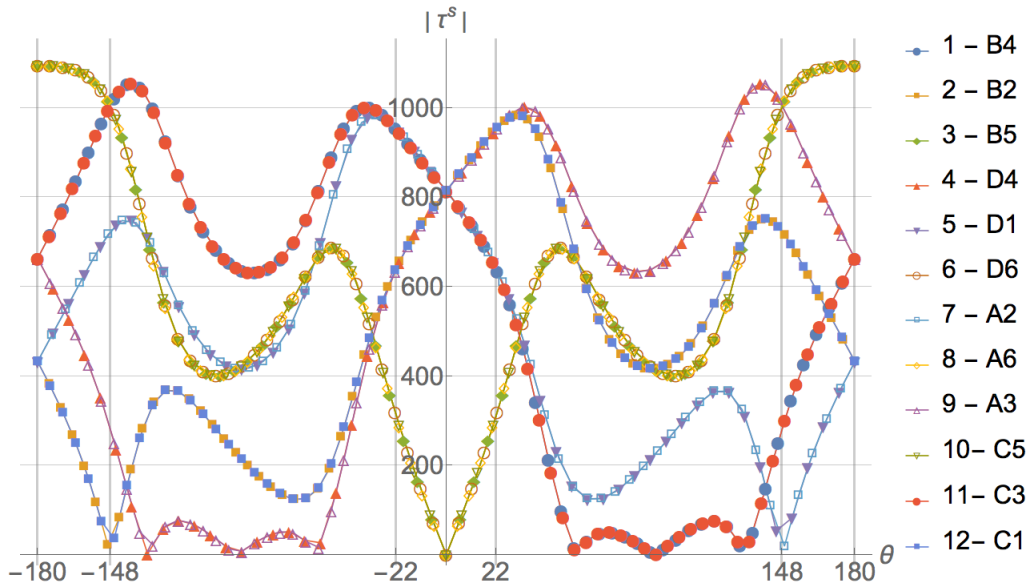


Figure 4.40: Resolved shear stresses distributions $|\tau^s|$ (MPa) of different slip systems at the region near the crack tip based on Hoenig's analytical solutions for material orientation $\gamma_{[100]}^{(010)}$ under pure *mode II* $K_{II}^\infty = 25 \text{ MPa}\sqrt{\text{m}}$ at a distance δ from the crack tip.

Table 4.8: Sectors of dominant slip systems for material orientation $\gamma_{[100]}^{(010)}$ under *mode II* at a distance δ from the crack tip.

Angle θ	$[-180^\circ, -148^\circ]$	$[-148^\circ, -22^\circ]$	$[-22^\circ, 0^\circ]$	$[0^\circ, 22^\circ]$	$[22^\circ, 148^\circ]$	$[148^\circ, 180^\circ]$
Dominant systems	$B5, C5$ $A6, D6$	$B4, C3$	$D1, A2$	$C1, B2$	$D4, A3$	$B5, C5$ $A6, D6$

Table 4.9: Sectors of dominant slip systems for material orientation $\gamma_{[100]}^{(010)}$ under *mode III* at a distance δ from the crack tip.

Angle θ	$[-180^\circ, -127^\circ]$	$[-127^\circ, 0^\circ]$	$[0^\circ, 127^\circ]$	$[127^\circ, 180^\circ]$
Dominant systems	$B2$	$D6$	$C5$	$A2$

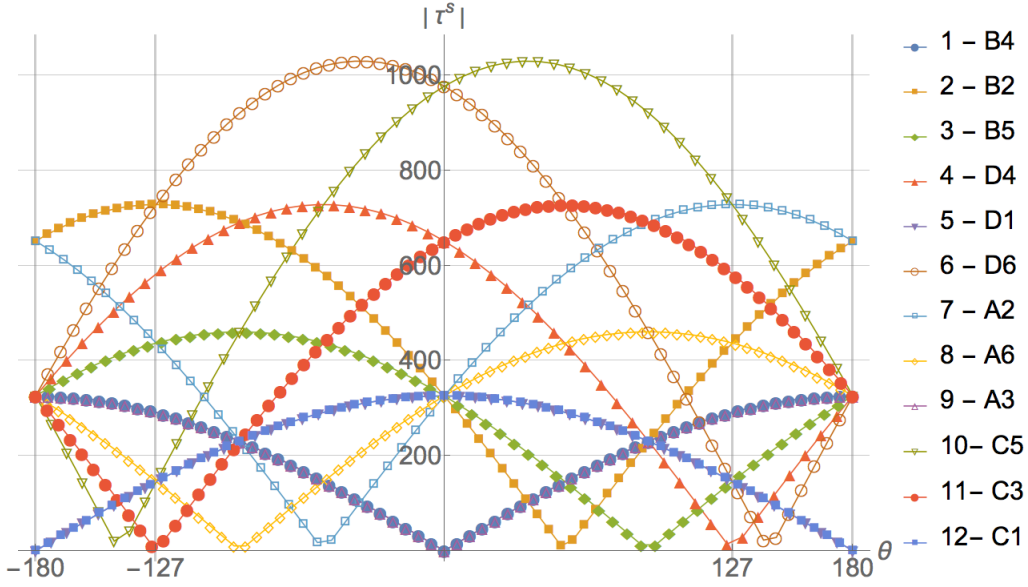


Figure 4.41: Resolved shear stresses distributions $|\tau^s|$ (MPa) of different slip systems at the region near the crack tip based on Hoenig's analytical solutions for material orientation $\gamma_{[100]}^{(010)}$ under pure *mode III* $K_{III}^\infty = 10 \text{ MPa}\sqrt{\text{m}}$ at a distance δ from the crack tip.

For instance, for the fracture *mode III*, the complementary reference field $\underline{\phi}_{III}^{pl,s}(\underline{x})$ is constructed based on table 4.9 as follows:

$$\underline{\phi}_{III}^{pl,s}(\underline{x}) = \begin{cases} \underline{\phi}^{pl,B2}(r, \theta) & \text{for } \theta \in [-180^\circ, -127^\circ] \\ \underline{\phi}^{pl,D6}(r, \theta) & \text{for } \theta \in [-127^\circ, 0^\circ] \\ \underline{\phi}^{pl,C5}(r, \theta) & \text{for } \theta \in [0^\circ, 127^\circ] \\ \underline{\phi}^{pl,A2}(r, \theta) & \text{for } \theta \in [127^\circ, 180^\circ] \end{cases} \quad (4.47)$$

The weak point of this method is that the obtained complementary reference fields may not verify the compatibility equations.

• Method 2:

The idea here is to transpose the local crystal plasticity model to the nonlocal scale of the crack. Therefore, a “nonlocal Schmid” factor has to be identified.

In fact, the resolved shear stress τ^s of a given slip system (s) is the projection of a stress state on the Schmid factor \underline{m}^s of the corresponding slip system. It can be seen also as the virtual work of the stress vector on this slip system per a unit displacement field. Along the same lines, an attempt was made to transpose this local Schmid factor to the scale of the crack region. The idea is to compute the virtual work of the Hoenig's elastic stress vector in a given slip system with the corresponding complementary reference field $\underline{\phi}^{pl,s}(\underline{x})$.

The Hoenig's elastic stress solution given in equation 4.41 can be written as follows:

$$\underline{\underline{\sigma}}^{Hoenig} = K_I^\infty \underline{\underline{\phi}}_I^{Hoenig}(r, \theta) + K_{II}^\infty \underline{\underline{\phi}}_{II}^{Hoenig}(r, \theta) + K_{III}^\infty \underline{\underline{\phi}}_{III}^{Hoenig}(r, \theta) \quad (4.48)$$

Figure 4.42 shows the distribution of the components of $\underline{\underline{\varphi}}_{\underline{\underline{I}}}^{Hoening}(r, \theta)$, $\underline{\underline{\varphi}}_{\underline{\underline{II}}}^{Hoening}(r, \theta)$ and $\underline{\underline{\varphi}}_{\underline{\underline{III}}}^{Hoening}(r, \theta)$ as function of the angular position θ for material orientation $\succ_{[100]}^{(010)}$.

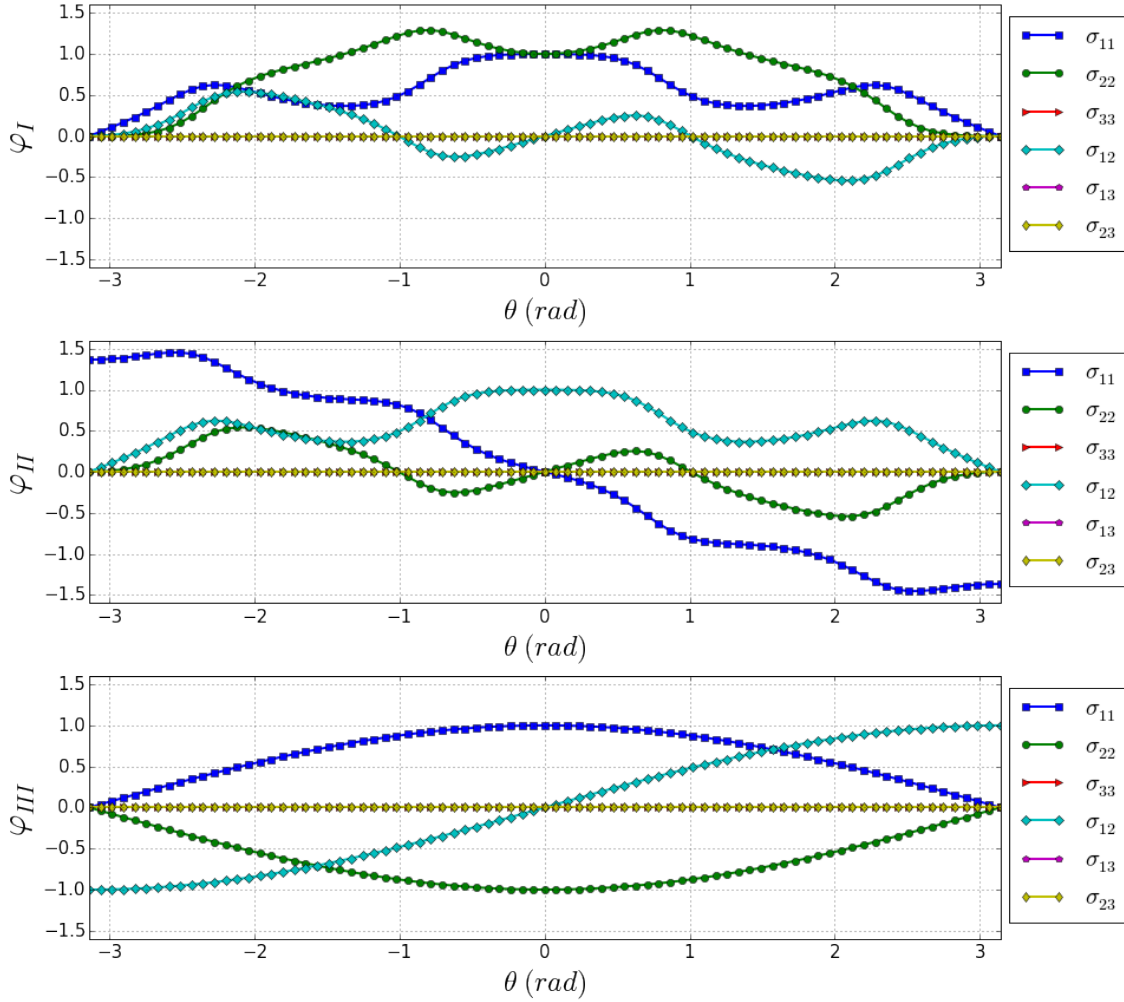


Figure 4.42: Components of Hoenig's stress tensors $\underline{\underline{\varphi}}_{\underline{\underline{I}}}^{Hoening}(r, \theta)$, $\underline{\underline{\varphi}}_{\underline{\underline{II}}}^{Hoening}(r, \theta)$ and $\underline{\underline{\varphi}}_{\underline{\underline{III}}}^{Hoening}(r, \theta)$ for material orientation $\succ_{[100]}^{(010)}$.

A stress vector \underline{T}_i can be computed for each fracture mode i on a given contour around the crack as shown on figure 4.43:

$$\underline{T}_i = \underline{\underline{\varphi}}_{\underline{\underline{i}}}^{Hoening}(r, \theta) \cdot \underline{n} \quad (4.49)$$

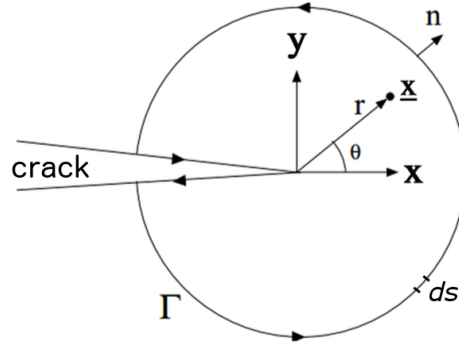
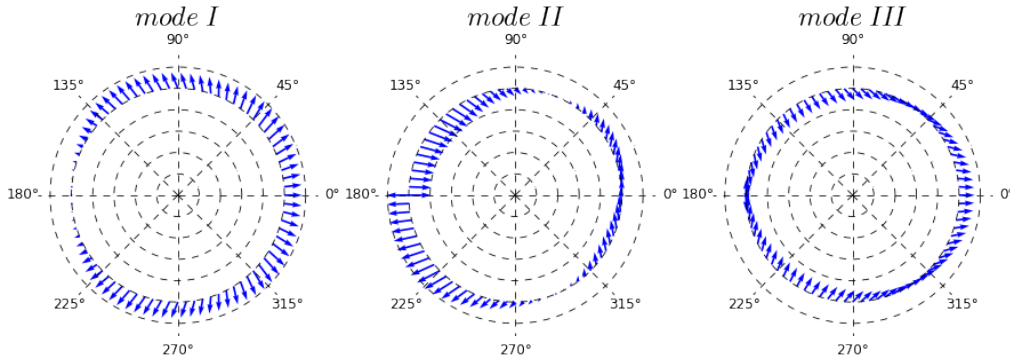


Figure 4.43: Contour around the crack tip.

Figure 4.44: Hoenig's stress vectors \underline{T}_I , \underline{T}_{II} and \underline{T}_{III} for material orientation $\gamma_{\begin{smallmatrix} (010) \\ [100] \end{smallmatrix}}$.

The “nonlocal Schmid” factor of the fracture mode i and the slip system s is computed as the virtual work of the Hoenig's stress vector of the fracture mode i (\underline{T}_i) in the complementary reference field $\underline{\phi}^{pl,s}(\underline{x})$ of the slip system s :

$$f_i^s = \int_{\theta=-\pi}^{\theta=\pi} \underline{T}_i \cdot \underline{\phi}^{pl,s}(\underline{x}) r d\theta \quad (4.50)$$

Finally, an equivalent stress intensity factor experienced by a slip system s can be computed as the sum of nominal stress intensity factors of different fracture modes weighted by the corresponding “nonlocal Schmid” factor:

$$K_s = f_I^s K_I^\infty + f_{II}^s K_{II}^\infty + f_{III}^s K_{III}^\infty \quad (4.51)$$

Once this equivalent stress intensity factor is obtained for each slip system for a given loading case, a constitutive law with an evolution law of internal variables can be used to describe the behavior of the plastic blunting ρ_{mod}^s associated to each slip system. For the sake of simplicity, and in concordance with the crystal plasticity model (see equation 4.7), a Norton law was used.

$$\dot{\rho}_{mod}^s = \left(\frac{|K_s - K_s^X|}{k} \right)^n \text{sign}(K_s - K_s^X) \quad (4.52)$$

For the sake of simplicity, a simple linear evolution law is associated to internal variable K_s^X .

$$\dot{K}_s^X = c\dot{\rho}^s \quad (4.53)$$

k , n and c are material parameters. The identification of these parameters is obtained by minimizing the error between the blunting intensity factor ρ_{mod}^s of a given slip system s obtained from the model and the blunting intensity factor ρ_{num}^s obtained from a direct projection of the total numerical kinematic field on the reference field $\underline{\phi}^{pl,s}(\underline{x})$ (see equation 4.54). Comparison is made for the same loading case.

$$\dot{\rho}_{num}^s(t) = \frac{\sum_{P \in D} \underline{v}^{FE}(P, t) \cdot \underline{\phi}^{pl,s}(P)}{\sum_{P \in D} \underline{\phi}^{pl,s}(P) \cdot \underline{\phi}^{pl,s}(P)} \quad (4.54)$$

Results

The identification was performed on a test case under a pure fracture *mode I* with a crystal plasticity model that contains all the twelve octahedral slip systems with material orientation $\succ_{[100]}^{(010)}$. Elastic-plastic kinematic fields $\underline{v}^{FE}(\underline{x}, t)$ were extracted from the region of interest near the crack tip. $\dot{\rho}_{num}^s$ was evaluated for each slip system based on expression 4.54. A minimization algorithm was used to identify a set of parameters k , n and c for all slip systems by minimizing the error between $\dot{\rho}_{num}^s$ and $\dot{\rho}_{mod}^s$ (see equation 4.52).

Figure 4.45 shows, for different slip systems, the $K_s - \dot{\rho}_{num}^s$ curves obtained numerically and $K_s - \dot{\rho}_{mod}^s$ curves obtained from the model for a given set of parameters n , k and c . The used parameters are the same for all slip systems. Generally speaking, results show a quite good agreement for some slip systems more than others. In fact, using a Norton law and a simple linear evolution law for the internal variable K_s^X to transpose the local crystal plasticity model to the scale of the crack may miss some details about the real behavior of the crystal at the near crack tip region.

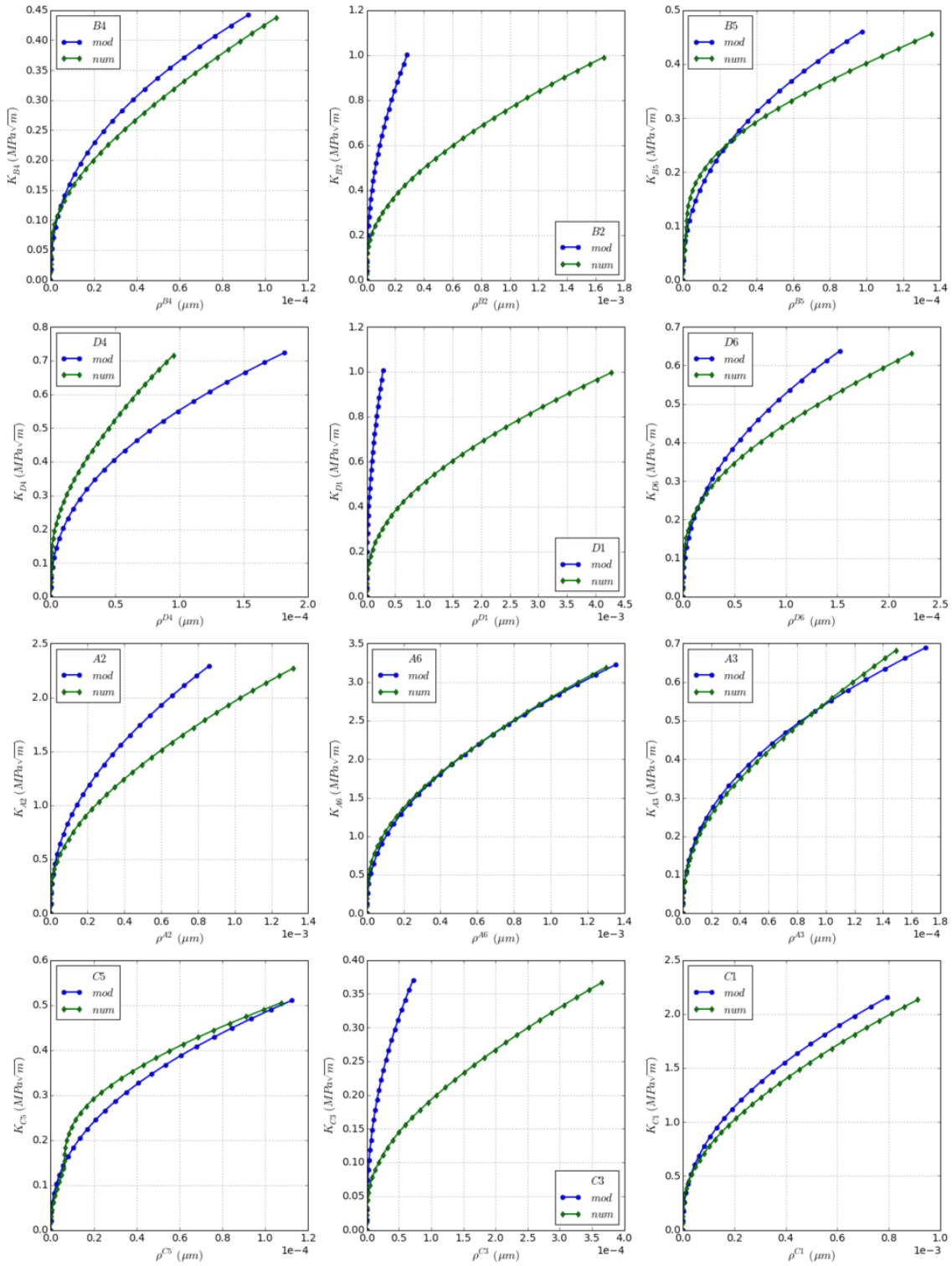


Figure 4.45: Evolution of K_s as function of ρ_{num}^s computed numerically and as function of ρ_{mod}^s from the model. The studied case is a pure fracture *mode I* of material orientation $\gamma_{[100]}^{(010)}$.

4.6 Conclusion

In this chapter, the problem of a crack in a FCC single crystal was studied. A crystal plasticity model was used to model the behavior of a cracked AM1 single crystal.

The kinematic basis used to reduce the number of the degrees of freedom of the problem was initially studied based on the partition of kinematic fields with respect to fracture modes. A plastic reference field $\underline{\phi}_i^{pl}(\underline{x})$ is identified for each fracture mode (i) and the problem is reduced to six degrees of freedom ($\dot{K}_I^\infty, \dot{K}_{II}^\infty, \dot{K}_{III}^\infty, \dot{\rho}_I, \dot{\rho}_{II}, \dot{\rho}_{III}$). However, the localization of the plastic strain caused by the activation of few slip systems under a given fracture mode indicates that this partition with respect to fracture modes may not be representative of the crack tip plasticity under mixed fracture modes.

A second partition methodology was studied based on the decomposition of plastic velocity field with respect slip systems, to take into account the activation of this systems, and based on fracture modes, in order to maintain the orthogonality the kinematic basis. Thus, a plastic reference field $\underline{\phi}_i^{pl,s}(\underline{x})$ is identified for each slip system (s) and for each fracture mode (i) and the problem of crack tip plasticity is reduced to 39 degrees of freedom ($\dot{K}_I^\infty, \dot{K}_{II}^\infty, \dot{K}_{III}^\infty, \dot{\rho}_i^s, i = I, II, III s = 1..12$).

It was shown that the yield domain of the region near the crack tip of a given slip system s is represented by two parallel planes in the $K_I^\infty - K_{II}^\infty - K_{III}^\infty$ space. Normals to these planes were identified based on a set FE simulations.

The resolved shear stress was evaluated analytically based on the Schmid factor and on Hoenig's solutions for elastic stress distributions near the crack tip region. The concept of dominant slip system, its persistence and uniqueness allowed the use of elastic solutions to evaluate sectors of dominant stresses at the crack tip. Promising results were found when comparing the analytical Schmid factor, experimental results and numerical ones.

Based on these analyses, a third methodology was proposed based on the partition with respect to slip systems. Thus, a plastic reference field $\underline{\phi}^{pl,s}(\underline{x})$ is identified for each slip system (s). A "nonlocal Schmid factor" was proposed as the virtual work of the Hoenig's stress vector in the plastic reference field. This factor was then used in a simple material behavior law to transpose the local crystal plasticity model to the scale of the crack. The identified condensed nonlocal model was able to predict the evolution of most plastic intensity factors ρ^s , despite its rather simple formulation.

Conclusion and perspectives

This work aims to model the plasticity at the region near the tip of a stationary crack subjected to mixed fracture modes $I + II + III$ in an anisotropic medium. It focuses on the case of the AM1 Nickel base superalloy single crystal. The study can be globally decomposed into two major parts.

In the first part, the material was described with a cubic elasticity model and a Von-Mises associated plasticity. Based on a set of hypotheses, the velocity field of the crack tip region is partitioned into two kinematically independent mechanisms, i.e. an elastic mechanism and a plastic one. Each part is the superposition of three fracture modes written as a product of an intensity factor rate and a spatial distribution field. A special interest was given to the determination of these spatial distributions since they form the kinematic basis required to reduce the model. A kinematic basis is comprised of the elastic reference fields $(\underline{\phi}_I^{el}(\underline{x}), \underline{\phi}_{II}^{el}(\underline{x}), \underline{\phi}_{III}^{el}(\underline{x}))$ and the plastic reference fields $(\underline{\phi}_I^{pl}(\underline{x}), \underline{\phi}_{II}^{pl}(\underline{x}), \underline{\phi}_{III}^{pl}(\underline{x}))$ of different fracture modes.

Elastic reference fields were derived from a Proper Orthogonal Decomposition analysis. In a first step, these fields were shown to verify Sih, Paris and Irwin's [Sih et al., 1965] asymptotic elastic solutions for the orthotropic case in which material axes are along the crack coordinates system. Then, it was shown that, for a random crystallographic orientation with respect to the crack plane and front, these fields can be represented by Hoenig's general elastic solution of displacement fields [Hoenig, 1982].

The determination of the plastic reference fields went through a verification procedure in order to ensure the hypotheses of the model. These fields exhibited a strong dependency on the crystallographic orientation even under Von-Mises "isotropic" plasticity.

Once a kinematic basis was identified for each studied material orientation, an extended yield criterion at the crack scale was proposed. This criterion is based on the density of the elastic shear energy and on LEFM fields given by Hoenig's general solution. The shape of this domain is highly affected by the loading history. Thus, a methodology was proposed to numerically explore the yield domain without distorting it. A plasticity criterion based on the reconstruction errors of kinematic fields was used to identify the yield domain. The position and the size of the yield locus can be considered as internal variables to enrich the condensed plasticity model. Their evolution laws take part in the blunting law in order to take into account the loading history effects and internal stresses.

In an analogy with a standard generalized model, a normality rule of the plastic flow was derived from the pseudopotential of dissipation. This rule is based on nonlocal blunting intensity factors $(\dot{\rho}_I, \dot{\rho}_{II}, \dot{\rho}_{III})$ and thermodynamic quantities similar to the energy release

rates (G_I, G_{II}, G_{III}). The choice of these dual quantities seems to be convenient for the isotropic case and for orientations where the material presents an orthotropic behavior with respect to the crack coordinate system. For other random orientations, the used kinematic basis was able to capture the anisotropy-induced mixed mode behavior of the plastic flow. However, the choice of the driving forces associated to $\dot{\rho}_I, \dot{\rho}_{II}$ and $\dot{\rho}_{III}$ has to be reviewed because of thermodynamic considerations.

In the second part of this work, a full anisotropic behavior of the material was studied via cubic elasticity and a crystal plasticity model. The twelve octahedral slip systems of the FCC single crystal were considered in the model.

The same partition proposed before was initially used. A plastic reference field was determined for each fracture mode. However, the localization of the plastic strain at the region near the crack tip, caused by the activation of few slip systems, urged the study of a new partition strategy. This strategy aimed to take into account the presence of easy slip planes and directions. For this reason, different separated analyses were performed on models. A unique slip system is implemented and independently studied per analysis. Based on these finite element analyses, it was shown that the yield domain of the cracked region is a superposition of different parallel pairs of planes in the space of nominal stress intensity factors $K_I^\infty - K_{II}^\infty - K_{III}^\infty$. Each pair of planes represents the opposite yield surfaces of one slip system. Based on information from these analyses, a plastic reference field $\underline{\phi}^{pl,s}(\underline{x})$ was identified for each slip system (s).

The use of the new constructed kinematic basis in the modeling required the study of activated slip systems through the Schmid law. Anisotropic Hoenig's solutions were used in the evaluation of the resolved shear stress at the region near the crack tip. The analytical expression exhibited a good agreement with numerical and experimental results from literature.

In order to maintain the nonlocal aspect of the model, the formulation of a "nonlocal Schmid factor" was proposed. It quantifies the contribution of each slip system (s) and fracture mode (i) in the kinematics at the crack tip when a random loading is applied. This factor is expressed as the virtual work of the Hoenig's stress vector of the fracture mode (i) in the plastic reference field of the slip system (s). Based on this quantity, a behavior law was proposed to describe the evolution of the plasticity through the blunting intensity factor $\dot{\rho}^s(t)$. The proposed model is written as a simple Norton law with a linear evolution law associated to the internal variable K_s^X . This mode contains three parameters to identify. It can be replaced in the future with a more sophisticated model with more parameters in order to provide a better description of the local crystal plasticity model.

This work presented the first exploration steps toward the condensed modeling of crack tip plasticity in an anisotropic medium. The final model enriches the usual linear elastic fracture mechanics functions by additional terms to account for the cyclic elastic-plastic behavior. Nevertheless, future works have to be done in order to fulfill the incorporation of this model in the incremental approach.

The evolution of internal variables due to plasticity ($\frac{\partial V_{int}}{\partial \rho}$) can be studied with the tools presented in this work. These evolutions equations are implemented in the incremental

model [Pommier and Hamam, 2007] to include history effects. Moreover, as the crack propagates, these variables have to be updated with the evolving crack length a to account for damage. Thus, an evolution law of internal variables as function of the crack propagation ($\frac{\partial V_{int}}{\partial a}$) has to be determined. It can be identified by numerically “growing” the crack without allowing plastic strains.

Based on the very first hypothesis of the incremental model, the propagation law relates the crack growth rate to the blunting at the crack tip. In the previous developments of the incremental model [Decreuse, 2010], [Fremy et al., 2012], a pure geometric relation was proposed to relate the new created surface to the blunting intensity factor: $\dot{a} \propto \sqrt{\dot{\rho}_I^2 + \dot{\rho}_{II}^2}$. For the crystal plasticity case presented in this work, a blunting intensity factor $\dot{\rho}^s(t)$ can be obtained from the model for each given slip system (s). The corresponding relation between the crack growth rate, i.e. the new created surface, and the crack tip plasticity can be written based on the geometrical considerations of the crack orientation with respect to the crystal frame and to different activated slip systems. A comparison with experimental results has to be performed to calibrate this relation. Different experimental analyses about crack initiation and propagation in Nickel base superalloy single crystals are available in the literature [Marchal, 2006],[Geuffrard, 2010], etc.

Plastic reference fields $\underline{\phi}^{pl,s}(\underline{x})$ used to transpose the local crystal plasticity model to the scale of the crack were obtained from monotonic loadings. This choice stems from the hypotheses of the model and from the persistence character of an activated slip system in a given sector near the crack tip. Besides, the crack can be considered as a “zero cohesion” slip system that is also capable of opening and that interacts with different octahedral slip systems while the interaction between different crystallographic slip systems was neglected. These interactions may be important in the modeling of the cyclic elastic-plastic behavior of the near crack tip region. In fact, according to experimental observations under cyclic loadings, the crystallographic slip may be intensified on the already activated slip systems whereas new slip systems can be activated as well. For instance, for the case of the AM1, the total inelastic strain rarely remains on a single slip direction for a given plane under cyclic loadings [Hanriot, 1993].

Once the incremental model is set for the case of a single crystal, it can be extended to the case of a bicrystal in a first step in order to examine the effect of the grain boundary and the presence of a single neighboring grain. In an advanced stage, the case of polycrystalline microstructure can be considered. In fact, the precise mapping of 3D grain shapes and crystallographic orientations in polycrystalline materials has become possible with nondestructive techniques such as the X-ray Diffraction Contrast Tomography (DCT) [Ludwig et al., 2009]. However, the numerical modeling of fatigue crack growth in polycrystalline materials with a crystal plasticity model is not a common study in literature because of its time consuming pre-processings and computations. Nevertheless, some three-dimensional FE simulations of short fatigue crack growth with a crystal plasticity model were recently performed on a mesh of a Titanium alloy microstructure imaged by DCT [Proudhon et al., 2017]. A local damage indicator was used to predict crack direction. This computation can provide a database to which the nonlocal model can be compared in the future. Yet, in order to fulfill such a comparison, the model has to be enriched to take into account various behaviors. Actually, the presence of neighboring grains and grain boundaries will create some perturbations in the mechanical fields near

the crack tip. For instance, internal stresses can be localized at the grain boundaries and can promote this perturbation. Moreover, under loading, the elastic anisotropy leads to a stress concentration at these boundaries [[Ludwig et al., 2009](#)]. These microstructural features and many others have to be considered in the extension of the model to the case of polycrystalline material.

Appendices

Asymptotic linear elastic solutions

The first order of the asymptotic expansion at the vicinity of a crack is given in this part for different cases of material elastic behavior. Solutions are developed for a through sharp crack in the plane of normal \vec{y} with the \vec{z} axis is along the crack front.

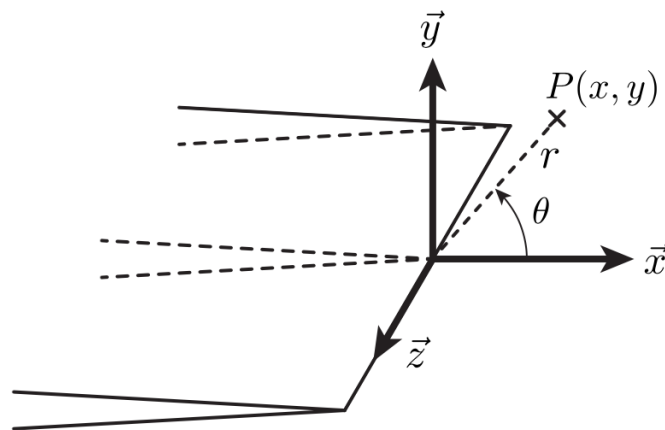


Figure A.1: Cartesian and polar coordinates systems at the crack tip region.

Isotropic case: Westergaard's solution

Westergaard [Westergaard, 1939] gave the first order of the asymptotic linear elastic solution of stress and displacement at the region near the crack tip for an isotropic material.

The stress is given as follows:

$$\begin{aligned}
 \text{mode I} & \begin{cases} \sigma_{xx} = \frac{K_I}{\sqrt{2\pi r}} \cos\left(\frac{\theta}{2}\right) \left[1 - \sin\left(\frac{\theta}{2}\right) \sin\left(\frac{3\theta}{2}\right)\right] \\ \sigma_{yy} = \frac{K_I}{\sqrt{2\pi r}} \cos\left(\frac{\theta}{2}\right) \left[1 + \sin\left(\frac{\theta}{2}\right) \sin\left(\frac{3\theta}{2}\right)\right] \\ \sigma_{xy} = \frac{K_I}{\sqrt{2\pi r}} \cos\left(\frac{\theta}{2}\right) \sin\left(\frac{\theta}{2}\right) \cos\left(\frac{3\theta}{2}\right) \end{cases} \\
 \text{mode II} & \begin{cases} \sigma_{xx} = -\frac{K_{II}}{\sqrt{2\pi r}} \sin\left(\frac{\theta}{2}\right) \left[2 + \cos\left(\frac{\theta}{2}\right) \cos\left(\frac{3\theta}{2}\right)\right] \\ \sigma_{yy} = \frac{K_{II}}{\sqrt{2\pi r}} \sin\left(\frac{\theta}{2}\right) \cos\left(\frac{\theta}{2}\right) \cos\left(\frac{3\theta}{2}\right) \\ \sigma_{xy} = \frac{K_{II}}{\sqrt{2\pi r}} \cos\left(\frac{\theta}{2}\right) \left[1 - \sin\left(\frac{\theta}{2}\right) \sin\left(\frac{3\theta}{2}\right)\right] \end{cases} \\
 \text{mode III} & \begin{cases} \sigma_{xz} = -\frac{K_{III}}{\sqrt{2\pi r}} \sin\left(\frac{\theta}{2}\right) \\ \sigma_{yz} = \frac{K_{III}}{\sqrt{2\pi r}} \cos\left(\frac{\theta}{2}\right) \end{cases}
 \end{aligned} \tag{A.1}$$

The displacement is given as follows:

$$\begin{aligned}
 \text{mode I} & \begin{cases} u_x = \frac{K_I}{2\mu} \sqrt{\frac{r}{2\pi}} \cos\left(\frac{\theta}{2}\right) [\kappa - \cos(\theta)] \\ u_y = \frac{K_I}{2\mu} \sqrt{\frac{r}{2\pi}} \sin\left(\frac{\theta}{2}\right) [\kappa - \cos(\theta)] \end{cases} \\
 \text{mode II} & \begin{cases} u_x = \frac{K_{II}}{2\mu} \sqrt{\frac{r}{2\pi}} \sin\left(\frac{\theta}{2}\right) [\kappa + 2 + \cos(\theta)] \\ u_y = -\frac{K_{II}}{2\mu} \sqrt{\frac{r}{2\pi}} \cos\left(\frac{\theta}{2}\right) [\kappa - 2 + \cos(\theta)] \end{cases} \\
 \text{mode III} & \begin{cases} u_z = 2\frac{K_{III}}{\mu} \sqrt{\frac{r}{2\pi}} \sin\left(\frac{\theta}{2}\right) \end{cases}
 \end{aligned} \tag{A.2}$$

with $\mu = \frac{E}{2(1+\nu)}$ the Lamé coefficient, $\kappa = \frac{3-\nu}{1+\nu}$ under plane stress and $\kappa = 3-4\nu$ under plane strain.

Cubic with $z = 0$ a plane of symmetry: Sih, Paris and Irwin's solution

Sih, Paris and Irwin [Sih et al., 1965] gave the first term of the asymptotic expansion of the stress and displacement for a crack in a monoclinic material with $z = 0$ a plane of symmetry for the material.

The generalized Hooke's law is written in Voigt notation as follows:

$$\underline{\underline{\varepsilon}} = \underline{\underline{S}} \cdot \underline{\underline{\sigma}} \tag{A.3}$$

with:

$$\varepsilon = \begin{pmatrix} \varepsilon_{xx} \\ \varepsilon_{yy} \\ \varepsilon_{zz} \\ 2\varepsilon_{yz} \\ 2\varepsilon_{xz} \\ 2\varepsilon_{xy} \end{pmatrix} \quad \sigma = \begin{pmatrix} \sigma_{xx} \\ \sigma_{yy} \\ \sigma_{zz} \\ \sigma_{yz} \\ \sigma_{xz} \\ \sigma_{xy} \end{pmatrix} \quad \approx S = \begin{pmatrix} S_{1111} & S_{1122} & S_{1133} & 0 & 0 & 0 \\ S_{2211} & S_{2222} & S_{2233} & 0 & 0 & 0 \\ S_{3311} & S_{3322} & S_{3333} & 0 & 0 & 0 \\ 0 & 0 & 0 & 4S_{2323} & 0 & 0 \\ 0 & 0 & 0 & 0 & 4S_{3131} & 0 \\ 0 & 0 & 0 & 0 & 0 & 4S_{1212} \end{pmatrix} \quad (\text{A.4})$$

Based on a complex variables formulation, the problem of two-dimensional anisotropic elasticity can be conducted to solving the fourth order and the second order characteristic equations:

$$S'_{11}\mu^4 - 2S'_{16}\mu^3 + (2S'_{12} + S'_{66})\mu^2 - 2S'_{26}\mu + S'_{22} = 0 \quad (\text{A.5})$$

$$S''_{44}\mu^2 + 2S''_{45}\mu + S''_{55} = 0 \quad (\text{A.6})$$

with, under plane strain conditions:

$$S'_{ij} = S_{ij} - \frac{S_{i3}S_{3j}}{S_{33}} \quad (\text{A.7})$$

and

$$S''_{ij} = \begin{cases} -\frac{S'_{ij}}{S'_{44}S'_{55} - S'^2_{45}} & (i \neq j) \\ \frac{S'_{44}S'_{55}}{S'_{ij}(S'_{44}S'_{55} - S'^2_{45})} & (i = j) \end{cases} \quad (\text{A.8})$$

Solutions of equations A.5 and A.6 are pairs of complex roots. Let μ_1, μ_2 be the two distinct complex solutions of equation A.5 and μ_3 be the root of equation A.6 that all share the same sign of the imaginary part.

The stress is given as follows:

$$\begin{cases} \text{mode I} \begin{cases} \sigma_{xx} = K_I \sqrt{\frac{1}{2\pi r}} \Re\left[\frac{\mu_1\mu_2}{\mu_1 - \mu_2} \left(\frac{\mu_2}{\sqrt{\cos\theta + \mu_2 \sin\theta}} - \frac{\mu_1}{\sqrt{\cos\theta + \mu_1 \sin\theta}}\right)\right] \\ \sigma_{yy} = K_I \sqrt{\frac{1}{2\pi r}} \Re\left[\frac{1}{\mu_1 - \mu_2} \left(\frac{\mu_1}{\sqrt{\cos\theta + \mu_2 \sin\theta}} - \frac{\mu_2}{\sqrt{\cos\theta + \mu_1 \sin\theta}}\right)\right] \\ \sigma_{xy} = K_I \sqrt{\frac{1}{2\pi r}} \Re\left[\frac{\mu_1\mu_2}{\mu_1 - \mu_2} \left(\frac{1}{\sqrt{\cos\theta + \mu_1 \sin\theta}} - \frac{1}{\sqrt{\cos\theta + \mu_2 \sin\theta}}\right)\right] \end{cases} \\ \text{mode II} \begin{cases} \sigma_{xx} = K_{II} \sqrt{\frac{1}{2\pi r}} \Re\left[\frac{1}{\mu_1 - \mu_2} \left(\frac{\mu_2^2}{\sqrt{\cos\theta + \mu_2 \sin\theta}} - \frac{\mu_1^2}{\sqrt{\cos\theta + \mu_1 \sin\theta}}\right)\right] \\ \sigma_{yy} = K_{II} \sqrt{\frac{1}{2\pi r}} \Re\left[\frac{1}{\mu_1 - \mu_2} \left(\frac{1}{\sqrt{\cos\theta + \mu_2 \sin\theta}} - \frac{1}{\sqrt{\cos\theta + \mu_1 \sin\theta}}\right)\right] \\ \sigma_{xy} = K_{II} \sqrt{\frac{1}{2\pi r}} \Re\left[\frac{1}{\mu_1 - \mu_2} \left(\frac{\mu_1}{\sqrt{\cos\theta + \mu_1 \sin\theta}} - \frac{\mu_2}{\sqrt{\cos\theta + \mu_2 \sin\theta}}\right)\right] \end{cases} \\ \text{mode III} \begin{cases} \sigma_{xz} = -K_{III} \sqrt{\frac{1}{2\pi r}} \Re\left[\frac{\mu_3}{\sqrt{\cos\theta + \mu_3 \sin\theta}}\right] \\ \sigma_{yz} = K_{III} \sqrt{\frac{1}{2\pi r}} \Re\left[\frac{1}{\sqrt{\cos\theta + \mu_3 \sin\theta}}\right] \end{cases} \end{cases} \quad (\text{A.9})$$

The displacement is given as follows:

$$\begin{aligned}
 \text{mode I} & \begin{cases} u_x = K_I \sqrt{\frac{2r}{\pi}} \Re \left[\frac{1}{\mu_1 - \mu_2} (\mu_1 p_2 \sqrt{\cos \theta + \mu_2 \sin \theta} - \mu_2 p_1 \sqrt{\cos \theta + \mu_1 \sin \theta}) \right] \\ u_y = K_I \sqrt{\frac{2r}{\pi}} \Re \left[\frac{1}{\mu_1 - \mu_2} (\mu_1 q_2 \sqrt{\cos \theta + \mu_2 \sin \theta} - \mu_2 q_1 \sqrt{\cos \theta + \mu_1 \sin \theta}) \right] \end{cases} \\
 \text{mode II} & \begin{cases} u_x = K_{II} \sqrt{\frac{2r}{\pi}} \Re \left[\frac{1}{\mu_1 - \mu_2} (p_2 \sqrt{\cos \theta + \mu_2 \sin \theta} - p_1 \sqrt{\cos \theta + \mu_1 \sin \theta}) \right] \\ u_y = K_{II} \sqrt{\frac{2r}{\pi}} \Re \left[\frac{1}{\mu_1 - \mu_2} (q_2 \sqrt{\cos \theta + \mu_2 \sin \theta} - q_1 \sqrt{\cos \theta + \mu_1 \sin \theta}) \right] \end{cases} \\
 \text{mode III} & \begin{cases} u_z = K_{III} \sqrt{\frac{2r}{\pi}} \Re \left[\frac{\sqrt{\cos \theta + \mu_3 \sin \theta}}{S''_{45} + \mu_3 S''_{44}} \right] \end{cases}
 \end{aligned} \tag{A.10}$$

with, for $j = 1, 2$, p_j and q_j are as follows:

$$\begin{aligned}
 p_j &= S'_{11} \mu_j^2 + S'_{12} - S'_{16} \mu_j \\
 q_j &= S'_{12} \mu_j + \frac{S'_{22}}{\mu_j} - S'_{26}
 \end{aligned} \tag{A.11}$$

Generally anisotropic medium: Hoenig's solution

For a general anisotropic case, Hoenig [Hoenig, 1982] proposed an asymptotic solution of displacement and stress at the vicinity of a crack tip based on the Lekhnitskii formalism [Lekhnitskii, 1963].

Following the same procedure as in the Lekhnitskii formalism, the problem of the crack is taken as a plane problem so that field quantities depend solely upon two coordinates (x, y) and are expressed in the final solution in polar coordinates (r, θ) (see figure A.1). The solution is based on the governing equations of an anisotropic elasticity problem. The stress and strain are connected through the constitutive law:

$$\varepsilon_{ij} = S_{ijkl} \sigma_{kl} \tag{A.12}$$

Let S_{ij} is the Voigt notation of the stiffness tensor. Notations are written as follows:

$$\underline{\varepsilon} = \begin{pmatrix} \varepsilon_{xx} \\ \varepsilon_{yy} \\ \varepsilon_{zz} \\ 2\varepsilon_{yz} \\ 2\varepsilon_{xz} \\ 2\varepsilon_{xy} \end{pmatrix} \quad \underline{\sigma} = \begin{pmatrix} \sigma_{xx} \\ \sigma_{yy} \\ \sigma_{zz} \\ \sigma_{yz} \\ \sigma_{xz} \\ \sigma_{xy} \end{pmatrix} \quad \underline{S} = \begin{pmatrix} S_{1111} & S_{1122} & S_{1133} & 0 & 0 & 0 \\ S_{2211} & S_{2222} & S_{2233} & 0 & 0 & 0 \\ S_{3311} & S_{3322} & S_{3333} & 0 & 0 & 0 \\ 0 & 0 & 0 & 4S_{2323} & 0 & 0 \\ 0 & 0 & 0 & 0 & 4S_{3131} & 0 \\ 0 & 0 & 0 & 0 & 0 & 4S_{1212} \end{pmatrix} \tag{A.13}$$

The reduced compliance matrix S'_{ij} is used in the solution. It derives from the compliance matrix S_{ij} written in Voigt notation (see equation A.13). Under plane strain assumption, S'_{ij} is evaluated as follows:

$$S'_{ij} = S_{ij} - \frac{S_{i3} S_{3j}}{S_{33}} \tag{A.14}$$

As given by Hoenig [Hoenig, 1982] and then rewritten by Banks-Sills and co-workers [Banks-Sills et al., 2005], the displacement is written as follows:

$$u_i = \sqrt{\frac{2r}{\pi}} \Re \left[\sum_{j=1}^3 m_{ij} N_{jl}^{-1} K_l^\infty Q_j \right] \quad (\text{A.15})$$

The components of the stress tensor are given as follows:

$$\begin{aligned} \sigma_{xx} &= \frac{1}{\sqrt{2\pi r}} \Re \left[\sum_{i=1}^3 \frac{p_i^2 N_{ij}^{-1} K_j^\infty}{Q_i} \right] & \sigma_{yy} &= \frac{1}{\sqrt{2\pi r}} \Re \left[\sum_{i=1}^3 \frac{N_{ij}^{-1} K_j^\infty}{Q_i} \right] \\ \sigma_{xy} &= -\frac{1}{\sqrt{2\pi r}} \Re \left[\sum_{i=1}^3 \frac{p_i N_{ij}^{-1} K_j^\infty}{Q_i} \right] & \sigma_{zx} &= \frac{1}{\sqrt{2\pi r}} \Re \left[\sum_{i=1}^3 \frac{p_i \lambda_i N_{ij}^{-1} K_j^\infty}{Q_i} \right] \\ \sigma_{zy} &= -\frac{1}{\sqrt{2\pi r}} \Re \left[\sum_{i=1}^3 \frac{\lambda_i N_{ij}^{-1} K_j^\infty}{Q_i} \right] & \sigma_{zz} &= \frac{1}{\sqrt{2\pi r}} \Re \left[\sum_{i=1}^3 \frac{\alpha_i N_{ij}^{-1} K_j^\infty}{Q_i} \right] \end{aligned} \quad (\text{A.16})$$

under plane strain assumption:

$$\alpha_i = -\frac{1}{S_{33}} \left[S_{31} p_i^2 + S_{32} - S_{34} \lambda_i + S_{35} p_i \lambda_i - S_{36} p_i \right] \quad (\text{A.17})$$

with $i \in \{1, 2, 3\}$ which is equivalent to $i \in \{x, y, z\}$, $\Re[*]$ is the real part of $*$ and m_{ij} is a matrix defined as follows:

$$\begin{aligned} m_{1i} &= S'_{11} p_i^2 - S'_{16} p_i + S'_{12} + \lambda_i (S'_{15} p_i - S'_{14}) \\ m_{2i} &= S'_{21} p_i - S'_{26} + \frac{S'_{22}}{p_i} + \lambda_i (S'_{25} - \frac{S'_{24}}{p_i}) \\ m_{3i} &= S'_{41} p_i - S'_{46} + \frac{S'_{42}}{p_i} + \lambda_i (S'_{45} - \frac{S'_{44}}{p_i}) \end{aligned} \quad (\text{A.18})$$

$$Q_i = \sqrt{\cos \theta + p_i \sin \theta} \quad (\text{A.19})$$

with θ the angular position with respect to the crack ligament (see figure A.1).

N_{ij}^{-1} and K_i^∞ are respectively the inverse of the matrix N_{ij} defined below and the vector of stress intensity factors:

$$N_{ij} = \begin{pmatrix} 1 & 1 & 1 \\ -p_1 & -p_2 & -p_3 \\ -\lambda_1 & -\lambda_2 & -\lambda_3 \end{pmatrix} \quad K_i^\infty = \begin{pmatrix} K_I^\infty \\ K_{II}^\infty \\ K_{III}^\infty \end{pmatrix} \quad (\text{A.20})$$

$$\lambda_i = -\frac{l_3(p_i)}{l_2(p_i)} \quad (\text{A.21})$$

where p_i ($i \in \{1, 2, 3\}$) are the roots of the characteristic sixth order polynomial equation A.22 obtained by coupling compatibility equations. These roots are always complex

and are obtained as pairs of complex conjugates. Distinct roots sharing the same sign of the imaginary part have to be chosen.

$$l_4(p)l_2(p) - l_3^2(p) = 0 \quad (\text{A.22})$$

with

$$\begin{aligned} l_2(p) &= S'_{55}p^2 - 2S'_{45}p + S'_{44} \\ l_3(p) &= S'_{15}p^3 - (S'_{14} + S'_{56})p^2 + (S'_{25} + S'_{46})p - S'_{24} \\ l_4(p) &= S'_{11}p^4 - 2S'_{16}p^3 + (2S'_{12} + S'_{66})p^2 - 2S'_{26}p + S'_{22} \end{aligned} \quad (\text{A.23})$$

Special cases

There are some special cases of anisotropy that lead to a mathematically degenerate development. These cases can be summarized in the ones where the plane $z = 0$ is a symmetry plane. This includes the monoclinic, the orthotropic and the cubic anisotropies where the crystal axes are normal to symmetry planes and of course the isotropic case.

The most general case among these special ones is the monoclinic anisotropy with $z = 0$ a plane of symmetry:

$$S'_{14} = S'_{24} = S'_{15} = S'_{25} = S'_{46} = S'_{56} = 0 \quad (\text{A.24})$$

These symmetries imply that $l_3(p) = 0$ which means that the coupling between the two compatibilities equations that led to equation A.22, is no more valid. This requires another development. The other two characteristic polynomial equations are written as follows:

$$\begin{aligned} l_4(p) &= 0 \\ l_2(p) &= 0 \end{aligned} \quad (\text{A.25})$$

p_1 and p_2 are the distinct solutions of the equation $l_4(p) = 0$ and p_3 is the solution of equation $l_2(p) = 0$. Roots that have the same sign of the imaginary part have to be chosen.

The matrix m_{ij} (equation A.18) is redefined as follows:

$$\left. \begin{aligned} m_{1i} &= S'_{11}p_i^2 - S'_{16}p_i + S'_{12} \\ m_{2i} &= S'_{21}p_i - S'_{26} + \frac{S'_{22}}{p_i} \\ m_{3i} &= 0 \end{aligned} \right\} \text{ for } i \in \{1, 2\} \text{ and } \begin{aligned} m_{13} &= 0 \\ m_{23} &= 0 \\ m_{33} &= S'_{45} - \frac{S'_{44}}{p_3} \end{aligned} \quad (\text{A.26})$$

These special cases lead to a solution in displacement identical to the solution given by Sih, Paris and Irwin [Sih et al., 1965] developed for materials with $z = 0$ presenting a plane of symmetry. Hoenig [Hoenig, 1982] and then Banks-Sills and co-workers [Banks-Sills et al., 2005][Banks-Sills et al., 2007] presented these solutions as follows:

$$u_i = \sqrt{\frac{2r}{\pi}} \Re \left[\sum_{j=1}^3 m_{ij} B_j Q_j \right] \quad (\text{A.27})$$

The stress is written as follows:

$$\begin{aligned}
 \sigma_{xx} &= \frac{1}{\sqrt{2\pi r}} \Re \left[\sum_{i=1}^2 \frac{p_i^2 B_i}{Q_i} \right] \\
 \sigma_{yy} &= \frac{1}{\sqrt{2\pi r}} \Re \left[\sum_{i=1}^2 \frac{B_i}{Q_i} \right] \\
 \sigma_{xy} &= -\frac{1}{\sqrt{2\pi r}} \Re \left[\sum_{i=1}^2 \frac{p_i B_i}{Q_i} \right] \\
 \sigma_{zx} &= \frac{1}{\sqrt{2\pi r}} \Re \left[\frac{p_3 B_3}{Q_3} \right] \\
 \sigma_{zy} &= -\frac{1}{\sqrt{2\pi r}} \Re \left[\frac{B_3}{Q_3} \right]
 \end{aligned} \tag{A.28}$$

where:

$$\begin{pmatrix} B_1 \\ B_2 \\ B_3 \end{pmatrix} = \frac{1}{p_2 - p_1} \begin{pmatrix} p_2 & 1 & 0 \\ -p_1 & -1 & 0 \\ 0 & 0 & p_1 - p_2 \end{pmatrix} \begin{pmatrix} K_I^\infty \\ K_{II}^\infty \\ K_{III}^\infty \end{pmatrix} \tag{A.29}$$

Interaction integral method for a general anisotropic case

The interaction integral method is an energy based method used to evaluate the stress intensity factors near the crack tip. This section presents this method as given in [Banks-Sills et al., 2005], [Banks-Sills et al., 2007] for the case of a generally anisotropic material based on Hoenig's [Hoenig, 1982] analytical solutions.

The J-integral defined by Rice [Rice, 1968] can be written as:

$$J = \int_{\Gamma} \left(W dy - T_i \cdot \frac{\partial u_i}{\partial x} \right) ds \quad (\text{B.1})$$

$T_i = \sigma_{ij}n_j$ is the traction vector, u_i is the displacement vector, n_i is the outward normal to the contour Γ describing the integration path and ds is the element of the arc length along this contour as shown in figure B.1.

The strain-energy density W is defined by:

$$W = \frac{1}{2} \sigma_{ij} \varepsilon_{ij} \quad (\text{B.2})$$

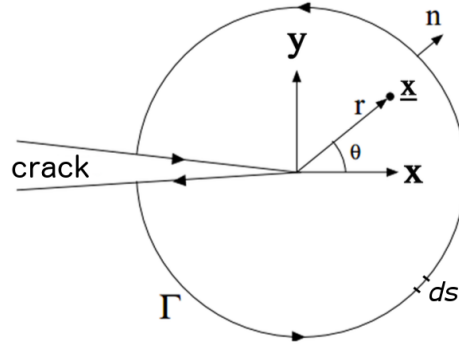


Figure B.1: Crack tip coordinates and path of the J-integral

The material behavior is linear elastic. Thus, it is possible to superpose two equilibrium solutions:

$$\begin{aligned}
 \sigma_{ij} &= \sigma_{ij}^{(1)} + \sigma_{ij}^{(2)} \\
 \varepsilon_{ij} &= \varepsilon_{ij}^{(1)} + \varepsilon_{ij}^{(2)} \\
 u_i &= u_i^{(1)} + u_i^{(2)}
 \end{aligned} \tag{B.3}$$

The stress intensity factors associated to these solutions are:

$$\begin{aligned}
 K_I &= K_I^{(1)} + K_I^{(2)} \\
 K_{II} &= K_{II}^{(1)} + K_{II}^{(2)} \\
 K_{III} &= K_{III}^{(1)} + K_{III}^{(2)}
 \end{aligned} \tag{B.4}$$

The solution (1) is the one we are looking for. The fields of this solution are obtained based on finite element simulations. The solution (2) contains three cases corresponding to the three fracture modes with a unit intensity factor for each mode. These auxiliary solutions are obtained analytically based on Hoenig's asymptotic solutions of stress and displacement presented in equations A.15 and A.16. The three cases are as follows:

$$\begin{aligned}
 K_I^{(2a)} &= 1, & K_{II}^{(2a)} &= 0, & K_{III}^{(2a)} &= 0 \\
 K_I^{(2b)} &= 0, & K_{II}^{(2b)} &= 1, & K_{III}^{(2b)} &= 0 \\
 K_I^{(2c)} &= 0, & K_{II}^{(2c)} &= 0, & K_{III}^{(2c)} &= 1
 \end{aligned} \tag{B.5}$$

Based on the superposition of the two solutions (1) and (2) for different case a, b and c , the J-integral can be written for a given loading case $\alpha = \{a, b, c\}$ as follows:

$$J = J^{(1)} + J^{(2\alpha)} + M^{(1,2\alpha)} \tag{B.6}$$

with $M^{(1,2\alpha)}$ is the interaction integral between both solutions (1) and (2α) . This integral is evaluated by two different ways.

The crack closure integral

Based on the crack closure integral, Hoenig [Hoenig, 1982] expressed the J-integral for a generally anisotropic material as follows:

$$J = \frac{1}{2} \left[K_I \Im(m_{2i} N_{ij}^{-1} K_j) + K_{II} \Im(m_{1i} N_{ij}^{-1} K_j) + K_{III} \Im(m_{3i} N_{ij}^{-1} K_j) \right] \quad (\text{B.7})$$

with $\Im(*)$ is the imaginary part of $*$. Matrices N_{ij} and m_{ij} depend on material parameters. They are detailed in Appendix A.

When expressions B.6, B.4 and B.5 are implemented in B.7, the interaction integral of different loading cases can be written as follows:

$$\begin{aligned} M^{(1,2a)} &= -\frac{1}{2} \left[2K_I^{(1)} \Im(m_{2i} N_{i2}^{-1}) + K_{II}^{(1)} \Im(m_{1i} N_{i1}^{-1} + m_{2i} N_{i2}^{-1}) + K_{III}^{(1)} \Im(m_{2i} N_{i3}^{-1} + m_{3i} N_{i1}^{-1}) \right] \\ M^{(1,2b)} &= -\frac{1}{2} \left[K_I^{(1)} \Im(m_{2i} N_{i2}^{-1} + m_{1i} N_{i1}^{-1}) + 2K_{II}^{(1)} \Im(m_{1i} N_{i2}^{-1}) + K_{III}^{(1)} \Im(m_{1i} N_{i3}^{-1} + m_{3i} N_{i2}^{-1}) \right] \\ &\text{and} \\ M^{(1,2b)} &= -\frac{1}{2} \left[K_I^{(1)} \Im(m_{2i} N_{i3}^{-1} + m_{3i} N_{i1}^{-1}) + K_{II}^{(1)} \Im(m_{1i} N_{i3}^{-1} + m_{3i} N_{i2}^{-1}) + 2K_{III}^{(1)} \Im(m_{3i} N_{i3}^{-1}) \right] \end{aligned} \quad (\text{B.8})$$

The three-dimensional J-integral

The three-dimensional integral can be written as follows: [Shih et al., 1986], [Bank-Sills et al., 1999]:

$$\int_0^{L_N} \mathcal{G}(z) l_x^{(N)} n_x dz = \int_V \left[\sigma_{ij} \frac{\partial u_i}{\partial x_1} - W \delta_{1j} \right] \frac{\partial q_1}{\partial x_j} dV \quad (\text{B.9})$$

with \mathcal{G} the energy release rate along the crack front in the z direction. For a given element N , $\delta l = l_x^{(N)} n_x$ is the normalized virtual crack extension with n_x is the unit vector normal to the crack front in the direction \vec{x} (see figure B.2a). The volume V is the volume containing the crack front limited by the surface S as shown on figure B.2b. The function q_1 is equal to l_x along the crack front and is equal to zero on S .

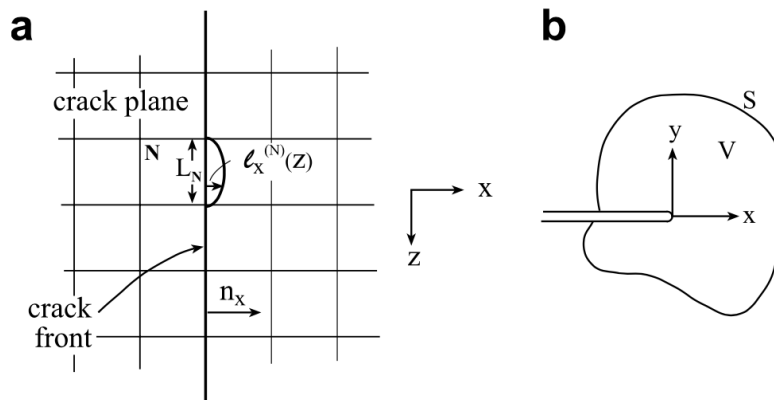


Figure B.2: (a) An illustration of the finite element mesh on the crack plane and front with the virtual crack extension δl of an element N and (b) the volume V containing the crack front (figure from [Banks-Sills et al., 2007])

The stress and the displacement are implemented in the expression of the J-integral presented in equation B.1.

$$\begin{aligned}
J^{(1)} &= \int_{\Gamma} \left(W^{(1)} dy - T_i^{(1)} \cdot \frac{\partial u_i^{(1)}}{\partial x} \right) ds \\
J^{(2\alpha)} &= \int_{\Gamma} \left(W^{(2\alpha)} dy - T_i^{(2\alpha)} \cdot \frac{\partial u_i^{(2\alpha)}}{\partial x} \right) ds \\
M^{(1,2\alpha)} &= \int_{\Gamma} \left(W^{(1,2\alpha)} dy - T_i^{(1)} \cdot \frac{\partial u_i^{(2\alpha)}}{\partial x} - T_i^{(2\alpha)} \cdot \frac{\partial u_i^{(1)}}{\partial x} \right) ds
\end{aligned} \tag{B.10}$$

with $W^{(1,2\alpha)}$ the interaction energy density

$$W^{(1,2\alpha)} = \sigma_{ij}^{(1)} \varepsilon_{ij}^{(2\alpha)} = \sigma_{ij}^{(2\alpha)} \varepsilon_{ij}^{(1)} \tag{B.11}$$

The contour interaction integral $M^{(1,2\alpha)}$ is transformed to a volume integral based on equation B.9. This gives the following expression:

$$M^{(1,2\alpha)} = \frac{1}{A_x} \int_V \left[\sigma_{ij}^{(1)} \frac{\partial u_i^{(2\alpha)}}{\partial x_1} + \sigma_{ij}^{(2\alpha)} \frac{\partial u_i^{(1)}}{\partial x_1} - W^{(1,2\alpha)} \delta_{1j} \right] \frac{\partial q_1}{\partial x_j} dV \tag{B.12}$$

with $\alpha = \{a, b, c\}$. A_x is the virtual extension area:

$$A_x = \int_0^{L_N} l_x^{(N)}(z) dz \tag{B.13}$$

Stress intensity factors extraction

We recall that the aim of this analysis is to determine the stress intensity factors $K_I^{(1)}$, $K_{II}^{(1)}$ and $K_{III}^{(1)}$ of a given finite element simulation (1). To do so, the interaction integral M is evaluated by two different ways. On the first hand, the stress, strain and displacement fields are extracted from a finite element simulation. They are used in the expression of the volume interaction integral in B.12 as solution (1). Solutions (2 α) in stress, strain and displacement are computed analytically for each loading case ($\alpha = a, b, c$) based on Hoenig's analytical solutions presented in equations A.15 and A.16. Thus, three interaction volume integrals $M^{1,2\alpha}$ are computed.

On the other hand, integrals $M^{1,2\alpha}$ can be given as function of $K_I^{(1)}$, $K_{II}^{(1)}$ and $K_{III}^{(1)}$ based on expressions B.8.

Finally, a linear system of three simultaneous equations is obtained for $K_I^{(1)}$, $K_{II}^{(1)}$ and $K_{III}^{(1)}$ which leads to the evaluation of these stress intensity factors.

Bibliography

- [Abdul-Latif et al., 1994] Abdul-Latif, A., Clavel, M., Ferney, V., and Saanouni, K. (1994). On the modeling of nonproportional cyclic plasticity of waspaloy. *Journal of engineering materials and technology*, 116(1):35–44.
- [Arakere et al., 2009] Arakere, N., Siddiqui, S., and Ebrahimi, F. (2009). Evolution of plasticity in notched Ni-base superalloy single crystals. *International Journal of Solids and Structures*, 46(16):3027–3044.
- [Arakere et al., 2008] Arakere, N. K., Knudsen, E. C., Wells, D., McGill, P., and Swanson, G. R. (2008). Determination of mixed-mode stress intensity factors, fracture toughness, and crack turning angle for anisotropic foam material. *International Journal of Solids and Structures*, 45(18-19):4936–4951.
- [Arakere et al., 2004] Arakere, N. K., Siddiqui, S., Magnan, S., Ebrahimi, F., and Forero, L. E. (2004). Investigation of three-dimensional stress fields and slip systems for FCC single crystal superalloy notched specimens. In *ASME Turbo Expo 2004: Power for Land, Sea, and Air*, pages 207–215. American Society of Mechanical Engineers.
- [Armstrong and Frederick, 1966] Armstrong, P. J. and Frederick, C. (1966). *A mathematical representation of the multiaxial Bauschinger effect*, volume 731. Central Electricity Generating Board [and] Berkeley Nuclear Laboratories
- [Aubin, 2001] Aubin, V. (2001). *Plasticité cyclique d’un acier inoxydable austéno-ferritique sous chargement biaxial non-proportionnel*. PhD thesis, Université des Sciences et Technologie de Lille-Lille I; Ecole Centrale de Lille.
- [Aubin, 2008] Aubin, V. (2008). *Dialogue modèle-expérience en fatigue oligocyclique des aciers inoxydables*. PhD thesis, Université des Sciences et Technologie de Lille-Lille I.
- [Aubin et al., 2002] Aubin, V., Quaegebeur, P., and Degallaix, S. (2002). Évolution de la surface de plasticité sous chargement biaxial dans un acier inoxydable duplex. In *Journal de Physique IV (Proceedings)*, volume 12, pages 195–202. EDP sciences.
- [Bank-Sills et al., 1999] Bank-Sills, L., Travitzky, N., Ashkenazi, D., and Eliasi, R. (1999). A methodology for measuring interface fracture properties of composite materials. *International Journal of Fracture*, 99(3):143–161.
- [Banks-Sills et al., 2005] Banks-Sills, L., Hershkovitz, I., Wawrzynek, P. A., Eliasi, R., and Ingraffea, A. R. (2005). Methods for calculating stress intensity factors in anisotropic materials: Part I— $z=0$ is a symmetric plane. *Engineering Fracture Mechanics*, 72(15):2328–2358.

- [Banks-Sills et al., 2007] Banks-Sills, L., Wawrzynek, P. A., Carter, B., Ingraffea, A. R., and Hershkovitz, I. (2007). Methods for calculating stress intensity factors in anisotropic materials: Part II—arbitrary geometry. *Engineering Fracture Mechanics*, 74(8):1293–1307.
- [Barnett and Asaro, 1972] Barnett, D. and Asaro, R. (1972). The fracture mechanics of slit-like cracks in anisotropic elastic media. *Journal of the Mechanics and Physics of Solids*, 20(6):353–366.
- [Barré de Saint Venant and Navier, 1864] Barré de Saint Venant, J. and Navier, C. (1864). Résumé des leçons sur l’application de la mécanique.
- [Belytschko and Black, 1999] Belytschko, T. and Black, T. (1999). Elastic crack growth in finite elements with minimal remeshing. *International journal for numerical methods in engineering*, 45(5):601–620.
- [Benallal and Marquis, 1987] Benallal, A. and Marquis, D. (1987). Constitutive equations for nonproportional cyclic elasto-viscoplasticity. *Journal of engineering materials and technology*, 109(4):326–336.
- [Bernard et al., 2012] Bernard, P.-E., Moës, N., and Chevaugeon, N. (2012). Damage growth modeling using the Thick Level Set (TLS) approach: Efficient discretization for quasi-static loadings. *Computer Methods in Applied Mechanics and Engineering*, 233:11–27.
- [Bettge and Österle, 1999] Bettge, D. and Österle, W. (1999). “cube slip” in near-[111] oriented specimens of a single-crystal Nickel-base superalloy. *Scripta Materialia*.
- [Bonnand, 2006] Bonnand, V. (2006). *Etude de l’endommagement d’un superalliage monocristallin en fatigue thermo-mécanique multiaxiale*. PhD thesis, Paris, ENMP.
- [Brugier, 2017] Brugier, F. (2017). *Modèle condensé de plasticité pour la fissuration et influence de la contrainte T*. PhD thesis, École normale supérieure Paris-Saclay.
- [Bui, 1969] Bui, H. D. (1969). *Etude de l’évolution de la frontière du domaine élastique avec l’écroutissage et relations de comportement élasto-plastique des métaux cubiques*. PhD thesis, Université Pierre et Marie Curie.
- [Calloch, 1997] Calloch, S. (1997). *Essais triaxiaux non-proportionnels et ingénierie des modèles de plasticité cyclique*. Laboratoire de mécanique et technologie.
- [Crone and Shield, 2001] Crone, W. and Shield, T. (2001). Experimental study of the deformation near a notch tip in copper and Copper–Beryllium single crystals. *Journal of the Mechanics and Physics of Solids*, 49(12):2819–2838.
- [Crone and Shield, 2003] Crone, W. and Shield, T. (2003). An experimental study of the effect of hardening on plastic deformation at notch tips in metallic single crystals. *Journal of the Mechanics and Physics of Solids*, 51(8):1623–1647.
- [Cuitino and Ortiz, 1996] Cuitino, A. and Ortiz, M. (1996). Three-dimensional crack-tip fields in four-point-bending copper single-crystal specimens. *Journal of the Mechanics and Physics of Solids*, 44(6):863–904.

- [Decreuse, 2010] Decreuse, P.-Y. (2010). *Fissuration en mode mixte I+ II non proportionnel: approche expérimentale et modélisation de la plasticité*. PhD thesis, École normale supérieure de Cachan-ENS Cachan.
- [Decreuse et al., 2009] Decreuse, P.-Y., Pommier, S., Gentot, L., and Pattofatto, S. (2009). History effect in fatigue crack growth under mixed-mode loading conditions. *International Journal of Fatigue*, 31(11-12):1733–1741.
- [Doquet, 1993] Doquet, V. (1993). Twinning and multiaxial cyclic plasticity of a low stacking-fault-energy fcc alloy. *Acta metallurgica et materialia*, 41(8):2451–2459.
- [Doquet and Clavel, 1996] Doquet, V. and Clavel, M. (1996). Stacking-fault energy and cyclic hardening of fcc solid solutions under multiaxial nonproportional loadings. In *Multiaxial Fatigue and Design*, pages 43–60. MEP, Londres.
- [Ebrahimi et al., 2006] Ebrahimi, F., Forero, L., Siddiqui, S., and Arakere, N. (2006). Effect of notch orientation on the evolution of plasticity in superalloy single crystals. *Materials Science and Engineering: A*, 426(1-2):214–220.
- [efatigue, 2008] efatigue (2008). Rainflow illustration.
- [Elber, 1971] Elber, W. (1971). The significance of fatigue crack closure. In *Damage tolerance in aircraft structures*. ASTM International.
- [Erdogan, 2000] Erdogan, F. (2000). Fracture mechanics. *International Journal of Solids and Structures*, 37(1):171–183.
- [Fedelich, 1999] Fedelich, B. (1999). A microstructure based constitutive model for the mechanical behavior at high temperatures of Nickel-base single crystal superalloys. *Computational Materials Science*, 16(1-4):248–258.
- [Fedelich, 2002] Fedelich, B. (2002). A microstructural model for the monotonic and the cyclic mechanical behavior of single crystals of superalloys at high temperatures. *International Journal of Plasticity*, 18(1):1–49.
- [Fleury, 1991] Fleury, É. (1991). *Endommagement du superalliage monocristallin AM1 en fatigue isotherme et anisotherme*. PhD thesis, Paris, ENMP.
- [Flouriot, 2004] Flouriot, S. (2004). Détermination expérimentale et simulation numérique des phénomènes de localisation de la déformation en pointe de fissure dans un monocristal cfc ph. d. *PhD Thesis, Ecole des Mines de Paris*.
- [Frémy, 2012] Frémy, F. (2012). *Fatigue crack growth in mixed mode I+III+III non proportionnal loading conditions in a 316 stainless steel : analyses of the effects of crack tip plasticity*. Thesis, École normale supérieure de Cachan - ENS Cachan.
- [Fremy et al., 2012] Fremy, F., Pommier, S., Galenne, E., and Courtin, S. (2012). A scaling approach to model history effects in fatigue crack growth under mixed mode I+ II+ III loading conditions for a 316l stainless steel. *International Journal of Fatigue*, 42:207–216.
- [Gao et al., 1992] Gao, H., Abbudi, M., and Barnett, D. (1992). Interfacial crack-tip field in anisotropic elastic solids. *Journal of the Mechanics and Physics of Solids*, 40(2):393–416.

- [Geuffrard, 2010] Geuffrard, M. (2010). *Amorçage et micro-propagation de fissure en fatigue à haute température à partir de défauts dans un superalliage monocristallin*. PhD thesis, École Nationale Supérieure des Mines de Paris.
- [Griffith, 1920] Griffith, A. (1920). The phenomena of rupture and flow in solids. *Phil. Trans. Roy. Soc., Ser. A*, 221:163–198.
- [Griffith, 1924] Griffith, A. (1924). The theory of rupture. In *First Int. Cong. Appl. Mech*, pages 55–63.
- [Hamam, 2006] Hamam, R. (2006). *Simulation de la propagation des fissures par fatigue dans les toiles des roues de train sous chargement à amplitude variable*. PhD thesis, École normale supérieure de Cachan-ENS Cachan.
- [Hamam et al., 2007] Hamam, R., Pommier, S., and Bumbieler, F. (2007). Variable amplitude fatigue crack growth, experimental results and modeling. *International Journal of Fatigue*, 29(9-11):1634–1646.
- [Hanriot, 1993] Hanriot, F. (1993). *Etude du comportement du superalliage monocristallin AM1 sous sollicitations cycliques*. PhD thesis, Thèse de doctorat, ENSMP, 25 mai.
- [Hoenig, 1982] Hoenig, A. (1982). Near-tip behavior of a crack in a plane anisotropic elastic body. *Engineering Fracture Mechanics*, 16(3):393–403.
- [Hutchinson, 1968] Hutchinson, J. (1968). Plastic stress and strain fields at a crack tip. *Journal of the Mechanics and Physics of Solids*, 16(5):337–342.
- [Inglis, 1913] Inglis, C. E. (1913). Stresses in a plate due to the presence of cracks and sharp corners. *Trans Inst Naval Archit*, 55:219–241.
- [Irwin, 1960a] Irwin, G. (1960a). Plastic zone near a crack and fracture toughness. *Seventh Sagamore Ordnance Materials Research Conference Proceedings*, 4:63–78.
- [Irwin and Kies, 1954] Irwin, G. and Kies, J. (1954). Welding j. *Res. Suppl*, 33:1935.
- [Irwin, 1948] Irwin, G. R. (1948). Fracture dynamics. *Fracturing of metals*, pages 147–166.
- [Irwin, 1957] Irwin, G. R. (1957). Analysis of stresses and strains near the end of a crack traversing a plate. *J. appl. Mech.*
- [Irwin, 1958] Irwin, G. R. (1958). Fracture. In Flügge, S., editor, *Elasticity and Plasticity / Elastizität und Plastizität*, Handbuch der Physik / Encyclopedia of Physics, pages 551–590. Springer Berlin Heidelberg.
- [Irwin, 1960b] Irwin, G. R. (1960b). Fracture mode transition for a crack traversing a plate. *Journal of Basic Engineering*, 82(2):417–423.
- [Ishikawa, 1980] Ishikawa, H. (1980). J integral of a mixed mode crack and its application. In *Proc. 3rd Int. Conf. Mechanical Behaviour of Materials.*, volume 3, pages 447–455. Pergamon.
- [Kaminski, 2007] Kaminski, M. (2007). *Modélisation de l'endommagement en fatigue des superalliages monocristallins pour aubes de turbines en zone de concentration de contrainte*. PhD thesis, École Nationale Supérieure des Mines de Paris.

- [Karhunen, 1947] Karhunen, K. (1947). *Über lineare Methoden in der Wahrscheinlichkeitsrechnung*, volume 37. Sana.
- [Khan and Wang, 1993] Khan, A. S. and Wang, X. (1993). An experimental study on subsequent yield surface after finite shear prestraining. *International Journal of Plasticity*, 9(8):889–905.
- [Laird, 1967] Laird, C. (1967). The influence of metallurgical structure on the mechanisms of fatigue crack propagation. In *Fatigue crack propagation*. ASTM International.
- [Lamé, 1833] Lamé, G. (1833). *Mémoire sur l'équilibre intérieur des corps solides homogènes*.
- [Lekhnitskii, 1963] Lekhnitskii, S. (1963). *Theory of elasticity of an anisotropic elastic body*. Holden-Day, San Francisco.
- [Lemaitre and Chaboche, 1994] Lemaitre, J. and Chaboche, J.-L. (1994). *Mechanics of solid materials*. Cambridge university press.
- [Li, 1989] Li, C. (1989). Vector ctd criterion applied to mixed mode fatigue crack growth. *Fatigue & Fracture of Engineering Materials & Structures*, 12(1):59–65.
- [Love, 1906] Love, A. E. H. (1906). *A treatise on the mathematical theory of elasticity*. at the University Press.
- [Ludwig et al., 2009] Ludwig, W., King, A., Reischig, P., Herbig, M., Lauridsen, E. M., Schmidt, S., Proudhon, H., Forest, S., Cloetens, P., Du Roscoat, S. R., et al. (2009). New opportunities for 3D materials science of polycrystalline materials at the micrometre lengthscale by combined use of X-ray diffraction and X-ray imaging. *Materials Science and Engineering: A*, 524(1-2):69–76.
- [Marchal, 2006] Marchal, N. (2006). *Propagation de fissure en fatigue-fluage à haute température de superalliages monocristallins à base de Nickel*. PhD thesis, École Nationale Supérieure des Mines de Paris.
- [Matsuishi and Endo, 1968] Matsuishi, M. and Endo, T. (1968). Fatigue of metals subjected to varying stress. *Japan Society of Mechanical Engineers, Fukuoka, Japan*, 68(2):37–40.
- [McInnes and Meehan, 2008] McInnes, C. and Meehan, P. (2008). Equivalence of four-point and three-point rainflow cycle counting algorithms. *International journal of fatigue*, 30(3):547–559.
- [Méric and Cailletaud, 1991] Méric, L. and Cailletaud, G. (1991). Single crystal modeling for structural calculations: Part 2—Finite element implementation. *Journal of Engineering Materials and Technology*, 113(1):171–182.
- [Méric et al., 1991] Méric, L., Poubanne, P., and Cailletaud, G. (1991). Single crystal modeling for structural calculations: Part 1—Model presentation. *Journal of Engineering Materials and Technology*, 113(1):162–170.
- [Metallurgyandmaterials.wordpress.com, 2015] Metallurgyandmaterials.wordpress.com (2015). Liberty ship s.s. schenectady failure. [Online; accessed December 25, 2015].

- [Moës et al., 1999] Moës, N., Dolbow, J., and Belytschko, T. (1999). A finite element method for crack growth without remeshing. *International journal for numerical methods in engineering*, 46(1):131–150.
- [Moës et al., 2002] Moës, N., Gravouil, A., and Belytschko, T. (2002). Non-planar 3d crack growth by the extended finite element and level sets—Part I: Mechanical model. *International Journal for Numerical Methods in Engineering*, 53(11):2549–2568.
- [Moës et al., 2011] Moës, N., Stolz, C., Bernard, P.-E., and Chevaugeon, N. (2011). A level set based model for damage growth: the thick level set approach. *International Journal for Numerical Methods in Engineering*, 86(3):358–380.
- [Morice, 2014] Morice, E. (2014). *Fissuration dans les matériaux quasi-fragiles: approche numérique et expérimentale pour la détermination d’un modèle incrémental à variables condensées*. PhD thesis, École normale supérieure de Cachan-ENS Cachan.
- [Neumann, 1969] Neumann, P. (1969). Coarse slip model of fatigue. *Acta metallurgica*, 17(9):1219–1225.
- [Nouailhas, 1990] Nouailhas, D. (1990). Lois de comportement en viscoplasticité cyclique anisotrope: application au cas des matériaux à symétrie cubique. *La Recherche aérospatiale*, (3):11–28.
- [Nouailhas and Cailletaud, 1995] Nouailhas, D. and Cailletaud, G. (1995). Tension-torsion behavior of single-crystal superalloys: experiment and finite element analysis. *International Journal of Plasticity*, 11(4):451–470.
- [Nouailhas and Culié, 1991] Nouailhas, D. and Culié, J. (1991). Development and application of a model for single-crystal superalloys. *ONERA, TP no. 1991-214*, page 11.
- [Orowan, 1948] Orowan, E. (1948). Fracture and strength of solids. *Reports on Progress in Physics*, 12:183.
- [Paris, 1957] Paris, P. (1957). The mechanics of fracture propagation and solutions to fracture arrester problem. *Document D2-2195*.
- [Paris, 1961] Paris, P. C. (1961). A rational analytic theory of fatigue. *The trend in engineering*, 13:9.
- [Paris, 2014] Paris, P. C. (2014). A brief history of the crack tip stress intensity factor and its application.
- [Pelloux, 1969] Pelloux, R. (1969). Mechanism of formation of ductile fatigue striations. *Transaction. American Society Mechanical Engineering*, 62:281–285.
- [Philipp et al., 2013] Philipp, S., A Sar, F., and Gudmundsson, A. (2013). Effects of mechanical layering on hydrofracture emplacement and fluid transport in reservoirs. *Frontiers in Earth Science*, 1.
- [Philipps and Lee, 1979] Philipps, A. and Lee, C.-W. (1979). Yield surfaces and loading surfaces—experiments and recommendations. *International Journal of Solids and Structures*, 15(9):715–729.

- [Pommier, 2002] Pommier, S. (2002). Plane strain crack closure and cyclic hardening. *Engineering Fracture Mechanics*, 69(1):25–44.
- [Pommier, 2016] Pommier, S. (2016). Memory effects in variable amplitude and multiaxial fatigue crack growth: an incremental approach. *Procedia Structural Integrity*, 2:50–57.
- [Pommier, 2017] Pommier, S. (2017). Basics elements on linear elastic fracture mechanics and crack growth modeling. Lecture.
- [Pommier and Hamam, 2007] Pommier, S. and Hamam, R. (2007). Incremental model for fatigue crack growth based on a displacement partitioning hypothesis of mode I elastic–plastic displacement fields. *Fatigue & Fracture of Engineering Materials & Structures*, 30(7):582–598.
- [Pommier et al., 2009] Pommier, S., Lopez-crespo, P., and Decreuse, P. (2009). A multi-scale approach to condense the cyclic elastic-plastic behaviour of the crack tip region into an extended constitutive model. *Fatigue & Fracture of Engineering Materials & Structures*, 32(11):899–915.
- [Pommier and Risbet, 2005] Pommier, S. and Risbet, M. (2005). Time-derivative equations for fatigue crack growth in metals. *International Journal of fracture*, 131(1):79–106.
- [Proudhon et al., 2017] Proudhon, H., Li, J., Ludwig, W., Roos, A., and Forest, S. (2017). Simulation of short fatigue crack propagation in a 3d experimental microstructure. *Advanced Engineering Materials*, 19(8):1600721.
- [Raju et al., 1988] Raju, I., Crews Jr, J., and Aminpour, M. (1988). Convergence of strain energy release rate components for edge-delaminated composite laminates. *Engineering fracture mechanics*, 30(3):383–396.
- [Randle and Engler, 2014] Randle, V. and Engler, O. (2014). *Introduction to texture analysis: microtexture, microtexture and orientation mapping*. CRC press.
- [Réthoré et al., 2010] Réthoré, J., Roux, S., and Hild, F. (2010). Hybrid analytical and extended finite element method (HAX-FEM): A new enrichment procedure for cracked solids. *International Journal for Numerical Methods in Engineering*, 81(3):269–285.
- [Rice et al., 1990] Rice, J., Hawk, D., and Asaro, R. (1990). Crack tip fields in ductile crystals. In *Non-linear fracture*, pages 301–321. Springer.
- [Rice and Rosengren, 1968] Rice, J. and Rosengren, G. F. (1968). Plane strain deformation near a crack tip in a power-law hardening material. *Journal of the Mechanics and Physics of Solids*, 16(1):1–12.
- [Rice and Saeedvafa, 1987] Rice, J. and Saeedvafa, M. (1987). Crack tip singular fields in ductile crystals with taylor power-law hardening. *J. Mech. Phys. Solids*, 36:189–214.
- [Rice, 1968] Rice, J. R. (1968). A path independent integral and the approximate analysis of strain concentration by notches and cracks. *Journal of applied mechanics*, 35(2):379–386.
- [Rice, 1987] Rice, J. R. (1987). Tensile crack tip fields in elastic-ideally plastic crystals. *Mechanics of Materials*, 6(4):317–335.

- [Rice and Thomson, 1974] Rice, J. R. and Thomson, R. (1974). Ductile versus brittle behaviour of crystals. *Philosophical magazine*, 29(1):73–97.
- [Risbet and Feaugas, 2008] Risbet, M. and Feaugas, X. (2008). Some comments about fatigue crack initiation in relation to cyclic slip irreversibility. *Engineering Fracture Mechanics*, 75(11):3511–3519.
- [Risbet et al., 2018] Risbet, M., Feaugas, X., BIGERELLE, M., ZHANG, E., et al. (2018). Surface roughness based characterization of slip band for damage initiation in a Nickel base superalloy. *Materials Science*, 24(1):112–117.
- [Ruiz-Sabariego and Pommier, 2009] Ruiz-Sabariego, J. A. and Pommier, S. (2009). Oxidation assisted fatigue crack growth under complex non-isothermal loading conditions in a Nickel base superalloy. *International Journal of Fatigue*, 31(11-12):1724–1732.
- [Sabnis, 2012] Sabnis, P. (2012). *Modelling the propagation and bifurcation of plasticity induced cracks in Nickel base single crystal superalloys*. PhD thesis, Ecole Nationale Supérieure des Mines de Paris.
- [Sabnis et al., 2012] Sabnis, P., Mazière, M., Forest, S., Arakere, N. K., and Ebrahimi, F. (2012). Effect of secondary orientation on notch-tip plasticity in superalloy single crystals. *International Journal of Plasticity*, 28(1):102–123.
- [Saeedvafa and Rice, 1989] Saeedvafa, M. and Rice, J. R. (1989). Crack tip singular fields in ductile crystals with Taylor power-law hardening: II: Plane strain. *Journal of the Mechanics and Physics of Solids*, 37(6):673–691.
- [Sander and Richard, 2006] Sander, M. and Richard, H. (2006). Experimental and numerical investigations on the influence of the loading direction on the fatigue crack growth. *International Journal of Fatigue*, 28(5-6):583–591.
- [Schmid and Boas, 1935] Schmid, E. and Boas, W. (1935). Crystal plasticity with a special consideration for metals. *J. Springer*, 17.
- [Shih et al., 1986] Shih, C., Moran, B., and Nakamura, T. (1986). Energy release rate along a three-dimensional crack front in a thermally stressed body. *International Journal of Fracture*, 30(2):79–102.
- [Shih and Asaro, 1988] Shih, C. F. and Asaro, R. J. (1988). Elastic-plastic analysis of cracks on bimaterial interfaces: Part I—small scale yielding. *Journal of Applied Mechanics*, 55(2):299–316.
- [Sih et al., 1965] Sih, G. C., Paris, P., and Irwin, G. R. (1965). On cracks in rectilinearly anisotropic bodies. *International Journal of Fracture Mechanics*, 1(3):189–203.
- [Stroh, 1958] Stroh, A. (1958). Dislocations and cracks in anisotropic elasticity. *Philosophical magazine*, 3(30):625–646.
- [Stroh, 1962] Stroh, A. (1962). Steady state problems in anisotropic elasticity. *Journal of Mathematics and Physics*, 41(1-4):77–103.
- [Sun and Jih, 1987] Sun, C. T. and Jih, C. (1987). On strain energy release rates for interfacial cracks in bi-material media. *Engineering Fracture Mechanics*, 28(1):13–20.

- [Suo, 1990] Suo, Z. (1990). Singularities, interfaces and cracks in dissimilar anisotropic media. *Proc. R. Soc. Lond. A*, 427(1873):331–358.
- [Suresh, 1983] Suresh, S. (1983). Micromechanisms of fatigue crack growth retardation following overloads. *Engineering Fracture Mechanics*, 18(3):577–593.
- [Suresh, 1985] Suresh, S. (1985). Further remarks on the micromechanisms of fatigue crack growth retardation following overloads. *Engineering fracture mechanics*, 21(6):1169–1170.
- [Suresh, 1998] Suresh, S. (1998). *Fatigue of materials*. Cambridge university press.
- [Tanaka, 1994] Tanaka, E. (1994). A nonproportionality parameter and a cyclic viscoplastic constitutive model taking into account amplitude dependences and memory effects of isotropic hardening. *European journal of mechanics. A. Solids*, 13(2):155–173.
- [Timoshenko, 1983] Timoshenko, S. (1983). *History of strength of materials: with a brief account of the history of theory of elasticity and theory of structures*. Courier Corporation.
- [Ting, 1996] Ting, T. C.-t. (1996). *Anisotropic elasticity: theory and applications*. Number 45. Oxford University Press on Demand.
- [Todhunter and Pearson, 1886] Todhunter, I. and Pearson, K. (1886). *A history of the theory of elasticity and of the strength of materials: from Galilei to the present time. Vol. 1. Galilei to Saint-Venant, art. 995*. Cambridge University Press.
- [Tresca, 1869] Tresca, H. (1869). *Mémoires sur l'écoulement des corps solides*. Imprimerie impériale.
- [Turk and Levoy, 1994] Turk, G. and Levoy, M. (1994). Zippered polygon meshes from range images. In *Proceedings of the 21st annual conference on Computer graphics and interactive techniques*, pages 311–318. ACM.
- [Vilchaise et al., 2002] Vilchaise, P., Sabatier, L., and Girard, J. (2002). On slip band features and crack initiation in fatigued 316l austenitic stainless steel: Part 1: Analysis by electron back-scattered diffraction and atomic force microscopy. *Materials Science and Engineering: A*, 323(1-2):377–385.
- [Westbrooke, 2005] Westbrooke, E. F. (2005). *Effect of crystallographic orientation on plastic deformation of single crystal Nickel-base superalloys*.
- [Westergaard, 1939] Westergaard, H. M. (1939). Bearing pressures and cracks. *Journal of applied mechanics*, 6(2):A49–A53.
- [Wheeler, 1972] Wheeler, O. E. (1972). Spectrum loading and crack growth. *Journal of basic engineering*, 94(1):181–186.
- [Willenborg et al., 1971] Willenborg, J., Engle, R., and Wood, H. (1971). A crack growth retardation model using an effective stress concept. Technical report, Air Force Flight Dynamics Lab Wright-Patterson Afb Oh.
- [Williams, 1957] Williams, M. L. (1957). On the Stress Distribution at the Base of a Stationary Crack. *Journal of Applied Mechanics*, 24(1):109–114.

- [Wu and Yeh, 1991] Wu, H. C. and Yeh, W. C. (1991). On the experimental determination of yield surfaces and some results of annealed 304 stainless steel. *International Journal of Plasticity*, 7(8):803–826.
- [Zhang, 2016] Zhang, W. (2016). *Fatigue crack growth in large scale yielding condition*. Thesis, Université Paris-Saclay.

Titre : Stratégie de réduction de modèle pour prédire les effets mémoire de la plasticité en fissuration par fatigue dans un milieu anisotrope: application à la plasticité cristalline.

Mots clés : Fissuration par fatigue, Plasticité condensée, Réduction de modèle, Anisotropie, Plasticité cristalline

Résumé : Les aubes des turbines à haute pression des réacteurs d'avion subissent des chargements complexes dans un environnement réactif. Prédire leur durée de vie peut nécessiter une approche en tolérance aux dommages basée sur la prédiction de la propagation d'une fissure supposée. Mais cette approche est confrontée au comportement non linéaire sous des chargements à amplitudes variables et au coût énorme des calculs elasto-plastiques des structures 3D complexes sur des millions de cycles. Dans ce cadre, un modèle incrémental de fissuration a été proposé. Ce modèle est basé sur la plasticité comme mécanisme principal de propagation de fissure par fatigue pure. Cette modélisation passe par une réduction de modèle de type POD. La plasticité en pointe de la fissure est alors modélisée par un nombre réduit de variables non locales ($\underline{\dot{K}}^\infty, \underline{\dot{\rho}}$) et des variables internes. Un ensemble d'hypothèses doit être respecté pour garantir la validité de cette modélisation. Pour décliner ce modèle dans le cas d'un matériau anisotrope

représentatif du comportement des monocristaux, une première étude a été faite sur le cas d'une élasticité cubique avec de la plasticité de Von-Mises. Une stratégie a été proposée pour identifier un modèle matériau basé sur les facteurs d'intensité non locaux ($\underline{\dot{K}}^\infty, \underline{\dot{\rho}}$). Cette stratégie comporte une détermination de la fonction critère basée sur les solutions élastiques en anisotrope. L'étude des directions d'écoulement plastique avec les variables non locales montre une forte dépendance à l'anisotropie élastique du modèle même avec une plasticité associée de Von-Mises. La stratégie comporte également une identification des variables internes. Dans la deuxième partie, le problème d'une fissure avec un modèle de plasticité cristalline a été traité. L'activation de différents systèmes de glissement a été alors prise en compte dans la modélisation. Finalement, différentes méthodologies ont été explorées en vue de transposer le modèle local de plasticité cristalline à l'échelle non locale de la région en pointe de la fissure.

Title: A model reduction strategy to predict plasticity induced memory effects in fatigue crack growth in an anisotropic medium: application to crystal plasticity.

Keywords: Fatigue crack growth, Condensed plasticity, Model reduction, Anisotropy, Crystal plasticity

Abstract: The fatigue life prediction of high pressure turbine blades may require a damage tolerance approach based on the study of possible crack propagation. The nonlinear behavior of the material under complex nonproportional loadings and the high cost of running long and expensive elastic-plastic FE computations on complex 3D structures over millions of cycles are some major issues that may encounter this type of approach. Within this context, an incremental model was proposed based on plasticity as a main mechanism for fatigue crack growth. A model reduction strategy using the Proper Orthogonal Decomposition (POD) was used to reduce the cost of FEA. Based on a set of hypotheses, the number of the degrees of freedom of the problem is reduced drastically. The plasticity at the crack tip is finally described by a set of empirical equations of few nonlocal variables ($\underline{\dot{K}}^\infty, \underline{\dot{\rho}}$) and some internal variables. In order to apply this modeling strategy to the case of anisotropic materials

that represent the behavior of single crystals, a first study was done with cubic elasticity and a Von-Mises plasticity. Elastic and plastic reference fields, required to reduce the model, were determined. Then, a material model of the near crack tip region was proposed based on nonlocal intensity factors ($\underline{\dot{K}}^\infty, \underline{\dot{\rho}}$). A yield criterion function was proposed based on Hoenig's asymptotic solutions for anisotropic materials. The study of plastic flow directions with the nonlocal variables of the model shows a strong dependency on the cubic elasticity. A strategy to identify internal variables is proposed as well. In the second part, a crystal plasticity model was implemented. The activation of different slip systems was taken into account in the model reduction strategy. A kinematic basis was constructed for each slip system. Finally, a strategy was proposed to transpose the local crystal plasticity model to the nonlocal scale of the crack.